Semiconductors, Vol. 34, No. 2, 2000, pp. 123–140. Translated from Fizika i Tekhnika Poluprovodnikov, Vol. 34, No. 2, 2000, pp. 129–147.

REVIEW

Modification of Semiconductors with Proton Beams. A Review

V. V. Kozlovskiĭ*, V. A. Kozlov, and V. N. Lomasov***

** Ioffe Physicotechnical Institute, Russian Academy of Sciences, Politekhnicheskaya ul. 26, St. Petersburg, 194021 Russia*

*** St. Petersburg State Technical University, Politekhnicheskaya ul. 29, St. Petersburg, 195251 Russia*

E-mail: kozlovski@tuexph.sty.neva.ru

Submitted March 29, 1999; accepted for publication July 14, 1999

Abstract—Analysis is given of the progress in the modification of semiconductors by proton beams in fields such as proton-enhanced diffusion, ion-beam mixing, and formation of porous layers. This method of modification (doping) is shown to have high potential in monitoring the properties of semiconductor materials and designing devices of micro and nano electronics as compared to the conventional doping techniques such as thermal diffusion, epitaxy, and ion implantation. *© 2000 MAIK "Nauka/Interperiodica".*

1. INTRODUCTION

The continuous increase in the complexity of problems of semiconductor electronics, the development of new directions such as microwave electronics and optoelectronics showed the insufficient potential of the currently used technological processes of doping and predetermined the inevitable search for, and development of, new methods. One of the most promising techniques is radiation doping, i.e., the intentional, directional modification of the properties of semiconductors under the action of various types of radiation. The modification of semiconductor properties upon radiation doping occurs due to changes in the content of impurities and defects. Unlike the impurity atoms, which are usually the "defects of composition," the radiation defects (RDs), i.e., vacancies, interstitials, divacancies, etc., are the "defects of structure" of the semiconductor material. However, the effects of both the compositional and structural defects on the properties of semiconductors are similar. Usually, the formation of defects is accompanied by the appearance of local energy levels in the forbidden band of the semiconductor. The defects are either donors or acceptors, or serve as centers of recombination for the nonequilibrium charge carriers. The controllable introduction of RDs in combination with a proper heat treatment permits one to change the electrophysical properties of semiconductors in a wide range. At present, four main directions were developed in the field of radiation doping [1]:

—doping semiconductor materials by radiation defects;

—ion doping (ion implantation);

—transmutation (nuclear) doping; and

—ion-stimulated processes, including radiation-enhanced diffusion.

It is known that neutral particles, such as neutrons and γ photons, find wide application to provide the uniform doping of semiconductor wafers and ingots [2]. The most widely used methods are the uniform doping of silicon with phosphorus by irradiation with slow neutrons (neutron-transmutation doping) and the modification of the doping properties of silicon by radiation defects via the irradiation of wafers or finished devices with gamma photons or electrons with the purpose of changing the material parameters, mainly such as the lifetime of the nonequilibrium charge carriers [2]. However, the modern semiconductor technology is mainly based on the creation of structures that are doped quite nonuniformly in depth. When using radiation doping, the nonuniform doping profiles can only be obtained by the application of radiations that can ensure the effective modification of the properties of a semiconductor at predetermined depths. From this standpoint, the optimum method is the use of charged particles with a short range, such as accelerated ions, owing to the specific profile of their energy losses during stopping. In recent years, a special attention has been paid to the use of the lightest ions, i.e., protons, for this purpose. The interest in protons is due to the wide range of the material depths that can be treated in this case (from 0.1 μm to 1 mm) and the absence, after proton irradiation, of radiation defect complexes with high annealing temperatures. The main factors that affect the changes in the properties of semiconductors after proton irradiation are the formation of new impurities produced by nuclear reactions, the radiation defect formation, and the accumulation of hydrogen atoms in local regions of the crystal. Therefore, to the above general directions in the development of radiation doping, a new direction should be added, which is effectively realized only when proton beams are used as the radiation instrument. We think that it is expedient to sepa-

1063-7826/00/3402-0123$20.00

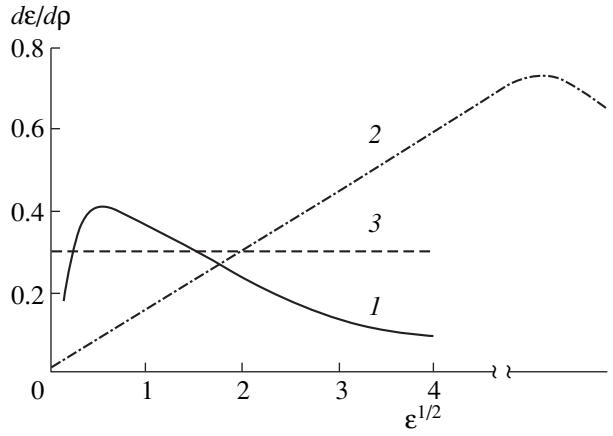

Fig. 1. Calculated curves of the energy losses of a bombarding particle for (*1*) nuclear and (*2*) electronic stopping; curve *3* stands for the approximate total energy loss ($d\varepsilon/d\rho = 0.327$) for a screened potential of the form r^{-2} [6].

rate, as an independent, fifth direction of radiation doping, the formation of porous layers, since it is this direction that is developed most intensely in the last five years.

At present, the problem that has been studied in most detail in literature is the accumulation of defects and the transmutation formation of impurities in semiconductors under the effect of proton radiation [1, 3, 4]. No analytical reviews concerning the use of proton-induced doping and the direct introduction of hydrogen atoms for the modification of semiconductor properties exists at present. Our review is aimed to fill the gap.

2. INTERACTION OF PROTONS WITH SEMICONDUCTOR CRYSTALS

It is known that the slowing down of a bombarding particle in a solid occurs at the expense of its scattering by the electron subsystem of the matrix atoms (electron stopping) and by the atomic nuclei of the matrix (nuclear stopping) [5]. Here, we will not consider the use of high-energy protons (of about 1 MeV), in which case one should take into account losses due to nuclear reactions, since this problem has already been treated in sufficient detail previously [4] upon the analysis of the nuclear doping of semiconductors. Electron stopping leads to the excitation and ionization of electron shells of matrix atoms, while the interaction with the nuclei of the matrix atoms (nuclear stopping), which is associated with the transfer of large energies, leads to the formation of lattice defects (Frenkel pairs, in the simplest case). The curves of energy losses, in accordance with the Lindhard–Scharff–Schiøtt (LSS) theory, are given in dimensionless units in Fig. 1, borrowed from Ref. [6]. As is seen from the figure, the energy losses of the particles due to nuclear stopping and, consequently, the processes of radiation damage prevail at small values of the reduced energy ε. The calculations show that the threshold value of the absolute proton energy at which nuclear losses are prevalent is, for most atoms entering into semiconductors, a few keV (1030 eV for Si) [7]. Thus, only a few percent of the total energy of ions is spent on the formation of RDs. The other part goes on the excitation and ionization of the semiconductor atoms. Since the generation of RDs occurs mainly after the proton is decelerated to an energy of ~1 keV, the generation is strongly nonuniform along the proton track. Since the cross section for the radiation defect formation increases by almost an order of magnitude with decreasing proton energy from 10 to 1 keV [8], the rate of RD generation in the region of the end of the proton path (at a depth close to the projected range R_p) may exceed the rate of generation at $x \ll R_p$ by an order of magnitude as well. The change in the energy of bombarding ions mainly leads to a change in the position of the region of the maximum generation of RDs.

3. ION-BEAM-INDUCED PROCESSES

3.1. Proton-Enhanced Diffusion

3.1.1. Dopant redistribution in semiconductors upon high-temperature proton irradiation. It was revealed in early 1960s that proton bombardment at temperatures 700–1000°C of silicon *p–n* junctions produced by thermal diffusion of Groups III and V impurities leads to a displacement of the *p–n* junction [9]. To explain this effect, the vacancy model of the proton-enhanced diffusion (PED) [10] was used, which suggested that the generation of radiation-induced vacancies by a proton beam is capable of enhancing the diffusion of substitutional impurities, since in silicon at 600–1000°C the factor that restricts the rate of diffusion is just the rate of defect generation rather than the relatively fast motion of radiation vacancies. In order to describe this enhanced diffusion, Fick's equation in which the diffusion coefficient (D_{PED}) depended on the coordinate was used.

In the 1970s, in connection with the development of new analytic methods for the analysis of impurity in-depth profiles in semiconductors and, in particular, of the method of secondary-ion mass spectrometry (SIMS), the PED profiles were shown to have one or several extrema near R_p (see, e.g., Fig. 2 borrowed from Ref. [11]). Since the simple vacancy model could only explain bends in the profiles, but could not account for the extrema, new models had to be developed. In the mid-1970s, two models appeared almost simultaneously, namely, a model that took into account the uphill diffusion of the impurity and the double-flux model of PED. It was shown in [12] that Fick's equation does not apply for the case of inhomogeneous defect generation and, in particular, for the case of PED. The continuity equation for the concentration of impurity atoms should contain a term that accounts for the uphill diffusion or the diffusion of substitutional impurities under the effect of the vacancy gradient. The

calculations performed in [12] show that, if the generation of radiation-induced vacancies occurs nonuniformly with the depth of the crystal, the resulting profile of the impurity distribution after PED should have a maximum in the region of the maximum concentration of irradiation-produced vacancies, i.e., at a depth close to R_p (in the "R_p region"). In order that distinct maxima were formed in the impurity concentration profiles in terms of this model, the equilibrium concentration of radiation vacancies should be greater than 10^{17} cm^{-3} [13]. This value is unrealistic, since even at the temperatures used for thermal diffusion (1000–1200°C) the vacancy concentration in silicon does not exceed 10^{15} cm^{-3} [14]. This is confirmed by the data on the radiation damage in silicon [15]. The calculations performed in [11] show that the maximum possible value of the peak height in impurity profiles after PED is ~20%. Note that in PED experiments the impurity concentration near R_p was usually minimum; this suggests that the contribution of the uphill diffusion to the PED processes is quite insignificant.

To explain the complex character of the redistribution of impurities near R_p, the double-flux model of diffusion was used [11]. This model suggests that the intense generation of Frenkel pairs in the R_p region upon PED produces a large number of interstitial impurity atoms by the Watkins reaction [16]

$$C_S + I \longrightarrow C_I \quad C_I + V \longrightarrow C_S. \qquad (1)$$

Here, C_S and C_I are the impurity concentrations in the sites and interstices, respectively; and V and I are the concentrations of vacancies and self-interstitials, respectively. Assuming that the interstitial component of the impurity has a large diffusion coefficient, we obtain a depletion of the R_p region of the impurity. Indeed, in this approximation, the substitutional ("site") component of the impurity can be regarded immobile; the escape of the fast interstitial impurity atoms from the R_p region leads to the formation of a minimum in the impurity profile at this depth.

The estimation of the effect was made on the basis of a characteristic such as the ratio of the impurity concentrations at the maximum and minimum of the impurity distribution using the data of [11] that were obtained by SIMS upon the investigation of PED in silicon. This estimation suggests that the experimentally observed minimum in the in-depth impurity profile, whose value does not, as a rule, exceed 50%, can be explained in terms of the double-flux model of PED. The experimental results [17–19] indicate that the formation of such extrema occurs at concentrations of the doping impurity of ~10^{19} cm^{-3}.

In 1980s, for the first time, a clearly pronounced maximum was revealed in the impurity profile at a depth equal to R_p (see Fig. 3 borrowed from [20]); previously, only weak minima were found in such profiles. The condition required for the formation of a maximum at a depth equal to R_p is the use of sufficiently large

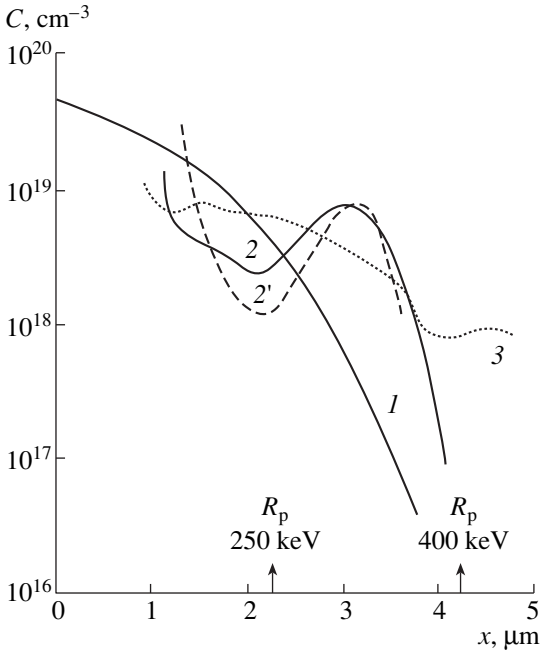

Fig. 2. Boron distribution in silicon measured by various methods: (*1–3*) by SIMS; (*2'*) by nuclear reaction method; (*1*) unirradiated; (*2*, *3*) irradiated with protons with an energy of (*2*) 250 and (*3*) 400 keV. Irradiation temperature T_{irr} = 850°C, dose 2×10^{17} cm^{-2}. Borrowed from [11].

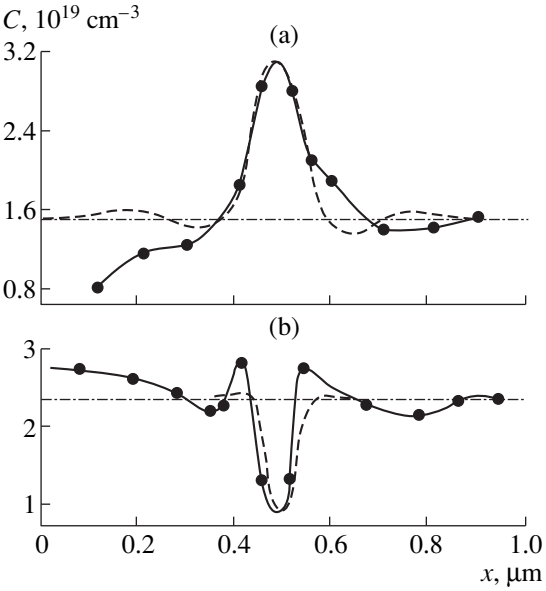

Fig. 3. Boron distribution in silicon measured by SIMS after irradiation with 100-keV H_2^+ ions for the initial concentrations of impurity C_0 equal to (a) 1.5×10^{17} and (b) 2.5×10^{19} cm^{-3}. Irradiation temperature T_{irr} = 700°C. Dashed lines represent calculated profiles that are solutions to the set of equations (2) [21].

beam current densities and relatively small doping levels ($C \approx 10^{17}$ cm^{-3}). Of special importance is the change in the sign of the extremum revealed in the impurity profiles obtained under the same irradiation conditions at higher doping levels ($C \approx 10^{19}$ cm^{-3}). These results could not be explained satisfactorily in terms of the existing models of PED. Indeed, the appearance of an impurity concentration minimum in the R_p region could not be explained on the basis of the simple vacancy model of diffusion, which considers only one flux of diffusing impurity. The double-flux model of PED also could not explain the results obtained, since the change in the impurity concentration by only two orders of magnitude under fixed irradiated conditions could not significantly change the relationship between the fast and slow diffusion flows.

The main disadvantage of the above models of PED is that in all of them the PED is regarded as the diffusion of neutral species, although it is known that even upon the conventional thermal diffusion the doping impurities, especially those producing shallow levels in the forbidden band of the semiconductor, diffuse in the ionized form. This circumstance caused the necessity of developing a new model.

This new model takes into account at least three factors: (1) the formation, in the process of proton bombardment, of excess vacancies, which increases the impurity diffusion coefficient; (2) the appearance of impurity complexes with radiation defects in the R_p region, where the concentration of defects is maximum; and (3) the electrostatic interaction of these complexes with the diffusing impurity. The advantage of this model is that, in this case, a relatively small portion of the impurity that forms low-mobile complexes effectively controls the process of the redistribution of the main body of impurities; the flux of the impurities and defects that causes complex formation is negligibly small in this case in comparison with the recombination (for defects) and diffusional fluxes.

The complete set of equations describing the redistribution of the impurities in the process of PED in terms of this model includes the continuity equations for the vacancies and interstitials, for the flux of impurities diffusing by the vacancy mechanism ("slow" diffusion component), for the "fast" impurity diffusion component, and for the Poisson equation. The continuity equation for the PED of impurity atoms diffusing through vacancies has the form [21]

$$A\frac{\partial C_S}{\partial t} = V\frac{\partial^2 C_S}{\partial x^2} - C_S\frac{\partial^2 V_S}{\partial x^2} + qC_S\frac{\partial V}{\partial x}\frac{\partial \varphi}{\partial x} + qV\frac{\partial C_S}{\partial x}\frac{\partial \varphi}{\partial x} + qVC_S\frac{\partial^2 \varphi}{\partial x^2} + \gamma_1 VC_I - \gamma_2 VC_S, \quad (2)$$

where A is a constant; φ is the electrostatic potential (in kT/e units); γ_1 and γ_2 are the recombination coefficients; and q is the charge of the diffusing ion. The first term on the right-hand side of equation (2) describes the thermal diffusion of the impurity; the second term accounts for the uphill diffusion of the impurity under the action of the vacancy gradient; and the next three terms correspond to the impurity motion in the inhomogeneous electrostatic field. The last two terms in equation (2) take into account the passage of the impurity from a site into an interstice by reactions (1). The allowance for the electrostatic interaction makes it possible to explain the experimental data that were obtained when studying the effect of the doping level on the redistribution of the impurity under the action of intense proton beams. At small concentrations of the impurity (boron) and $\varphi_0(x = R_p) > 2.5kT/e$, the main contribution to the PED comes from the electrostatic interaction (attraction in this case) between the defects and impurities. At large impurity concentrations ($C \simeq 10^{19}$ cm^{-3}), strong screening of the charge of radiation defects by free charge carriers occurs, and the effect of the electrostatic interaction on the redistribution of impurities can be neglected. As was shown by calculations, the impurity profiles at such doping levels can be explained on the basis of the two-flux diffusion model.

For a long time, the problem of the origin of the low-mobile defects that cause the electrostatic effect on the diffusing impurity remained debatable. It was established in [22] that such complexes must contain oxygen. In order to explain the electrostatic attraction between a radiation defect and a boron ion (with the result that an experimentally observed maximum appears in the impurity concentration profile (Fig. 3), the radiation defect must have a positive charge. The simplest of the oxygen-containing complexes—the A center (a vacancy–oxygen complex)—usually has a negative charge or is neutral in silicon [15] and, therefore, cannot provide the experimentally observed "pulling" of negative boron ions into the region near R_p. The positively charged K center (a vacancy–oxygen–carbon complex) may pretend to the role of such a defect. The donor energy level of the positively charged K center lies 0.30 eV above the top of the valence band. The probability of the formation of a positively charged defect (the probability of the absence of an electron at a donor level) depends on the position of the Fermi level in the material and is approximately 10% for silicon doped with an acceptor impurity to a concentration of 10^{17} cm^{-3} ($E_F \approx E_v + 0.40$ eV at the irradiation temperature $T_{irr} = 1000$ K). It follows from the calculations by equation (2) that for the experimental results on the PED in silicon to be explained, it is necessary that the concentration of uncompensated positive radiation complexes be on the order of 10^{16} cm^{-3}, i.e., the total concentration of K centers should be ~10^{17} cm^{-3}. Note that the probability of the formation of a positively charged defect increases with increasing concentration of charge carriers and, for the concentration of ~10^{19} cm^{-3}, it is 90% ($E_F \approx E_v + 0.1$ eV at $T_{irr} = 1000$ K). However, since the shielding distance for

such a defect is inversely proportional to the root of the charge carrier concentration, the effect of the Coulomb interaction will decrease with increasing concentration of the doping impurity. At $C \approx 10^{19}$ cm^{-3}, the shielding distance becomes less than the average distance between the ionized impurity atoms, so that the internal electric field can be neglected.

A theoretical analysis made it possible to estimate the contribution of each of the four mechanisms of proton-enhanced diffusion and adequately interpret literature [11, 17, 19, 20] experimental data that could not be explained in terms of any one model of PED.

The establishment of the nature of PED made it possible to efficiently use this method in practice. The main advantage of PED is the possibility of creating complex impurity profiles, which cannot be produced by other methods. Thus, in the process of PED an impurity can be redistributed in a manner that enhances its gradient. Kozlovskiĭ *et al.* [17] successfully obtained profiles with a concentration gradient of $\sim 2 \times 10^{24}$ cm^{-4}. The location of the steep-gradient region in the sample is controlled by the proton energy. The steep impurity profiles are of great interest, especially for the production of microwave devices. The strength of the method of producing such devices using PED is in that it permits one to form steep impurity profiles at a given depth using temperatures much lower than those employed for thermal diffusion. In addition, using this method, one can govern the impurity profile in each of the layers of a multilayer structure. Another interesting example of the application of PED is the creation of the so-called "stepped" impurity profiles necessary for the production of the structures of avalanche diodes [1].

PED is of great interest as a method of irradiation-aided localization of the active region in stripe AlGaAs heterolasers [23]. Experiments on the local control of aluminum depth distribution in quantum-well heterostructures by proton irradiation show that the irradiation at temperatures of 200–250°C makes it possible to efficiently redistribute aluminum in local regions of GaAs/GaAlAs heterostructures and thereby ensure the lateral electron and optical restriction of the active region of the stripe heterolaser. The separate effects of annealing at the above temperatures or irradiation at lower temperatures does not lead to aluminum migration because of either the small concentration of point defects or their small mobility.

3.1.2. Impurity diffusion into a preliminarily irradiated semiconductor crystal. A characteristic feature of this mode of PED is that the processes of generation of radiation defects responsible for PED and the processes of migration of the impurity are separated in time. When using this type of PED, the single crystals are irradiated at temperatures close to room temperature, after which thermal diffusion in the irradiated material is carried out. It was shown in [24] that the available experimental data can be described in terms of the vacancy mechanism of diffusion, according to which the impurity applied onto the surface of the crystal after irradiation migrates via vacancies that are generated in the course of annealing of complex radiation defects. The surface in this calculation was considered to be a sink for vacancies. The concentration C of the impurity diffusing via vacancies was determined from the continuity equation [24]

$$\frac{\partial C}{\partial t} = \frac{D_V}{N}\left(V\frac{\partial^2 C}{\partial x^2} - C\frac{\partial^2 V}{\partial x^2}\right), \quad (3)$$

where D_V is the diffusion coefficient of vacancies, and N is the concentration of matrix atoms. The vacancy distribution in the process of diffusion annealing was calculated from the equation

$$\frac{\partial V}{\partial t} = B\frac{K(x)}{\tau_c}\exp\left(-\frac{t}{\tau_c}\right) - \frac{V}{\tau_V} + D_V\frac{\partial^2 V}{\partial x^2}. \quad (4)$$

Here, τ_c and τ_V are the lifetimes of the complexes and vacancies, respectively; $K(x)$ is the concentration of complexes, and B is the number of vacancies released upon the decomposition of a single complex. The first term on the right-hand side of equation (4) yields the rate of generation of vacancies upon the decomposition of vacancy complexes; the second term describes the loss of vacancies to the approximation of monomolecular recombination, and the third term describes the diffusion of vacancies. Numerical calculations show that at $D_V < 10^{-6}$ cm^2 s^{-1} the vacancy distribution profile to a good accuracy, reproduces the profile of radiation complexes produced by proton irradiation [24]. In the case of small D_V, the last term in equation (4) can be omitted, and equation (4) is then solved analytically by direct integration to give

$$V = K(x)\left[\exp\left(-\frac{t}{\tau_c}\right) - \exp\left(-\frac{t}{\tau_V}\right)\right]\frac{\tau_V}{\tau_c - \tau_V}. \quad (5)$$

The simultaneous solution of the continuity equations for the vacancies and the impurity made it possible to estimate the effect of the concentration, diffusion coefficient, and lifetime of defects on the dopant profile. A comparison of the calculated results with the experimental data obtained upon the investigation of the diffusion of sulfur and copper in the proton-irradiated GaAs [24] yields the following values of the above-mentioned parameters (for $T_{irr} = 1000$ K): $D_V = 3 \times 10^{-4}$ cm^2 s^{-1}, $\tau_c = 100$ s, $\tau_V = 10^{-4}$ s, and $K(R_p) \approx 10^{17}$–10^{18} cm^{-3}.

The concepts of impurity diffusion into a preliminarily irradiated crystal also proved to be very effective for the explanation of the experimental data on the earlier stages of low-temperature annealing of ion-implanted layers in semiconductors [25]. The deviation of the impurity profiles from the Gaussian shape can be explained on the assumption that at the starting instant of annealing, the diffusion of substitutional impurities is strongly affected by the generation of vacancies that are formed upon the decomposition of vacancy com-

plexes. At this stage of low-temperature annealing, we should consider diffusion in a crystal with a spatially nonuniform (in depth) and nonstationary distribution of vacancies.

3.2. Processes of Ion-Beam Mixing

The development of microelectronics calls forth progressing interest in processes that occur near the free surface of the semiconductor and near the metal–semiconductor interface. The investigations of the influence of irradiation on the semiconductor surface show the existence of at least two effects, which have a great practical importance; these are the accumulation of defects in the near-surface zone and the radiation-induced introduction of impurities into the single-crystal semiconductor from a source applied onto the surface. In particular, it was established that as a result of ion irradiation of a metal–semiconductor structure, a higher level of doping of the semiconductor surface with a metal can be obtained at relatively small doses in comparison with the high-dose implantation. Upon the irradiation of a heterogeneous system, e.g., a metallic film (which serves as a diffusion source)–semiconductor, apart from the incorporation of the atoms of the film material into the semiconductor substrate, also the introduction of the atoms of the semiconductor into the metallic film may be observed. These processes obtained the common denomination of ion-beam mixing (IBM). The high expected technological efficiency of the IBM attracted a great attention to this method; however, in spite of numerous publications, the nature of the effect remains unknown. To date, several hypotheses were suggested to explain this complex phenomenon. Their brief description and analysis are given in section 3.2.1.

Note that in the majority of published works, irradiation of the samples was performed not only with protons but also with heavier ions, but the mechanism of the phenomenon remains the same, irrespective of the type of ions. A comparison of the results of the irradiation of control samples with ions of various masses and energies makes it possible to arrive at reliable conclusions on the applicability of various models of the phenomenon.

3.2.1. Theoretical concepts of the physics of radiation-enhanced processes at the metal–semiconductor interface. A historically first attempt to theoretically explain the nature of ion-beam mixing was the reduction of the phenomenon to the implantation of recoil atoms, which was connected with the appearance in the lattices of the metal and semiconductor of a cascade of displacements (collision cascade) produced by a primary ion. In the final result, the displaced atoms are incorporated into the semiconductor. In this case, the distribution of implanted atoms proves to be non-Gaussian, in contrast to the direct ion implantation.

For the first time, this problem was rigorously solved in [26]. In order to obtain a theoretical profile of impurity distribution based on the theory of collision cascades, a radiation damage (cascade) function was written with allowance for the inelastic losses of ion energy and anisotropy of scattering. Proceeding from the resulting energy spectra of the displaced (cascade) atoms, the total number of recoil atoms that reach the substrate, the dependence of the number of recoil atoms on the metal film thickness, and the distribution profile of the recoil atoms in the substrate were calculated. The number of atoms ν displaced by a single incident ion was determined by the expression [26]

$$\nu = 0.303\left(\frac{E_m}{E_d}\right)^{1/2}, \tag{6}$$

where E_d is the binding energy of an atom in the lattice (displacement threshold);

$$E_m = \frac{4M_1M_2}{(M_1 + M_2)^2}E, \tag{7}$$

E is the ion energy; M_1 is the ion mass; and M_2 is the metal atom mass. It is evident from the above formulas that the number of recoil atoms may exceed the number of bombarding ions.

The total number of metal atoms implanted into the semiconductor was calculated by the authors of the theory [26] by integrating the spectrum of knocked-out atoms with allowance for their passage through the corresponding portion of the metallic film. The calculation performed for the case of the bombardment of a tin film (10 nm thick on a graphite substrate) with 100-keV P^+ ions shows that the change in the concentration by two orders of magnitude (in comparison with the surface concentration) occurs at a depth of about 10 nm. This small depth of penetration is due to the fact that the majority of recoil atoms have energy of about 10 eV and their motion is limited by distances of 1–2 atomic layers.

The number of metal atoms implanted into the semiconductor is determined at a fixed energy of bombarding particles by only the irradiation dose, only slightly changes with temperature, and is independent of the flux of bombarding particles. The efficiency of implantation of metal atoms into a semiconductor increases with increasing mass of the bombarding atoms, although in general the implantation of recoil atoms is possible under the action of any particles possessing a sufficiently high energy.

It is obvious that other approaches to the calculation of the number of atoms displaced by an incident ion are possible, e.g., one based on the calculation of the total energy spent in elastic collisions using the Lindhard–Scharff–Schiøtt theory with the subsequent application of the Khinchin–Pease formula. Note, however, that this approach does not change the fundamental consequences of the theory, which cannot explain many of the experimentally observed phenomena such as the temperature dependence of the doping level of the semiconductor, the nonlinear dependence of the mixing

effect on the number of atoms in bombarding ions, doping the semiconductor with the metal upon the irradiation of a metal–semiconductor structure with electrons with an energy of about 1 MeV [27]. Some of these difficulties is lifted in the model of thermal spikes.

The hypothesis of thermal spikes represents a macroscopic description of the processes of energy transfer from a moving ion to atoms residing at lattice sites. The displacements of atoms from the sites and the resultant collision cascade is considered as a form of heat transfer. This approach is very demonstrative, but has obvious disadvantages: the excited region is never in equilibrium and therefore cannot be characterized by a certain temperature—the macroscopic laws of heat conduction are not applicable to the field of small time intervals and small distances.

The model of thermal spikes is used in those cases where not all atoms are displaced from their lattice positions. Thus, according to the model, the "linear" energy losses of the bombarding ion are liberated upon its slowing down instantaneously in the form of thermal energy in a small volume of the crystal and then dissipate according to the classical laws of heat conduction. Calculations show that a typical lifetime of a thermal spike is on the order of a picosecond, its diameter is about 10 nm, and the temperature in the center of the spike can exceed the melting temperature of the material.

According to the hypothesis of thermal spikes, the process of intermixing in the interface region is connected with the occurrence of thermal diffusion in the region of the thermal spike. The natural difficulties are related to the choice of diffusion constants. Numerical calculations performed within this model (see, e.g., [28]) show the impossibility of quantitatively describing the available experimental results, which is connected, first of all, with the small lifetime of a thermal spike.

The theory can be qualitatively improved by allowing for the effects related to radiation-enhanced diffusion (RED). Above, we have already discussed the possible factors that may enhance impurity diffusion upon irradiation. The main of them are the generation of excess vacancies and interstitials and a decrease in the energy barriers for diffusion due to ionization processes in the crystal upon irradiation. The total diffusional flux of impurity atoms can arbitrarily be described by the sum of two fluxes, one of which is caused by thermal diffusion and the other by irradiation-related diffusion. This approach satisfactorily describes the temperature course of intermixing in a wide temperature range and the dependence of this effect on irradiation. It is obvious, however, that even this approach does not make it possible to theoretically obtain the exact values of diffusion constants.

Experiments show that, in the course of ion-beam mixing, the number of implanted atoms depends on the substrate temperature upon irradiation [29, 30]. This dependence is of the activation nature and the corresponding activation energy turns out to be much smaller than for the analogous thermal process. Thus, it is 0.11 and 0.33 eV for Ni–Si and Co–Si, respectively, instead of the usual value 1.5 eV. In the case of Nb–Si, these energies are 0.25 and 2.7 eV, respectively, while for Cr–Si, they are 0.2 and 1.4 eV, respectively. The mechanism of this lowering of the activation energy is not clear at present, but the occurrence of such experimental dependences speaks in favor of the important role of RED.

The above model also makes it possible to naturally explain the observed doping of the semiconductor with the metal during relatively low-energy electron irradiation if the electron energy is greater than the defect formation threshold.

3.2.2. Ion-implantation-stimulated processes of the formation of chemical compounds. Some metals, when being applied on the surface of silicon, react with it to form chemical compounds upon annealing or ion bombardment. To the present day, systems such as Ni–Si, Pd-Si, Cr–Si, and Pt–Si have been studied in great detail. The main trend that was established in the studies of silicide formation is the reduction of the temperature of their formation upon ion irradiation as compared to the conventional heat treatment. The main role in the decreasing of the temperature of silicide formation are the processes of displacement of metal and silicon atoms out of the sites of the corresponding lattices due to the ion bombardment.

This is vividly confirmed by the data on the formation of a Pt_2Si compound upon the implantation of ions such as Ar, Kr, and Xe with an energy of 300 keV [30]. The thickness of the intermixed layer grows as a square root of the implantation dose. Since upon thermal diffusion the thickness of the doped layer is proportional to the square root of time, we may conclude that the mechanisms of these processes are close. The kinetics of the formation of Pt_2Si depends on the mass of implanted ions. Thus, at a fixed implantation dose, the proportion of the silicide layer thicknesses for Xe, Kr, and Ar is 3 : 2.2 : 1, which is close to the ratio of their masses (3.2 : 2.1 : 1) and nuclear energy losses per unit range (7.1 : 4 : 1) in Pt films, i.e., to the ratio of the damage rates. In [31], when studying the processes of ion-beam mixing of thin Fe films applied on a silicon surface and irradiated with 380-keV Xe^+ ions, it was also found that the thickness of the mixed layer grew as a square root of the implantation dose and increased with increasing irradiation temperature.

Based on the above, we can make some conclusions on the mechanisms of ion-beam mixing. At the first stage of the process, the bombarding particle displaces atoms of the semiconductor and the metal out of their lattice sites. The displaced atoms move (because of the presence of concentration gradients) via vacancies or interstices as in the usual thermal diffusion, but with a lower activation energy. The decrease in the activation

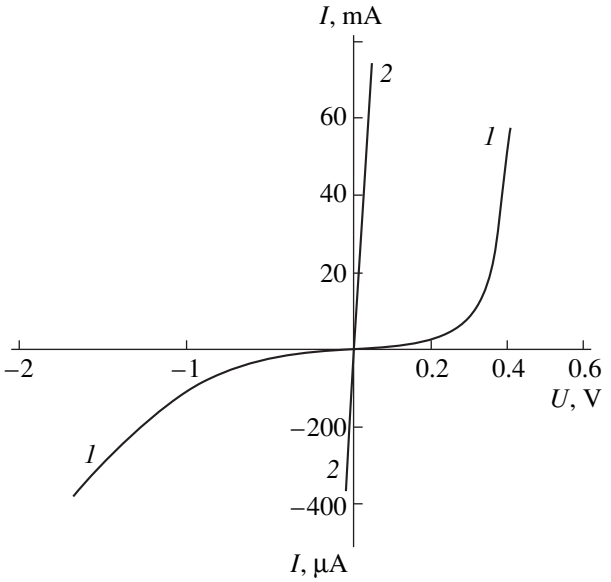

Fig. 4. Current–voltage characteristics of an AuGe–GaAs junction: (*1*) prior to and (*2*) after irradiation.

energy may be related to the processes of ionization of the bulk of the irradiated materials. An additional argument in favor of this hypothesis is a comparative investigation of thermal and ion-stimulated growth of silicides [32] with the use of "markers"—thin films of metals that do not form silicides—applied between silicon and the metal to be studied. These experiments showed the existence of counter diffusional fluxes of metal and silicon atoms in the course of both processes studied.

In most works that have been published to date, the investigations of the ion-stimulated processes of doping were conducted at near-room temperatures. Under such conditions, radiation damage arises in semiconductors, which in many cases exerts harmful effect on the electrical properties of the metal–semiconductor interface. At the same time, it is precisely the electrical properties of the interfaces that are most important from the application viewpoint.

In [33, 34], we studied the processes of proton-stimulated doping of the surface of Si and GaAs single crystals in a temperature range of 20–500°C. As the dopants, we selected Ni and Au metals. A metal film was applied onto a chemically purified surface of the semiconductor single crystals by thermal evaporation in a vacuum or by electrochemical deposition. The film thickness was selected to be greater, smaller, or equal to the mean projected range of the protons used for irradiation. To study the composition of the surface layers of the semiconductor materials prior to and after irradiation, we used the method of electron spectroscopy for chemical analysis (ESCA); the electrical properties of the junctions were studied by measuring current–voltage characteristics; the impurity distribution was controlled by the secondary-ion mass spectrometry (SIMS) and the tracer method. The efficiency of doping of the surface region of the semiconductor with the impurity selected is evidenced by the current–voltage curve of the AuGe–GaAs junction shown in Fig. 4. The samples were irradiated with 25-keV protons at a temperature $T_{irr} = 250$°C. The thickness of the evaporated AuGe film was close to the projected range of protons. It can be seen from the figure that the current–voltage characteristic became linear after irradiation and the sheet resistance of the contact decreased to 1.3×10^{-4} Ω cm^2, which is no more than that obtained upon the thermal firing of the AuGe alloy at a temperature of 450°C.

The investigation of the surface composition of semiconductor single crystals by ESCA after the irradiation and removal of the metal layer shows that the highest level of surface doping at a fixed irradiation temperature is reached when the thickness of the metal film coincides with the projected range of protons, and it increases with increasing irradiation temperature to saturate at a level of several volume percent at temperatures of 200–250°C. Electrochemical sectioning and layer-by-layer measurements of the impurity concentration show that the enrichment of the semiconductor with the impurity occurs to depths of about a few tenths of a micron. If the projected range of protons is smaller (by several stragglings) than the metal film thickness, then no dependence of the level and the depth of doping on the irradiation temperature is observed. This suggests that the process of doping occurs in two stages; at the first stage, the metal atom is incorporated into the semiconductor, and at the second stage, radiation enhanced diffusion of these atoms occurs with the participation of defects generated by irradiation. The incorporation of the metal atoms may occur either due to the implantation of recoil atoms or the irradiation-induced lowering of the energy barrier for thermal diffusion at the metal–semiconductor interface.

When studying the processes of ion-stimulated formation of chemical compounds in the Ni–Si system, the proton energy was selected such that their range was smaller, greater, or equal to the thickness of the metal film applied on silicon. Such experiments permit one to estimate the relative contributions of the radiation damage and the excitation of the electron subsystem (lowering of the energy barriers for diffusion and chemical reactions) in the process of silicide formation.

For the irradiation with protons, we used KDB-10 silicon samples 300 μm thick. On both sides of the wafers, a Ni layer of thickness $d = 0.5$ μm were applied chemically. After one side of the sample was irradiated with protons, Ni was chemically etched off. Figure 5 displays the ESCA spectra taken from the face side of the sample irradiated with 50-keV protons ($d > R_p$) at a temperature of 280°C and from the opposite, control side. The peaks with energies of 99.5 and 103.4 eV correspond to 2*p* electrons of Si in the single-crystal Si and

SiO_2; the peak at 853.5 eV corresponds to 2*p* electrons of Ni in the silicide. As can be seen from Fig. 5, the presence of Ni is only detected on the irradiated side of the sample. According to ESCA data, the Ni concentration at the surface is 25–30 at. %. The closeness of this composition and of the ESCA spectra obtained to the composition and the spectra of $NiSi_2$ suggests that it is most likely this compound that is formed upon irradiation. At irradiation temperatures below 150°C, no chemical compound formation was found by the ESCA method. The $NiSi_2$ compound was also found to form at 200–250°C in that case where the projected range of protons was smaller than the metal film thickness. In this case, the ionization losses at the interphase interface exceed the elastic losses, and the contribution of the recoil implantation into the doping effect decreases.

The role of electron excitations and ionization in the region of the metal–semiconductor interface was studied experimentally in [35], where silicon single-crystal samples with Ti and Ni films 15 nm thick applied on their surface were irradiated with 0.89 GeV Ta ions at a temperature of 80 K (to prevent thermal migration of radiation defects). With such an energy of bombarding ions, the main energy losses near the metal–semiconductor interface are related to electron excitations and ionization of silicon atoms. The irradiation was found to provide mixing of the Ti/Si boundary to depths of about 5 nm. The possible mechanisms of mixing have not been discussed in the work.

Thus, the data on the irradiation-induced doping of the surface of semiconductor materials can be explained by the effective lowering of energy barriers for chemical reactions at the interface. The possible factors that may cause the lowering of these energy barriers have been considered in detail in [36].

At present, only scarce data are available in literature that concerned the investigation of ion-stimulated processes at the surface of single crystals of complex narrow-gap compounds and the comparison of data obtained for these materials with analogous data for traditional single-crystal semiconductors. In [37], processes of the irradiation-induced doping of single crystals of *n*-type PbSe with an Ag impurity from a source applied onto the surface of the samples were investigated. The impurity distribution was studied by the radioactive tracer technique (using ^{110}Ag). The Ag distribution after the irradiation of the sample with protons with an energy of 150 keV at a temperature of 10°C differs from that obtained upon thermal diffusion. If we assume that Ag migrates in PbSe via vacancies, then the vacancy diffusion length is, according to the results of these experiments, about 5 μm. The Ag atoms introduced under irradiation are electrically active; this follows from the comparison of the current–voltage characteristics of the samples that were irradiated under the same conditions but differed in the diffusion source, which represented a thin film of nonradioactive silver applied onto the surface by thermal deposition in a vacuum.

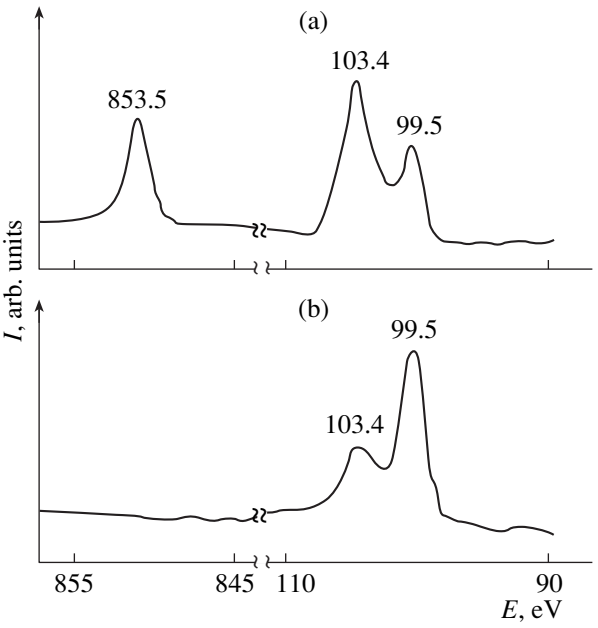

Fig. 5. ESCA spectra obtained from (a) irradiated and (b) unirradiated sides of an Ni/Si sample.

Thus, the results of electrical measurements and the impurity distribution indicate the preferential doping of the near-surface region of the semiconductor by the atoms of the surface metal film as the latter is irradiated with protons. This effect cannot be explained as being purely thermal. The results of these experiments can be explained proceeding from the fact that irradiation efficiently generates atoms with an energy that is sufficient to the overcome the metal–semiconductor barrier. Subsequently, the impurity atoms diffuse deeper into the semiconductor. The diffusional nature of these processes is evidenced by the fact that the contact resistance decreases when the irradiation is performed at enhanced temperatures.

Note that the main trends observed upon ion-beam mixing at the metal–semiconductor interface are also characteristic of other materials, e.g., of the metal–ceramic structures [38].

3.3. Effect of Surface on the Radiation Damage and Impurity Redistribution in Silicon upon High-Temperature Proton Irradiation

Investigation of high-temperature radiation damage in surface regions of semiconductor crystals is of importance from the viewpoint of studying both the effects of surface on the radiation damage and the effects of radiation damage on the surface properties of semiconductors.

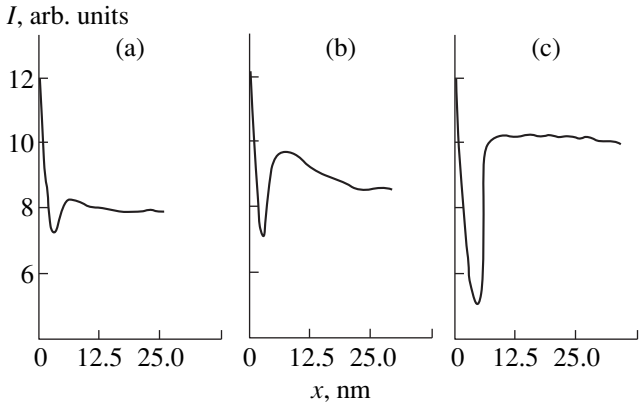

Fig. 6. Effect of temperature on the redistribution of boron in surface regions of silicon. Irradiation conditions: H_2^+ ion energy, 50 keV; irradiation time, 1800 s; and ion current density, 2 μA cm^{-2}. Irradiation temperature: (a) 340; (b) 520; and (c) 700°C.

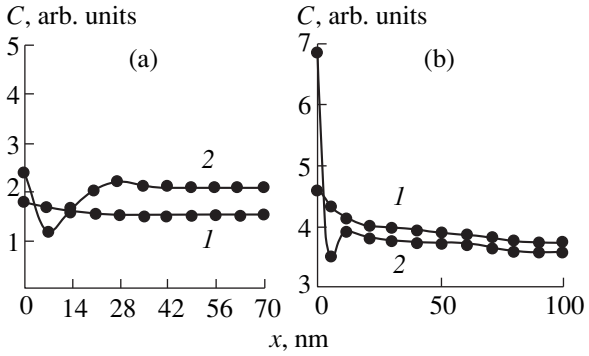

Fig. 7. Distribution of (a) antimony and (b) phosphorus in the surface layers of silicon (*1*) prior to and (*2*) after irradiation with H_2^+ ions at a temperature of 700°C to a dose of 2×10^{16} cm^2.

Since the migration of both primary (vacancies and interstitials) and secondary (vacancy–impurity complexes) radiation defects is accompanied by the corresponding migration of impurities, the processes of radiation damaging can be studied by measuring impurity distribution profiles. In [39, 40], we investigated the near-surface distribution of phosphorus, antimony, and boron caused by proton irradiation. The impurity profiles were measured by SIMS; the surface composition was controlled by ESCA.

The degree of surface segregation (enrichment) depends on the type of the impurity, irradiation dose, and irradiation temperature. As was shown by ESCA, the concentration of impurities in the surface layer may increase by two to three orders of magnitude as compared to the bulk concentration. Figure 6 displays the effect of the irradiation temperature on the boron distribution in silicon. It can be seen that in the near-surface layers the redistribution of boron occurs at already as low temperatures as 340°C. With increasing temperature, the efficiency of the redistribution process increases.

In order to explain these impurity distributions, we should consider the development of radiation damage in near-surface layers of crystals. As is known, a characteristic feature of the process of defect formation upon proton bombardment is the existence of a maximum of defect concentration near the end of proton paths (in the R_p region) in the bulk of the crystal. There are known, however, works (see, e.g., [41]), in which a surface maximum of radiation damage (SMRD) was observed along with the bulk maximum. The characteristic dimensions of the region of SMRD do not exceed 20 nm, which correlates well with the dimensions of the regions of the near-surface redistribution of impurity concentrations.

Several possible causes for the formation of an SMRD were noted in literature. Among them are the migration of defects to the surface and the enhanced rate of generation of radiation damage in the near-surface region of silicon either due to the ionization mechanism of defect formation (especially, for silicon doped with donor impurities) or due to the lowering of the threshold energy for damage in the near-surface portion of the semiconductor crystal.

A comparison of the available data on the existence of SMRD with the data obtained from the results of impurity redistribution measurements makes it possible, in our opinion, to obtain additional data on the surface properties. Thus, if we assume that the surface is a sink for vacancies, then the flux of impurity atoms that migrate via the vacancy mechanism will be directed oppositely (uphill diffusion), which will lead to the depletion of the surface region of the impurity if the uphill diffusion is dominating in the impurity migration. The really observed effect can be explained if we assume that the surface is a region of intense generation of vacancies. In this case, the flux of vacancies from the surface should cause a counter flux of impurity, which leads to the enrichment of the surface with the impurity. The depth of the region in which impurity migration is observed should then correspond to the diffusion length of vacancies. The enhanced radiation damage formation near the surface may be caused by a decrease in the binding energy of atoms in the silicon lattice in this region.

This assumption contradicts, however, the results obtained upon the investigation of the impurity redistribution in the bulk of the crystal in the course of the high-temperature irradiation with protons. It is known that at doping levels of about 10^{19} cm^{-3} in silicon there arises a minimum in the impurity distribution profile at depths of about R_p. This fact is explained in terms of the two-flux model of diffusion by the existence of a fast component of the diffusion flux. It is assumed that such a component may be either impurity atoms or vacancy–

impurity complexes. The accumulation of the impurity at the surface means that the surface is a sink for the fast diffusion component. If the fast diffusion flux consists of vacancy–impurity complexes, then the concentration of the impurity near the surface should be smaller than in the bulk because of the intense generation of vacancies and, as a consequence, of vacancy complexes. Since, on the one hand, the fast diffusion fluxes of both phosphorus and antimony are related to the migration of complexes and, on the other hand, as is seen from Fig. 7, the surface become enriched with the impurity upon irradiation, a conclusion should be made that the surface is not a source of vacancies.

It follows from the data on the redistribution of Sb and P that the surface is a sink for vacancy–impurity complexes and the data on the proton-enhanced diffusion of boron suggest the intense migration of self-interstitials to the surface. Thus, the surface plays the role of sink for radiation defects.

4. FORMATION OF BURIED NANOSIZE POROUS LAYERS IN SEMICONDUCTORS

The effects of the formation of nanosized pores, voids, and porous layers in solids after a high-dose implantation of light inert gases have been known for a sufficiently long time [42–44]. In the greatest detail, these effects were studied for metals that are used as the materials for the first wall of fusion reactors. The main cause for such interest of researchers in the pore formation is the problem of radiation damage stability of metallic walls of the reactor under the intense bombardment with light ions, which leads to "swelling" and destruction of the surface layers of the metal. In semiconductor crystals, the effects of the formation of pores, voids, and cavities upon the implantation with light ions were investigated in much less detail as compared to metals. This situation is determined by the lack of the real practical importance of these effects for the technology of semiconductor materials and for the operation of semiconductor devices. The discovery of the photoluminescence of porous silicon in the visible range has stimulated a new interest in porous semiconductors and, in particular, in the investigation of the properties and regimes of the production of porous layers in crystals by the use of high-dose implantation with protons and α particles. Let us consider the main features of the formation and properties of such layers.

It is known that the solubility of inert gases in solids is small and usually does not exceed 10^{16} cm^{-3}. Therefore, beginning from certain threshold implantation doses, nanosized pores and voids filled with implanted-gas molecules can form in the irradiated material. The distribution of implanted ions in the irradiated material is usually nonuniform in depth below the irradiated surface. Therefore, the pore formation also occurs nonuniformly. The depth at which the pores are mainly formed depends on the ion energy and coincides with R_p. The thickness of the porous layer is determined by the straggling (spread of the projected ranges) of ions and increases with increasing implantation energy. The size of nanopores and the density of their distribution in the material are determined by the ion energy and implantation dose; in addition, they may essentially depend on the conditions of postimplantation annealing [44–46]. Thus, the radiation technology provides the possibility of governing, with a high accuracy and reproducibility, the process of the formation of buried porous layers in the crystals, with the parameters of the nanopores specified by a proper choice of implantation conditions and postimplantation annealing.

In most detail, the dynamics of changes in the structure of pores depending on the various technological factors has been analyzed in [45] for the case of helium implantation in silicon. The investigation of the pore parameters was carried out by their direct detection using transmission electron microscopy. The authors of [45] established that the minimum dose required for the formation of pores in Si upon helium implantation increases from 5×10^{15} to 10^{16} cm^{-2} with increasing ion energy from 20 to 300 keV and is in good agreement with the data on the increasing straggling of ions with increasing energy. The threshold value of the local concentration of helium required for pore formation was found to be 3.5×10^{20} cm^{-3} for any implantation energies. The authors of [45] have also found the main trends in the changes of pore size with increasing postimplantation annealing temperature and time:

(1) an increase in the pore diameter (from ~10 to ~100 nm);

(2) a decrease in the pore density in the porous layer (from ~10^{16}–10^{17} to ~10^{14} cm^{-3});

(3) a decrease in the thickness of the porous layer.

The postimplantation annealing of crystals with pores leads to a faceting of the internal surface of the pores with the appearance of planes of minimum surface energy. In silicon, these are (111), (110), and (100) planes. Pore faceting was observed by may authors and was used in some of them to determine the equilibrium forms of silicon crystals and relative values of the surface energy of various planes [47–49].

The pore formation in semiconductor crystals upon high-dose proton implantation has some specific features as compared to helium implantation. In contrast to helium, hydrogen is a chemically active impurity and reacts intensely with broken ("dangling") bonds, defects, and impurity background of the crystal. This interaction decreases the mobility of hydrogen atoms in the crystal lattice of the semiconductor crystal, which prevents the formation of pores directly in the process of implantation. According to the data of [50–52], after high-dose implantation, hydrogen in silicon is in atomic or molecular states, or it is captured by extended defects that are formed in (100) and (111) planes and

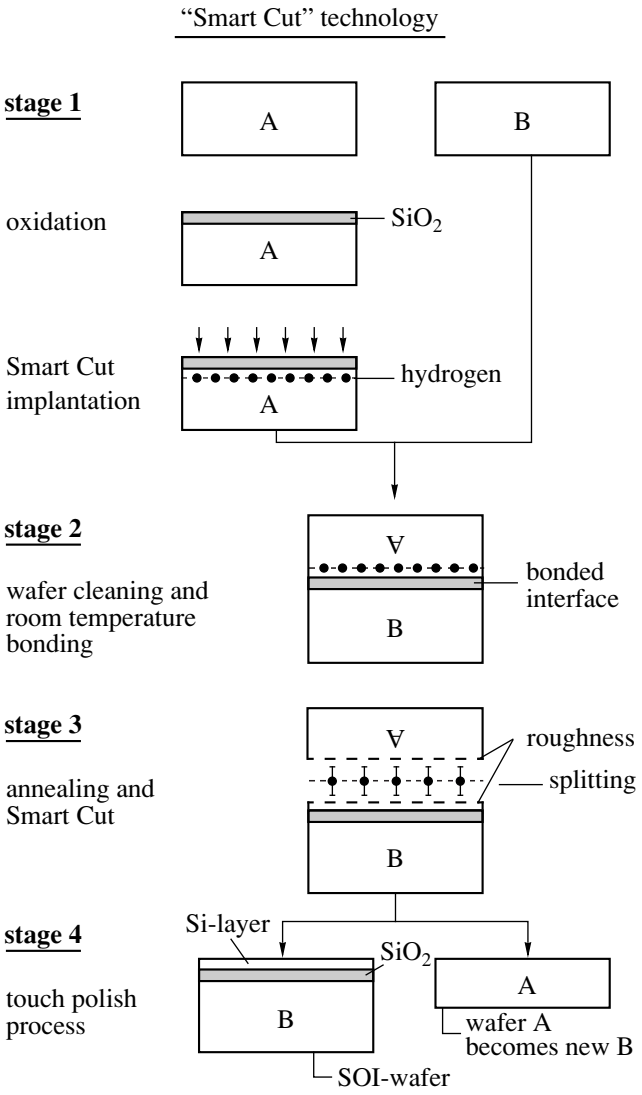

Fig. 8. Main stages of the Smart Cut technology upon fabrication of silicon-on-insulator structures.

have an average size of ~7 nm [50]. To obtain a porous layer in the semiconductor crystal after high-dose implantation, the crystal is subjected to a special annealing. In the course of such an annealing, the vacancy–hydrogen complexes decompose to form clusters of molecular hydrogen consisting of four hydrogen molecules [50]. Upon subsequent annealing, these clusters are merged into coarser pores, producing a clearly pronounced porous layer. At annealing temperatures below ~400°C, hydrogen is retained in the pores at a high pressure (up to 10^9 Pa), but as the temperature of postimplantation annealing increases further, it diffuses into the crystal and goes out of the pores almost completely at $T_{ann} \geq 700$°C [53, 54]. Note that the available literature on the investigation of porous layers produced by proton implantation in semiconductors is almost fully restricted to the behavior of pores in silicon.

5. POROUS LAYERS IN THE TECHNOLOGY OF SEMICONDUCTOR MATERIALS AND DEVICES

The formation of porous layers in semiconductors using implantation with protons and α particles is one of the "youngest" directions in the field of modification of material properties by the bombardment with light ions. Nevertheless, at present this technique has already found practical application and the works in this direction continue to be developed intensively. Let us briefly consider the main directions.

5.1. "Smart Cut" Technology

In 1995, Bruel reported [55] the main principles of a new technology of fabrication of "silicon-on-insulator" (SOI) structures, which was based on the use of buried porous layers produced by proton implantation. This technology was called "Smart Cut" and is used at present in the industrial production of SOI materials. Such SOI materials are an alternative to the conventional semiconductor materials and are very promising for the production of low-voltage and low-power ULSI circuits [56].

The "Smart Cut" technology includes two technological processes:

(i) high-dose implantation of hydrogen; and

(ii) solid-phase bonding of semiconductor wafers [57].

A simplified scheme of the process is shown in Fig. 8. At the first stage, a preliminarily oxidized silicon wafer *A* is subjected to proton implantation to a dose which is sufficient for the formation of a porous layer upon subsequent thermal treatment of the wafer. The second stage of the process consists of the chemical cleaning of the wafer *A*, and of a second wafer *B* with their subsequent joining together into a close pair at room temperature. The chemical cleaning of the wafers makes their surfaces hydrophilic, so that they become strongly adhered to one another when being in intimate contact, owing to the formation of hydrogen bonds [57].

The third stage of the process consists of a heat treatment of the bonded wafers. This stage is divided into a low-temperature and high-temperature phases. During the first phase, a buried porous layer is produced in the wafer *A*, which leads to the splitting of the wafer along the plane of the porous layer. During the second phase of stage 3, a high-temperature annealing of the wafer *B* with a thin layer of silicon on the silicon oxide is carried out to ensure the final joining (the formation of covalent chemical bonds) of the thin layer formerly belonging to the wafer *A* with the wafer *B* and the annealing of radiation defects present in the silicon film on the insulating "substrate" is performed. The last stage consists of a chemical-mechanical polishing of the wafers *A* and *B* on the porous-layer side. At this stage, the outer damaged layer is removed to a depth of several angstroms. Thus, as a result of the process, there

is formed an SOI wafer and a residual, wafer *A*, which may be used repeatedly, now as wafer *B*.

The use of hydrogen implantation and the formation of a buried porous layer along which splitting of the wafers occurs is the key link of the Smart Cut technology. The effect of splitting of the wafers along the porous layer is based on the phenomenon of pore coarsening in the porous layer, which occurs anisotropically and mainly in directions parallel to the surface of the wafers. The situation is illustrated in Fig. 9. The buried damaged layer formed under the surface due to hydrogen implantation consists of pores that are filled with molecular hydrogen (H_2) and are coated with atomic hydrogen (H) captured at broken Si bonds at the pore surface. The Si-H bonds are substantially stronger as compared to the H–H bonds that arise between the atomic Si planes in the damaged layer [58]. Upon heating, progressively greater part of implanted hydrogen passes from the atomic into the molecular state, additional clusters of molecular hydrogen are formed in the nanopores, which increases the internal pressure in, and size of, such nanopores. The high internal pressure in the pores is the driving force for the anisotropic expansion of the bubbles along the planes saturated with atomic hydrogen, owing to the breaking of relatively weak H–H bonds. Thus, hydrogen favors the growth and coalescence of pores along the planes parallel to the wafer surface. When all such voids become connected, the detachment of a thin film from the wafer *A* occurs along its entire area. Naturally, the delamination occurs along many parallel planar segments rather than along a single plane. Therefore, the surface in the plane of delamination exhibits strong microroughness (~100 Å).

The splitting of the wafers used in the Smart Cut technology has the same physical nature as the well-known phenomenon of "blistering" characteristic of the surface layers of metals and semiconductors subjected to high-dose implantation with protons [54, 59, 60]. By blistering, the effect of spalling of small scales (a few microns long, with a thickness on the order of the projected range of hydrogen in the material) is meant [54]. Upon blistering, a thin layer of the material located under the buried damaged layer containing pores does not sustain the high internal pressure of hydrogen in the pore cavities. This leads to a premature breakage of small scales before all the internal cavities in the porous layer coalesce through the entire area of the porous layer. In the Smart Cut technology, this thin working layer of the material of the wafer *A* is bonded to the wafer *B*, which prevents pore opening up to the moment when the film is delaminated over the entire area of the wafer *A*. The activation energy E_a for blistering and wafer splitting do not differ in the Smart Cut technology [61], which confirms the like physical nature of these processes. According to [61], the time t required for the complete splitting of the wafers in the Smart Cut process exceeds by approximately an order of magnitude, the time necessary for the development of blistering upon postimplantation annealing, the conditions of proton implantation and crystal annealing being the same in both cases. These times decrease with increasing annealing temperature T_{ann} by the law

$$t = A\exp(E_a/kT_{ann}),$$

where A is the proportionality coefficient depending on the implantation dose.

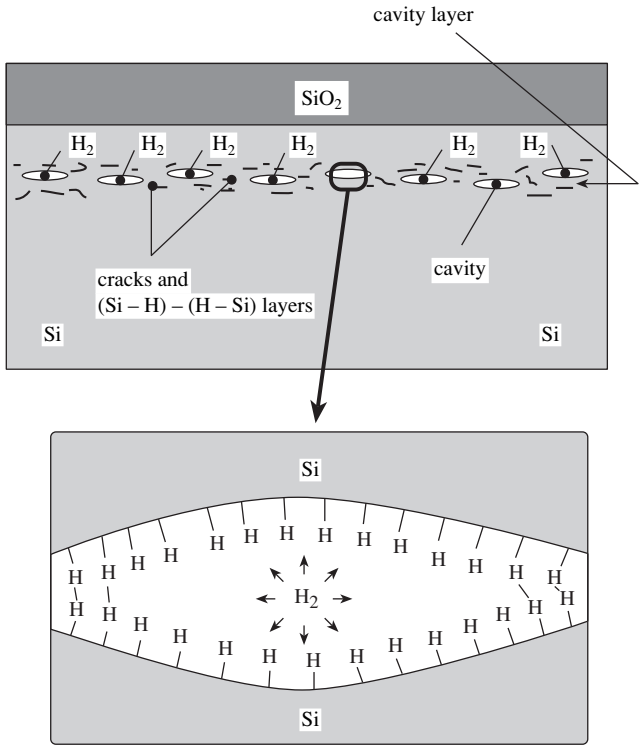

Fig. 9. Silicon crystal after high-dose implantation of hydrogen (schematic). The scheme illustrates the formation of microcracks and cavities in a buried layer saturated with hydrogen.

Note that to effectively realize the Smart Cut process, the dose of protons implanted into the semiconductor crystal must exceed a certain critical level. At a typical value of the energy of implanted protons of about 50 keV, the implantation dose is usually $(4–8) \times 10^{16}$ cm^{-2}, depending on the regime of the postimplantation annealing. An important practical task is the decreasing of the proton irradiation dose, since this increases the economic efficiency of the process and decreases the degree of radiation damage of the semiconductor crystal. In this connection, the work of Agarwal *et al.* [62] should be noted, who suggested using in the Smart Cut technology of simultaneous implantation of hydrogen and helium to decrease the total ion implantation dose. The authors of [62] showed that when the implantation of only protons (with an energy of 30 keV) and postimplantation annealing at 750°C for 20 s are used to provide the entire splitting of silicon wafers, the minimum dose of implanted protons is 6×10^{16} cm^{-2}. This dose can be decreased to $7.5 \times$

10^{15} cm^{-2} if helium is implanted to a dose of 10^{16} cm^{-2} after hydrogen implantation. Thus, the total minimum implantation dose of hydrogen and helium is 1.75×10^{16} cm^{-2}, which is less by a factor of 3.4 than the dose necessary for the conventional Smart Cut process with the use of only proton implantation.

The successful use of the Smart Cut technology for the production of SOI structures stimulated the development of works on the application of this process in the technology of structures of other semiconductors on insulators. Thus, the authors of [63, 64] have demonstrated that the Smart Cut technology can be used for the production of "silicon carbide-on-insulator" (SiC-OI) structures. Wafers (30 mm in diameter) of 6H and 4H SiC polytypes were used in these experiments. Before the implantation of hydrogen, a layer of thermal oxide was first grown on the wafer, then a layer of SiO_2 (of ~1 μm thick) was deposited. Hydrogen ions with an energy of 90 keV were implanted to doses of 5×10^{16} to 10^{17} cm^{-2}; the optimum dose was found to be $\geqslant 8 \times 10^{16}$ cm^{-2}. During the Smart Cut process, the SiC wafers were bonded to substrates of silicon or polycrystalline silicon carbide using a two-stage heat treatment [64] at temperatures of ~900°C and above 1000°C. The first, "low-temperature" stage of annealing was used to provide the splitting of the SiC wafer along the defect porous layer; the second stage was used to ensure the final bonding of the SiC film to the substrate. After the final bonding and polishing of the working layer of SiC, SiC-on-insulator structures with a diameter of 30 mm and thickness of ~0.3 μm were formed on the wafers. The investigation of crystal defects in these structures showed that the quality of SiC films was at least the same as of conventional crystalline silicon carbide wafers.

The investigation of electrical characteristics of the SiC-OI structures have not virtually been performed to date. In [64], the voltage–capacitance technique was used to show that the SiC films obtained after the completion of the Smart Cut process were insulating (the doping level of the initial SiC wafers was of an order of 10^{17} cm^{-3}). This indicates either the passivation of the dopant by the implanted hydrogen or the high residual concentration of radiation defects. On the other hand, the electrical characteristics of the films prepared by the Smart Cut process with the use of SiC wafers with a doping level of 10^{19} cm^{-3} retained their electrical conductivity.

Among the works on the SOI and SiC-OI structures prepared by the Smart Cut technology, that of Tong *et al.* [65] may be noted, in which high-temperature implantation of protons was suggested. The authors of [65] showed that the Smart Cut process can be performed at implantation temperatures of hydrogen in Si and SiC equal to 400 and 800°C, respectively. The use of higher implantation temperatures provides a lesser level of radiation damage, which subsequently permits one to decrease the temperature of the postimplantation annealing of the wafers during the bonding operation. This opens new opportunities for the use of the Smart Cut process for transfer semiconductor films onto substrates that substantially differ in their thermal expansion coefficients from the semiconductor. In [65], this technique was used to obtain Si and SiC films on glass substrates.

Another important work is the realization of blistering and Smart Cut processes for crystals of silicon, germanium, silicon carbide, and diamond [61]. In that work, the authors found that the activation energies of this processes for Si, Ge, SiC, and diamond were 1.2, 1, 4, and 4.2 eV, respectively. Using the Smart Cut technology, SOI, SiC-OI, and Ge-OI structures were prepared. The Si, Ge, and SiC films were transferred onto substrates of a high-melting glass that had a thermal expansion coefficient close to that of Si and retained stability up to 800°C. Note that a comparison of the activation energies of blistering for crystals of Si and SiC according to [61] and [65] shows a strong difference between these energies for Si. This difference may be due to the different methods of implantation used in these works: high-temperature proton implantation in [65] and room-temperature implantation in [61].

Apart from semiconductor materials of Group IV and silicon carbide, of great practical importance for electronics, are films of III–V compounds on substrates of Si or glass. These materials can find wide application in optoelectronics, microwave electronics, and optoelectronic integrated circuits that combine the optoelectronic properties of the III–V compounds with the electronic circuits based on Si. The first successful realization of GaAs-OI structures based on the Smart Cut technology was described by Jalaguir *et al.* [66], who used wafers of semi-insulating GaAs with a (100) orientation and Si coated with a SiO_2 layer. After implantation of 100-keV protons and bonding of the wafers through a layer of SiO_2 using heat treatment in a temperature range of 400–700°C, the GaAs wafer was successfully split along the plane of the damaged porous layer through its entire area. The final result of the work was the production of continuous single-crystal films of GaAs on silicon substrates with an insulating layer of SiO_2. The working diameter of the GaAs-OI structures was 76 mm.

Thus, the results of the investigations in the field of the Smart Cut technology performed in the last four years, considered above, show the possibility of its wide application in the production of multilayer semiconductor structures for modern electronics. The main advantages of this technology are its high preciseness and reproducibility, fabricability, relative simplicity, and small cost in combination with the high quality of the semiconductor materials produced. Today, the Smart Cut technology is a real alternative to the well-known SIMOX technology (Separation by Implanted Oxygen), which is used in a number of firms in the United States, France, and Japan for the production of

high-quality SOI structures [56]. In the SIMOX technology, the insulating barrier layer of SiO_2 is formed by thermal treatment of silicon wafers that were subjected to a high-dose implantation of oxygen ions. In the course of the high-temperature annealing, the implanted oxygen reacts with silicon atoms to form a buried layer of SiO_2 in an oxygen-enriched region located at a depth of about R_p. In this case, a very high annealing temperatures ($T_{ann} \simeq 1300$°C) and large implantation doses (~10^{18} cm^{-2}) are necessary to synthesize SiO_2. These factors are the main disadvantages of the SIMOX technology, since the practical realization of this process requires high-cost superpower implanters and specialized equipment for heat treatment. The Smart Cut technology has no such disadvantages. Moreover, in the Smart Cut technology the working layer of silicon is insulated from the substrate by thermally grown SiO_2 layers, whose quality is higher than that of SiO_2 layers obtained by oxygen implantation. Owing to these advantages, the Smart Cut method has already in 1997 been used in the industrial production of SOI structures.

5.2. Gettering of Impurities by Porous Layers

Gettering is a technological process used to remove uncontrolled impurities and defects out of the active zone of semiconductor devices into passive zones. To this end, either special sinks or centers of precipitation of the impurities to be gettered are formed (relaxation gettering) or conditions that enhance the solubility of these impurities are created (segregation gettering) in the passive zones of the wafers or devices. The impurities to be gettered are removed either from the near-surface working layer of the wafer into its volume (internal, or intrinsic, gettering) or from the working surface and the volume to the back side of the wafer (external, or extrinsic, gettering onto the back side).

In the last years, a considerable attention was paid to the development of gettering processes based on a high-dose ion implantation of various elements such as B, C, N, Ne, Si, Ar, H, He [45, 53, 67–71]. The main advantage of this method of gettering is its preciseness and reproducibility in the creation of gettering regions in the immediate proximity to the active zones of semiconductor devices. This makes it possible to decrease the paths of the diffusion migration of the gettered impurities to sinks, lower temperature, decrease the duration of the gettering process, and thereby increase the efficiency of the removal of uncontrolled impurities. Note that a comparison of the technology of gettering with the use of implantation with various ions shows that the implantation with hydrogen ions or helium in the regime of the formation of buried porous layers has a number of advantages. Among them are the simplicity of creating deep buried gettering layers with the help of standard low-energy accelerators, the small degree of radiation damage in the working layers of the crystal over the gettering layer, and the high efficiency of gettering. The higher efficiency of gettering in the case of porous layers is explained by the presence of a large internal surface of pores with unsaturated chemical bonds that serve as effective traps for impurity atoms. Let us briefly consider the main works concerning the gettering of impurities by porous layers.

The majority of works on gettering refers to the investigation of gettering of metallic impurities, since it is these impurities that are most frequently contaminate the active layers of semiconductor devices and lead to the degradation of their electrical characteristics. Wong-Leung *et al.* [53] investigated the efficiency of gettering copper in silicon. The porous layer was produced at a depth of ~1 μm below the surface of (100)Si wafers by implantating protons (H^+) with an energy of 100 keV to a dose of 3.2×10^{16} cm^{-2}. Copper ions (70 keV) were implanted into the same surface of the wafer to a dose of 3×10^{15} cm^{-3}, which ensured their localization in a surface layer of ~0.1 μm thick. In the process of postimplantation annealing, the copper ions redistributed from the surface of the crystal onto the internal surface of pores present in the damaged layer. With increasing annealing temperature, the amount of copper localized near the surface decreased, while its amount in the porous layer increased to exceed 95% of the implanted amount at 780°C. Note that under equilibrium conditions at $T_{ann} = 780$°C approximately one-third of the implanted copper could be dissolved in the silicon wafer to ensure an average concentration at a level of the copper solubility in silicon (~3×10^{16} cm^{-3}). Nevertheless, almost all copper was absorbed by the porous layer, filling the internal surface of the pores and even forming a volume phase of composition Cu_3Si. The results of investigations that evidence the high efficiency of gettering copper on porous layers created by helium implantation may be found in [45, 72] in the case of external gettering on the back surface of the wafers.

In [73], Wong-Leung *et al.* carried out a comparative analysis of the efficiency of gettering gold using high-dose implantation of hydrogen and silicon ions. The hydrogen implantation was conducted using H^+ ions with an energy of 97 keV to a dose of 3×10^{16} cm^{-2}; silicon ions Si^+ had an energy of 250 keV and were implanted to a dose of 10^{15} cm^{-2}; gold ions (95 keV, dose 10^{15} cm^{-2}) were implanted on the gettering layer side. The process of gettering gold by the buried porous layer was analogous to gettering copper; with using a postimplantation annealing at $T_{ann} = 850$°C, almost all gold (~96%) was accumulated in a narrow porous layer. The investigation of the dynamics of gold accumulation in the porous layer showed that first a gold atom is captured by unsaturated chemical bonds on the surface of the pores; when the whole surface of the pores turns out to be coated with a monolayer of gold atoms, the process of the formation of a bulk phase in the form of a eutectic Si–Au melt becomes possible. Upon the subse-

quent cooling, gold-enriched crystallites are formed in the pores of the damaged layer. The efficiency of gold gettering by porous layers was maximum as compared to the capture of gold by defect layers produced by implanting silicon ions or in the case of gold precipitation near the surface. The most comprehensive theoretical and experimental investigation of the processes of gettering gold y buried porous layers in silicon was performed by Myers and Petersen [74], who studied the redistribution of gold atoms from a near-surface layer of precipitates of the equilibrium Au–Si phase into the buried porous layer and from one porous layer into another. The data obtained made it possible to determine the free energy of interaction of gold with the pore walls and theoretically describe the process of gettering gold by internal porous layers. One practically important consequence of that work is the possibility of determining optimal regimes of gettering impurities by buried porous layers with the help of a theoretical simulation of the process.

A detailed investigation of gettering iron by porous layers was performed in [75]. A distinctive feature of that work was a comparison of the efficiency of gettering iron using internal gettering and gettering by buried porous layers produced by implanting 1.5-MeV helium ions. The results given in that work showed that the gettering by porous layers had a number of advantages:

(a) the porous layer can be formed in the immediate proximity to the working surface;

(b) the pores in the porous layer form a dense quasi-continuous system of gettering sinks, in contrast to the centers of internal gettering that are distributed (divided) over the whole volume of the wafer;

(c) the gettering of impurities in pores occurs at the expense of both the impurity capture on the unsaturated bonds on the internal surface of pores and the formation and growth of metal silicides.

The first two advantages ensure the accelerated kinetics of gettering metallic impurities because of the short paths of impurity diffusion to the gettering layer. The third advantage makes it possible to decrease the concentration of the gettered impurity to substantially smaller values in comparison with the case of internal gettering. The limitations connected with the physical mechanism of internal gettering prevent the decrease in the concentration of metallic impurities to below the level of their equilibrium solubility in the crystal, since the decrease in the impurity concentration in the working layer of the wafers occurs at the expense of the formation and growth of metal silicides at the internal gettering sinks (SiO_2 inclusions). This is possible only if the initial concentration of impurities in the crystal exceeds the equilibrium solubility limit at the temperature of the gettering annealing. Upon gettering by a porous layer, apart from the formation of silicides, the gettered impurity is captured by the unsaturated bonds existing on the inner surface of pores, i.e., an additional mechanism of gettering works, namely, chemisorption. The action of this mechanism is independent of the initial concentration of the impurity to be gettered, which makes it possible to decrease the concentration of metallic impurities in the working layer of wafers to far below their solubility limit. All this makes the gettering technology with the use of porous layers more efficient as compared to the methods of internal gettering. Analogous results were obtained in [76] for the case of gettering copper. Apart from the above considered examples, the effect of gettering metallic impurities by porous layers was also demonstrated for Pt, Ni, and Co [45, 77–79].

Summarizing the results of gettering impurities by buried porous layers, we may conclude that this method is most effective for gettering metallic impurities in silicon wafers. It can be successfully used both for external gettering onto the back side of wafers and the local gettering of impurities from the device zone of integrated circuits onto closely located sinks.

6. CONCLUSION

The analysis of the existing directions of the modification of semiconductors by proton beams given in previous reviews[1, 3, 80, 81] and in the present paper, shows that this method of modification (doping) opens new opportunities for controlling properties of semiconductor materials and designing devices based on these materials in comparison with the conventional methods of doping such as diffusion, epitaxy, ion implantation.

A common feature of all the doping methods, analyzed above, is their locality. The depth of the modified layer is determined by the proton energy and their stopping power in a given semiconductor and may be varied from tens of nanometers to hundreds of microns.

Previously [3, 80], we have already noted that proton transmutation doping is most promising for the fabrication of power and galvanomagnetic devices.

Doping with radiation defects using proton irradiation is successfully used in the fabrication of electronic devices (MOSFET transistors, avalanche-transit-time diodes, high-power diodes and thyristors, integrated circuits) and optoelectronic devices (semiconductor heterolasers, light-emitting diodes, photodiodes) devices [1, 2, 81].

The main advantage of proton-enhanced diffusion is the possibility of creating complex impurity distribution profiles, which cannot be produced by other methods. Thus, steep impurity profiles obtained by proton-stimulated diffusion have great potential for the production of microwave devices.

A very perspective direction is the use of ion-beam mixing in the production of semiconductor devices presently. This direction is intensively developed, and a number of experimental results have already been obtained with the application of modern analytical methods, such as secondary-ion mass spectrometry,

Rutherford backward scattering of ions, electron microscopy, which indicate the real possibility of practical application of ion-beam mixing, e.g., for the production of ohmic contacts to III–V compound materials.

The works that have been analyzed give sufficiently full information on the formation of porous layers upon proton irradiation of semiconductors. The use of porous layers is very promising for gettering impurities and precision splitting of semiconductor wafers (Smart Cut technology). However, no experimental data on the direct comparison of the possibilities of ion beams of three types—hydrogen, oxygen, and nitrogen—in the formation of silicon-on-insulator structures have yet been obtained.

The application of proton beams is not restricted to the sphere of semiconductor electronics; they can also be applied in related fields such as ferroelectric materials, high-temperature superconductors, fullerenes, etc. [82, 83].

ACKNOWLEDGMENTS

This work was supported in part by the Perspective Technologies and Devices of Micro and Nano Electronics program, Ministry of Science and Technologies, Russian Federation, project no. 02.04.330.89.1.2. We are also grateful to V.F. Masterov† (deceased), who initiated the writing of this review and was its first benevolent referee.

REFERENCES

1. I. V. Vasil'eva, G. A. Efremov, V. V. Kozlovskiĭ, V. N. Lomasov, and V. S. Ivanov, *Radiation-Related Processes in the Manufacture of Materials and Electronic Components* [in Russian], Ed. by V. S. Ivanov and V. V. Kozlovskiĭ (Énergoatomizdat, Moscow, 1997).
2. V. S. Vavilov, B. M. Gorin, N. S. Danilin, A. E. Kiv, Yu. L. Nurov, and V. I. Shakhovtsov, *Radiation Methods in Solid-State Electronics* [in Russian] (Nauka, Moscow, 1990).
3. L. F. Zakharenkov, V. V. Kozlovskiĭ, and B. A. Shustrov, Fiz. Tekh. Poluprovodn. (St. Petersburg) **26**, 3 (1992) [Sov. Phys. Semicond. **26**, 1 (1992)].
4. L. F. Zakharenkov and V. V. Kozlovskiĭ, in *Semiconductor Technology: Processing and Novel Fabrication Techniques*, Ed. by M. Levinshtein and M. Shur (Wiley, New York, 1997), Chap. 2, p. 17.
5. N. B. Pleshivtsev and A. I. Bazhin, *Physics of the Ion Beams Effects on the Materials* [in Russian] (Vuzovskaya Kniga, Moscow, 1998).
6. J. Lindhard, M. Scharff, and H. Schiett, Kgl. Danske vid selskab. mat. fys. medd **33** (14), 3 (1963).
7. *Problems of Radiation Technology of Semiconductors* [in Russian], Ed. by L. S. Smirnov (Nauka, Novosibirsk, 1980).
8. *Surface Modification and Alloying by Laser, Ion, and Electron Beams*, Ed. by J. M. Poate, G. Foti, and D. C. Jacobson (Plenum, New York, 1983; Mashinostroenie, Moscow, 1987).
9. P. Baruch, C. Constantin, J. C. Pfister, and R. Saintesprit, Discuss. Faraday Soc. **31**, 86 (1961).
10. G. J. Dienes and A. C. Damask, J. Appl. Phys. **29**, 1713 (1958).
11. P. Baruch, Inst. Phys. Conf. Ser. **31**, 126 (1977).
12. Y. Morikawa, K. Yamamoto, and K. Nagami, Appl. Phys. Lett. **36**, 997 (1980).
13. E. D. Gornushkina, I. V. Kirillova, and R. Sh. Malkovich, Fiz. Tverd. Tela (Leningrad) **24**, 1088 (1982) [Sov. Phys. Semicond. **24**, 694 (1982)].
14. T. D. Dzhafarov, *Radiation-Stimulated Diffusion in Semiconductors* [in Russian] (Énergoatomizdat, Moscow, 1991).
15. *Physical Processes in Irradiated Semiconductors* [in Russian], Ed. by L. S. Smirnov (Nauka, Novosibirsk, 1977).
16. G. D. Watkins, in *Effekts des Rayonnements sur les Semiconductors*, Ed. by P. Baruch (Dunod, Paris, 1964), p. 97.
17. V. V. Kozlovskiĭ, V. N. Lomasov, and L. S. Vlasenko, Radiat. Eff. **106**, 37 (1988).
18. G. A. Kachurin, V. I. Obodnikov, V. Ya. Prints, and I. E. Tyschenko, Fiz. Tekh. Poluprovodn. (St. Petersburg) **28**, 519 (1994) [Semicond. **28**, 313 (1994)].
19. G. A. Kachurin, G. V. Gadiyak, V. I. Shatrov, and I. E. Tyschenko, Fiz. Tekh. Poluprovodn. (Leningrad) **26**, 1977 (1992) [Sov. Phys. Semicond. **26**, 1111 (1992)].
20. V. V. Kozlovskiĭ, V. N. Lomasov, G. M. Gur'yanov, and A. P. Kovarskiĭ, Fiz. Tekh. Poluprovodn. (Leningrad) **16**, 2089 (1982) [Sov. Phys. Semicond. **16**, 1350 (1982)].
21. V. V. Kozlovskiĭ and V. N. Lomasov, Zh. Tekh. Fiz. **54**, 1157 (1984) [Sov. Phys. Tech. Phys. **29**, 658 (1984)].
22. V. V. Kozlovskiĭ and V. N. Lomasov, Fiz. Tekh. Poluprovodn. (St. Petersburg) **19**, 143 (1985) [Sov. Phys. Semicond. **19**, 87 (1985)].
23. V. V. Kozlovskiĭ, S. A. Mazurov, B. Ya. Ber, *et al.*, Pis'ma Zh. Tekh. Fiz. **19** (23), 65 (1993) [Tech. Phys. Lett. **19**, 762 (1993)].
24. V. N. Abrosimova, V. V. Kozlovskiĭ, N. N. Korobkov, and V. N. Lomasov, Izv. Akad Nauk SSSR, Neorg. Mater. **26**, 488 (1990) [Inorgan. Mater. **26**, (1990)].
25. O. V. Aleksandrov, V. V. Kozlovskiĭ, V. V. Popov, and B. E. Samorukov, Phys. Status Solidi A **110**, K61 (1988).
26. M. A. Betuganov, M. U. Digilov, V. I. Kosticov, and M. A. Kumakhov, Phys. Status Solidi A **59** (2), 835 (1980).
27. Yu. N. Kazarinov, V. V. Kozlovskiĭ, V. N. Lomasov, and M. V. Pitkevich, Fiz. Tekh. Poluprovodn. (Leningrad) **20**, 1577 (1986) [Sov. Phys. Semicond. **20**, 989 (1986)].
28. E. Ibe, Nucl. Instrum. Methods Phys. Res., Sect. B **39**, 148 (1989).
29. L. S. Hung, Q. Z. Hong, and J. W. Mayer, Nucl. Instrum. Methods Phys. Res., Sect. B **37/38**, 414 (1989).
30. J. W. Mayer, B. Y. Tsaur, S. S. Lau, and L. S. Hung, Nucl. Instrum. Methods Phys. Res. **181/183**, 1 (1981).

31. D. L. Santes, J. P. de Souza, L. Amaral, and H. Boudinov, Nucl. Instrum. Methods Phys. Res., Sect. B **103**, 56 (1995).
32. L. S. Hung, J. W. Mayer, C. S. Pai, and S. S. Lau, J. Appl. Phys. **58**, 1527 (1985).
33. V. V. Kozlovskiĭ and V. N. Lomasov, Poverkhnost., No. 3, 146 (1987).
34. V. N. Lomasov, Vysokochist. Veshchestva, No. 3, 57 (1992).
35. R. Leguay, A. Dunlop, and F. Dunstetter, Nucl. Instrum. Methods Phys. Res., Sect. B **106**, 28 (1995).
36. V. S. Vavilov, A. E. Kiv, and O. R. Niyazova, *Mechanisms of the Formation and Migration of Defects in Semiconductors* [in Russian] (Nauka, Moscow, 1981).
37. Yu. N. Kazarinov, V. N. Lomasov, B. A. Tallerchik, and É. R. Katilene, Élektron. Tekh., Ser. 6: Mater., No. 6 (121), 9 (1983).
38. K. Neubeck, C.-E. Lefaucheur, and H. Halm, Nucl. Instrum. Methods Phys. Res., Sect. B **106**, 589 (1995).
39. V. V. Kozlovskiĭ and V. N. Lomasov, Fiz. Tekh. Poluprovodn. (Leningrad) **18**, 956 (1984) [Sov. Phys. Semicond. **18**, 597 (1984)].
40. V. V. Kozlovskiĭ, V. N. Lomasov, G. M. Gur'yanov, and A. P. Kovarskiĭ, Fiz. Tekh. Poluprovodn. (Leningrad) **18**, 958 (1984) [Sov. Phys. Semicond. **18**, 598 (1984)].
41. I. A. Abroyan, A. I. Andronov, and A. I. Titov, *Physical Foundations of the Electron and Ion Technology* [in Russian] (Vysshaya Shkola, Moscow, 1984).
42. S. E. Donnelly, A. A. Lucas, J. P. Vigneron, and J. C. Rife, Radiat. Eff. **78**, 337 (1983).
43. S. E. Donnelly, Radiat. Eff. **90**, 1 (1985).
44. C. C. Griffioen, J. H. Evans, P. C. De Jong, and A. Van Veen, Nucl. Instrum. Methods Phys. Res., Sect. B **27**, 417 (1987).
45. V. Raineri, P. G. Fallica, G. Percolla, *et al.*, J. Appl. Phys. **78**, 3727 (1995).
46. R. Tonini, F. Corni, S. Frabboni, *et al.*, J. Appl. Phys. **84**, 4802 (1998).
47. D. M. Follstaedt, Appl. Phys. Lett. **62**, 1116 (1993).
48. D. J. Eaglesham, A. E. White, L. C. Feldman, N. Moriya, and D. C. Jacobson, Phys. Rev. Lett. **70**, 1643 (1993).
49. S. M. Myers, D. M. Follstaedt, H. J. Stein, and W. R. Wampler, Phys. Rev. B **45**, 3914 (1992).
50. C. F. Cerefolini, L. Meda, R. Balboni, *et al.*, Phys. Rev. B **46**, 2061 (1992).
51. R. N. Hall, IEEE Trans. Nucl. Sci. **NS-31**, 320 (1984).
52. S. J. Jeng and G. S. Oehrlein, Appl. Phys. Lett. **50**, 1912 (1987).
53. J. Wong-Leung, C. E. Ascheron, M. Petravic, *et al.*, Appl. Phys. Lett. **66**, 1231 (1995).
54. X. Lu, N. W. Cheung, M. D. Strathman, *et al.*, Appl. Phys. Lett. **71**, 1804 (1997).
55. M. Bruel, Electron. Lett. **31**, 1201 (1995).
56. A.-J. Auberton-Herve, Solid State Technol. **37**, 89 (1994).
57. S. Bengtsson, J. Electron. Mater. **21**, 841 (1992).
58. C. M. Varma, Appl. Phys. Lett. **71**, 3519 (1997).
59. W. K. Chu, R. H. Kastl, R. F. Lever, *et al.*, Phys. Rev. B **16**, 3851 (1977).
60. C. C. Criffoen, J. H. Evans, P. C. De Jong, and A. Van Veen, Nucl. Instrum. Methods Phys. Res., Sect. B **27**, 417 (1987).
61. Q.-Y. Tong, K. Gutjahr, S. Hopfe, *et al.*, Appl. Phys. Lett. **70**, 1390 (1997).
62. A. Agarwal, T. E. Haynes, V. C. Venezia, *et al.*, Appl. Phys. Lett. **72**, 1086 (1998).
63. L. D. Cioccio, Y. Le Tiec, F. Letertre, *et al.*, Electron. Lett. **32**, 1144 (1996).
64. L. D. Cioccio, Y. Le Tiec, C. Jaussand, *et al.*, Mater. Sci. Forum **264–268**, 765 (1998).
65. Q.-Y. Tong, T.-H. Lee, L.-J. Huang, *et al.*, Electron Lett. **34**, 407 (1998).
66. E. Jalaguir, B. Aspar, S. Pocas, *et al.*, Electron. Lett. **34**, 408 (1998).
67. H. Wong, N. W. Cheung, and P. K. Chu, Appl. Phys. Lett. **52**, 889 (1988).
68. M. H. F. Overwijk, J. Politiek, R. C. M. Kruif, and P. C. Zalm, Nucl. Instrum. Methods Phys. Res., Sect. B **96**, 257 (1995).
69. C. J. Barbero, J. W. Corbett, C. Deng, and Z. Atzmon, J. Appl. Phys. **78**, 3012 (1995).
70. W. Skorupa, R. Kogler, K. Schmalz, *et al.*, Nucl. Instrum. Methods Phys. Res., Sect. B **74**, 70 (1993).
71. P. A. Stolk, J. L. Benton, D. J. Eaglesham, *et al.*, J. Appl. Phys. **68**, 51 (1995).
72. S. M. Myers, D. M. Bishop, D. M. Follstaedt, *et al.*, Mater. Res. Soc. Symp. Proc. **283**, 549 (1993).
73. J. Wong-Leung, E. Nygren, and J. S. Williams, Appl. Phys. Lett. **67**, 416 (1995).
74. S. M. Myers and G. A. Petersen, Phys. Rev. B **57**, 7015 (1998).
75. S. A. McHugo, E. R. Weber, S. M. Myers, and G. A. Petersen, J. Electrochem. Soc. **145**, 1400 (1998).
76. S. A. McHugo, E. R. Weber, S. M. Myers, and G. A. Petersen, Appl. Phys. Lett. **69**, 3060 (1996).
77. S. J. Pearton, J. W. Corbett, and M. Stavola, *Hydrogen in Crystalline Semiconductors* (Springer Verlag, Heidelberg, 1992).
78. S. M. Myers, D. M. Follstaedt, and D. M. Bishop, Mater. Res. Soc. Symp. Proc. **316**, 53 (1994).
79. S. M. Myers, G. A. Petersen, and C. H. Seager, J. Appl. Phys. **80**, 3717 (1996).
80. V. V. Kozlovskiĭ and L. F. Zakharenkov, Radiat. Eff. Defects Solids **138**, 75 (1996).
81. V. V. Kozlovskiĭ, L. F. Zakharenkov, T. I. Kol'chenko, and V. M. Lomako, Radiat. Eff. Defects Solids **138**, 63 (1996).
82. V. V. Kozlovskiĭ, Poverkhnost., No. 8, 66 (1997).
83. V. A. Didik, V. V. Kozlovskiĭ, R. Sh. Malkovich, and E. A. Skoryatina, Fiz. Tverd. Tela (St. Petersburg) **40**, 2189 (1998) [Phys. Solid State **40**, 1985 (1998)].

Translated by S. Gorin

Semiconductors, Vol. 34, No. 2, 2000, pp. 141–145. Translated from Fizika i Tekhnika Poluprovodnikov, Vol. 34, No. 2, 2000, pp. 148–152.

ATOMIC STRUCTURE AND NONELECTRONIC PROPERTIES OF SEMICONDUCTORS

Electronic Properties of Variably Charged Defects in Crystalline Semiconductors

A. N. Kraĭchinskiĭ, L. I. Shpinar, and I. I. Yaskovets

Institute of Physics, National Academy of Sciences of Ukraine, pr. Nauki 144, Kiev, 258650 Ukraine

Submitted March 17, 1999; accepted for publication August 26, 1999

Abstract—The electronic properties of defects with various spatial configurations are examined in relation to corresponding sets of valence bonds. The examination is based on the analysis of the energy functional, in which the elastic energy in the anharmonic approximation, the variation in the electronic term of the defect quasi-molecule defined by the electron localization, and Hubbard's interaction energy are taken into account. Two types of such defects are recognized, namely, the defects with strong and weak electron–atom interaction. For defects of the first type, which are characterized by positive effective correlation energy, no variations of the adiabatic potential topology are observed after the electron localization. The pair of carbon atoms (C_iC_s) and donor–acceptor pairs in the crystalline silicon belong to this type of defect. The effective occupancy is calculated for this type of defects as a function of adiabatic potential parameters. Transformation of the initial double-well potential into the single-well potential after the localization of the carriers is substantial for the properties of the second type defects. In this case, the effective correlation energy can be either positive or negative. The analysis of the known experimental results permits us to assume that the interstitial boron atom in silicon belongs to this type of defect. The adiabatic potential (in which the interstitial boron atom moves), the activation energies for transitions between different charge states of this defect, and the effective occupancy are calculated from the experimental data reported by Watkins. © *2000 MAIK "Nauka/Interperiodica".*

Stable defects forming in semiconductors on irradiation constitute complex agglomerates including both impurity atoms and host-material atoms. The character of bonding between the atoms of the defect quasi-molecule, as a rule, differs from that typical of the given material. For this reason, deep levels in a forbidden gap of a semiconductor are typical of the radiation defects, in contrast to Coulombic defects [1]. Capture (emission) of electrons by the states of radiation defects, e.g., vacancy-like defects [2], usually causes the formation (breaking) of the bonds between the atoms of the defect quasi-molecules. For this reason, these defects are characterized by a rather strong electron–vibrational interaction, since the atomic coordinates R_i in the defect quasi-molecules vary because of the variation in bonding between them as the charge state changes.

The energy $E_j(x)$ of the defect quasi-molecules involving j localized electrons can be presented in a single-mode approximation in the form

$$E_j(x) = V(x) + j\delta E(x) + U_c(x)\delta_{ij}, \qquad (1)$$

where x is the generalized configuration coordinate, $V(x)$ is the elastic energy of the quasi-molecule in the reference state ($j = 0$), $\delta E(x) = E_q(x) - E_q$ is the change of the quasi-molecule term q due to the electron occupancy of a term, and $U_c(x)$ is the energy of Hubbard's electron–electron interaction in the case of localization of two charge carriers of equal sign. For vacancy-like defects in the crystalline Si (e.g., the vacancy, the A-center, and the defects caused by the presence of Au, Pt, or Ni impurities), the role of the generalized coordinate is played by the "breathing" mode. In this case, the $E_j(x)$ energy is usually determined using the harmonic approximation only, assuming the atomic displacements (x) are small compared to the interatomic distance a ($x \ll a$).

The defects of another type can occur in various spatial configurations n with their own characteristic set of covalent bonds. Each configuration can be realized with the probability P_j^n for a given number of localized electrons j. Examples of these defects in Si are the pair of carbon atoms, one of which is located at the interstitial site, while the other is located at the substitutional site (C_iC_s); the (B, V) defect, where B is the boron atom and V is the vacancy; and the series of the donor–acceptor pairs. It seems likely that the interstitial boron atom, which appears in silicon as a result of treatment by the electron beam and γ-radiation, belongs to this type of defect. Actually, the experimental results [3, 4] confirm the rearrangement of chemical bonds as the charge state of the boron atom changes.

Electronic properties of multistable defects were investigated both experimentally and theoretically [5, 6]. Here, we consider a simple model, which permits us to describe the electronic properties of multistable defects and the probabilities of electronic transitions between various charge states of bistable defects. For defects with a variable configuration, the adiabatic

potentials are substantially anharmonic. In order to describe the electronic properties of these defects, it is necessary to use the approach differing from the common "polaron" one [7], which is used to describe the vacancy-like defects.

When describing the electrical and optical properties of defects in the deformable lattice, the problem is reduced to determining the adiabatic potentials $E(j, x)$. These potentials can be described on the basis of the known microscopic models of defects, which are constructed on the basis of experimental data. The simplest analytical expression, which describes the bistable defect in a single-mode approximation, takes the form

$$E_j(x) = A(\eta x^2 + tx^3 + x^4) + jE_0 + jQx + U_c\delta_{j2}, \qquad (2)$$

which follows from (1) if $E_q(x)$ is expanded in a power of x (the j-dependence of coefficients of x^n can be neglected for $n \geq 2$ [8, 9]). The potential of the form (1)–(2) was used for the analysis of the electronic states in the forbidden gap from the data on mobility in chalcogenide vitreous semiconductors [10, 11]. Crystalline semiconductors differ from chalcogenide vitreous semiconductors by the concentration of rearrangeable defects. It is significantly lower for crystalline semiconductors. The distribution $F(\eta, t)$ of parameters η and t, which characterizes the defect quasi-molecule, is δ-shaped in this case. In (2), $A = (1/2)k_0a_0^2 \approx 10$–$30$ eV. Here, a_0 is the quantity on the order of the atomic radius, whereas A and k_0 are the usual scales of the elastic energies and constants for covalent semiconductors. The quantities η ($|\eta| \ll 1$) and t ($t^2 \ll 1$) are defined by the specific structure of the defect quasi-molecule and have the significance of the parameters characterizing the defect "softness" and potential asymmetry. For a j-fold ($j = 0, 1, 2$) occupancy of the E_q term, the electron–atom interaction is proportional to the constant Q. This interaction can cause deformation of the medium and strong lowering of the term $\delta E_q(x) = E_q(x) - E_q \leq Q$. In general, a new additional bond appears in this case. This causes a variation in the spatial configuration of the defect quasi-molecule, which implies the transition from one potential minimum to another. The complete analysis of potential (2) is rather tedious. However, we can point out the following properties. Potential (2) has one minimum irrespective of electron occupancy j, as long as $p = 1 - 8\eta/3t^2 < 0$. For $p > 0$, i.e., for the case of interest, the potential topology is defined by the quantity

$$D = \left(\frac{\eta}{3} + \frac{t^2}{8}\right)^3 - \frac{1}{8}\left(\frac{\eta t}{2} + \frac{t^2}{8} + \frac{jQ}{A}\right)^2. \qquad (3)$$

As this takes place, two classes of defects with type (2) potential can be recognized. These are the defects with the strong ($D < 0$) and weak ($D > 0$) electron–atom interaction. The function D divides the phase space of the parameters ($q = Q/A$, t, η) of the defect quasi-molecule by the surfaces

$$q_{1,2} = -\frac{\eta^* t}{2} - \frac{t^2}{8} \pm \sqrt{\frac{1}{64}\left(t^2 + \frac{8\eta}{3}\right)^3} \qquad (4)$$

into three regions. The region of values $Q_1 > Q > Q_2$ corresponds to double-well potentials, and the defect quasi-molecules with single-well potentials exist in regions $Q > Q_1$ and $Q < Q_2$. The region $\eta \ll 1$ ($\eta > 0$) corresponds to critical potentials, which define the properties of electronic states in the mobility gap region for chalcogenide vitreous semiconductors investigated in [10, 11].

The possible transformation of the initial double-well potential (for occupancy $j = 0$) into the single-well potential ($j = 1, 2$) is typical of the defects with a strong electron–atom interaction. To illustrate these general properties of potential (2), let us consider the role of the localized charge carriers in the adiabatic potential formation for low values of its "trial" asymmetry ($t^2 \ll 1$, $\eta = -\sigma < 0$). In this case, the double-well potential exists on the condition that $(1/8)(jQ/A)^2 < |\eta|^3/27$, and the single-well potential exists for the opposite sign of this inequality. Once this inequality is valid, the arrangement of minima and the corresponding values of potential in these minima are defined by the expressions

$$x_{2,1} = -\left(\frac{3}{8}t + j\frac{Q}{4A\sigma}\right) \pm \left(\sqrt{\frac{\sigma}{2}} - \frac{t}{8}\sqrt{\frac{18}{\sigma}}\frac{jQ}{4A\sigma}\right), \qquad (5)$$

$$E_j(x_{2,1}) = \left(-\frac{A}{4}\sigma + U_c\delta_{j2} + jE_0 - \frac{3}{8}jQt\right) \pm \left(\frac{1}{4}A\sigma\sqrt{2\sigma} + jQ\sqrt{\frac{\sigma}{2}}\right). \qquad (6)$$

Hence, for the difference of potentials in minima ($\delta E_{12} \equiv E_j(x_{2\min}) - E_j(x_{1\min})$), we have

$$\delta E_{12} = A\sigma t\sqrt{\frac{\sigma}{2}} + jQ\sqrt{2\sigma}. \qquad (7)$$

This difference can be either positive or negative depending on the relationship between the values and signs of the parameters Q and t. In the case of strong electron–atom interaction ($D < 0$ and $j \neq 0$), the adiabatic potential has a single minimum at the point

$$x_{\min} \approx -\frac{1}{2}\left[\left(j\frac{2Q}{A}\right)^{1/3} + \frac{1}{3}\left(\frac{4A}{jQ}\right)^{1/3} + \frac{t}{2}\right], \qquad (8)$$

in which the value of the potential is defined by the expression

$$E_j(x_{\min}) \approx -\frac{1}{4}\left[A\sigma\left(\frac{jQ}{A}\right)^{1/3} + jQ\right]t - \frac{3}{8}jQ\left(j\frac{2Q}{A}\right)^{1/3} - \frac{1}{4}A\sigma\left(j\frac{2Q}{A}\right)^{2/3} - \frac{1}{6}A\sigma^2 + jE_0 + U_c\delta_{j2}. \quad (9)$$

Hence, the defects with a variable configuration are divided into two types: those with strong and those with weak electron–atom interaction. The localization of carriers causes the asymmetry of a double-well potential. This asymmetry is enhanced for the equal sign of t and Q and diminishes or changes the sign otherwise. In the case of large values of $|Q|$, the character of the potential topology changes (see figure).

It seems likely that the donor–acceptor pairs, as well as the C_iC_s and BV defects in the irradiated crystalline silicon, belong to the type characterized by weak electron–atom interaction. Actually, the EPR studies demonstrate that, in the case of C_iC_s, no appreciable electron–vibrational interaction is observed, and the adiabatic potentials remain double-well with a variation in the charge number. In the case of defects with a weak interaction, the effective correlation energy $U_{\text{eff}} = E_2(x_{\min}) + E_0(x_{\min}) - 2E_1(x_{\min})$ is positive, whereas, in the presence of a strong electron-atomic interaction

$$U_{\text{eff}} \approx U_c - 0.19Q\left(\frac{2Q}{A}\right)^{1/3} + \frac{1}{2}A\sigma\left[0.26\left(\frac{2Q}{A}\right)^{2/3} + 0.37\left(\frac{Q}{A}\right)^{1/3}t\right], \quad (10)$$

it can be either positive or negative.

To describe the defects with a variable configuration, we start from the canonical distribution, according to which the probability of finding for the defect in the state that is characterized by the total energy $E_{\text{tot}}(x, j) = E_j(x) - jF$, where F is the Fermi energy, has the form

$$P(x, j) = A(j)\exp\left(-\frac{E(x, j)}{kT}\right),$$
$$A(j) = \left[\sum_{j=0}^{2}\iint\exp\left(-\frac{E(x, j)}{kT}\right)dxdp\right]^{-1}. \quad (11)$$

In this case, the probability of finding the defect in the jth ($j = 0, 1, 2$) charge state equals

$$P(J) = \left[\sum_{j=0}^{2}\iint\exp\left(-E\frac{(x, j)}{kT}\right)dxdp\right]^{-1} \times \iint\exp\left(-\frac{E(x, j)}{kT}\right)dx. \quad (12)$$

As is seen from this expression, the vicinities of minima x_k of the potential $E_j(x)$ give the major contribution

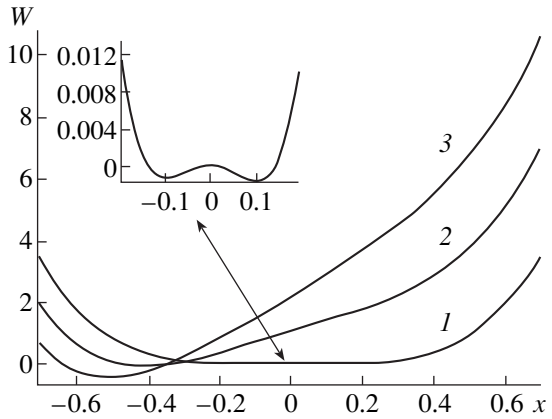

The potential of the defect as a function of the generalized coordinate x for the number of localized electrons j = (*1*) 0, (*2*) 1, and (*3*) 2.

into integrals. Close to the minima, $E_j(x) \approx E_j(x_k) + \frac{1}{2}B_{jk}(x - x_k)^2$ and

$$\int_0^\infty\exp\left(-\frac{E_i(x)}{kT}\right)dx \approx \sum_{k=1}^{n}\left(\frac{2\pi}{B_{ik}}\right)^2\exp\left(-\frac{E_i(x_k) - iF}{kT}\right), \quad (13)$$

where B_{jk} are the quantities characterizing the strain susceptibility in a given configuration, and, conversely, the summation is performed over all k-minima, whose number should not necessarily equal the number of charge states of the defect (j). It is evident that the deepest minimum gives the largest contribution. For identical minima, the result of summation reduces to multiplication by the number of minima. This circumstance can be accounted for by introducing the degeneracy factor $g_n(j)$, where n is the number of identical minima. This number can be different for various j. Let us denote the electron degeneracy factor by $g_e(j)$; in doing so, the total degeneracy factor $g_k(j) = g_e(j)g_n(j)/\sqrt{B_{jk}}$. Hence, the expression for probability of finding the defect in the jth charge state in the vicinity of kth minimum takes the form

$$P_k(j) = \frac{g_k(j)\exp\left(-\frac{E_j(x_k) - jF}{kT}\right)}{\sum_{j=0}^{2}\sum_{k=1}^{n}g_k(j)\exp\left(-\frac{E_j(x_k) - jF}{kT}\right)}. \quad (14)$$

Let us analyze the transition of defects from the charge state j, which is characterized by the generalized coordinate x, into the state with the parameters y and $k = j + 1$. This implies that a certain other state $\psi_R(r)$ with the energy ε_R, which is provided by the excess electron, occurs in the system. The occupancy probability for this state is defined by the Fermi distribution $f_0(\varepsilon_R)$. The single-electron transitions proceed accord-

ing to the energy conservation law: $E_{tot}(x, j) = E_{tot}(y, k)$, where $E_{tot}(x, j) = E_j(x) + \varepsilon_R$, and $E_{tot}(y, k) = E_k(y)$. The total transition rate $R_R(j, k)$ for $j \longrightarrow k$ transitions via the R states can be obtained as follows. The initial probability $f_0(\varepsilon_R)P_j(x)$ is multiplied by the rate $R_R(j, k)$ and the delta function of energy with subsequent integration in phase spaces x and y ($k = j + 1$). Using the Born–Oppenheimer approximation, it is possible to demonstrate that the expression defining the activation energy E_{ij}^a for transitions from the charge state i to state j takes the form [7]

$$R_R(i, j)/P(i) = \int_0^\infty f_0(\varepsilon_R)P_i(x_{ij})\Phi_R\sqrt{\varepsilon_R}d\varepsilon_R \sim \exp(-E_{ij}^a/kT), \quad (15)$$

where $\varepsilon_R^{1/2}d\varepsilon_R$ is the density of electron states at the bottom of the conduction band. Let us consider the above expressions for the potential of the strong electron–atomic interaction as well as for the coordinates of the minimums and intersection for the adiabatic potential curves for different population numbers. The expressions describing the activation energy E_{ij}^a for transitions of defects from the charge state i to the charge state j can be written as:

$$E_{01}^a \approx A\left(l_1^4 + tl_1^3 - \eta l_1^2 + \frac{\eta^2}{4} + \frac{\sqrt{2}}{4}\eta^{3/2}t\right), \quad (16)$$

$$E_{12}^a \approx A\left(l_2^4 - tl_2^3 - \eta l_2^2 + \frac{\eta^2}{6} + \frac{2^{1/3}}{4}t\eta^2 q_A^{1/3}\right) + \frac{1}{4}tQ - (E_0 + U_c) + 3\frac{2^{1/3}}{8}Qq_A^{1/3} + \frac{2^{2/3}}{4}Aq_A^{2/3}\eta, \quad (17)$$

$$E_{10}^a \approx A\left(l_1^4 - tl_1^3 - \eta l_1^2 + \frac{\eta^2}{6} + \frac{2^{1/3}}{4}\eta^2 tq_A^{1/3} - \frac{2^{2/3}}{4}\eta q_A^{2/3}\right) + 2^{1/3}\frac{3}{8}Qq_A^{1/3} + \frac{1}{4}tQ - E_0, \quad (18)$$

$$E_{21}^a \approx A\left(l_2^4 - tl_2^3 - \eta l_2^2 + \frac{\eta^2}{6} + \frac{2^{1/3}}{4}\eta^2 tq_A^{1/3} - \frac{1}{2^{1/3}}\eta q_A^{2/3}\right) + 2^{2/3}\frac{3}{4}Qq_A^{1/3} - 2(E_0 + U_c), \quad (19)$$

where $l_1 = Q/A$, $l_2 = (E_0 + U_c)/A$, and $q_A = Q/A$. Transitions $2 \longrightarrow 1$ and $1 \longrightarrow 0$ are related to the electron transfer into the conduction band, and, for low values of E_{10}^a and E_{21}^a, their rates are defined by the position of the Fermi level. In principle, the expressions obtained for the activation energies of transitions between different charge states permit us to determine the parameters of defects with a strong electron–atom interaction from the experimental data. The activation energies found from the nonequilibrated EPR and DLTS experiments are usually used as these experimental data. As for experiments using the equilibrated electronic properties of defects, the energies of thermal transitions $E_{th}(j \longrightarrow j + 1) = E[j, x_{min}(j)] - E[j + 1, x_{min}(j + 1)]$ are of importance. These energies are attributed to the variation of the occupation numbers $j + 1 \longrightarrow j$, where $x_{min}(j)$ is the value of the coordinate, which minimizes $E_j(x)$ for a given occupation number j. For defects with a strong electron–atom interaction, we have

$$E_{th}(1 \longrightarrow 2) = 0.72Qq_A^{1/3} - (E_0 + U_c) + \frac{1}{4}tQ + 0.233\eta Aq_A^{2/3} + 0.082\eta tAq_A^{1/3}, \quad (20)$$

$$E_{th}(0 \longrightarrow 1) = 0.47Qq_A^{1/3} - E_0 + \frac{tQ}{4} - 0.35A\eta^{3/2}t - 0.4\eta Aq_A^{2/3} + 0.31\eta tAq_A^{1/3} - \frac{1}{12}A\eta^2. \quad (21)$$

Let us consider the special features of equilibrium electronic properties of bistable defects for the case of weak electron–atom interaction, namely, when the potential's topology is the variation in the electron occupancy. The obtained expressions (14) for the occupation probability permit us to obtain the relationships linking the occupation probabilities for each potential well. As a result, the expression can be found, e.g., for the bistable singly charged centers:

$$N_B^- = \frac{nN_B}{n + Q_{B(2)}f},$$

where N_B is the total concentration of bistable defects, n is the concentration of free electrons in the conduction band, $Q_{B(2)} = N_c\exp(-\varepsilon_2/kT)$, N_c is the density of states at the conduction-band bottom, and ε_2 is the population of the bistable defect in the second well. The function f describes the contribution of the another metastable state and has the form

$$f = \left[1 + \exp\left(-\frac{\varepsilon_{12}^0}{kT}\right)\right]/\left[1 + \exp\left(-\frac{\varepsilon_{12}^-}{kT}\right)\right].$$

Here, $\varepsilon_{12}^0 = E_1^0 - E_2^0$ and $\varepsilon_{12}^- = E_1^- - E_2^-$ are the differences between positions of minimums for the double-well potential in the neutral and negative singly charged states. Hence, it is possible to introduce the effective occupancy for the bistable defect

$$\varepsilon_{eff} = \varepsilon_2 - kT\ln f, \quad (22)$$

which includes the parameters of the double-well potential and, generally speaking, depends on temperature.

In conclusion, let us dwell on the radiation defect in silicon, namely, the interstitial boron atom B_i in the sil-

icon lattice. It is known [3] that the interstitial boron atom can have three charge states: B^+, B^0, and B^-. The transition from the B^0 charge state to the B^- state is characterized by high lattice relaxation energy. This causes inversion of donor and acceptor levels; i.e., this defect is a center with a negative correlation energy. The behavior of the EPR signal for the B^0 state and the variations in the bonding configuration are indicative of a high lattice relaxation energy. The microscopic models [3] confirm that this system should be considered in close relation to the phenomenological model of defects, which was considered in previous sections. According to the experimental data [3], we have $E_{10}^a = (0.13 \pm 0.01)$ eV and $E_{21}^a = (0.45 \pm 0.08)$ eV. These data are inadequate to unambiguously determine all of the parameters involved in (16)–(21). For this purpose, it is necessary to carry out a special experiment to determine the population of a vacancy in *p*-Si similar to [12], for example. Nevertheless, we can estimate the parameters and clarify the adiabatic potential character. The parameters involved are of the following order of magnitude: $Q \approx 1$–3 eV and $A \approx 10$–30 eV. The quantity E_0 has the significance of the "trial" energy level, which is occupied by electrons in the course of varying the electron occupation number. This energy is reckoned from the top of the valence band. Consequently, its magnitude is approximately equal to the forbidden gap energy E_g for a semiconductor: $E_0 \le E_g < Q$. According to the available estimates [7, 13], $U_c \approx 0.2$–0.3 eV. Estimations for various numerical values of parameters under consideration demonstrate that the best agreement with the known experimental values of activation energies is obtained for $t = -0.01$, $\sigma = 0.12$, $Q = 3.5$, $E_0 = 1.0$, $A = 15$, and $U_c = 0.2$. In this case, we have $E_{21}^a = 0.42$ eV, $E_{10}^a \approx 0.14$ eV, $E_{01}^a \approx 0.08$ eV, and $E_{21}^a \approx 0.03$ eV. We obtain the effective correlation energy value $U_{\text{eff}} \approx -0.31$ eV. The activation energy values E_{21}^a, E_{10}^a, and E_{01}^a, which are found in such a manner, are close to the experimental ones [5, 6]. The effective energy of the occupied level $E_{\text{occ}} \approx 0.22$ eV. The adiabatic potentials for the interstitial boron atom in various charge states, which were calculated from the parameters found, are presented in the figure. The potential flatness in the B^+ state, which is typical of the soft configurations in chalcogenide vitreous semiconductors [8], and low activation energy ($\approx$0.03 eV) for the $B^0 \longrightarrow B^-$ transition are typical of the adiabatic potentials found. These special features of potentials can define the specific features of interstitial boron migration, which is stimulated by the recombination of minority charge carriers.

REFERENCES

1. J. A. Van Vechten and C. D. Thurmond, Phys. Rev. B: Solid State **14** (8) 3551 (1976).
2. G. D. Watkins, Physica B (Amsterdam) **117–118**, 9 (1983).
3. G. D. Watkins and J. R. Troxell, Phys. Rev. Lett. **44** (9), 593 (1980).
4. R. D. Harris, J. L. Newton, and G. D. Watkins, Phys. Rev. B: Condens. Matter **36** (2), 1094 (1987).
5. K. Chartre and L. C. Kimerling, in *Proceedings of XV International Conference on Defects in Semiconductors*, Budapest, Hungary (1988) [Mater. Sci. Forum **38–41**, 391 (1989)].
6. V. M. Siratskiĭ, V. I. Shakhovtsov, V. L. Shindich, *et al.*, Sov. Phys. Semicond. **24** (10), 1117 (1990).
7. C. A. Baraff, E. O. Kane, and M. Shluter, Phys. Rev. B: Condens. Matter **21** (8), 3563 (1980).
8. M. I. Klinger, Usp. Fiz. Nauk **146** (1), 105 (1985).
9. M. I. Klinger, Phys. Rep. **165** (5–6), 275 (1988).
10. M. I. Klinger and V. G. Karpov, Zh. Éksp. Teor. Fiz. **82** (5), 1687 (1982).
11. M. I. Klinger, L. I. Shpinar, and I. I. Yaskovets, Fiz. Tverd. Tela (Leningrad) **28** (2), 470 (1986).
12. V. V. Emtsev, T. V. Mashovets, and M. A. Margaryan, Fiz. Tekh. Poluprovodn. (Leningrad) **18** (8), 1516 (1984) [Sov. Phys. Semicond. **18**, 950 (1984)].
13. L. I. Shpinar, I. I. Yaskovets, and M. I. Klinger, Fiz. Tekh. Poluprovodn. (Leningrad) **24** (7), 1153 (1990) [Sov. Phys. Semicond. **24**, 729 (1990)].

Translated by N. Korovin

Semiconductors, Vol. 34, No. 2, 2000, pp. 146–149. Translated from Fizika i Tekhnika Poluprovodnikov, Vol. 34, No. 2, 2000, pp. 153–156.

ELECTRONIC AND OPTICAL PROPERTIES OF SEMICONDUCTORS

Electrical Properties of InP Irradiated with Fast Neutrons in a Nuclear Reactor

N. G. Kolin*, D. I. Merkurisov*, and S. P. Solov'ev**

** Karpov Institute of Physical Chemistry (Obninsk Branch), Obninsk, Kaluga oblast, 249020 Russia*
e-mail: FCI@meteo.ru
*** Institute of Nuclear-Power Engineering, Obninsk, Kaluga oblast, 249020 Russia*
Submitted January 11, 1999; accepted for publication May 27, 1999

Abstract—Electrical properties of single-crystal InP samples with various initial concentrations of charge carriers were studied in relation to the dose of irradiation with fast reactor neutrons and subsequent heat treatments in the temperature range of 20–900°C. It is shown that the behavior electrical properties depends on the doping level of the starting material and that the heat treatment in the aforementioned range of temperatures results in a complete elimination of radiation defects, which makes it possible to apply the method of nuclear-transmutation doping to InP samples. The contribution of nuclear reaction initiated by intermediate-energy neutrons to the total level of nuclear-transmutation doping amounts to about 10%. *© 2000 MAIK "Nauka/Interperiodica".*

Only a few publications have been devoted to studies of radiation defects formed in InP samples as a result of neutron irradiation [1–5]. A practical implementation of the method of nuclear-transmutation doping for III–V semiconductor compounds necessitated closer examination of radiation-induced physical processes occurring in such materials under the effect of irradiation with nuclear-reactor neutrons. However, study of radiation defects in the course of nuclear-transmutation doping due to thermal reactor neutrons is complicated by the fact that impurities are introduced in the material. This work is devoted to the study of the effects of irradiation with fast nuclear-reactor neutrons and subsequent heat treatments on electrical properties of InP single crystals.

As starting samples, we used the Czochralski-grown InP single crystals, both undoped and doped with tellurium to various concentrations in the course of growth. All the samples were *n*-type in the as-grown state. The electrical parameters of the samples prior to irradiation (concentration of charge carriers n, their mobility μ, and resistivity ρ) are listed in the table.

InP samples were irradiated in Cd cans at temperatures no higher than 70°C in vertical channels of the active zone of a VVR-ts water-cooled and water-moderated nuclear reactor, with the flux density of fast neutrons (with energy $E > 0.1$ MeV) being $\varphi_f = 5 \times 10^{13}$ cm^{-2} s^{-1}. The duration of irradiation was chosen such that the integrated fluxes of neutrons varied in the range of $F_f = 8 \times 10^{15}$–2.27×10^{19} cm^{-2}. The use of Cd cans precluded the effect of nuclear-transmutation doping initiated by thermal neutrons. The influence of resonance neutrons (the energy $E = 1.46$ eV and the cross section $\sigma = 2.2 \times 10^4$ b) was eliminated by grinding off a layer ~50 μm thick from both faces of an irradiated sample. The irradiated InP samples had high induced radioactivity after irradiation; therefore, they were kept in special boxes for 4–18 months, depending on the dose of neutrons. After the induced radioactivity decayed to a permissible level, the samples were subjected to decontaminative rinsing, grinding, and etching in a $HNO_3 : HCl = 3 : 1$ solution. Electrical parameters of InP samples were determined by the Van der Pauw method at room temperature.

Figures 1a and 2a show the dependences of electrical parameters of InP samples with various initial concentrations of charge carriers (n) on the integrated flux of fast neutrons (F_f). It is evident that the concentration and mobility (μ) of charge carriers decrease with irradiation as a consequence of formation of radiation defects. Furthermore, the higher is the doping level of the starting material, the larger are the integrated fluxes of neutrons corresponding to the onset of a decrease in n. In the case of large integrated fluxes, i.e., $F_f \geq 1 \times 10^{18}$ cm^{-2} for the samples with initial concentration $n = (2–4) \times 10^{16}$ cm^{-3} and $F_f \geq 1 \times 10^{19}$ cm^{-2} for the samples with $n = 3.9 \times 10^{18}$ cm^{-3}, electron concentration and electrical conductivity increase with F_f and tend to constant values in accordance with the limiting position of the Fermi level in highly irradiated InP samples [6]. Apparently, this can be attributed to an overlap of the shells of disordered regions and to a manifestation of the hopping conduction [7]

The rate of variation of mobility of charge carriers also depends on initial values of n. If the integrated flux is equal to about 5×10^{17} cm^{-2}, a decrease in μ amounts to 80% of the initial value for undoped InP samples and to 92% of the initial value for heavily doped samples. This indicates that the presence of impurities in the

Electrical parameters of starting and irradiated InP samples

Sample no.	As-grown samples			Impurity	F_f, 10^{17} cm^{-2}	After irradiation in reactor and subsequent annealing at 900°C		
	n, 10^{17} cm^{-3}	μ, 10^3 cm^2/(V s)	ρ, 10^{-3} Ω cm			n, 10^{17} cm^{-3}	μ, 10^3 cm^2/(V s)	ρ, 10^{-2} Ω cm
1	0.18	4.20	80.00	–	0.51	0.25	6.60	3.90
2	0.18	4.20	80.00	–	5.10	1.17	2.90	1.83
3	0.18	4.20	80.00	–	50.40	11.00	1.83	0.31
4	4.00	2.80	5.60	Te	0.51	5.30	2.35	0.50
5	4.00	2.80	5.60	Te	5.10	5.80	2.75	0.39
6	4.00	2.80	5.60	Te	50.40	14.60	1.70	0.25
7	39.00	1.90	0.85	Te	0.51	35.00	1.63	0.11
8	39.00	1.90	0.85	Te	5.10	20.50	2.00	0.15
9	39.00	1.90	0.85	Te	50.40	33.00	1.54	0.12
10	0.35	3.76	–	–	0.08	0.44	3.20	4.40
11	0.35	3.76	–	–	2.74	0.51	3.50	3.50
12	0.35	3.76	–	–	5.27	0.92	3.50	2.00
13	1.80	3.03	–	Te	0.08	2.80	2.70	0.83
14	1.80	3.03	–	Te	2.74	2.30	2.75	0.99
15	1.80	3.03	–	Te	5.27	2.60	2.88	0.82
16	7.50	2.49	–	Te	0.08	7.30	2.25	0.38
17	7.50	2.49	–	Te	2.74	8.60	2.50	0.38
18	7.50	2.49	–	Te	5.27	8.90	2.10	0.33
19	7.50	2.49	–	Te	227.00	16.00	1.90	0.21

starting material is conducive to a decrease in mobility of charge carriers in the case of F_f as high as 5×10^{17} cm^{-2}; however, for larger integrated fluxes, the rate of degradation of μ in undoped InP samples becomes higher than that in heavily doped samples. For $F_f \sim 5 \times 10^{18}$ cm^{-2}, a decrease in the mobility of charge carriers is almost the same for undoped and heavily doped samples and is approximately equal to 98–99%.

In order to study the thermal stability of radiation defects, we annealed the samples (placed in evacuated sealed quartz ampules) for 20 min in the temperatures range T = 20–900°C at a step of 100°C. Figures 1b and 2b show the dependences of electrical parameters of irradiated samples on the annealing temperature. As is evident, the concentration and mobility of charge carriers in all the samples increase as the annealing temperature increases and then tend to constant values after annealings in the temperature range of T = 700–900°C. The rate of change in the parameters is highest in the temperature range of 300–600°C irrespective of the doping level in the initial state.

The final value of n depends on both the initial concentration of charge carriers and the integrated flux of neutrons that irradiated the sample. The latter is related to the fact that the intermediate-energy neutrons are not cut off by the walls of Cd cans and are strongly absorbed in InP; as a result, in InP, as in other In-containing III–V semiconductor compounds, the samples become doped with Sn according to the reaction $^{115}\mathrm{In}(n, \gamma)^{116}\mathrm{In} \xrightarrow{\beta-} {}^{116}\mathrm{Sn}$. Since Sn atoms are found in the In sublattice, they act as donors for the starting material and, thus, increase the concentration of free electrons, as indicated by the final values of n (Fig. 1b, curves *1*, *3*, *4*) obtained after the annealing of InP samples that had identical initial values of n but were exposed to neutrons with different integrated fluxes.

For large integrated fluxes (Fig. 1b, curves *4*, *5*, *7*) and, correspondingly, high concentrations of radiation defects, a stage of "negative recovery" of charge-carrier concentration is observed in the temperature range of 200–400°C; apparently, this is due (as in the case of GaAs [8]) to rearrangement of shallow-level radiation defects and formation of more complex defects that anneal out at higher temperatures.

It is evident from Fig. 2b that the larger the integrated flux of irradiating neutrons (and, consequently, the higher the concentration of Sn impurity introduced as a result of nuclear reactions involving the intermediate-energy neutrons), the lower the temperature corresponding to the onset of recovery of μ. It follows then that the presence of impurities in InP samples is conducive to an increase in the rate of both the formation and annealing of radiation defects.

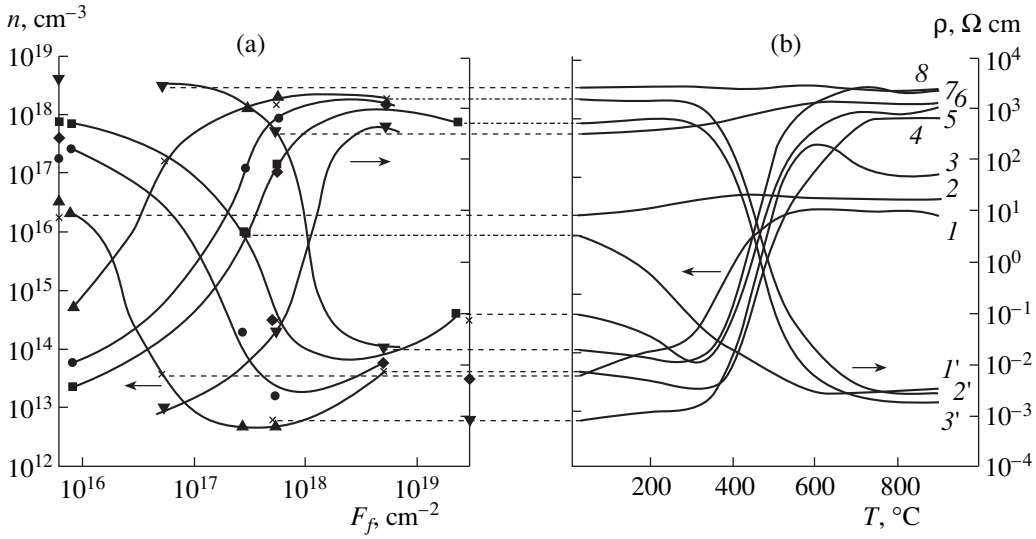

Fig. 1. Dependences of concentration of charge carriers n and resistivity ρ (a) on the integrated flux of fast neutrons F_f for various InP samples (initial values of n and ρ are indicated on the vertical axis) and (b) on the annealing temperature T for different InP samples (see table) after irradiation with integrated fluxes of fast neutrons F_f (expressed in 10^{17} cm^{-2}) equal to (curve *1*) 0.51 (sample 1), (*2*) 0.08 (sample 10), (*3*) 5.10 (2), (*4*) 50.40 (3), (*5*) 227.0 (19), (*6*) 5.10 (8), (*7*) 50.40 (9), (*8*) 0.51 (7), (*1*') 2.74 (17), (*2*') 50.40 (3), and (*3*') 227.0 (19); the curves denoted by primed numbers correspond to variations of resistivity.

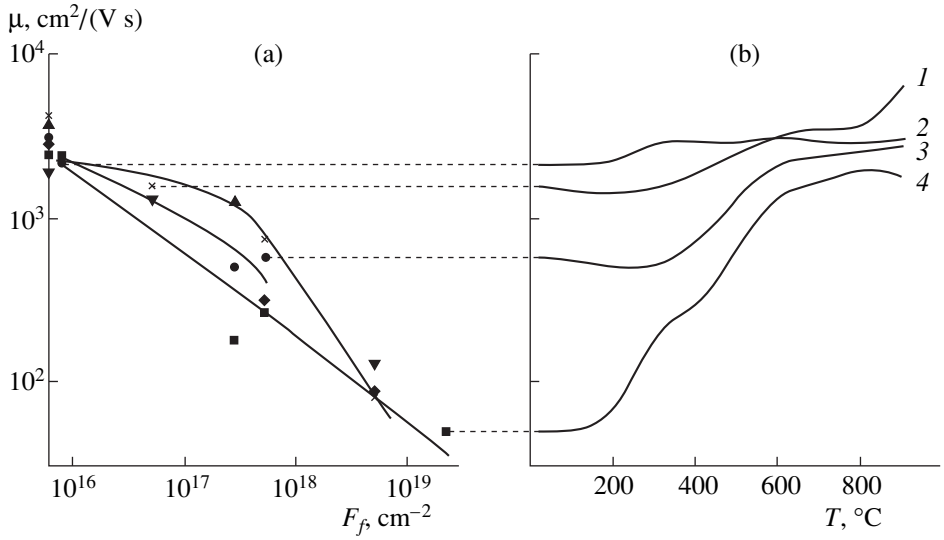

Fig. 2. Dependence of mobility μ of charge carriers (a) on the integrated flux F_f of fast neutrons for different InP samples (initial values of μ are indicated on the vertical axis) and (b) on the annealing temperature T for different InP samples (see table) after irradiation with fast-neutron integrated fluxes equal to (*1*) 5.1×10^{16} cm^{-2} (sample 1), (*2*) 8×10^{15} cm^{-2} (sample 10), (*3*) 5.27×10^{17} cm^{-2} (sample 15), and (*4*) 50.40×10^{17} cm^{-2} (sample 3).

Thus, the experimental results we obtained make it possible to recognize three main stages in the annealing of radiation defects in InP samples irradiated with fast neutrons. Stage I (T = 100–300°C) is characterized by an annealing of point and small-sized defects and by formation of more complex radiation defects.

Stage II (T = 300–600°C) is characterized by a sharp increase in both concentration and mobility of charge carriers, which indicates that radiation defects are efficiently annealed out. Apparently, as in the case of GaAs, the disordered regions and more complex defects formed at stage I are annealed out at stage II.

The behavior of n and μ indicates that there is also a stage III (T = 700–900°C) where n and μ tend to final constant values; this stage is apparently related to certain secondary processes occurring in the material.

Figure 3 shows the dependences of the charge-carrier concentration on the integrated flux of neutrons for

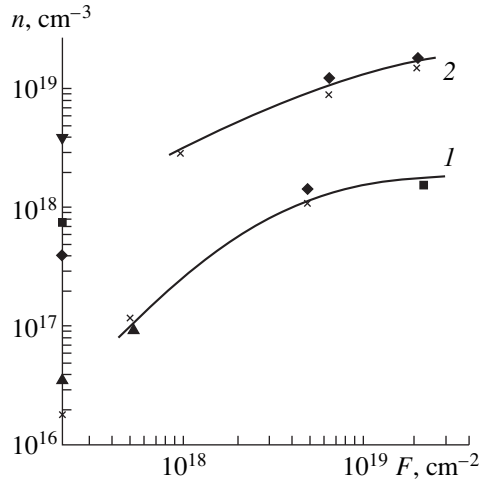

Fig. 3. Dependence of concentration of charge carriers n on the integrated flux of neutrons F for InP samples irradiated in the same channel of a VVR-ts water-cooled and water-moderated reactor in (*1*) Cd cans and (*2*) without Cd cans and annealed at $T = 900$°C (the initial values of n are indicated on the vertical axis).

irradiated InP samples after an annealing for 20 min at 900°C. Curve *1* corresponds to the samples irradiated in Cd cans, whereas curve *2* is for the samples irradiated in the same channel without Cd cans; in the latter case, the samples were exposed to the entire spectrum of reactor neutrons, with the ratio of the flux densities for the thermal and fast neutrons being equal to $\varphi_s/\varphi_f \approx 1$. These data, with allowance made for the effect of polytropy in the case of high concentrations of impurities, support the previously made conclusion [9] that doping of In-containing III–V semiconductor compounds due to reactions involving intermediate-energy neutrons amounts to about 10% of the total level of nuclear-transmutation doping for the samples irradiated in the channels of the active zone of a VVR-ts water-cooled and water-moderated nuclear reactor.

The results we obtained may be summarized as follows:

(i) annealing for 20 min at 900°C of InP samples irradiated with fast neutrons almost completely eliminates the radiation defects affecting the electrical parameters of the material, which can serve as the basis for practical implementation of the technology of nuclear-transmutation doping as applied to InP;

(ii) the level of initial doping of InP affects substantially the rates of formation of radiation defects during irradiation and the rate of their elimination during annealings;

(iii) the magnitude of the effect of doping of InP due to nuclear reactions initiated by intermediate-energy neutrons can be described by the empirical dependence $n = 0.2F_f$.

ACKNOWLEDGMENTS

This work was supported by the Ministry of Science and Technological Policy of the Russian Federation in the framework of the State Scientific and Technological Program “Research and Development in the Priority Fields of Science and Technology in the Nonmilitary Domain” (project no. 045) and by USIC under subcontract no. 4616510 with the Lawrence National Laboratory (Berkeley, California).

REFERENCES

1. L. W. Aukerman, in *Semiconductors and Semimetals*, Ed. by R. K. Willardson and A. C. Beer (Academic, New York, 1968), Vol. 4, p. 343.
2. N. P. Kekelidze and G. P. Kekelidze, Inst. Phys. Conf. Ser. **1**, 387 (1977).
3. V. N. Broudnyĭ, V. A. Charchenko, N. G. Kolin, *et al.*, Phys. Status Solidi A **93**, 195 (1986).
4. B. Lee, N. Pan, G. E. Stillman, *et al.*, J. Appl. Phys. **62**, 1129 (1987).
5. V. N. Brudnyĭ, N. G. Kolin, and V. A. Novikov, Phys. Status Solidi A **132**, 35 (1992).
6. V. N. Brudnyĭ and S. N. Grinyaev, Fiz. Tekh. Poluprovodn. (St. Petersburg) **32** (3), 315 (1998).
7. N. G. Kolin, L. V. Kulikova, V. B. Osvenskiĭ, *et al.*, Fiz. Tekh. Poluprovodn. (Leningrad) **18** (12), 2187 (1984) [Sov. Phys. Semicond. **18**, 1364 (1984)].
8. N. G. Kolin, V. B. Osvenskiĭ, V. V. Tokarevskiĭ, *et al.*, Fiz. Tekh. Poluprovodn. (Leningrad) **19** (9), 1558 (1985) [Sov. Phys. Semicond. **19**, 958 (1985)].
9. N. G. Kolin, V. B. Osvenskiĭ, N. S. Rytova, *et al.*, Fiz. Khim. Obrab. Mater., No. 6, 3 (1986).

Translated by A. Spitsyn

Semiconductors, Vol. 34, No. 2, 2000, pp. 150–154. Translated from Fizika i Tekhnika Poluprovodnikov, Vol. 34, No. 2, 2000, pp. 157–161.

ELECTRONIC AND OPTICAL PROPERTIES OF SEMICONDUCTORS

Electrical Properties of Transmutation-Doped Indium Phosphide

N. G. Kolin*, D. I. Merkurisov*, and S. P. Solov'ev**

** Karpov Institute of Physical Chemistry (Obninsk Branch), Obninsk, Kaluga oblast, 249020 Russia*

e-mail: FCI@meteo.ru

*** Institute of Nuclear-Power Engineering, Obninsk, Kaluga oblast, 249020 Russia*

Submitted January 11, 1999; accepted for publication May 27, 1999

Abstract—Experimental results of studying the process of transmutation doping of InP single crystals by irradiating with nuclear-reactor neutrons are reported; the possibility of doping with tin in a wide range of concentrations and obtaining the concentration of free electrons as high as 2×10^{19} cm^{-3} is demonstrated. Electrical properties of InP and their behavior under irradiation and in the course of subsequent heat treatments were studied. The prospects for utilization of the nuclear-transmutation method for doping are assessed. © *2000 MAIK "Nauka/Interperiodica".*

The method of nuclear-transmutation doping by irradiation with thermal reactor neutrons has found a wide application in modern semiconductor technology, especially concerning silicon [1–3] and gallium arsenide [3–8]. By now, there are a large number of publications devoted to nuclear-transmutation doping of III–V semiconductor compounds, such as InAS [9, 10], InSb [11–13], and InP [14, 15], including a series of publications concerned with transmutation doping by irradiation with charged particles [16–18]; however, information related to the above compounds is clearly inadequate, and data on the technology of transmutation doping by irradiation with reactor neutrons are almost completely lacking.

The objective of this work was to gain deeper insight into the process of transmutation doping of InP single crystals by irradiating them with reactor neutrons and to determine the behavior of electrical properties of InP under the effect of irradiation and subsequent heat treatments for further practical implementation of this method of doping for this semiconductor compound.

As the starting samples, we used the [111]-oriented Czochralski-grown InP single crystals with a diameter of up to 40 mm; the crystals were either undoped or doped with tellurium to the concentration of 4×10^{17}–3.9×10^{18} cm^{-3}.

The samples were irradiated at a temperature no higher than 70°C in vertical channels of the active zone of a VVR-ts water-cooled and water-moderated reactor, with the flux density of thermal neutrons being $\varphi_s = 5 \times 10^{13}$ cm^{-2} s^{-1} and the ratio of the flux densities of thermal and fast (with an energy $E > 0.1$ MeV) neutrons being equal to $\varphi_s/\varphi_f \approx 1$.

The main nuclear reactions occurring in InP under the irradiation with thermal neutrons are listed in Table 1. As can be seen, the cross section of absorption of thermal neutrons for the main isotope ^{115}In (σ = 145 b) is appreciably larger than that for ^{31}P nuclei, which practically determines the end product of transmutation doping as ^{116}Sn.

The large cross section of absorption of thermal neutrons by ^{115}In nucleus brings about a pronounced effect of self-screening in the InP sample during irradiation. The flux density of thermal neutrons is attenuated by *e* times at a depth of 1.4 mm. In connection with this, the samples for transmutation doping were prepared in the shape of platelets with a thickness no larger than 2 mm. The effect of absorption of resonance neutrons (E = 1.46 eV and $\sigma = 2.2 \times 10^4$ b), whose flux density is attenuated by *e* times at a depth of about several micrometers, was eliminated by grinding off a layer ~50 μm thick from both surfaces of irradiated samples.

Concentration of tin impurity (N_{Sn}) introduced in InP as a result of nuclear reaction with thermal neutrons was calculated with the formula

$$N_{Sn} = N_0 k \sigma F_s,$$

where N_0 is the number of InP isotope atoms per unit volume, k is the atomic percentage of the isotope, σ is the cross section of thermal-neutron absorption, and F_s is the integrated flux of thermal neutrons.

Duration of irradiation was chosen such that the concentration of introduced tin impurity varied in the range of 2×10^{18}–7×10^{19} cm^{-3}. Calculated values of tin concentration and the values obtained by spectrochemical analysis are listed in Table 2. As can be seen, good agreement between calculated and experimental values of the concentration is observed in the entire range of concentrations.

Properties of the crystals exposed to the full spectrum of reactor neutrons are defined both by the atoms

Table 1. Products of (n, γ) nuclear reactions in indium phosphide

Element	Isotope	k, %	σ, b	$T_{1/2}$	n_{tr}/F_s	Reaction products (fraction)	Ultimate product of reactions
In	Natural		190 ± 10				Tin (99.82%)
	^{113}In	4.23	58 ± 12	50.1 days	5.14×10^{-2}	^{114}Sn (0.980)	Sulfur (0.1%)
						^{114}Cd (0.010)	Cadmium (0.02%)
	^{115}In	95.77	145 ± 20	54 min	2.91	^{116}Sn (1.000)	Other elements
P	^{31}P	100	0.2 ± 0.02	14.3 days	4.47×10^{-3}	^{32}S (1.000)	(0.06%)

Note: k is the isotope content, σ is the cross section of absorption of thermal neutrons; $T_{1/2}$ is the half-life; and n_{tr}/F_s is the efficiency of transmutation doping per cm^{-1}.

Table 2. Properties of the as-grown and transmutation-doped samples of indium phosphide

Sample no.	As-grown crystals				F_s, 10^{18} cm^{-2}	N^{th}, 10^{18} cm^{-3}	N_{Sn}^{cha}, 10^{18} cm^{-3}	After irradiation and subsequent annealing for 20 min at 900°C	
	n, 10^{17} cm^{-3}	μ, 10^3 cm^2/(V s)	ρ, 10^{-3} Ω cm	Impurity				n, 10^{18} cm^{-3}	μ, 10^2 cm^2/(V s)
1	0.18	4.20	80.00	–	0.97	2.87	2.90	2.90	15.80
2	0.18	4.20	80.00	–	6.57	19.45	17.40	9.10	11.00
3	0.18	4.20	80.00	–	21.00	62.16	72.50	14.90	8.40
4	0.35	3.76	–	–	0.30	0.89	–	–	–
5	4.00	2.80	5.60	Te	6.57	19.45	17.40	12.00	9.96
6	4.00	2.80	5.60	Te	21.00	62.16	72.50	17.90	7.10
7	39.00	1.90	0.85	Te	21.00	62.16	72.50	16.90	7.90

Note: n and μ are the concentration and mobility of charge carriers, respectively, and ρ is the resistivity. The as-grown crystals were of n-type. F_s is the unperturbed integrated flux of thermal neutrons, N^{th} is the calculated concentration of the impurity introduced, and N_{Sn}^{cha} is the concentration of introduced impurity according to the data of spectrochemical analysis.

of doping impurities introduced as a result of nuclear transmutations and by radiation defects formed in the course of neutron irradiation. Electrical properties are also affected by the concentration of charge carriers and growth defects in the starting InP crystals.

As a consequence of high induced radioactivity, the irradiated InP samples were kept in special boxes for 4–24 months, depending on the integrated flux of neutrons. After the induced radioactivity decayed to the permissible level, the samples were decontaminated, rinsed, ground, and etched in a $HNO_3 : HCl = 3 : 1$ solution. Electrical parameters of the samples were determined from the Hall measurements by the Van der Pauw method at room temperature. The samples were annealed in evacuated sealed quartz ampules for 20 min in the temperature range of 20–900°C.

Figures 1 and 2 show the dependences of concentration n and mobility μ of charge carriers and also the resistivity ρ of InP samples on the integrated flux of thermal neutrons F_s and the temperature T of subsequent heat treatments. It can be seen that, as the integrated flux of neutrons increases to $F_s \simeq 10^{19}$ cm^{-2}, concentration and mobility of charge carriers decrease, and, correspondingly, the resistivity ρ increases; this is due to an increase in the concentration of radiation defects, whose influence on electrical properties of InP is more profound than that of the doping impurity introduced. For integrated fluxes $F_s > 10^{19}$ cm^{-2}, an increase in the concentration of charge carriers and a decrease in ρ with an increase in F_s are observed; apparently, this is caused, as in the case of GaAs [4], by an overlap of the shells of disordered regions as their concentration increases and by the emergence of hopping conduction. In this case, the Fermi level tends to a limiting position in the heavily irradiated InP ($E_c - 0.25$ eV) [19]. As distinct from GaAs, the $n \longrightarrow p$ conversion is not observed in InP, and the maximal values of ρ can be as large as $\sim 10^3$ Ω cm [4].

It is evident from Figs. 1 and 2 that the trend in variation of electrical properties of InP crystals subjected to annealing after having been irradiated with different integrated fluxes of neutrons is qualitatively the same. Concentration and mobility of charge carriers increase as the annealing temperature increases and attain different final values, depending on the integrated fluxes of neutrons. The most drastic changes of the parameters

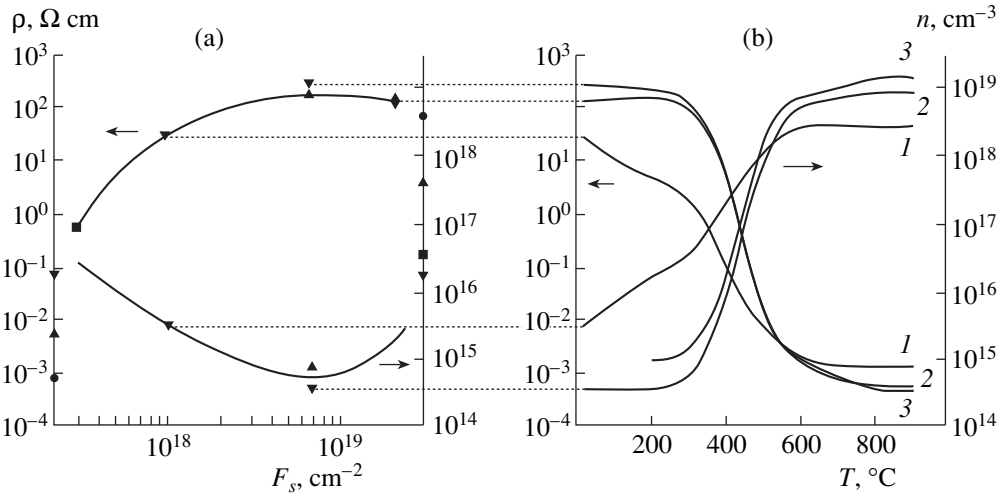

Fig. 1. Dependences of concentration of charge carriers n and resistivity ρ (a) on the integrated flux of thermal neutrons F_s for several InP samples (preirradiation values of n and ρ are indicated on the vertical axis) and (b) on the annealing temperature T for InP samples that had initial concentration $n = 1.8 \times 10^{16}$ cm^{-3} and were irradiated with thermal neutrons, with integrated fluxes being equal to (*1*) 0.97×10^{18}, (*2*) 6.57×10^{18}, and (*3*) 2.1×10^{19} cm^{-2}.

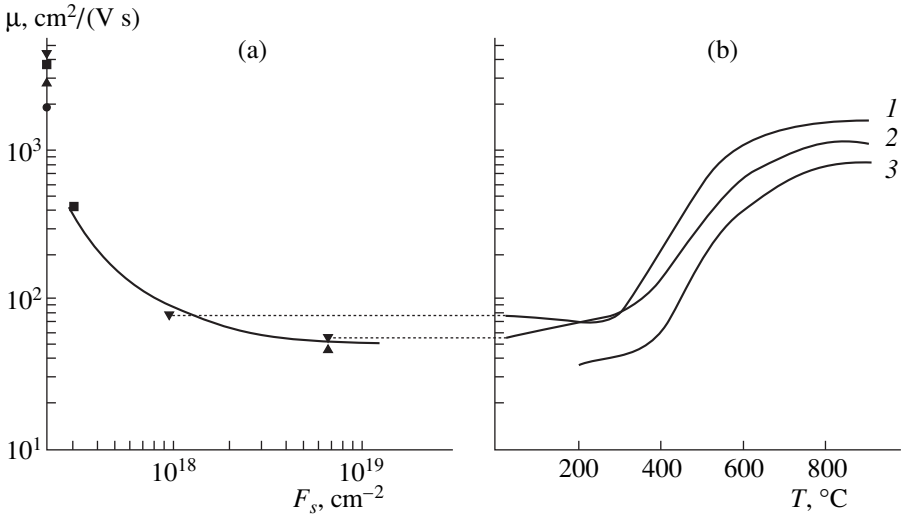

Fig. 2. Dependences of mobility of charge carriers μ (a) on the integrated flux of thermal neutrons F_s for several InP samples (preirradiation values of μ are indicated on the vertical axis) and (b) on the annealing temperature for InP samples that had initial concentration $n = 1.8 \times 10^{16}$ cm^{-3} and mobility μ = 4200 cm^2/(V s) and were irradiated with thermal neutrons, with integrated fluxes being equal to (*1*) 0.97×10^{18}, (*2*) 6.57×10^{18}, and (*3*) 2.1×10^{19} cm^{-2}.

is observed in the course of annealing within the temperature range of 300–600°C. The largest value of ρ (~500 Ω cm) attained as a result of irradiation decreases as the annealing temperature T increases. For T = 900°C, the resistivity is 10^{-3}–10^{-4} Ω cm, which is appreciably lower than that before irradiation and is governed by the concentration of doping impurities introduced as a result of nuclear transmutations.

As can be seen from Fig. 3, the trend in variations and the absolute values of n and ρ for InP samples that had different concentrations of charge carriers prior to irradiation and were irradiated with integrated thermal-neutron flux of 2.1×10^{19} cm^{-2} are virtually the same in the entire range of annealing temperatures. This indicates that electrical properties of InP irradiated with large integrated fluxes of neutrons are largely determined by the concentrations of transmutation-introduced impurity and radiation defects. The phenomenon of "negative" annealing (reported previously in the case of gallium arsenide [4]) observed in the range of heat-treatment temperatures of 100–300°C can be apparently attributed to rearrangement of point radiation

defects (if their concentration becomes high) with formation of more complex defects that are annealed out at higher temperatures.

The experimental results obtained are indicative of the existence of three stages in the annealing of radiation defects in InP samples irradiated with neutrons.

In stage I corresponding to the annealing-temperature range of 100–300°C, relatively small variations in electrical parameters of InP are observed, which is apparently related both to partial annihilation of point defects (by their migration to sinks and recombination of interstitial atoms and vacancies) and to formation of more complex defects.

Stage II corresponds to the annealing-temperature range of 300–600°C. A drastic change in electrical parameters of InP is characteristic of this stage; this is apparently due to elimination of disordered regions and complex radiation defects formed predominantly at lower temperatures with subsequent rapid annihilation of point defects.

The trend in variations of electrical properties suggests that there exists a stage III in annealing in the temperature range of 600–900°C. This stage is characterized by occurrence of secondary processes involving the impurity atoms and native point lattice defects.

Figure 4 shows the saturation free-electron concentration obtained after annealing of irradiated InP samples at a temperature of 900°C as a function of the concentration of impurity (Sn) introduced in InP as a result of nuclear transmutations and measured by the spectrochemical method (N_{Sn}^{cha}). It can be seen that good agreement between the concentration of introduced donor impurity N_{Sn}^{cha} and the free-electron concentration n measured after the samples were annealed at 900°C is observed only for $N_{Sn}^{cha} < 2.9 \times 10^{18}$ cm^{-3}. For higher concentrations of the introduced doping impurity, the values of n are significantly smaller than N_{Sn}^{cha}. There can be two main causes of this phenomenon: (i) for large integrated fluxes of neutrons, the defects that have higher thermal stability and are annealed off at higher temperatures are formed and (ii) for sufficiently high concentrations of doping impurities, the well-known phenomenon of polytropy is observed [20]. It is noteworthy that the phenomenon of polytropy in InP crystals doped in the course of growth is observed for lower concentrations of impurities (~5×10^{17} cm^{-3}) than in the case of transmutation-doped samples; this constitutes one of the advantages of transmutation-induced doping.

On the basis of the results obtained in this study, we can draw the following conclusions:

(i) the method of transmutation doping can be used with good results to obtain InP single crystals doped with Sn to a wide range of concentrations, with the whole of the introduced impurity being in the electrically active state up to a concentration of about 3×10^{18} cm^{-3};

(ii) in view of high radioactivity induced by irradiation with thermal neutrons, the method of transmutation doping is most promising when used to obtain InP crystals with low or moderate levels of doping, i.e.,

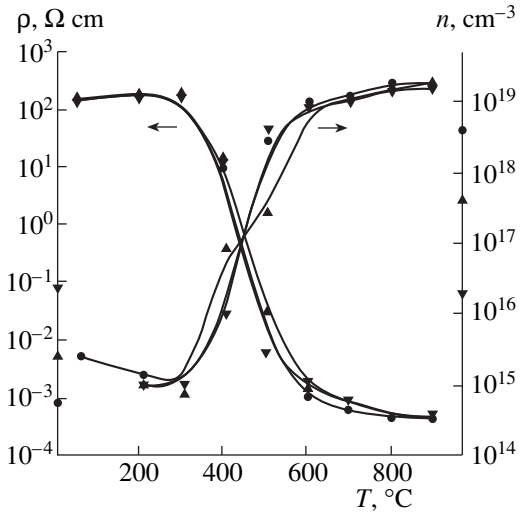

Fig. 3. Dependences of concentration of charge carriers n and resistivity ρ on the annealing temperature T for InP samples that differed in the initial concentration of charge carriers (initial values of n are indicated on the vertical axis) and were irradiated with thermal neutrons, with their integrated flux being equal to $F_s = 2.1 \times 10^{19}$ cm^{-2}.

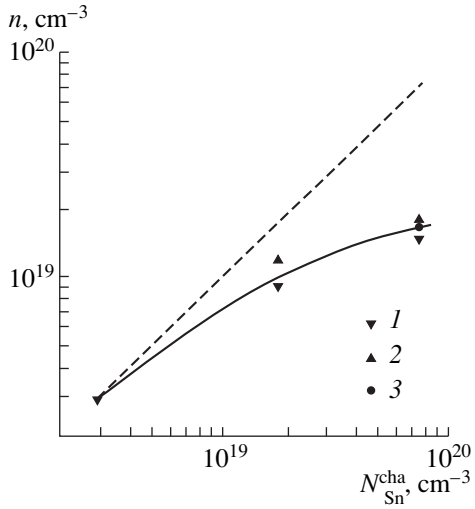

Fig. 4. Dependence of saturation concentration of free electrons n in irradiated InP samples annealed at T = 900°C on the concentration of introduced impurity determined by spectrochemical analysis N_{Sn}^{cha}. The as-grown InP crystals had the concentration of charge carriers n = (*1*) 1.8×10^{16}, (*2*) 4.00×10^{17}, and (*3*) 39.00×10^{17} cm^{-3}. The dashed line represents the result of theoretical calculation.

$N_{Sn} \leq (1–5) \times 10^{17}$ cm^{-3}, or to dope the built-in epitaxial layers in multilayer semiconductor structures at various stages of their fabrication.

ACKNOWLEDGMENTS

This work was supported by the Ministry of Science and Technological Policy of the Russian Federation in the framework of the State Scientific and Technological Program "Research and Development in the Priority Fields of Science and Technology in the Nonmilitary Domain" (project no. 045) and by USIC under subcontract no. 4616510 with the Lawrence National Laboratory (Berkeley, California).

REFERENCES

1. *Neutron Transmutation Doping of Semiconductors* [a collection of papers translated from English into Russian], Ed. by V. N. Mordkovich (Mir, Moscow, 1982), No. 11 in the series "News in the Solid-State Physics".
2. L. S. Smirnov, S. P. Solov'ev, V. F. Stas', and V. A. Kharchenko, *Doping of Semiconductors by the Method of Nuclear Reactions* (Nauka, Novosibirsk, 1981).
3. N. G. Kolin, S. P. Solov'ev, and A. A. Stuk, Izv. Vyssh. Uchebn. Zaved., Yad. Tekh., Nos. 2–3, 98 (1994).
4. N. G. Kolin, L. V. Kulikova, V. B. Osvenskiĭ, *et al.*, Fiz. Tekh. Poluprovodn. (Leningrad) **18**, 2187 (1984) [Sov. Phys. Semicond. **18**, 1364 (1984)].
5. L. N. Kolesnik, N. G. Kolin, A. M. Loshinskiĭ, *et al.*, Fiz. Tekh. Poluprovodn. (Leningrad) **19**, 1211 (1985) [Sov. Phys. Semicond. **19**, 742 (1985)].
6. Sh. M. Mirianashvili, D. I. Nanobashvili, and Z. G. Razmadze, Fiz. Tverd. Tela (Leningrad) **7**, 3566 (1965).
7. N. G. Kolin, L. V. Kulikova, and V. B. Osvenskiĭ, Fiz. Tekh. Poluprovodn. (Leningrad) **22**, 1025 (1988) [Sov. Phys. Semicond. **22**, 646 (1988)].
8. V. N. Brudnyĭ, N. V. Kamenskaya, and N. G. Kolin, in *Impurities and Defects in Narrow-Gap Semiconductors* (Akad. Nauk SSSR, Pavlodar, 1989), Part 2.
9. N. G. Kolin, V. B. Osvenskiĭ, N. S. Rytova, *et al.*, Fiz. Tekh. Poluprovodn. (Leningrad) **20**, 822 (1986) [Sov. Phys. Semicond. **20**, 519 (1986)].
10. N. G. Kolin, V. B. Osvenskiĭ, E. S. Yurova, *et al.*, Fiz. Khim. Obrab. Mater., No. 4, 4 (1987).
11. N. G. Kolin, V. T. Bublik, V. B. Osvenskiĭ, *et al.*, Fiz. Khim. Obrab. Mater., No. 3, 28 (1987).
12. V. N. Brudnyĭ, N. G. Kolin, V. V. Peshev, *et al.*, Fiz. Tekh. Poluprovodn. (Leningrad) **31**, 811 (1997) [Semicond. **31**, 686 (1997)].
13. V. N. Brudnyĭ, N. V. Kamenskaya, and N. G. Kolin, Izv. Vyssh. Uchebn. Zaved., No. 7, 99 (1991).
14. V. N. Brudnyĭ, N. G. Kolin, V. A. Novikov, *et al.*, Phys. Status Solidi A **93**, 195 (1986).
15. V. N. Brudnyĭ, N. G. Kolin, and V. A. Novikov, Phys. Status Solidi A **132**, 35 (1992).
16. L. F. Zakharenkov, V. V. Kozlovskiĭ, and B. A. Shustrov, Phys. Status Solidi A **117**, 85 (1990).
17. B. V. Zabrodin, L. F. Zakharenkov, V. V. Kozlovskiĭ, *et al.*, At. Energ. **68** (6), 432 (1990).
18. V. V. Kozlovskiĭ, L. F. Zakharenkov, and B. A. Shustrov, Fiz. Tekh. Poluprovodn. (St. Petersburg) **26** (1), 3 (1992) [Sov. Phys. Semicond. **26**, 1 (1992)].
19. V. N. Brudnyĭ and S. N. Grinyaev, Fiz. Tekh. Poluprovodn. (St. Petersburg) **32** (3), 315 (1998) [Semicond. **32**, 284 (1998)].
20. V. I. Fistul', *Heavily Doped Semiconductors* (Nauka, Moscow, 1967; Plenum, New York, 1969).

Translated by A. Spitsyn

Semiconductors, Vol. 34, No. 2, 2000, pp. 155–160. Translated from Fizika i Tekhnika Poluprovodnikov, Vol. 34, No. 2, 2000, pp. 162–167.

ELECTRONIC AND OPTICAL PROPERTIES OF SEMICONDUCTORS

Thermal Acceptors in Irradiated Silicon

V. F. Stas', I. V. Antonova, E. P. Neustroev, V. P. Popov, and L. S. Smirnov

Institute of Semiconductor Physics, Siberian Division, Russian Academy of Sciences, pr. akademika Lavrent'eva 13, Novosibirsk, 630090 Russia

Submitted June 3, 1999; accepted for publication June 23, 1999

Abstract—Comparative analysis of the conditions for the formation of shallow acceptor centers upon high-temperature annealing in silicon irradiated with electrons, neutrons, and energetic ions is performed. The introduction of a sufficiently large (in comparison with the initial concentration of impurities and defects) concentration of radiation-induced distortions of the silicon lattice is shown to lead to the formation of thermal acceptors stable up to annealing temperature of ~650°C. The acceptor formation is supposed to be due to the interaction of background acceptor impurities (supposedly boron) with vacancies "stored" in multivacancy clusters and released upon their breakup. © *2000 MAIK "Nauka/Interperiodica".*

INTRODUCTION

The problem of the transformation of the defect–impurity subsystem of semiconducting silicon in the range of the working temperatures of microelectronic devices and technological treatments used in their manufacture is very complex. The main cause is the participation, in the structural transformations, of nonequilibrium and uncontrolled (background) impurities and "native" (grown-in) defects. It is known that, depending on the technique and regime of growing single crystals, either vacancy or interstitial defects can be predominant in silicon [1]. It is also known, that the main impurities, which are always present in silicon crystals, are oxygen and carbon. Another impurity that can be removed from single-crystal silicon only with difficulty is boron [2]. Irradiation of silicon with various particles is in many cases a good test for the presence of uncontrolled components. The spectrum of defects that are introduced upon irradiation with various particles includes a good many species, from the simplest point defects such as vacancies (V) and self-interstitials (I) (upon electron irradiation with energies $E < 10$ MeV [3]) to pileups of cluster-type defects (irradiation with neutrons and ions [3–6]). Since the direct recombination of V and I is not a dominant process [7], an accumulation of point defects in the form of complexes and clusters of various complexity occurs upon irradiation. It is known that the V and I defects interact with virtually all impurities and other crystal imperfections [8]. When the concentrations of defects introduced by irradiation, on the one hand, and of the background defects and impurities, on the other hand, are comparable, then individual properties of the material manifest themselves to the greatest extent. These individual properties will also determine the transformation of the initial impurity–defect system upon subsequent annealing of the irradiated material. By using high-purity crystals (with a minimum concentration of impurities and other imperfections) and irradiation with particles that introduce a sufficiently large number of distortions into the crystal, we can create conditions for the most efficient manifestation of the defect-subsystem properties in the irradiated crystal. Upon irradiation, the electrical conductivity of silicon tends to become intrinsic, but sometimes, when high-resistivity n-Si crystals are used, p-type conductivity was noted [3]; i.e., conductivity conversion took place.

In this work, we investigated the conditions for the formation of acceptor centers upon the annealing of silicon crystals, initially differing in both the type and concentration of dopants and oxygen content, after irradiation with electrons, reactor neutrons, and energetic ions. The use of various types of radiation (differing in both the amount of produced displacements and their density and spatial distribution) revealed the existence of a correlation between the effect of radiation on the crystal and the concentration of initial impurities and defects necessary for the formation of thermal acceptors.

EXPERIMENTAL

For the investigation, we used silicon single crystals grown by both the Czochralski technique (Cz-Si) and float-zone melting (FZ-Si). Both kinds of crystals had the n-type conductivity. The initial values of the charge-carrier concentrations, their mobilities, and the concentrations of oxygen in the samples are given in the table and in figure captions. The irradiation was performed with electrons with an energy of $E = 3.5$ MeV and a dose of $D = 10^{15} - 3 \times 10^{16}$ cm^{-2}, neutrons ($D = 2.5 \times 10^{17}$ cm^{-2}, or 10^{14} cm^{-2} upon combined irradiation), and N^+ ions ($E = 16$ MeV, $D = 2 \times 10^{14} - 2 \times 10^{15}$ cm^{-2}); silicon was of grade KDB-30). The thickness of the samples did not exceed 1 mm. The projected range R_p of N^+ ions (16 MeV) was 11.6 μm. The investigations were per-

1063-7826/00/3402-0155$20.00

Concentrations and mobilities of charge carriers in silicon (at room temperature) irradiated with electrons and neutrons and annealed at various temperatures T_{ann}

Irradiatiation	T_{ann},°C	Conductivity type	p, n, cm^{-3}	Mobility, cm^2/(V s)
Neutrons	init.	*n*	2.6×10^{13}	1356
$D = 2.5 \times 10^{17}$ cm^{-2}	100	*p*	2.6×10^{11}	130
$N_0 = 5.5 \times 10^{16}$ cm^{-3}	300	*p*	1.0×10^{12}	227
	460	*p*	1.2×10^{13}	210
	600	*p*	2.1×10^{14}	362
	650	*p*	3.8×10^{14}	331
Neutrons	init.	*n*	2.4×10^{13}	1392
$D = 2.5 \times 10^{17}$ cm^{-2}	100	*p*	3.8×10^{11}	132
$N_0 = 4.0 \times 10^{17}$ cm^{-3}	300	*p*	5.4×10^{11}	257
	460	*p*	8.0×10^{12}	174
	600	*p*	4.2×10^{14}	166
	650	*p*	3.0×10^{14}	332
Electrons	init.	*n*	3.5×10^{13}	1212
$D = 3 \times 10^{16}$ cm^{-2}	375	*p*	1.6×10^{13}	98
	425	*p*	2.7×10^{13}	161
	475	*p*	2.2×10^{13}	133
Electrons	init.	*n*	8.8×10^{12}	1194
$D = 3 \times 10^{16}$ cm^{-2}	375	*p*	4.4×10^{13}	250
	425	*p*	6.6×10^{13}	253
	475	*p*	9.5×10^{13}	201
Neutrons	init.	*n*	2.3×10^{13}	1389
($D = 10^{14}$ cm^{-2}) +	400	*p*	4.5×10^{13}	71
electrons	500	*p*	9.2×10^{11}	100
($D = 10^{15}$ cm^{-2})				
Neutrons	init.	*n*	1.8×10^{13}	1462
($D = 10^{14}$ cm^{-2}) +	400	*p*	4.2×10^{13}	185
electrons	500	*p*	3.6×10^{13}	106
($D = 3 \times 10^{15}$ cm^{-2})				
Neutrons	init.	*n*	1.8×10^{13}	1578
($D = 10^{14}$ cm^{-2}) +	400	*p*	6.2×10^{13}	121
electrons	500	*p*	4.0×10^{13}	155
($D = 10^{16}$ cm^{-2})				
KDB-40	init.	*p*	4.2×10^{14}	334

Note: N_0, oxygen concentration; init., initial crystal; p, n, hole and electron concentrations, respectively; and KDB-40, silicon grade (*p*-Si:B, $\rho = 40\ \Omega$ cm).

formed by measuring capacitance–voltage characteristics, concentration and mobility of charge carriers (using the Van der Pauw method), and deep-level transient spectroscopy (DLTS). Heat treatments were conducted at temperatures of up to 900°C. In order to obtain the in-depth profiles of defects, we used layer-by-layer etching in an HF : HNO_3 (1 : 100) solution.

RESULTS

Irradiation of FZ-Si with electrons with a dose of 3×10^{16} cm^{-2} leads to an increase in the resistivity to over $3 \times 10^5\ \Omega$ cm. Annealing of a "low-resistivity" starting silicon ($\rho_{st} \simeq 200\ \Omega$ cm) shows that the *n*-type conductivity is retained up to $T_{ann} = 200$°C. Then, the transition to the *p*-type conductivity occurs, and the hole concentration first grows, but then drops sharply at $T \simeq 500$°C (Fig. 1, curve *1*). The "high-resistivity" starting material ($\rho_{st} \simeq 800\ \Omega$ cm) is converted the into *p* type beginning from low annealing temperatures, and the increase in the hole concentration occurs in two stages (see the range of $T_{ann} \simeq 300$–400°C in Fig. 1, curve *2*). It can be seen from the figure that the concentration of acceptors that are formed upon annealing of the purer material of higher resistivity is higher and the acceptors are observed in a wider temperature range.

Upon irradiation with reactor neutrons (Fig. 2), the *p*-type conductivity is clearly fixed directly after irradiation. The annealing behavior and the concentration of charge carriers are virtually independent of the oxygen concentration in the samples. The hole concentration reveals no substantial changes up to $T_{ann} \simeq 250$°C. Beginning from $T_{ann} \simeq 300$°C, the hole concentration increases, showing a tendency towards saturation at $T_{ann} \simeq 450$–500°C, but then it again increases sharply. After it reaches a maximum at $T_{ann} \simeq 600$°C, the hole concentration decreases sharply (at $T_{ann} > 650$°C) and the conversion of the conductivity type occurs.

Irradiation of FZ-Si samples ($\rho_{st} \simeq 200\ \Omega$ cm) with electrons with doses less than $D = 10^{16}$ cm^{-2} or with neutrons to doses less than $D = 10^{14}$ cm^{-2} yields no conversion of the conductivity type in either irradiation or in the process of isochronal anneals. However, upon combined irradiation (first with neutrons with a dose $D = 10^{14}$ cm^{-2} and then with electrons with doses $D = 10^{15}$–3×10^{16} cm^{-2}), the *p*-type conductivity can arise in the process of isochronal annealing at temperatures $T_{ann} > 250$°C (Fig. 3). The hole concentration increases with increasing electron flux. However, the temperature range of stability of the acceptors, as in the case of irradiation with electrons alone, is restricted to the annealing temperature $T_{ann} = 500$°C.

A similar formation of additional acceptor centers also takes also place upon implantation with high-energy ions after analogous anneals. Figures 4 and 5 display the in-depth profiles of the hole concentration in crystals irradiated with nitrogen ions with an energy of 16 MeV and annealed at temperatures of 500 and 570°C, respectively. It can be seen that the spatial distribution of the hole concentration is strongly affected by the annealing temperature.

In all the samples, the hole mobility is low, until the annealing temperature reaches $T_{ann} \simeq 600$°C (see table). For comparison, we also give in the table the hole mobility in unirradiated silicon samples of grade KDB-40. Anneals at 600–650°C restore the mobility of charge carriers, retaining the high concentration of high-temperature acceptors.

Measurements using the DLTS technique show that anneals at T_{ann} = 400–600°C do not introduce deep levels in the lower half of the forbidden band. The only level that was observed after annealing at 450–550°C in the upper half of the energy gap of implanted Cz Si is associated with the introduction of thermal donors.

DISCUSSION

The occurrence of the *n*-Si ⟶ *p*-Si conversion is observed upon both neutron and electron irradiation (Figs. 1, 2). Most vividly, the effect manifests itself upon subsequent heat treatments. A distinct correlation is observed between the appearance of mobile vacancies and the formation of acceptor centers in the crystal. Thus, it is seen from Fig. 1 that, after the annealing of a low-resistivity material at T_{ann} = 200–220°C, the *p*-type conductivity is observed (at T_{ann} = 200°C, the sample retains the *n*-type conductivity). Annealing at temperatures of 250–300°C increases the hole concentration (Figs. 1–3). Note that, as is known, the annealing of trivacancies occurs at 200–220°C, while at 250–350°C divacancies and *A* centers (oxygen + vacancy complexes in oxygen-containing material) vanish [4, 5, 9]. These processes lead to the appearance of mobile vacancies in the volume of the sample.

Which of the defects can be related to the arising acceptor centers? We should at once reject a whole class of defects connected with interstitial atoms. These defects usually behave as donor or neutral centers. Based on Fig. 2, we should also discard the defects that contain oxygen. As to the pure vacancy defects, such defects as di-, tri-, and tetravacancies should be rejected because of their low thermal stability. At first glance, pentavacancies (EPR *P*1 centers) seem to be acceptable, at least by their thermal stability, because they exist up to $T_{ann} \simeq 500$°C. However, pentavacancies usually arise at higher doses of neutrons or ions [10]. It is also known that the pentavacancy introduces a deep level with an energy E_v + 0.44 eV into the forbidden band [11]. However, the nature of the *P*1 center has not been established unambiguously. Thus, Chadi and Chang [12] believe that it is the V_{10} defects that better suit the properties of the *P*1 center. Our DLTS measurements show that, under the conditions of the existence of the acceptor centers at hand (at least, above T_{ann} = 400°C), no deep centers arise in the lower half of the energy gap. It may be supposed that the acceptor centers are defects that contain phosphorus impurity atoms (Figs. 1, 3); i.e., these are *E*-type defects (phosphorus atom + vacancy) but more complex in their structure and including more than one vacancy. This supposition also is not applicable, because the maximum concentration of acceptor centers substantially exceeds the initial concentration of phosphorus (Fig. 1; see also table), even if we take into account the possible compensation of the major doping impurity.

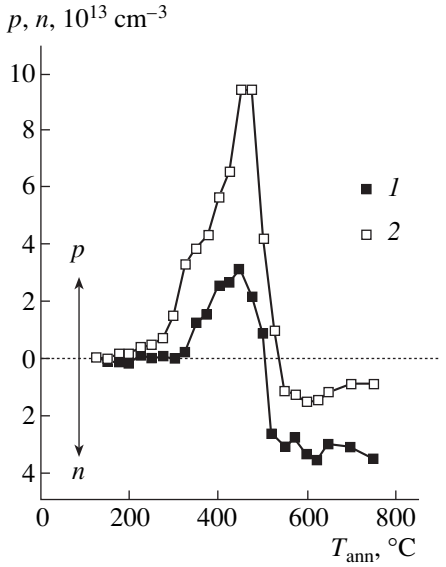

Fig. 1. Dependences of the charge-carrier concentration on annealing temperature T_{ann} for FZ-Si crystals irradiated with electrons with an energy of 3.5 MeV and dose $D = 3 \times 10^{16}$ cm^{-2}. Initial concentration of electrons in the crystals was n_{st} = (*1*) 3.5×10^{13} and (*2*) 1×10^{13} cm^{-3}. The area above the horizontal line corresponds to *p* type and that below this line, to *n*-type.

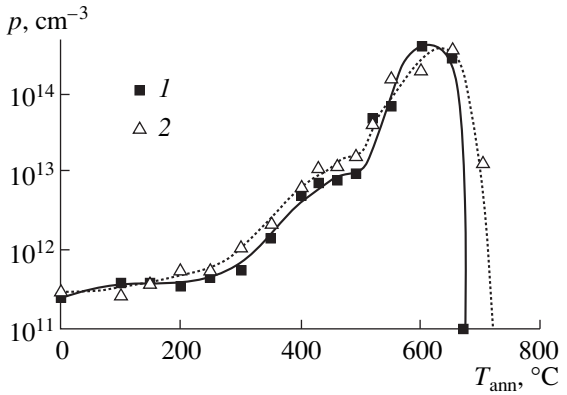

Fig. 2. Concentration of holes *p* as a function of annealing temperature T_{ann} for (*1*) Cz-Si and (*2*) FZ-Si crystals irradiated with fast reactor neutrons with a close of $D = 2.5 \times 10^{17}$ cm^{-2}. For $T_{ann} \geq 650$°C, both crystals become of *n*-type.

Since none of the known radiation-induced defects can be associated with the arising acceptor centers, it is logical to suppose that we deal with an impurity atom of Group III, and the most probable candidate for this role is boron. Boron is an impurity that is always present in silicon, even in the high-purity crystals [2].

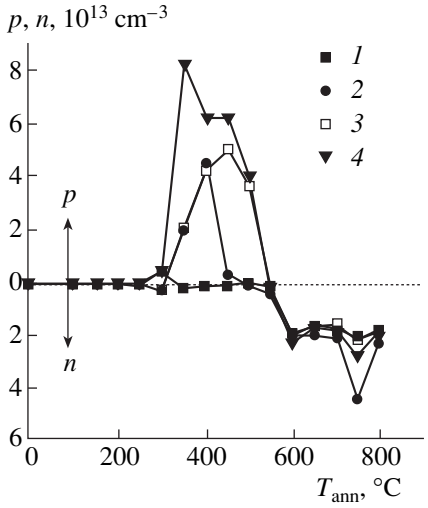

Fig. 3. Dependences of the charge-carrier concentration on annealing temperature T_{ann} for FZ-Si crystals irradiated (*1*) with fast reactor neutrons with a dose $D = 10^{14}$ cm^{-2} and then with electrons with doses $D =$ (*2*) 1×10^{15}, (*3*) 3×10^{15}, and (*4*) 1×10^{16} cm^{-2}. Concentration of oxygen in the starting samples was $N_O \leq 5 \times 10^{16}$ cm^{-3}. The same vertical scale is used here for concentration of electrons *n* and concentration of holes *p*, as in Fig. 1.

When present in a lattice site, boron introduces a shallow level into the forbidden band. But part of boron is in an electrically inactive state, and it is unknown up to date what precisely this inactive state is. Upon irradiation, boron atoms located at lattice sites (B_S) efficiently interact with self-interstitial silicon atoms (*I*), forming an interstitial boron atom (B_I) by the reaction

$$B_S + I \longrightarrow B_I. \quad (1)$$

In the presence of mobile vacancies (*V*), the following reaction is possible:

$$B_I + V \longrightarrow B_S \quad (2)$$

by which the boron atoms occupy positions at the lattice sites.

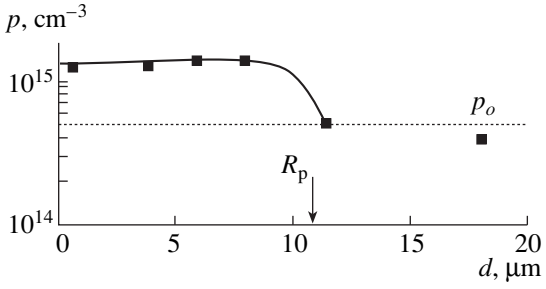

Fig. 4. Distribution of hole concentration over the depth in a Cz-Si crystal implanted with N^+ ions with an energy of 16 MeV and dose $D = 5 \times 10^{14}$ cm^{-2} and then annealed at $T_{ann} = 500$°C for 2 h. R_p stands for the projected range of N^+ ions.

Since the direct annihilation of *V* and *I* defects is difficult [3, 7], either the annihilation at some centers can occur, when reactions (1) and (2) occur sequentially, or the accumulation (coalescence) of defects may proceed. The existence of defects containing a relatively large number of vacancies (more than five) follows from the EPR studies of silicon irradiated with neutrons [13]. Chadi and Chang [12] calculated some properties of multivacancy complexes (V_6, V_{10}). Since the vacancies *V* and self-interstitials *I* are introduced in equal concentrations, when vacancies coalesce, there arises an excess of interstitial silicon atoms *I*, and they necessarily form defects. Some defects are paramagnetic centers [14], and the others manifest themselves in electron-microscopic investigations (see, e.g., [15]). Thus, after irradiation, electrically inactive boron is formed in the bulk of the crystal as a result of reaction (1), which, interacting with vacancy defects upon subsequent annealing, may transform into an electrically active state. For this to occur, it is necessary that a large portion of the vacancies that are generated could still coalescence during irradiation. This is possible upon irradiation, with large doses of electrons, of "pure" silicon (i.e., containing small concentrations of recombination centers, in order that the recombination could not be the predominant process), or when using the irradiation with species (e.g., neutrons or ions) that provide a large rate of generation of simplest defects such as *V* and *I*. In these cases, the appearance of acceptor centers is observed both in pure silicon (Figs. 1, 3) and in silicon grown by the Czochralski technique (Figs. 2, 4, 5).

In our opinion, the observation of changes in the concentration of electrically active acceptors makes it possible to judge the processes that occur in crystals upon heat treatments. If the concentration of acceptors decreases, there are grounds to believe that mobile *I* defects appeared in the volume and reaction (1) is dom-

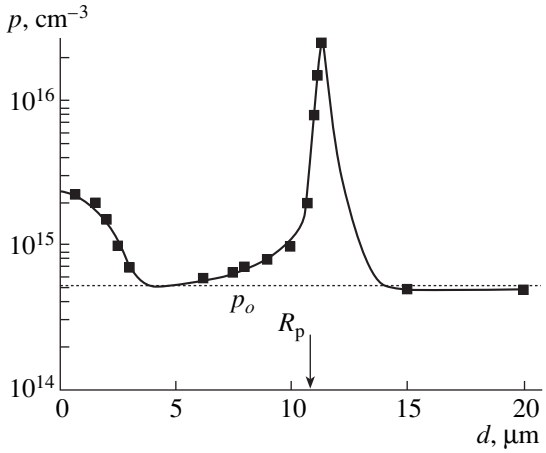

Fig. 5. Distribution of hole concentration over the depth in a Cz-Si crystal implanted with N^+ ions ($E = 16$ MeV and $D = 2 \times 10^{15}$ cm^{-2}) and then annealed for 3.7 h at $T_{ann} = 570$°C. R_p stands for the projected range of N^+ ions.

inant; on the contrary, the increase in the concentration of acceptors implies the occurrence of reaction (2) and, respectively, the existence of mobile vacancies.

The above concepts permit us to understand the processes that occur upon heat treatments irrespective of the type of irradiation (electrons, ions, or neutrons). At annealing temperatures above 250°C, a decomposition of divacancies (and of *A* centers in oxygen-containing silicon) occurs, reaction (2) proceeds, and the observed concentration of holes reaches a maximum (Figs. 1, 3) or tends towards saturation (Fig. 2). Curve *2* in Fig. 1 is especially demonstrative; here, a bend in the $p(T_{ann})$ first takes place, then a maximum is reached, a sharp decrease in the hole concentration is observed, and a transition into the *n* region occurs. The decrease in the hole concentration indicates that reaction (1) is dominant. However, the run of curve *2* in Fig. 1 suggests that the *I* defects also interact with coarse (stable) vacancy complexes; i.e., the following reaction proceeds:

$$V_n + I \longrightarrow V_{n-1}. \quad (3)$$

However, the stability of V_{n-1} complexes is less than that of V_n complexes, so that their decomposition can occur by the reaction

$$V_{n-1} \longrightarrow (n-1)V, \quad (4)$$

and a situation takes place where both mobile vacancies *V* and mobile interstitials *I* exist simultaneously in the bulk of the crystal. In this case, the reverse reaction is possible, which leads to the restoration of a stable configuration, i.e.,

$$V_{n-1} + V \longrightarrow V_n. \quad (5)$$

As long as reaction (2) is dominant, we see an increase in the hole concentration (Fig. 1, curve *2*). When the supply of vacancies due to reaction (4) decreases but generation of interstitials is continued, reaction (1) becomes dominant and a sharp decrease in the concentration of holes is observed. When the concentration of centers that generate interstitials becomes exhausted, we see the saturation of the acceptor concentration with increasing annealing temperature.

Judging from Fig. 4, the spatial distribution of acceptors in the bulk of the crystals appears to be relatively uniform at the macrolevel. However, with decreasing concentration of "stored" vacancies (e.g., produced by reactions (3) and (4)), the acceptors are retained only at those regions that serve as preferable sinks for vacancies (Fig. 5).

Figure 3 indicates that the coalescence of defects is more efficient upon heterogeneous nucleation. A preliminary irradiation with neutrons ($D = 10^{14}$ cm^{-2}), which does not lead by itself to the conversion of the conductivity type, introduces centers (e.g., disordered regions) that can serve as sinks for vacancies. The subsequent irradiation with even small doses of electrons favors the effective separation of *V* and *I* defects and the creation of conditions suitable for the formation of acceptors.

Upon electron irradiation, the majority of interstitial defects are annealed out as the temperature reaches $T_{ann} \simeq 500$°C [16]. As a result, it is at this temperature that free interstitials appear in the crystal; they interact with vacancy clusters to yield the restoration of the initial conductivity of the samples. At stronger actions (irradiation with neutrons or ions), the annealing out of interstitial defects mainly occurs at higher temperatures $T_{ann} \simeq 650$°C (see Figs. 2, 4, 5 and data given in [16]). Which particular defects are supplied by the mobile interstitials at this stage is unknown at present, but the fact that mobile interstitials exist at this stage is confirmed by the large rate of formation of stable interstitial defects that were well studied by electron microscopy [15]. Most likely, it is the flux of mobile defects such as self-interstitials *I* that causes a redistribution of the hole concentration in ion-irradiated samples (Figs. 4, 5), which distinctly confirms that reactions (1)–(5) proceed in the crystals.

Finally, we discuss one more question, namely, why the holes in these crystals have a low mobility (see table). Such low mobilities cannot be explained by the conventional mechanisms of scattering. Such low mobilities of holes are characteristic of samples with a strongly nonuniform potential relief, which can be due to either the presence of coarse charged defects or a nonuniform distribution of hole concentration. The last cause seems to be more probable. Thus, upon neutron irradiation, disordered regions (vacancy clusters) surrounded by a shell of interstitial atoms are introduced uniformly over the whole volume of the samples [3]; i.e., the nonuniform distribution of vacancy and interstitial defects takes place and, consequently, the possibility of fluctuations in the distribution of the hole concentration exists. Low mobility is characteristic not only of holes. If FZ Si ($\rho_{st} \simeq 200\ \Omega$ cm) is irradiated with electrons to a small dose, such as $D = 3 \times 10^{15}$ cm^{-2}, then the sample retains the conductivity of the *n* type. However, upon heat treatments at T_{ann} = 450–500°C, the concentration of electrons decreases sharply and the measured values of the mobility of electrons become ~400 cm^2/(V s) or even smaller.

As follows from the experimental data, boron that supposedly takes part in the formation of acceptors does not manifests itself (does not become electrically active) upon further high-temperature heat treatments (at $T_{ann} \geq 900$°C). This is most likely to occur, because the initially electrically inactive (background) component of the impurity boron is present in the form of stable complexes of boron with other impurities (e.g., carbon) rather than as isolated atoms in interstitial positions. The formation of coarse vacancy clusters in the crystal favors the activation of the boron contained in such complexes (clusters). The arising fluxes of self-interstitials and their annihilation again lead to the transition of such complexes (clusters) into the initial position in the lattice. Therefore, in all the above concepts concerning the formation and annealing of thermal

acceptors, we assumed that boron took part just in that form in which it was present as an electrically inactive component in silicon crystals.

CONCLUSION

In this work, we performed an analysis of the conditions required for the formation of shallow acceptor centers in the process of high-temperature annealing of irradiated silicon. As a result, we revealed the following trends in the transformation of the defect subsystem upon annealing:

1. The formation of thermal acceptors is observed up to the annealing temperatures of $T_{ann} \simeq 650°C$ and is supposedly related to the activation of boron atoms (which are always present in silicon in the electrically inactive state) by vacancies stored in multivacancy clusters and released as the clusters break up.

2. The occurrence of a flux of silicon self-interstitials favors the irreversible annealing of defects. Separate stages of annealing can be distinguished, at least in the temperature range of 450–650°C.

ACKNOWLEDGMENTS

This work was supported in part by the Russian Foundation for Basic Research, project nos. 96-02-19385 and 96-15-97272. We are also very grateful to T. A. Belykh who performed irradiation of silicon with nitrogen ions.

REFERENCES

1. V. V. Voronkov, R. Falster, and J. C. Holzer, Electrochem. Proc. **97** (22), 3 (1997).
2. M. C. Ohmer and J. E. Lang, Appl. Phys. Lett. **34**, 750 (1979).
3. *Problems of the Radiation Technology of Semiconductors* [in Russian], Ed. by L. S. Smirnov (Nauka, Novosibirsk, 1980).
4. A. Agarwal, K. Christensen, D. Venables, *et al.*, Appl. Phys. Lett. **69** (25), 3899 (1996).
5. B. G. Svensson, C. Jagadish, A. Hallen, and J. Lalita, Phys. Rev. B **55**, 10498 (1997).
6. R. A. Brown, O. Konopchuk, G. A. Rozgonyi, *et al.*, J. Appl. Phys. **84**, 2459 (1998).
7. L. I. Fedina, A. K. Gutakovskii, and L. A. Aseev, Philos. Mag. A **77** (2), 423 (1998).
8. B. C. MacEvoy, G. Hall, and K. Gill, Phys. Rev. A **374**, 12 (1996).
9. J. W. Corbett, J. C. Bourgoin, L. J. Cheng, J. C. Correlli, J. H. Lee, P. M. Moonney, and C. Weigel, in *Radiation Effects in Semiconductors*, Ed. by N. B. Urlin and J. W. Corbett, Inst. Phys. Conf. Ser., No. 31 (Inst. of Physics, Bristol, 1976).
10. J. H. Lee, P. R. Brosious, and J. W. Corbett, Radiat. Eff. **22**, 69 (1974).
11. V. F. Stel'makh, V. P. Tolstykh, and L. V. Zvirko, Fiz. Tekh. Poluprovodn. **19**, 1860 (1985) [Sov. Phys. Semicond. **19**, 1145 (1985)].
12. D. J. Chadi and K. J. Chang, Phys. Rev. B **38**, 1523 (1988).
13. *Physical Processes in Irradiated Semiconductors* [in Russian], Ed. by L. S. Smirnov (Nauka, Novosibirsk, 1977).
14. G. H. Hastings, S. K. Estreicher, and P. A. Fedders, Phys. Rev. B **56**, 10215 (1997).
15. A. L. Aseev, L. I. Fedina, D. Heél', and Kh. Barch, *Clysters of Interstitial Atoms in Silicon and Germanium* [in Russian] (Nauka, Novosibirsk, 1991).
16. J. H. Lee, J. W. Corbett, and N. N. Gerasimenko, Phys. Rev. B **14**, 4506 (1976).
17. A. V. Dvurechenskiĭ, A. A. Karanovich, R. Grötzshel, *et al.*, Fiz. Tverd. Tela (St. Petersburg) **40** (2), 217 (1998) [Phys. Solid State **40**, 195 (1998)].

Translated by S. Gorin

Semiconductors, Vol. 34, No. 2, 2000, pp. 161–162. Translated from Fizika i Tekhnika Poluprovodnikov, Vol. 34, No. 2, 2000, pp. 168–169.

ELECTRONIC AND OPTICAL PROPERTIES OF SEMICONDUCTORS

Influence of Au and Pt on the Concentration Profile of Mn in Si

G. S. Kulikov and Sh. A. Yusupova

Ioffe Physicotechnical Institute, Russian Academy of Sciences, Politekhnicheskaya ul. 26, St. Petersburg, 194021 Russia

Submitted July 14, 1999; accepted for publication July 15, 1999

Abstract—The influence of diffusion of gold and platinum from the layer deposited on the silicon surface on the concentration profile of ^{54}Mn in the bulk is investigated using the radiochemical technique. The data obtained indicate that the manganese concentration in the bulk of silicon is reduced due to annealing of the samples Si⟨^{54}Mn⟩ with the gold or platinum layer on the surface. © *2000 MAIK "Nauka/Interperiodica".*

In this work, the interaction between fast diffusing gold and platinum dopants, which introduce deep levels in the band gap of silicon, and the influence of gold and platinum diffusion on the concentration profile and content of manganese in silicon were investigated.

The Czochralski-grown *n*-Si with the resistivity $\rho \approx 5\ \Omega$ cm was used for investigations. The sample dimensions were $13 \times 6 \times 1$ mm. The manganese radioisotope ^{54}Mn and nonradioactive Au and Pt were used as diffusants.

Radioisotope ^{54}Mn was deposited on one of the large surfaces of the sample in the form of manganese salt solution. Subsequent to drying in air, the Si samples were doped via diffusion of manganese at 1200°C for 2 h in sealed quartz ampules with subsequent quenching by dropping the ampules in water. The excess manganese was removed from the surface by grinding. Then the samples were washed in a boiling acid-peroxide solution $HCl : H_2O_2 = 1 : 1$. Autoradiographs taken after the diffusion annealing indicated that manganese saturated the bulk of the samples uniformly. The exposure duration was chosen depending on the sample radioactivity. Subsequently, the layer of nonradioactive impurity (Au or Pt) about 1 μm thick was sputtered on one of the surfaces of the sample saturated by radioactive manganese. The diffusion annealing was repeated under conditions corresponding to the regime of introducing the radioactive ^{54}Mn. The reference samples without the radioactive diffusant deposited were annealed simultaneously.

Radiography of the samples after Au or Pt diffusion demonstrated that the film optical density for the Si surface with the deposited metal was sufficiently higher than that for other surfaces including the reference samples. The reason is that the annealing of Si⟨^{54}Mn⟩ with the Au or Pr layer causes extraction of manganese atoms into the surface layers of the samples with the metal deposited.

The results obtained by the layer-by-layer radiometry of the samples indicate that the total manganese concentration N_{Mn} in the bulk of the annealed samples with the metal layers is more than half an order of magnitude less compared to the reference samples (see figure).

Hence, gold and platinum deposited on the Si⟨^{54}Mn⟩ surface are getters for Mn in Si. Diffusive introduction of Au or Pt from the surface layer into the bulk of man-

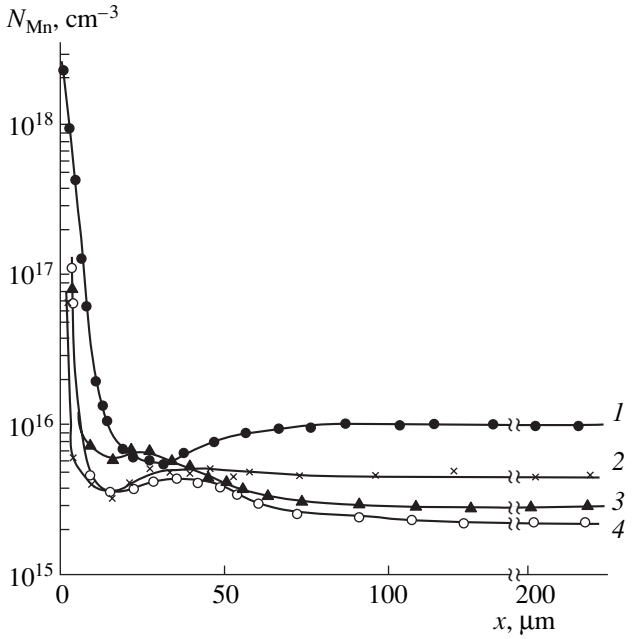

Concentration distributions of ^{54}Mn in silicon for (*1*) the starting sample after manganese diffusion, (*2*) the reference sample without the layer of nonradioactive Au or Pt, (*3*) the sample with the Au surface layer, and (*4*) the sample with the Pt surface layer. The temperature of both diffusion-induced doping by manganese and repeat annealing is 1200°C; duration is 2 h.

1063-7826/00/3402-0161$20.00 © 2000 MAIK "Nauka/Interperiodica"

ganese-doped silicon causes silicon to be freed of impurities due to manganese gettering by the surface and near-surface layers. We believe that the gettering mechanism is characterized by the formation of complex silicides containing both metals and oxygen, which is always contained in silicon.

Previously, we obtained similar results on Ni and Fe gettering by the layers of certain metals (Mn, Au, Pt, and Co) [1, 2].

REFERENCES

1. K. P. Abdurakhmanov, Kh. S. Daliev, G. S. Kulikov, *et al.*, Fiz. Tekh. Poluprovodn. (St. Petersburg) **27**, 1222 (1993) [Semicond. **27**, 674 (1993)].
2. G. S. Kulikov, Yu. A. Chichikalyuk, and Sh. A. Yusupova, Fiz. Tekh. Poluprovodn. (St. Petersburg) **29**, 469 (1995) [Semicond. **29**, 242 (1995)].

Translated by N. Korovin

Semiconductors, Vol. 34, No. 2, 2000, pp. 163–165. Translated from Fizika i Tekhnika Poluprovodnikov, Vol. 34, No. 2, 2000, pp. 170–171.

ELECTRONIC AND OPTICAL PROPERTIES OF SEMICONDUCTORS

Variation in Resistance of a Nitrogen-Enriched Silicon Layer as a Result of the Long-Range Effect of Ion Implantation

E. S. Demidov*, V. V. Karzanov, and K. A. Markov

Nizhni Novgorod State University, pr. Gagarina 23, Nizhni Novgorod, 630600 Russia

**e-mail: ett@phys.unn.runnet.ru*

Submitted August 3, 1998; accepted for publication July 14, 1999

Abstract—An improvement in the insulating properties of a synthesized silicon nitride layer under the influence of ion-beam treatment of the back surface of silicon wafer was detected. This result is consistent with the infrared-spectroscopy data obtained previously and is related to the long-range effect of ion implantation. *© 2000 MAIK "Nauka/Interperiodica".*

Studies of the long-range effect of ion implantation have shown that the action of an ion beam on one of the surfaces of a semiconductor wafer can cause an appreciable change in the properties of the other surface or in the bulk at distances of hundreds of micrometers from the surface, i.e., at distances exceeding the ion ranges by several orders of magnitude. These changes are found to be more considerable if the entire crystal or its part are far from the equilibrium state (for example, if a supersaturated solid solution of a certain impurity is formed in a crystal, as shown in [1]). In [2], a shift of the nitrogen concentration profile under the influence of implantation of ions into the back surface of the wafer was reported. The results reported in [3] gave grounds to state that the long-range effect could also stimulate the formation of chemical bonds. We used infrared (IR) spectroscopy to show that, if the back surface of Si samples whose front surface had been preliminarily implanted with nitrogen was irradiated with argon, the IR absorption by Si–N bonds increased, which was characteristic of the Si_3N_4 phase in the vicinity of $\nu = 850$ cm^{-1} [4, 5]. However, if a fraction of the Si_3N_4 phase becomes larger in the Si:N layer, this is bound to affect the insulating properties of the layer. In this paper, the results of the verification of this inference are reported.

We studied the electrophysical properties of the structures formed by implanting nitrogen ions into the front surface of silicon wafers whose back surface was irradiated with argon ions. Schematic representation of irradiation of the sample is shown in Fig. 1a.

The energy of N^+ ions was $E = 40$ keV, and the dose for various samples was varied in the range of $\Phi_N = (1–5) \times 10^{17}$ cm^{-2}. In the course of ion implantation, the temperature of the sample was $T_{impl} = 673$ K. The parameters of irradiation with Ar ions were the same as in [4, 5]: $E = 40$ keV, $\Phi_{Ar} = 3 \times 10^{17}$ cm^{-2}, and $T_{impl} = 773$ K. In order to recognize the changes in electrical properties of the nitrogen-enriched layer more clearly and to reduce the contribution of the series resistance metal–semiconductor contacts, we used the samples of a nearly degenerate KEF-0.005 *n*-Si (Si:P, $\rho = 0.005\ \Omega$ cm) with (111) orientation. Arrangement of the contacts on the samples under study in measuring the current–voltage (*I–V*) characteristics is shown in Fig. 1b. The circular contacts 5 mm in diameter were formed by vacuum deposition of aluminum through a mask onto the substrate heated to 673 K. The *I–V* characteristic of each sample was measured after each irradiation. Prior to irradiation, the aluminum contacts were etched off with the use of hydrochloric acid. The

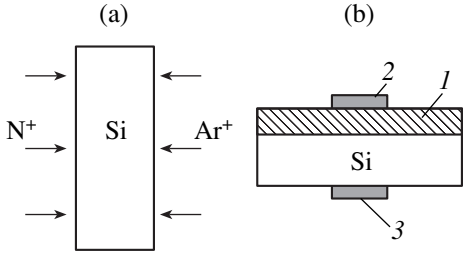

Fig. 1. (a) Schematic representation of irradiation of Si samples with N^+ and Ar^+ ions (the doses and energies of the ions are given in the text); (b) position of contacts to the samples under study: (*1*) the Si:N layer at the "operating" (front) surface of the wafer, (*2*) the metal contact (Al film) to the front surface of the wafer, and (*3*) the metal contact (Al film) to the back surface of the wafer.

1063-7826/00/3402-0163$20.00 © 2000 MAIK "Nauka/Interperiodica"

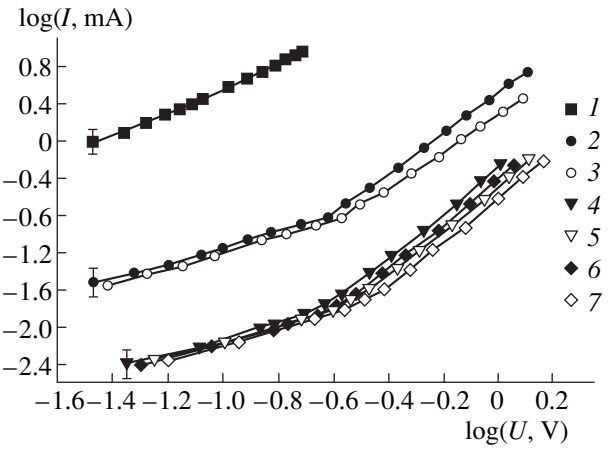

Fig. 2. Current–voltage characteristics of the Si sample as measured (*1*) immediately after the contacts were formed, (*2*, *3*) after irradiation with nitrogen ($\Phi_N = 10^{17}$ cm^{-2}), (*4*, *5*) after additional irradiation with argon, and (*6*, *7*) after the argon-implanted layer was etched off; curves *2*, *4*, and *6* correspond to the forward-bias characteristics, whereas curves *3*, *5*, and *7* represent the reverse-bias characteristics.

I–V characteristics of all irradiated samples had linear and parabolic portions, which corresponds to the mechanism of currents in a dielectric as described by Lampert [6]. The resistivity was measured within the linear portion of the *I–V* characteristic. Typical forward and reverse *I–V* characteristics of a Si sample irradiated with nitrogen ($\Phi_N = 10^{17}$ cm^{-2}) before and after irradiation with argon are shown in Fig. 2.

After irradiation with nitrogen (curves *2*, *3*), the resistivity of a Si:N layer of about 0.13 μm in thickness amounted to $\rho = 1.5 \times 10^7$ Ω cm and increased to $\rho = 10^8$ Ω cm after irradiation with argon; i.e., the insulating characteristics of the synthesized Si_xN_y layer were improved by almost an order of magnitude. If the dose of implanted nitrogen was close to the one ($\Phi_N = 5 \times 10^{17}$ cm^{-2}) yielding the stoichiometric composition, the effect was qualitatively the same; however, the resistivity after the implantation of nitrogen attained the value of $\rho = 1.5 \times 10^{11}$ Ω cm and was equal to $\rho = 4.5 \times 10^{11}$ Ω cm after irradiation of the back surface by argon ions.

We carried out the check experiments in which the samples with implanted nitrogen were kept for 1 h at a temperature of 773 K but were not irradiated with argon. In this case, the *I–V* characteristic remained almost unchanged; i.e., the temperature rise during irradiation with Ar ions did not affect the electrical properties of the samples. In order to assess the contribution of the layer damaged by Ar irradiation into resistance, we dynamically etched the Ar irradiated surface; the thickness of the etched-off layer was about 0.15 μm, which was nearly twice as large as the quantity $R_p + \Delta R_p \simeq 0.076$ μm for the given parameters of Ar implantation [7]. The surface of the sample implanted with nitrogen was coated with a chemically resistant varnish prior to etching. After the above procedure, the *I–V* characteristic of the sample has the form shown in Fig. 2 (curves *6*, *7*) and, within the experimental error, coincides with *I–V* characteristic measured prior to etching; i.e., the layer formed as a result of Ar implantation does not introduce significant errors into the measurements, which is indicative of the fairly high electrical conductance of this layer. This inference is also consistent with the data reported in [7, Chapter 2; 8], according to which the dose of $\Phi_{Ar} = 3 \times 10^{17}$ cm^{-2} implanted at $T_{impl} = 773$ K is insufficient for amorphization of silicon and the electrically active defects are annealed at $T > 600$ K. Figure 2 (curve *1*) also shows the *I–V* characteristic of Al–Si contacts measured immediately after the contacts were formed; it is evident that the contribution of the contacts to total resistance is about 3%. All the above suggests that, in the structures studied, almost the entire voltage drops across the Si:N layer; it is this layer that determines the shape of the *I–V* characteristic. A slight asymmetry of the *I–V* characteristic in forward and reverse directions (see Fig. 2) is apparently related to the nonlinearity of the transition region between the Si_xN_y layer and the bulk of Si; this asymmetry is significantly reduced as a result of irradiation with Ar.

Thus, we showed that implantation of Ar ions with a dose of $\Phi_{Ar} > 10^{17}$ cm^{-2} into the back surface of the wafer brings about an increase in the resistance of the silicon layer ion-implanted with N at the front surface of the wafer. By comparing these results with the IR spectroscopy data [4, 5], we may state that the ion-beam treatment of the back surface of the silicon wafer stimulates the synthesis of the Si_3N_4 dielectric phase in the Si:N layer at the front surface of Si crystal; it may also be concluded that the long-range effect of ion implantation can be used to improve the insulating properties of Si_xN_y layers without resorting to postimplantation annealing, which is used in fabrication of the silicon-on-insulator structures following the conventional technology [9].

ACKNOWLEDGMENTS

This work was supported by the Competition Center of the Ministry of Education of the Russian Federation for basic research in the fields of nuclear physics and the physics of ionizing-radiation beams (grant for 1998–1999).

REFERENCES

1. V. V. Karzanov, P. V. Pavlov, and E. S. Demidov, Fiz. Tekh. Poluprovodn. (Leningrad) **23**, 2064 (1989) [Sov. Phys. Semicond. **23**, 1276 (1989)].

2. V. N. Mordkovich, Élektron. Prom-st. **4**, 62 (1986).
3. P. V. Pavlov, E. S. Demidov, and V. V. Karzanov, Vysokochist. Veshchestva **3**, 31 (1993).
4. P. V. Pavlov, K. A. Markov, V. V. Karzanov, *et al.*, Vysokochist. Veshchestva **2**, 56 (1995).
5. V. V. Karzanov, K. A. Markov, and D. V. Masterov, Neorg. Mater. **9**, 34 (1998).
6. M. A. Lampert and P. Mark, *Current Injection in Solids* (Academic, New York, 1970; Mir, Moscow, 1973).
7. H. Ryssel and I. Ruge, *Ionenimplantation* (Teubner, Stuttgart, 1978; Nauka, Moscow, 1983).
8. E. I. Zorin, P. V. Pavlov, and D. I. Tetel'baum, *Ion-Implantation Doping of Semiconductors* [in Russian] (Energiya, Moscow, 1975), Chap. 2, p. 41.
9. A. B. Danilin, Élektron. Prom-st. **4**, 55 (1990).

Translated by A. Spitsyn

Semiconductors, Vol. 34, No. 2, 2000, pp. 166–170. Translated from Fizika i Tekhnika Poluprovodnikov, Vol. 34, No. 2, 2000, pp. 172–176.

ELECTRONIC AND OPTICAL PROPERTIES OF SEMICONDUCTORS

Contribution of the Electron Subsystem of Crystal into Reactions between Multicharge Centers in Semiconductors

N. I. Boyarkina and A. V. Vasil'ev

Institute of Semiconductor Physics, Siberian Division, Russian Academy of Sciences, pr. akademika Lavrent'eva 13, Novosibirsk, 630090 Russia

Submitted January 21, 1998; accepted for publication August 18, 1999

Abstract—The reactions of defect-complex formation in semiconductors is considered. The contribution of the electron subsystem of a crystal into the reaction rate is considered in terms of an additional change in the energy barrier of reaction. The comparison of the results of calculation with the experimental data is carried out for the case of the accumulation of the radiation-induced *A*- and *E*-centers in silicon. Satisfactory agreement between theoretical and experimental results gives evidence in favor of the suggested mechanism of participation of electron subsystem of a crystal in the processes in an atomic subsystem. *© 2000 MAIK "Nauka/Interperiodica".*

INTRODUCTION

The reaction rates of the formation and dissociation of defect complexes in semiconductors are known to depend both on temperature of the crystal and on the charge state of electrically active components of the reaction. The effect of these parameters is observed in the experiments with irradiation and annealing of silicon single crystals (see, for example, [1–5]).

In calculations of the reaction rates for radiation-induced formation of the complexes [6], the effect of the charge state of the initial components of reaction was regarded as an additional contribution of Coulomb and deformation barriers to the reaction barrier. In the literature (see, for example, [7]) a great deal of attention is given to the fact that the system of electron levels of defects in the forbidden band of a semiconductor crystal is modified as a result of the reaction between the multicharge centers: the levels of the initial components disappear, instead, the levels of the final components come into existence. The change in the energy-level system in the forbidden band is accompanied by the rearrangement of the electron subsystem of the crystal due to the exchange of electrons between the conduction and valence bands and the levels of the components of the reaction. In [8], the expressions for the rate constants for unimolecular and bimolecular reactions are obtained with consideration for the effect of charge states of the initial and final reactants. The Coulomb interaction energy of initial components and the energy expenditure related to their recharging are taken into account by the addition of these values to the reaction energy barrier.

However, the disappearance (or appearance) of a multicharge center in its admissible charge state disturbs the quasi-equilibrium distribution of these centers over the charge states. This disturbance produces the exchange of electrons between the remaining centers of this type and the allowed bands. This exchange tends to recover the disturbed equilibrium. The energy spent on these electron transitions was not taken into account in calculation [8] of the reaction rate constants. Even in the case of "electron-neutral" reaction considered in [8],

$$A^0 + B^0 \longrightarrow C^0 \tag{1}$$

(*A*, *B*, and *C* are the components of the reaction, with the superscripts referring to their charge states), the change in concentration of any type from the neutral-charged multicharge centers (*A*, *B*, or *C*) alters the distribution of these centers over the charge states. In this work, we suggest a new mechanism of participation of electron system of the crystal in reactions of multicharge centers in semiconductors and a method of considering the energy consumption associated with the participation of electron subsystem in these reactions.

CALCULATIONS

Let us consider the reaction of formation of the complex *C* consisting of *A* and *B* centers:

$$A + B \xrightarrow{k_{AB}} C, \tag{2}$$

1063-7826/00/3402-0166$20.00

where k_{AB} is the reaction rate constant. The reaction rate can be written as

$$\frac{d[C]}{dt} = k_{AB}[A][B], \tag{3}$$

where $[A]$, $[B]$, and $[C]$ are the concentration of the centers A, B, and C, respectively.

Following [8], we assume that reaction (2) proceeds independently over separate channels differing in charge state X and Y of the A and B centers; i.e., we have

$$A^X + B^Y \xrightarrow{k_{AB}^{XY}} C_{XY} + Ne, \tag{4}$$

where C_{XY} is the fraction of complexes C, which is formed in each of those channels; k_{AB}^{XY} is the reaction rate constant, i.e.,

$$\frac{d[C_{XY}]}{dt} = k_{AB}^{XY}[A^X][B^Y]; \tag{5}$$

the term Ne is the "electron yield" of the reaction (N is a certain function of the parameters X, Y, and k_{AB}^{XY}; and e is the elementary charge). Obviously,

$$[C] = \sum_{X,Y}[C_{XY}]. \tag{6}$$

Combining (3), (5), and (6), we arrive at

$$\begin{aligned}\frac{d[C]}{dt} &= \sum_{X,Y}\frac{d[C_{XY}]}{dt} = \sum_{X,Y}k_{AB}^{XY}[A^X][B^Y] \\ &= \sum_{X,Y}k_{AB}^{XY}f_A^X f_B^Y[A][B],\end{aligned} \tag{7}$$

where f_A^X, f_B^Y are the probabilities of finding the A and B centers in the charge states X and Y, respectively.

Comparing (3) and (7), we obtain the expression for k_{AB}:

$$k_{AB} = \sum_{X,Y}k_{AB}^{XY}f_A^X f_B^Y. \tag{8}$$

It is assumed in [8] that the electron exchange between the components of the reaction A, B, C, and conduction and valence bands occurs prior to the commencement and after the completion of the reaction. In this work it is assumed that the exchange occurs in the course of the reaction, so that the electron subsystem is able to follow the processes of rearrangement in an atomic subsystem. This assumption is based on the known adiabatic approximation.

The energy of electron subsystem of the crystal in the process of reaction changes. An increase in the energy of the electron subsystem by δu produces the same decrease in the energy of the atomic subsystem. This energy change of atomic-subsystem energy may be treated as an increase in energy barrier of the reaction. The contribution of the electron subsystem of the crystal into the reaction rate constant (2) may be accounted for by the addition of energy variation of electron subsystem in the course of reaction to the energy barrier of the reaction

$$k_{AB}^{XY} = \kappa_{AB}^{XY}\exp(-\Delta W_{AB}^e/kT), \tag{9}$$

where κ_{AB}^{XY} is the reaction rate constant for the reaction of the reactants A^X and B^Y without considering the electron subsystem of the crystal; and ΔW_{AB}^e is the change in energy of electron subsystem due to the reaction per single resulting complex C.

The expression for κ_{AB}^{XY} can be derived by using the formulas (1.40), (2.11a), and (2.11b) in [8]. To calculate ΔW_{AB}^e, we consider the crystal of unit volume. In the course of the reaction (2) with formation of the C complexes in the amount of $\delta[C]$, the following electron transitions occur (for the sake of definiteness, we consider the crystal with n-type conductivity).

(i) The amount of electrons transferred from the conduction band to generated C centers is $\delta n = \delta[C^-] + 2\delta[C^{--}] + \ldots - (\delta[C^+] + 2\delta[C^{++}] + \ldots)$. The corresponding change in electron subsystem energy is

$$\begin{aligned}\delta w_C^e &= (E_C^- - E_c)\delta[C^-] + [(E_C^- - E_c) \\ &+ (E_C^{--} - E_c)]\delta[C^{--}] + \ldots - (E_C^+ - E_c)\delta[C^+] \\ &- [(E_C^+ - E_c) + (E_C^{++} - E_c)]\delta[C^{++}] - \ldots \\ &= -[\varepsilon_C^- f_C^- + (\varepsilon_C^- + \varepsilon_C^{--})f_C^{--} + \ldots]\delta[C] \\ &+ [\varepsilon_C^+ f_C^+ + (\varepsilon_C^+ + \varepsilon_C^{++})f_C^{++} + \ldots]\delta[C],\end{aligned} \tag{10}$$

where E_C^-, E_C^{--}, E_C^+, E_C^{++} are the energy levels of the C complex in the charged states –1, –2, +1, +2 in a forbidden band, respectively; and E_C is the energy position of the conduction-band bottom.

(ii) The disappearance of the A centers with the X-charge state in the amount of $\delta[A^X]$ generates the exchange of electrons between these centers and the conduction band. At the completion of the reaction, the relations $[A^j] = f_A^j[A]$ remain unchanged for all j. It thus follows that $\delta[A^j] = f_A^j\delta[A]$, and $\delta[A] = -\delta[C]$ since $\delta[A^j] = -f_A^j\delta[C]$.

The change in the energy of electron subsystem of a crystal is determined by the change in the concentration of the charged A centers:

$$\begin{aligned}\delta w_A^e &= (E_A^- - E_c)\delta[A^-] + [(E_A^- - E_c) \\ &+ (E_A^{--} - E_c)]\delta[A^{--}] + \ldots - (E_A^+ - E_c)\delta[A^+]\end{aligned}$$

$$-[(E_A^+ - E_c) + (E_A^{++} - E_c)]\delta[A^{++}] - \ldots \quad (11)$$

$$= [\varepsilon_A^- f_A^- + (\varepsilon_A^- + \varepsilon_A^{--}) f_A^{--} + \ldots]\delta[C]$$
$$-[\varepsilon_A^+ f_A^+ + (\varepsilon_A^+ + \varepsilon_A^{++}) f_A^{++} + \ldots]\delta[C].$$

(iii) The same considerations for the B centers yields

$$\delta w_B^e = [\varepsilon_B^- f_B^- + (\varepsilon_B^- + \varepsilon_B^{--}) f_B^{--} + \ldots]\delta[C] \quad (12)$$
$$-[\varepsilon_B^+ f_B^+ + (\varepsilon_B^+ + \varepsilon_B^{++}) f_B^{++} + \ldots]\delta[C].$$

Finally, we obtain the following expression for ΔW_{AB}^e

$$\Delta W_{AB}^e = \frac{\delta w^e{}_C + \delta w_A^e + \delta w_B^e}{\delta[C]}$$
$$= -[\varepsilon_C^- f_C^- + (\varepsilon_C^- + \varepsilon_C^{--}) f_C^{--} + \ldots]$$
$$+ [\varepsilon_C^+ f_C^+ + (\varepsilon_C^+ + \varepsilon_C^{++}) f_C^{++} + \ldots]$$
$$+ [\varepsilon_A^- f_A^- + (\varepsilon_A^- + \varepsilon_A^{--}) f_A^{--} + \ldots] \quad (13)$$
$$-[\varepsilon_A^+ f_A^+ + (\varepsilon_A^+ + \varepsilon_A^{++}) f_A^{++} + \ldots]$$
$$+ [\varepsilon_B^- f_B^- + (\varepsilon_B^- + \varepsilon_B^{--}) f_B^{--} + \ldots]$$
$$-[\varepsilon_B^+ f_B^+ + (\varepsilon_B^+ + \varepsilon_B^{++}) f_B^{++} + \ldots].$$

It is noteworthy that ΔW_{AB}^e is independent of the charge states of the A and B components which enter into reaction, i.e., of X and Y.

COMPARISON OF CALCULATIONS WITH EXPERIMENT

As a specific example we consider the formation of the A and E centers under the irradiation of n-Si with light particles, such as electrons or γ-quanta.

For the reaction of formation of the A center (a vacancy-oxygen complex)

$$V + \mathrm{O} \xrightarrow{k_{VO}} A \quad (14)$$

we obtain

$$\Delta W_{VO}^e = -\varepsilon_A f_A^- + \varepsilon_V^- f_V^- + (\varepsilon_V^- + \varepsilon_V^{--}) f_V^{--}; \quad (15)$$

$$k_{VO} = \sum_X k_{VO}^{X0} f_V^X f_O^0$$
$$= \exp(-\Delta W_{VO}^e/kT)\sum_X \kappa_{VO}^{X0} f_V^X f_O^0 \quad (16)$$
$$= \exp(-\Delta W_{VO}^e/kT)(\kappa_{VO}^{00} f_V^0 + \kappa_{VO}^{-10} f_V^- + \kappa_{VO}^{-20} f_V^{--}).$$

For the reaction of the formation of E center (a complex of vacancy with doping donor impurity of Group V, for example, of phosphorus)

$$V + \mathrm{P} \xrightarrow{k_{VP}} E \quad (17)$$

we have

$$\Delta W_{VP}^e = -\varepsilon_E f_E^- + \varepsilon_P f_P^+ + \varepsilon_V^- f_V^- + (\varepsilon_V^- + \varepsilon_V^{--}) f_V^{--}; \quad (18)$$

$$k_{VP} = \sum_{X,Y} k_{VP}^{XY} f_V^X f_P^V = \exp(-\Delta W_{VP}^e/kT)$$
$$\times \sum_{X,Y} \kappa_{VP}^{XY} f_V^X f_P^V = \exp(-\Delta W_{VP}^e/kT) \quad (19)$$
$$\times \sum_X f_V^X(\kappa_{VP}^{X0} f_P^0 - \kappa_{VP}^{X1} f_P^+).$$

If $\kappa_{VP}^{X0} f_P^0 \ll \kappa_{VP}^{X1} f_P^+$ and $f_P^+ \simeq 1$,

$$k_{VP} = \exp(-\Delta W_{VP}^e/kT)$$
$$\times(\kappa_{VP}^{01} f_V^0 + \kappa_{VP}^{-11} f_V^- + \kappa_{VP}^{-21} f_V^{--}). \quad (20)$$

The ratio of the reaction rate constants for formation of E and A centers is

$$\sigma = \frac{k_{VP}}{k_{VO}} = \exp\left(\frac{\Delta W_{VO}^e - \Delta W_{VP}^e}{kT}\right)$$
$$\times \frac{\kappa_{VP}^{01} f_V^0 + \kappa_{VP}^{-11} f_V^- + \kappa_{VP}^{-21} f_V^{--}}{\kappa_{VO}^{00} f_V^0 + \kappa_{VO}^{-10} f_V^- + \kappa_{VO}^{-20} f_V^{--}} \quad (21)$$
$$= \exp\left(\frac{\varepsilon_E f_E^- + \varepsilon_P f_P^+ - \varepsilon_A f_A^-}{kT}\right)$$
$$\times \frac{\kappa_{VP}^{01} f_V^0 + \kappa_{VP}^{-11} f_V^- + \kappa_{VP}^{-21} f_V^{--}}{\kappa_{VO}^{00} f_V^0 + \kappa_{VO}^{-10} f_V^- + \kappa_{VO}^{-20} f_V^{--}}.$$

The accumulation rates of A and B centers are calculated in the following manner [9]:

$$\eta_A = \beta\frac{1}{1 + \sigma[\mathrm{P}]/[\mathrm{O}]}, \quad \eta_E = \beta\frac{\sigma[\mathrm{P}]/[\mathrm{O}]}{1 + \sigma[\mathrm{P}]/[\mathrm{O}]}, \quad (22)$$

where η_A and η_E are the accumulation rates of A and B centers under irradiation; [O] and [P] are the concentrations of oxygen and phosphorus, respectively; and β is the coefficient of proportionality dependent on irradiation intensity.

The figure shows the dependences of the rate-constant ratio for the creation of the E and A centers on the irradiation temperature of n-Si obtained from the

experimental data [1, 2] on temperature variations of the accumulation rates for these complexes:

$$\sigma = \frac{\eta_E[\mathrm{O}]}{\eta_A[\mathrm{P}]}. \quad (23)$$

The results obtained from experimental data [1] (phosphorus concentration [P] = 4.2×10^{15} cm^{-3} and the position ε_F of the Fermi level ranging from E_c = –0.23 eV to E_c = –0.36 eV in the temperature range from 300 to 450 K) fit well the dependence $\sigma \sim \exp(0.16/kT)$ where energy is expressed in eV (the points and the dashed line in Fig. 1a). In this case, the above dependence can be obtained without taking into account the contribution of the electron subsystem of a crystal because the value $\Delta W^e_{VO} - \Delta W^e_{VP} = \varepsilon_E f^-_E + \varepsilon^+_P f^+_P - \varepsilon_A f^-_A$ depends weakly on the position of the Fermi level. However, the results obtained in [2] ([P] = 6×10^{13} cm^{-3}, the position of Fermi level ε ranges from E_c = –0.35 eV at T = 300 K to E_c = –0.47 eV at T = 405 K) cannot any longer be described by the above dependence (the dashed line in Fig. 1b), because f^-_E and σ appreciably change in this temperature range. The calculations made with consideration of Coulomb interaction of the reacting centers and of the contribution of electron subsystem of a crystal, yield, in both cases, a satisfactory agreement between the calculated and experimental data (shown by the solid lines in Figs. 1a and 1b).

In [9], the dependences of accumulation rates for the *E* and *A* centers on the concentration of donor impurity (phosphorus) under the γ-irradiation of *n*-Si were calculated. The value of σ is assumed to be constant and equal to 20 ± 5, i.e., both Coulomb interaction of reactants and the electron subsystem contribution were not taken into account. A good agreement between the calculated and experimental data was obtained. However, the calculated value of σ, which can be obtained from the experimental data with the aid of (23), actually includes the contribution of the charge states of reactants and the electron subsystem of a crystal. In our case, the dependences of η_E and η_A on the concentration of donor impurity were calculated with consideration for both Coulomb interaction and the contribution of the electron subsystem of a crystal; these dependences are consistent with the results published in [9]. In calculations, the difference between the energy barriers in the reactions of formation of the *E* and *A* centers is assumed to be equal to 0.59 ± 0.01 eV.

It is noteworthy that in the process of irradiation when the ionization of a crystal occurs under the beam, the charge states of the centers can, generally speaking, deviate from the equilibrium states if the excess concentration of electron–hole pairs Δn becomes comparable with the equilibrium electron concentration n_0. For typical current densities of a beam (~1 μA/cm^2) and the lifetime of electron–hole pairs under irradiation (~10^{-6} s), the value of Δn can be estimated to be ~10^{12} cm^{-3}; therefore, for the crystals with resistivity $\rho \le 60\ \Omega$ cm, the condition $\Delta n \ll n_0$ is fulfilled, and the effect of the ionization is negligible.

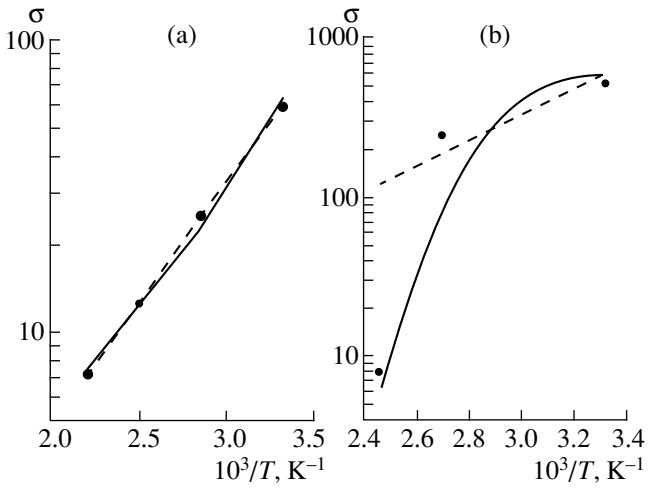

Fig. 1. Calculated and experimental values of σ as a function of the temperature of electron irradiation of *n*-Si. Solid lines represent the calculations made with the aid of (21); dashed lines correspond to the dependence $\sigma \sim \exp(0.16/kT)$ where energy is expressed in eV. The experimental data (shown by points) are taken (a) from [1] and (b) from [2] [(a) [P] = 4.2×10^{15} cm^{-3}, [O] = 8.7×10^{17} cm^{-3}, electron energy is 3.5 MeV; (b) [P] = 6×10^{13} cm^{-3}, [O] = 2×10^{16} cm^{-3}, electron energy is 2.2 MeV].

CONCLUSION

The proposed model of the participation of electron subsystem of a crystal in the reactions between the multicharged centers in semiconductors leads to results which are in satisfactory agreement with the experimental data on the accumulation of the *A* and *E* centers in the process of irradiation of silicon having the *n*-type conductivity. Thus, the electron subsystem of a crystal can be taken into account in calculations of reaction rates for the formation of complexes in semiconductors by modifying the energy barrier of the reaction in the manner described above.

ACKNOWLEDGMENTS

We are grateful to S.S. Shaĭmiev, A.I. Baranov, L.S. Smirnov, and L.N. Safronov for their helpful participation in discussions.

This work was supported by the Russian Foundation for Basic Research, project no. 96-15-97272.

REFERENCES

1. A. V. Vasil'ev, V. I. Panov, S. A. Smagulova, *et al.*, Fiz. Tekh. Poluprovodn. (Leningrad) **21**, 573 (1987) [Sov. Phys. Semicond. **21**, 352 (1987)].
2. L. S. Milevskiĭ and T. A. Pagava, Fiz. Tekh. Poluprovodn. (Leningrad) **10**, 1287 (1976) [Sov. Phys. Semicond. **10**, 763 (1976)].
3. V. I. Gubskaya, P. V. Kuchinskiĭ, and V. M. Lomako, Phys. Status Solidi A **85**, 585 (1984).
4. E. F. Uvarov and M. V. Chukichev, *Radiation Physics of Nonmetal Crystals* (Naukova Dumka, Kiev, 1989).
5. L. C. Kimerling, H. M. DeAngelis, and C. P. Garnes, Phys. Rev. B: Condens. Matter **3**, 427 (1971).
6. V. V. Mikhnovich, Doctoral Dissertation (Lytkarino, 1990).
7. A. I. Baranov, A. V. Vasil'ev, L. S. Smirnov, *et al.*, Fiz. Tekh. Poluprovodn. (Leningrad) **20**, 1132 (1986) [Sov. Phys. Semicond. **20**, 713 (1986)].
8. A. I. Baranov, A. V. Vasil'ev, V. F. Kuleshov, *et al.*, *Rate Constants for Reactions between the Multicharged Centers in Semiconductors*, Preprint (Chernogolovka, 1985).
9. A. S. Zubrilov and S. V. Koveshnikov, Fiz. Tekh. Poluprovodn. (Leningrad) **25**, 1332 (1991) [Sov. Phys. Semicond. **25**, 804 (1991)].

Translated by A. Zalesskiĭ

Semiconductors, Vol. 34, No. 2, 2000, pp. 171–173. Translated from Fizika i Tekhnika Poluprovodnikov, Vol. 34, No. 2, 2000, pp. 177–179.

ELECTRONIC AND OPTICAL PROPERTIES OF SEMICONDUCTORS

Control of the Excitation Conditions and the Parameters of Self-Sustained Oscillations of Current in Compensated Silicon Doped with Manganese

M. K. Bakhadyrkhanov, Kh. Azimkhuzhaev, N. F. Zikrillaev, A. B. Sabdullaev, and É. Arzikulov

Tashkent State University, Universitetskaya ul. 95, Vuzgorodok, Tashkent, 700095 Uzbekistan

Submitted May 25, 1999; accepted for publication August 18, 1999

Abstract—Silicon samples doped with boron and compensated by manganese were studied. The conditions for excitation of self-sustained oscillations were established and the parameters of these oscillations were determined. © *2000 MAIK "Nauka/Interperiodica".*

Self-sustained oscillations of current were detected and studied in many elementary semiconductors and semiconducting compounds [1–8]. Analysis of the results obtained has shown that, in the majority of cases, the dependences of excitation conditions and parameters of self-sustained oscillations of current on basic electrical parameters of the material under study were not determined. In addition, the influence of the concentration of electrically active impurities on the conditions for excitation and the basic parameters of self-sustained oscillations was not discussed in [1–8]. In turn, this not only hindered identification of the phenomenon's mechanism but also offered no possibility of using the self-sustained oscillations for the development and fabrication of solid-state oscillators having controlled parameters and other devices based on self-sustained oscillations. The objective of this work was to determine (i) the thermodynamic conditions for excitation of self-sustained oscillations and (ii) regular trends in the dependences of parameters of these oscillations on the concentration of electrically active, compensating impurity. One of the main prerequisites to excitation of self-sustained oscillations of current in semiconductors consists in the presence of a certain concentration of deep centers with anisotropic cross sections for trapping. Therefore, it is important to determine the range of concentrations (from N_{min} to N_{max}) and the states of deep-level impurities that correspond to excitation of regular and stable self-sustained oscillations of current.

For a starting material, we used the commercial *p*-type Si single crystals with a resistivity of ρ = 220, 100, 10, 4.5, 2, and 1 Ω cm, with the concentration of doping boron impurity varying within the range of $N_B = 1 \times 10^{14}$–2×10^{16} cm^{-3}. We chose manganese as a compensating impurity, motivated by the fact that the diffusion technology of doping Si with Mn was well developed [9], which made it possible to obtain the material with reproducible parameters. The diffusion of manganese into silicon was performed in such a way that, irrespective of the initial concentration of boron, compensated and overcompensated silicon was obtained with a resistivity of $\rho = 10^2$–10^5 Ω cm. As a result, we were able to select and study the compensated samples with the same geometrical dimensions and crystallographic orientation [111], and with the resistivity differing due to a different concentration of compensating impurity of manganese. The concentration of electrically active manganese in the samples varied in the range of $N_{Mn} = 1 \times 10^{14}$–$2 \times 10^{16}$ cm^{-3}.

The studies showed that, if the manganese concentration $N_{Mn} < 2 \times 10^{14}$ cm^{-3}, self-sustained oscillations of current were not observed, irrespective of the boron

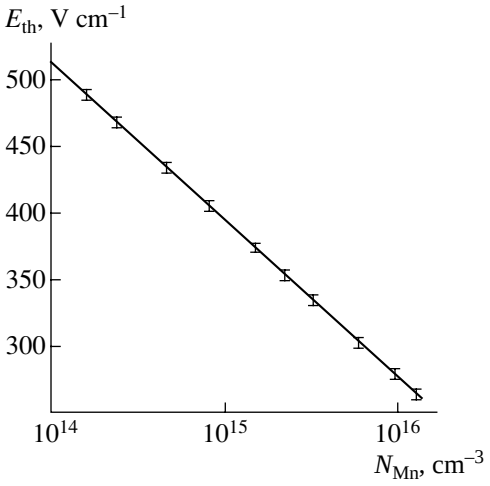

Fig. 1. Threshold field for excitation of self-sustained oscillations of current as a function of manganese concentration under identical conditions for the samples of Si:B,Mn with $\rho = 8 \times 10^4$ Ω cm.

1063-7826/00/3402-0171$20.00

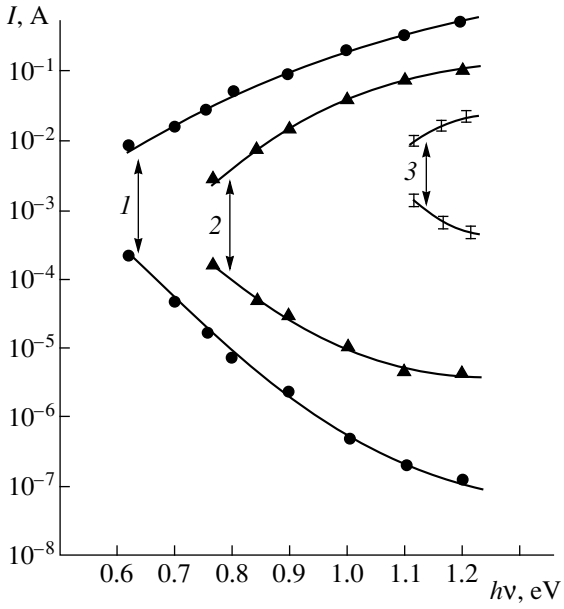

Fig. 2. Amplitude of self-sustained oscillations of current I (the maximal and minimal values of current are shown) as a function of the photon energy $h\nu$ in the Si:B,Mn samples under identical conditions. N_{Mn} = (*1*) 2×10^{16}, (*2*) 2×10^{15}, and (*3*) 2×10^{14} cm^{-3}.

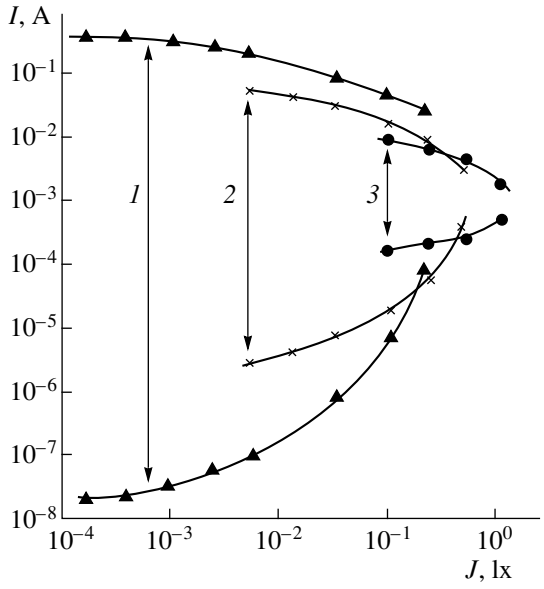

Fig. 3. Amplitude of self-sustained oscillations of current I (the maximal and minimal values of current are shown) as a function of the intensity of nonmonochromatic light J in Si:B,Mn samples with the concentration of manganese equal to (*1*) 2×10^{16}, (*2*) 2×10^{15}, and (*3*) 2×10^{14} cm^{-3}.

concentration and the resistivity of compensated Si:B,Mn samples. The largest value of Mn concentration $N_{Mn} = 2 \times 10^{16}$ cm^{-3} corresponds to the ultimate solubility of manganese in silicon. Thus, we determined the range of Mn concentrations for which the self-sustained oscillations of current were observed in Si:B,Mn samples; this range is given by $N_{Mn} = 2 \times 10^{14}$–$2 \times 10^{16}$ cm^{-3}. Figure 1 shows the dependence of the threshold strength of electric field E_{th} (the lowest value of the electric-field strength for which the stable and regular self-sustained oscillations are observed) on the manganese concentration. It is noteworthy that, in all cases, the experimental conditions, the resistivity of the samples, and their geometrical dimensions were identical ($\rho = 8 \times 10^4$ Ω cm and 4 mm × 8 mm × 1 mm). As evident from Fig. 1, the value of the threshold electric-field strength E_{th} decreases steadily as the Mn concentration increases. This concentration dependence can be described by the expression $E_{th} = E_0[1 + \alpha \ln(N_{Mn}/N^0_{Mn})]$, where E_0 is the threshold electric-field strength corresponding to the lowest Mn concentration $N^0_{Mn} = 2 \times 10^{-14}$ cm^{-3} for which the self-sustained oscillations are still observed, N_{Mn} is a given Mn concentration, and α is a coefficient (in the case under consideration, $\alpha = 8.5 \times 10^{-2}$). Such a dependence is also observed for the samples with different resistivity, which makes it possible to use the above expression for determining the value of the threshold electric-field strength as a function of Mn concentration. Thus, as Mn concentration increases from 2×10^{14} to 2×10^{16} cm^{-3}, the value of E_{th} decreases by more than two times; i.e., as the manganese concentration increases, it is possible to excite the self-sustained oscillations by lower electric fields.

The results of studying the spectral range of existence of self-sustained oscillations of current in compensated Si in relation to the concentration of compensating Mn impurity are shown in Fig. 2. In all cases, the electric field, resistivity of the samples, and the power of monochromatic incident radiation were the same. As evident from Fig. 2, as Mn concentration increases, the spectral range of excitation of self-sustained oscillations of current becomes appreciably wider. In the Si:B,Mn samples with the highest concentration of manganese (2×10^{16} cm^{-3}), the self-sustained oscillations of current are excited for $h\nu = 0.62$ eV, whereas the samples with identical resistivity and Mn concentration of $N_{Mn} = 2 \times 10^{14}$ cm^{-3} have to be exposed to radiation with photon energies of $h\nu \geq 1.1$ eV for the self-sustained oscillations to be observed. It is also noteworthy that, as Mn concentration increases, the amplitudes of self-sustained oscillations of current increase substantially (Fig. 2, curve *1*) and also increase with an increase in the photon energy of monochromatic radiation. As distinct from other materials, in boron-doped silicon compensated with manganese, regular and stable self-oscillations of current are observed under illumination not only with monochromatic light but also with background nonmonochromatic light. Therefore, it is of interest to determine the

range of intensities of nonmonochromatic light such that self-sustained oscillations of current are observed. In this case, the samples that had identical resistivities and various concentrations of compensating manganese and were obtained from the starting *p*-Si ingots with resistivities $\rho = 100$, 10, 4.5, 2, and 1 Ω cm were also studied. The studies showed (Fig. 3) that, as the manganese concentration increases, the range of intensities of nonmonochromatic illumination corresponding to the existence of self-sustained oscillations of current widens substantially. As the manganese concentration increases, the self-sustained oscillations of current are observed under lower intensity of nonmonochromatic illumination, and the amplitude of self-sustained oscillations of current increases. In all cases, the frequency range of self-sustained oscillations extends to lower frequencies as the manganese concentration increases.

According to the results obtained, the temperature range of the existence of self-oscillations of current is almost independent of manganese concentration; i.e., in all cases, the self-oscillations are observed in the temperature range of $T = 77$–180 K.

Thus, we determined the basic thermodynamic conditions for excitation of regular and stable self-oscillations of current in boron-doped Si compensated with Mn in relation to the concentration of compensating Mn impurity. This makes it possible to obtain Mn-doped Si crystals that have the required parameters and are based on the starting Si with various characteristics and to develop solid-state oscillators based on these crystals.

REFERENCES

1. B. V. Kornilov and A. V. Anfimov, Fiz. Tverd. Tela (Leningrad) **8**, 3420 (1966).
2. S. B. Bumyalene and Yu. K. Pozhela, Fiz. Tekh. Poluprovodn. (Leningrad) **20**, 1327 (1986) [Sov. Phys. Semicond. **20**, 836 (1986)].
3. A. Sh. Abdinov and V. K. Mamedov, Fiz. Tekh. Poluprovodn. (Leningrad) **14**, 754 (1980) [Sov. Phys. Semicond. **14**, 442 (1980)].
4. V. V. Antonov and L. I. Kats, Fiz. Tekh. Poluprovodn. (Leningrad) **16**, 1050 (1982) [Sov. Phys. Semicond. **16**, 672 (1982)].
5. Sh. I. Askarov, M. K. Bakhadyrkhanov, N. F. Zikrillaev, *et al.*, Fiz. Tekh. Poluprovodn. (Leningrad) **20**, 781 (1986) [Sov. Phys. Semicond. **20**, 268 (1986)].
6. Yu. I. Zavadskiĭ and B. V. Karnilov, Fiz. Tekh. Poluprovodn. (Leningrad) **4**, 2115 (1970) [Sov. Phys. Semicond. **4**, 1815 (1970)].
7. M. K. Bakhadyrkhanov, N. F. Zikrillaev, A. A. Tursunov, *et al.*, Dokl. Akad. Nauk UzSSR, No. 5, 26 (1985).
8. S. P. Kal'venas and A. A. Puchinskas, Fiz. Tekh. Poluprovodn. (Leningrad) **13**, 1752 (1979) [Sov. Phys. Semicond. **13**, 1019 (1979)].
9. N. F. Zikrillaev, Candidate's Dissertation (Tashkent, 1989).

Translated by A. Spitsyn

Semiconductors, Vol. 34, No. 2, 2000, pp. 174–180. Translated from Fizika i Tekhnika Poluprovodnikov, Vol. 34, No. 2, 2000, pp. 180–185.

SEMICONDUCTORS STRUCTURES, INTERFACES, AND SURFACES

Reconstruction Transition $(4 \times 2) \longrightarrow (2 \times 4)$ on the (001) Surfaces of InAs and GaAs

Yu. G. Galitsyn, S. P. Moshchenko, and A. S. Suranov

Institute of Semiconductor Physics, Siberian Division, Russian Academy of Sciences, 630090 Novosibirsk, Russia

e-mail: sergem@isp.nsc.ru

Submitted September 15, 1998; accepted for publication March 19, 1999

Abstract—Phase transitions involving various atomic configurations on the (001) surfaces of GaAs and InAs were studied by RHEED. A kinetic scheme of the interaction between the As_4 flow and the surface is proposed and the main equations describing the transitions are modified so as to correspond to the As_4 (rather than As_2) flux. A model of the $(4 \times 2) \longrightarrow (2 \times 4)$ transition is suggested for reconstruction of a layer of metal atoms with subsequent stabilization by the adsorption of arsenic atoms. A considerable difference of the surface transitions in GaAs from that in InAs consists in greater force constants (more rigid bonds) in the former case. A significant role in the continuous evolution from $(2 \times 4)\beta$ to (4×2) phase in GaAs belongs to metastable disordered phases.

INTRODUCTION

Various reconstructions on the polar (001) surfaces of GaAs and InAs were studied in much detail by the methods of reflection high-energy electron diffraction (RHEED) and scanning tunneling microscopy (STM). An exhaustive review of data on the GaAs(001) surface reconstruction was recently published in [1].

As the composition of the GaAs(001) surface deviates from stoichiometry (varying from As-rich to Ga-rich), the surface exhibits a broad spectrum of reconstructions: $c(4 \times 4) \longrightarrow (2 \times 4)\gamma \longrightarrow (2 \times 4)\beta \longrightarrow (2 \times 4)\alpha \longrightarrow (2 \times 6) \longrightarrow (3 \times 1) \longrightarrow (4 \times 2)\beta \longrightarrow (4 \times 6)_{cl} \longrightarrow (4 \times 8)$. At the same time, the (001) surface of InAs exhibits, in sharp contrast with the pattern in GaAs, only two reconstructions leading to the As-stabilized $(2 \times 4)\beta$ and In-stabilized $(4 \times 2)\beta$! structures. Evidently, the $(2 \times 4)\beta \longrightarrow (4 \times 2)\beta$ phase transition passes via two intermediate reconstructions, $(2 \times 4)\alpha \longrightarrow (2 \times 6) \longrightarrow (3 \times 1)$, while the same transition in InAs proceeds directly.

The most studied reconstructions on the GaAs(001) surface are those leading to the As-stabilized $(2 \times 4)\beta$ and the Ga-stabilized $(4 \times 2)\beta$ structures [1]. These surface phases possess absolutely identical morphologies. For example, the (2×4) phase terrace comprises periodically arranged trapezoidal grooves with a depth of ~3 Å and a bottom and top base width of 8 and 12 Å, respectively. The length of grooves in the $[\bar{1}10]$ direction typically amounts to ~1000 Å. The uppermost layer of the terrace is composed of As atoms arranged with a degree of coverage $\Theta_{As} = 0.5$. The second layer of the (2×4) phase is composed of Ga atoms with $\Theta_{Ga} = 0.75$. The third layer is completely filed with As atoms. The (4×2) reconstructed surface is topologically analogous, but the grooves are oriented in the [110] direction (orthogonal to $[\bar{1}10]$) and the uppermost layer is composed of Ga. The orientation of grooves in these structures is determined by the direction of dimerization of atoms in the uppermost layer, involving the formation of arsenic and gallium dimers in the (2×4) and (4×2) phases, respectively.

This "one-dimensional" character of reconstructed superstructures on the polar (001) face is related, first, to a decrease in the number of dangling bonds at the expense of dimers formed in the uppermost surface layer, on the one hand and, second, to a relaxation process involving the electron density transfer from gallium to arsenic. This charge transfer leads to the displacement of atoms and the formation of dimeric vacancies in the uppermost surface layer. For a surface atom of Ga, the hybridization type is close to p^0sp^2 (rather than to the usual sp^3), and for an As atom, to s^2p^3. The $(4 \times 2)\beta$ and $(2 \times 4)\beta$ structures satisfy the electron-count model of Chadi and Pashley [2, 3]. In the unit cells of GaAs and InAs, the dangling bonds of anion are filled with electrons, while the dangling bonds of cation remain uncompensated.

Despite the detailed knowledge of the surface structure of GaAs and InAs, neither the characters nor the microscopic patterns of phase transitions between reconstructed surface states in these semiconductors (unlike similar transitions in Si and Ge) have been given sufficient attention by researchers. The purpose of our work was to study the phase transitions from Ga(In)-stabilized (4×2) to As-stabilized (2×4) reconstructed surfaces in GaAs and InAs. Special attention was paid to the topological features of these transitions.

It is necessary to make several remarks concerning the types of structural transitions on the surface. The

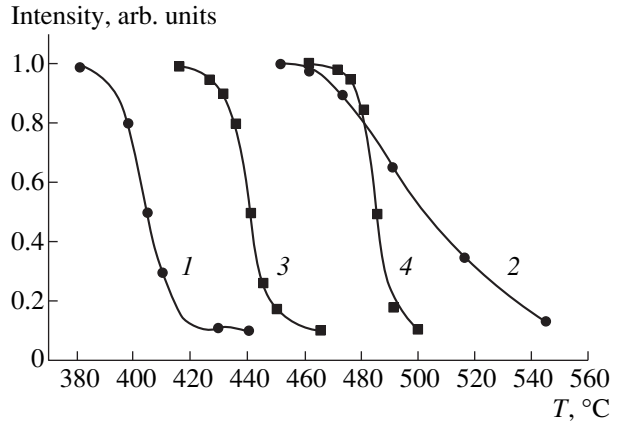

Fig. 1. Plots of the mirror reflection intensity versus temperature for various As_4 pressures in the gas phase: (*1*) InAs, $P = 3 \times 10^{-8}$ torr (this work); (*2*) GaAs, $P = 3 \times 10^{-8}$ torr (this work); (*3*) InAs, $P = 10^{-6}$ torr [8]; (*4*) InAs, $P = 7.8 \times 10^{-6}$ torr [8].

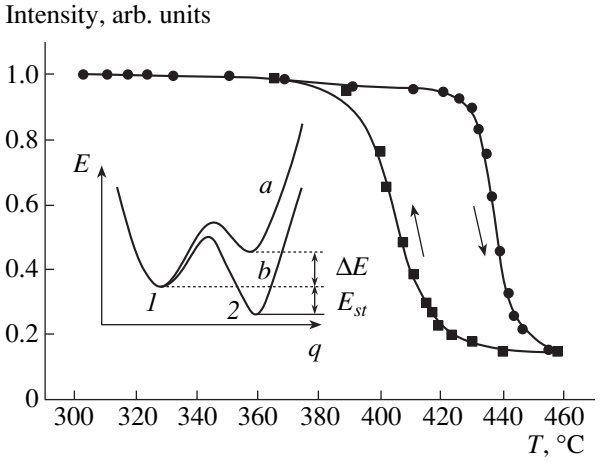

Fig. 2. Plots of the (0, 1/4) partial reflection intensity versus temperature for InAs. Insert: the plot of potential energy of an In(Ga) atom versus displacement q in the unit cell of a $(4 \times 2)\beta$ phase for (a) a clean (4×2) phase surface and (b) the same (4×2) phase surface upon As_2 chemisorption. *1* and *2* are special positions of Ga(In) atoms.

problem is not as simple as it might seem. For example, the phase transition $(7 \times 7) \longrightarrow (1 \times 1)$ on the Si(111) surface was determined by Zangwill [4] as the first-order transition, while Monch [5] described this transition as continuous; that is, as the second-order transition. It should be recalled that continuous phase transitions are characterized by smooth variation of the long-range order parameter and, hence, no phase coexistence can be observed during this transformation. On the contrary, the first-order transitions feature a coexistence of two phases, whereby a new phase nucleates and grows from the initial phase, and the order parameter exhibits a jumplike change. Direct STM observations confirmed simultaneous existence of the domains of both Ga(In)-stabilized and As-stabilized phases in semiconductors under consideration [6, 7]. Therefore, there is sufficient ground to believe that the $(4 \times 2) \longrightarrow (2 \times 4)$ transitions in GaAs and InAs are surface phase transitions of the first order.

The ordering of particles on the surface is usually studied by the electron diffraction techniques. Intensity of the partial reflections must be proportional to the square of the long-range order parameter. In principle, the method of electron diffraction allows a relationship between the order parameter and the reflection intensity to be correctly established. However, the reflected beam intensity depends in a complicated manner on the domain size and its distribution in a sample. In addition, the electron diffraction patterns always contain a background. Finally, the distribution of the diffracted beam intensities is affected by the inhomogeneity of the sample. All these factors complicate exact determination of the order parameter as a function of the temperature (necessary to determine the order of the transition) using only experimental data on the diffraction beam intensity variation. These diffraction measurements reliably reveal smooth variations over a temperature range a few tens of degrees wide or sharp changes in the refection intensity within a narrow (5–10°C wide) temperature interval. Thus, the smooth intensity variations can be interpreted as continuous phase transformations and the sharp changes, as discontinuous transitions. This very approach was used to determine the $(4 \times 2) \longrightarrow (2 \times 4)$ phase transition on the (001) surfaces of GaAs and InAs. Yamaguchi *et al.* [8] related sharp changes of the mirror reflection intensity observed in the RHEED pattern from InAs ($\Delta T < 10$°C) and smooth variations observed for GaAs ($\Delta T \approx 30$°C) to the surface phase transitions of the first and second order, respectively.

EXPERIMENTAL

Experiments on the experimental determination of phase transitions were performed in a Riber commercial molecular beam epitaxy (MBE) system. The samples had singular faces of the type $(001) \pm 0.2°$ with an area of 3×3 mm^2. The RHEED patterns were registered either using either a phosphorescent screen or a Photon-Micro video system. The primary electron beam energy was 10 keV. The sample temperature was varied within the range 450–600°C for GaAs and 350–500°C for InAs. The As_4 pressure was varied from 2×10^{-8} to 2×10^{-6} torr. Chemical pretreatment of the samples prior to placing them into the working chamber was described in detail elsewhere [9]. The reconstruction transitions were studied on the surface of 0.5-μm-thick buffer layers grown by MBE. The opti-

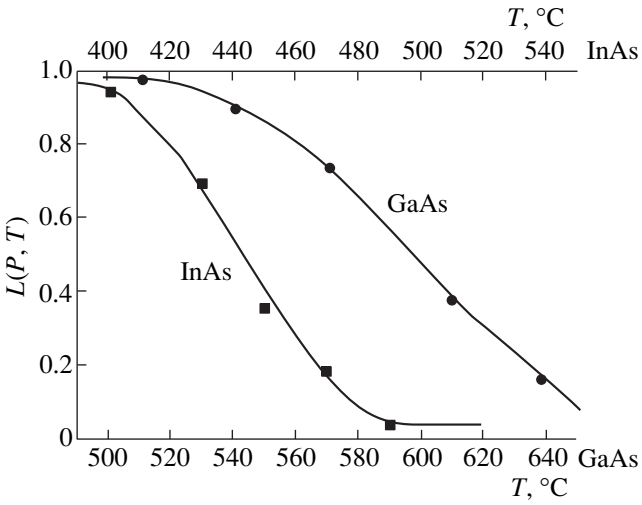

Fig. 3. The plots of $L(P, T)$ versus temperature for InAs (top scale) and GaAs (bottom scale) at $k_1P = 10^{-1}$ ($P = 10^{-7}$ Torr).

mum MBE growth conditions were selected in preliminary experiments so as to provide for the smooth surfaces with a $(2 \times 4)\beta$ structure.

RESULTS

Figure 1 shows variation of the mirror reflection intensity (MRI) in the RHEED pattern with the temperature during the $(4 \times 2) \longrightarrow (2 \times 4)$ phase transition on the (001) surfaces of GaAs and InAs. The rate of temperature variation was 3°C/min. The MRI change is actually related directly to the $(4 \times 2) \longrightarrow (2 \times 4)$ phase transition. Indeed, the character of intensity variation of the partial (0, 1/4) reflection of the (2×4) phase during the phase transition was generally the same as that observed for the mirror reflection.

Figure 2 shows variation of the same reflection in the RHEED pattern of InAs. First, note that the MRI changes are sharper in InAs than in GaAs, as was also pointed out in [8]. Second, the transition in InAs exhibits a hysteresis that is virtually absent in GaAs. As the As_4 pressure increases, the phase transition shifts toward higher temperatures. The effective transition activation energy determined from the Arrhenius plot of the pressure versus the inverse transition temperature for InAs is 2.5–3 eV.

EXISTING MODEL

Yamaguchi *et al.* [8] proposed a model describing the $(4 \times 2) \longrightarrow (2 \times 4)$ phase transition on the (001) surfaces of GaAs and InAs in the flow of As_4. As mentioned above, it was pointed out that the phase transition from Ga(In)-stabilized to As-stabilized surface is sharper in InAs than in GaAs. It was suggested that the transition is caused by the lateral interactions assumed to have the character of attraction between the nearest-neighbor As_2 dimers in the (2×4) phase and between the $Ga_2(In_2)$ dimers in the (4×2) phase. This assumption allowed some of the experimental features to be explained, including the transition hysteresis observed in InAs and absent in GaAs and sharper transition-induced changes in InAs than in GaAs. The main difference between InAs and GaAs, as pointed out in [8], consists in stronger lateral interaction between the surface As_2 dimers in the former semiconductor than in the latter. The transition appears continuous if the interaction energy is smaller than 0.12 eV; otherwise, it is the first-order transition. According to estimates of the lateral interaction energy obtained in [7], this parameter is 0.15 eV for InAs and 0.11 eV for GaAs.

However, a statistical analysis of the phase transition was based on an incorrect, in our opinion, assumption that the chemical potential of arsenic dimers on the surface is equal to that of arsenic tetramers in the gas phase. The fact is that the conversion reaction $As_4 \longrightarrow As_2$ is irreversible. Therefore, it would be more correct to speak of the adsorption–reaction equilibrium of arsenic in the gas phase and on the surface and interpret the results within the framework of a certain kinetic scheme of interaction between As_4 and the surface. In addition, there is some doubt as to whether the interaction between arsenic dimers can have the character of attraction. Indeed, molecules chemisorbed from the gas phase usually exhibit repulsion on the surface, as indicated by experimental data on the thermodesorption of arsenic from the (001) surfaces of both InAs and GaAs [10]. It should be noted that Yamaguchi *et al.* [8] proposed no microscopic mechanism of the phase transition and did not consider the role of intermediate structures (3×1) and (2×6) in GaAs. Finally, only the uppermost surface atomic plane was considered in [8], while it known that the surface phase transitions involve at least two atomic planes.

DISCUSSION OF RESULTS

Since the surface reconstruction transitions in the system studied are considered as proceeding in the flow of As_4, let us first analyze the reaction of $As_4 \longrightarrow As_2$ conversion. As previously and convincingly demonstrated in our works [11–14] and other works [15, 16], the dissociative chemisorption of As_4 involves pairwise interaction between two As_4^* molecules occurring on the surface in a preadsorbed (precursor) state. Desorption of the As_4 species from the precursor state is described by the rate constant $k_2 = k_2^0 \exp(-E_2/kT) = 0.625 \times 10^8 \exp(-0.4\ \text{eV}/kT)\ \text{s}^{-1}$ [16]. Within the framework of a simple reaction scheme, the interaction of As_4

with a substrate surface involves the following elementary reactions:

$$As_4^{gas} \longleftrightarrow As_4^* \Big| \frac{k_1}{k_2},$$

$$2As_4^* \longrightarrow 2As_2^{chem} + As_4^{gas} \Big| k_3,$$

$$As_2^{chem} \longrightarrow As_2^{gas} \Big| k_5.$$

If the substrate surface contains Ga atoms, the epitaxial growth is described by the reaction

$$2Ga + As_2^{chem} \longrightarrow 2GaAs | k_4.$$

We believe that As_2^{chem} can be considered as a unit determining structure of the uppermost layer of the (2×4) phase. In the approximation of a stationary state with respect to the intermediate products (As_2^{chem}, As_4^*), the degree of the substrate surface filling by arsenic atoms Θ_{As} is described by the equation

$$\Theta_{As} = \frac{k_1 P/k_5}{1 + k_1 P/k_5} \frac{1}{y} \left(\sqrt{1+y} - 1\right)^2 = L(P)F(y), \quad (1)$$

where

$$y = \frac{4k_1 k_3 P}{(k_1 P + k_2)^2} \left(1 + \frac{k_1 P}{k_4 + k_5}\right).$$

The function $F(y) \approx 1$ approaches unity when $y \longrightarrow \infty$ and $F(y) \ll 1$ for $y \longrightarrow 0$. The physical meaning of this function is to reflect a difference between the direct adsorption–desorption equilibrium of a substrate surface with As_2 in the gas phase (whereby As_2^{chem} particles are formed without an intermediate stage of cracking) and the adsorption–desorption equilibrium of the same surface with As_4 in the gas phase. Because the cracking reaction is a nonlinear process, the gas phases of As_2 and As_4 exhibit different properties already at a relatively small partial pressure P of arsenic. Under these conditions, the desorption flux of As_4^* from the surface is large as compared to the flux of the cracking products and, hence, $F(y) \ll 1$. This is illustrated by a significant difference between the coefficients of As_4 and As_2 built-in into the lattice sites in the course of the homoepitaxial process on GaAs(001): at $T = 595$°C, the coefficient for As_4 is 3–4 times smaller than that for As_2 even at $P = 10^{-6}$ torr [17].

A quasi-Langmuir isotherm $L(P)$ differs from the usual curve by reflecting the fact that As_4 particles are adsorbed, while As_2 species are desorbed. Figure 3 shows the $L(P, T)$ curves for InAs and GaAs at $P = 10^{-7}$ torr constructed using the constant k_5 taken from [10]. As seen from this figure, indium arsenide is characterized by sharper variations in qualitative agreement with experiment (Figs. 1 and 2). Taking into account

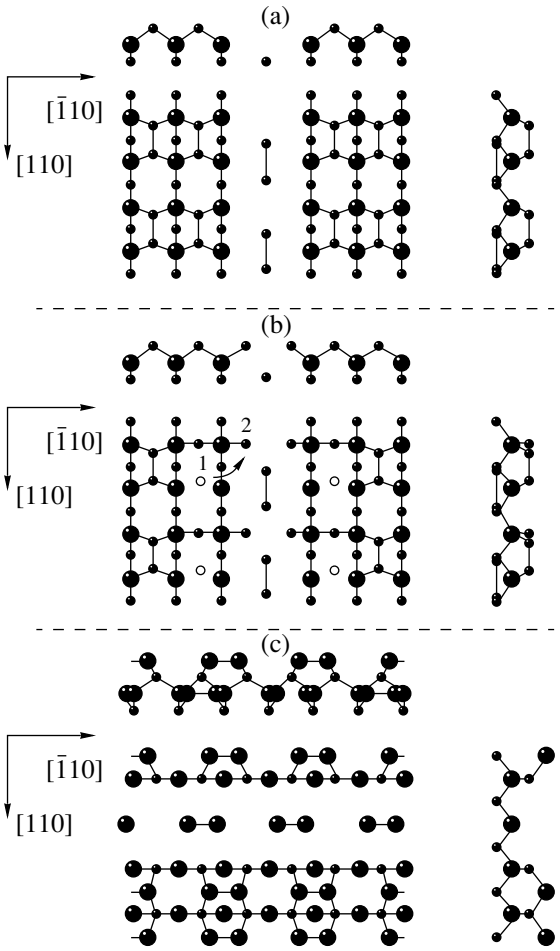

Fig. 4. Schematic diagrams illustrating the $(4 \times 2)\beta \longrightarrow (2 \times 4)\beta$ reconstruction involving In(Ga) atoms (small black balls) and As atoms (big balls): (a) initial $(4 \times 2)\beta$ phase; (b) intermediate reconstruction with arrows indicating the transfer of Ga(In) atoms from position *1* to *2*; (c) final $(2 \times 4)\beta$ phase. Note that the groove direction changes from [110] to [$\bar{1}$10].

the behavior of $F(y)$, we may, in principle, readily fit the temperature dependence in equation (1) to the experimental curves. However, as pointed out above, the measured diffracted beam intensity depends not only on Θ_{As}. Moreover, equation (1) does not contain terms accounting for a phase transition as such, representing essentially a usual monotonic variation of the degree of coverage as a function of the pressure and temperature. According to equation (1), no metastable or unstable regions exist in the phase diagram and, hence, the experimentally observed hysteresis (Fig. 2) cannot be explained. Thus, in contrast to the adsorption–desorption equilibrium of a substrate surface with As_2 in the gas phase, an adequate approximation for the system under consideration (featuring the adsorption–desorption equilibrium of the surface with As_4) is obtained by replacing the Θ_{As} value in the model equations describ-

ing the phase transition (see below) by the product $L(P)F(y)$.

PHASE TRANSITION MODEL

The $(4 \times 2)\beta$ phase on the GaAs surface contains a 0.5 monolayer (ML) of Ga atoms in the uppermost surface layer and a 0.75 ML of As atoms in the second layer, while the $(2 \times 4)\beta$ phase on the same surface contains a 0.5 ML of As atoms and a 0.75 ML of Ga atoms in the uppermost and second layers, respectively. Therefore, for the phase transition to take place, it is necessary for the surface to adsorb a 0.75 and 0.25 ML of As and Ga atoms, respectively. Of these, a 0.25 ML of As atoms is required for completion of the second layer of the $(4 \times 2)\beta$ phase, coinciding with a third layer of the $(2 \times 4)\beta$ phase, and a 0.5 ML of As atoms forms the uppermost layer of the new phase. Gallium atoms can be supplied from Ga clusters on the surface or appear upon "dissolution" of the (4×2) domains under the action of the As_4 adsorbate flow.

It is necessary to note the following important circumstance. When Ga atoms are supplied to a given unit cell from an "external" source, they occupy lattice sites of the (2×4) cell. However, this process is insufficient for the complete formation of a (2×4) phase domain. On the one hand, some lattice sites occupied by Ga atoms in the $(4 \times 2)\beta$ lattice will be vacant in the $(2 \times 4)\beta$ phase. On the other hand, all vacant sites in the $(4 \times 2)\beta$ phase must be occupied by Ga atoms in the $(2 \times 4)\beta$ lattice. Thus, a reaction transferring two Ga atoms per unit cell from one to another position is needed. Note that one transfer reaction is sufficient to satisfy both requirements formulated above. Figure 4 shows a schematic diagram illustrating this transfer reaction. After the transfer, the configuration of gallium atoms would become stable only upon the chemisorption of As_2, that is, the formation of an arsenic dimer on the surface. A change in the potential energy of the system after the transfer of two Ga atoms is shown in the inset on Fig. 2. The reverse transition of gallium atoms from position *2* to *1* is initiated by the desorption of As_2 from the surface. In fact, we observed an arsenic-adsorption-induced phase transition from (4×2) to (1×4) in a layer of gallium atoms. A similar phase transition induced by the adsorption of molecules from the Ga phase was described in [18]. The transfer of gallium atoms from position *1* to *2* involves the consumption of an energy ΔE. The free energy of a system comprising the adsorbed layer of arsenic atoms and the uppermost layer of gallium atoms is expressed within the framework of a usual statistical approach:

$$F_1 = \Delta E\Theta_{Ga} + kT[\Theta_{Ga}\ln\Theta_{Ga} + (1-\Theta_{Ga})\ln(1-\Theta_{Ga})] - E_c\Theta_{Ga}\Theta_{As}, \quad (2)$$

$$F_2 = -E_a\Theta_{As} + kT[\Theta_{As}\ln\Theta_{Ga} + (1-\Theta_{As})\ln(1-\Theta_{As})], \quad (3)$$

where E_c is the energy of stabililization in position *2* upon the adsorption of arsenic dimers and Θ_{Ga} is the fraction of gallium atoms transferred from position *2* to *1*. The chemical potential of adsorbed arsenic dimers is determined by the formula

$$\mu = \frac{d(F_1 + F_2)}{d\Theta_{As}} = -E_a + kT\ln\left(\left(\frac{\Theta_{As}}{(1-\Theta_{As})}\right) - E_c\Theta_{Ga}\right), \quad (4)$$

where the sum $F_1 + F_2$ should be minimized with respect to Θ_{Ga}. This implies that $d(F_1 + F_2)/d\Theta_{Ga} = 0$, and

$$\Delta E + kT\ln(\Theta_{Ga}/(1-\Theta_{Ga})) - E_c\Theta_{As} = 0. \quad (5)$$

Combining expressions (4) and (5), we arrive at

$$\exp(\mu + E_a)/kT = \Theta_{As}/(1-\Theta_{As}) \times \exp\{-E_c/kT(1 + \exp[(\Delta E - E_c\Theta_{As})/kT])\}. \quad (6)$$

Taking into account that $\mu_{gas} = kT\ln P/P_0$, we obtain

$$P = P_0\exp(-E_a/kT)\Theta_{As}/(1-\Theta_{As}) \times \exp\{-E_c/kT(1 + \exp[(\Delta E - E_c\Theta_{As})/kT])\}. \quad (7)$$

Equations (6) and (7) determine the phase diagram of the $(4 \times 2) \longrightarrow (2 \times 4)$ transition. If P denotes the As_4 pressure, we must perform the change $\Theta_{As} \longrightarrow L(P)F(y)$. At $T < T_c$, the system exhibits phase separation on the surface. In the temperature range 400–600°C (corresponding to the phase transitions in InAs), the ΔE and E_c values fall within the intervals 0.1–0.3 and 0.3–0.5 eV, respectively [18, 19]. In contrast to the model proposed in [8], where a physical driving force of the transition is the lateral attraction between chemisorbed arsenic dimers, in our model, the transition is caused by the interaction between arsenic and gallium atoms leading to a decrease in energy of the (1×4) layer of Ga atoms. In addition, equations (6) and (7) may take into account the repulsion between arsenic dimers on the surface. However, an allowance for this interaction does not lead to any significant change in the character of the phase transition for the usual lateral repulsion interaction energies (0.1–0.2 eV) [19].

The phase transition described above is more typical of InAs than of the GaAs surface. The phase transition in GaAs involves the formation of intermediate structures (3×1), (2×6), and $(2 \times 4)\alpha$. The (3×1) phase was not observed by STM but revealed in the RHEED patterns, while the formation of the (2×6) phase is well manifested in both RHEED and STM patterns [1]. Why does the transition proceeds directly in InAs and involve a number of intermediate phases in GaAs? One reason is a significant difference in elastic force constants for these two crystals. The interatomic bonds in GaAs are more rigid and the corresponding force constants exceed the values for InAs by 30–40%. It should

be also recalled that the temperature of the onset of intensive incongruent decomposition is 650°C for GaAs(001) crystals and 520°C for InAs.

There is a profound analogy between the phase transitions in the systems studied and the $(2 \times 1) \longrightarrow (7 \times 7)$ and $(2 \times 1) \longrightarrow c(2 \times 8)$ transitions in Si(111) and Ge(111), where the atomic force constants are significantly different as well. In Si crystals possessing more rigid bonds, the transition proceeds via an intermediate (5×5) configuration and the intensity of diffraction reflections varies continuously in the temperature rage from 250 to 500°C [5]. In the Ge crystals, there is a sharp transition in the region of 100°C. Then, a $(7 \times 7) \longrightarrow (1 \times 1)$ transition in Si takes place within a $\Delta T \sim 100$°C interval near 1120°C, while the $(2 \times 8) \longrightarrow (1 \times 1)$ transition in Ge occurs within $\Delta T \sim 3$°C at 300°C. The $(7 \times 7) \longrightarrow (1 \times 1)$ transition in silicon is related to the vanishing of defects such as the stacking faults, dimers, and corner holes, which requires considerable reorganization of the initial (7×7) unit cell. In contrast, the $(2 \times 8) \longrightarrow (1 \times 1)$ transition in germanium is determined only by a correlated diffusion of Ge atoms along the [110] direction [5, 20]. In silicon, no transitions with lattice distortions similar to those in germanium are impossible because of a considerable elastic interaction energy [5].

Thus, an energy barrier for the direct $(4 \times 2)\beta \longrightarrow (2 \times 4)\beta$ transition on the (001) surface of GaAs cannot be surmounted and the process passes via an intermediate reconstruction (3×1) and (2×6) requiring lower energy. If the second layer of arsenic atoms in the $(4 \times 2)\beta$ phase is completed as a result of adsorption, the subsequent transition to the (2×6) phase would require the adsorption of a 2/6 ML of As atoms and the supply of a 2/6 ML of Ga atoms from an external source. Thus, two (2×4) cells are formed from tree (4×2) cells. An analysis shows that only one gallium per (2×6) unit cell must be transferred in this system. Although this transfer would require much smaller energy as compared to the direct transition to $(2 \times 4)\beta$, the corresponding transition nevertheless involves an intermediate phase (3×1).

Initially, the adsorption of As atoms in a groove of the $(4 \times 2)\beta$ phase induces a diffusion flux of a 1/6 ML of Ga atoms to a given cell. Then the degree of coverage for the uppermost gallium layer would reach 2/3, which implies that two (of the total of three) dimers and one dimeric vacancy are present. The RHEED pattern exhibits a partial (0, 1/3) reflection of the (3×1) phase. The (3×1) phase is unstable and does not satisfy the electron-count model because two (3×1) cells would require 12 electrons of which only 11 are available (the deep state of arsenic remains unoccupied). When a new 1/6 ML portion of Ga atoms is added to the (3×1) phase and a 2/6 ML of As atoms is adsorbed, the (2×6) phase appears. This phase (albeit also not satisfying the electron-count model) is more stable since a regular arrangement of dimeric gallium and arsenic chains gives rise to minimum elastic stresses [1]. Note also that the degree of filling in the second layer of Ga atoms (5/6) in the (2×6) phase is greater as compared to that (0.75) in the stable $(2 \times 4)\beta$ phase. Therefore, the subsequent $(2 \times 6) \longrightarrow (2 \times 4)\beta$ phase transition proceeds via the $(2 \times 4)\alpha$ phase with a completed second layer of Ga atoms. The $(2 \times 4)\beta$ phase is obtained from (2×6) upon addition of the next 1/6 ML portion of Ga and As atoms.

There is one important point to be noted. The sequence of phase transformations in GaAs considered above represents the elementary events of Ga an As atoms building into the lattice sites. On the whole, the $(4 \times 2)\alpha \longrightarrow (2 \times 4)\alpha$ transition is equivalent to the epitaxial growth of a 0.5 monolayer on the (001) surface of GaAs. Adsorption of a certain amount of As atoms on the surface induces a diffusion flux delivering an equivalent amount of Ga atoms It is the sufficiently high stability of the half-filled uppermost surface layer of Ga atoms that allows the sequential phase reconstruction of the surface to proceed until its epitaxial completion to the monolayer. Apparently, the reverse process of arsenic desorption from the surface is accompanied by degradation of the lattice in the remaining gallium layer. As a result, Ga atoms not only enter into in the Ga-stabilized phase, but induce some kinds of disorder on the surface. At present, these nonregular disordered G-stabilized phases are extensively investigated by STM and RHEED [1, 6, 7, 21]. Reconstructions of the (001) surface of GaAs are essentially phase transitions of the order–disorder type.

A quite different process takes place in InAs. Here, the uppermost surface layer of In atoms in the $(2 \times 4)\alpha$ phase becomes unstable upon the adsorption of arsenic. The subsequent redistribution of In atoms between lattice sites in this layer leads to a new stable structure. This corresponds to a usual structural phase transition. Upon a partial desorption of arsenic, indium does not form disordered phases. Rather, weak binding of the uppermost layer of In atoms in the In-stabilized $(4 \times 2)\alpha$ surface phase leads to the formation of inert indium clusters and a stable $(2 \times 4)\beta$ phase. It is this difference in the mechanism of phase transition that principally distinguishes indium arsenide from gallium arsenide.

Thus, we have studied in much detail the phase transitions between various configurations on the (001) surfaces of GaAs and InAs. A kinetic scheme modeling the interaction of As_4 with these surfaces is proposed and modification of the main equations in the system describing the phase transition is suggested if the transformation takes place under the action of an As_4 (rather than As_2) adsorption flux. A model of the $(4 \times 2) \longrightarrow (2 \times 4)$ transition, representing reconstruction in a layer of metal atoms stabilized by the subsequent adsorption of arsenic, is developed. A significant difference between the surface phase transitions in GaAs and InAs

is related to more rigid lateral atomic interactions and greater atomic force constants in the former case.

REFERENCES

1. Q. Xue, T. Hashizume, A. Ichimiya, *et al.*, Sci. Rep. RITU A **44**, 113 (1997).
2. D. J. Chadi, J. Vac. Sci. Technol. A **5**, 834 (1987).
3. M. D. Pashley, Phys. Rev. B: Condens. Matter **40**, 10481 (1989).
4. A. Zangwill, *Physics at Surfaces* (Cambridge University Press, Cambridge, 1988).
5. W. Monch, *Semiconductor Surfaces and Interfaces* (Springer, Berlin, 1993), p. 336.
6. J. Behrend, M. Wassermeier, L. Daweritz, and K. H. Ploog, Surf. Sci. **342**, 63 (1995).
7. J. Behrend, M. Wassermeier, and K. H. Ploog, Surf. Sci. **372**, 307 (1997).
8. H. Yamaguchi and Y. Horikoshi, Phys. Rev. B: Condens. Matter **51**, 9836 (1995).
9. Yu. G. Galitsyn, V. G. Mansurov, V. I. Poshevnev, and R. A. Sokolov, Poverkhnost **7**, 59 (1992).
10. C. Sasaoka, Y. Kato, and A. Usui, Appl. Phys. Lett. **62**, 2338 (1993).
11. Yu. G. Galitsyn, V. G. Mansurov, and I. I. Marahovka, Phys. Low-Dimens. Struct. **5/6**, 75 (1997).
12. Yu. G. Galitsyn, V. G. Mansurov, and I. I. Marahovka, Phys. Low-Dimens. Struct. **7**, 55 (1997).
13. Yu. G. Galitsyn, I. I. Marahovka, and S. P. Moshchenko, Dokl. Akad. Nauk **359** 48 (1998).
14. Yu. G. Galitsyn, I. I. Marahovka, S. P. Moshchenko, and V. G. Mansurov, Pis'ma Zh. Tekh. Fiz. **24**, 31 (1998).
15. E. S. Tok, J. H. Neave, J. Zang, *et al.*, Surf. Sci. **371**, 277 (1997).
16. C. T. Foxon and B. A. Joyce, Surf. Sci. **50**, 434 (1975).
17. J. C. García, C. Neri, and J. Massies, J. Cryst. Growth **98**, 511 (1989).
18. V. P. Zhdanov, Surf. Sci. Rep. **12**, No. 5, 185 (1991).
19. V. P. Zhdanov, *Elementary Physicochemical Processes on the Surface* [in Russian] (Nauka, Moscow, 1988), p. 320.
20. N. Takeuchi, A. Selloni, and E. Tosatti, Phys. Rev. B: Condens. Matter **49**, 10757 (1994).
21. A. R. Avery, D. M. Holmes, T. S. Jones, *et al.*, Phys. Rev. B: Condens. Matter **50**, 8098 (1994).

Translated by P. Pozdeev

Semiconductors, Vol. 34, No. 2, 2000, pp. 181–188. Translated from Fizika i Tekhnika Poluprovodnikov, Vol. 34, No. 2, 2000, pp. 186–193.

SEMICONDUCTORS STRUCTURES, INTERFACES, AND SURFACES

Physicochemical Properties of the Surface and Near-Surface Region of Epitaxial *n*-GaAs Layers Modified by Atomic Hydrogen

N. A. Torkhov* and S. V. Eremeev,*****

** Research Institute of Semiconductors (NIIPP), State Research and Production Enterprise, Tomsk, 634045 Russia; e-mail: tna@ic.tsu.ru*

*** Siberian Physicotechnical Institute, Tomsk State University, Tomsk, 634050 Russia*

**** Institute of Strength Physics and Materials Science, Siberian Division, Russian Academy of Sciences, Tomsk, 634055 Russia*

Submitted May 28, 1999; accepted for publication June 16, 1999

Abstract—Changes in the static electrical parameters of the Au–GaAs Schottky barriers in the (n–n^+)-GaAs structures treated with atomic hydrogen are closely related to modification of the chemical properties of the surface layers in these structures, including changes in the rate of *n*-GaAs etching in a DMF-monoethanol amine (1:3) solution, in the electrochemical deposition rate and the structure of the resulting Au layer, and in the degree of passivation of linear defects emerging on the surface. The unprotected surface of epitaxial *n*-GaAs(100) layer exhibited virtually no etch pits upon the treatment in atomic hydrogen at 100°C. For *n*-GaAs protected with a 50-Å-thick SiO_2 film, a drop in the etching rate and a considerable decrease in the number of etch pits, as well as a decrease in the thickness of electrochemically deposited gold layer and a change in is structure, were observed for the samples treated in atomic hydrogen at all temperatures in the range studied (100–400°C). © *2000 MAIK "Nauka/Interperiodica".*

INTRODUCTION

As is known, exposure of the surface of semiconductors to atomic hydrogen (H) leads to etching of the intrinsic oxide and a decrease in the rate of oxidation in air [1–3]. This treatment also leads to a decrease in the electrical activity of various surface defects, including grain boundaries and linear defects emerging on the surface, which is detected by changes in the microcathodoluminescence spectra of H-treated samples [4].

According to some data [5, 6], the concentration of hydrogen atoms in the near-surface region of semiconductors may as high as 10^{20}–10^{21} cm^{-3}. Such a high content of dissolved hydrogen may not only significantly modify the electrophysical characteristics [7], but, probably, affects the chemical properties of the material as well [7]. For these reasons and in view of obviously restricted data available in the literature on this subject, it was expedient to perform a special investigation of the effect of hydrogenation on the rate of chemical etching of *n*-GaAs.

We have studied the rate of etching of epitaxial *n*-GaAs(100) films with the dimethylformamide–monoethanol amine (DM) 1 : 3 solution and the effects of H treatment upon the electrical activity of linear defects emerging on the surface and the rate of gold deposition in the course of electrochemical metallization process. We have also studied the morphology and structure of the surface of metal contacts by the method of scanning tunneling microscopy (STM).

EXPERIMENTAL

The hydrogenation experiments were performed with 0.5-μm thick epitaxial GaAs:Sn layers grown on (100)-oriented n^+-GaAs:Te substrates. The charge carrier concentration in the epitaxial layers and substrates was 3.5×10^{16} cm^{-3} and 2×10^{18} cm^{-3}, respectively. As is known, thin (50–100 Å thick) SiO_2 films, despite being fully permeable for atomic hydrogen [8], hinder the direct interaction between atomic hydrogen and the substrate. For this reason, the *n*-GaAs substrates were coated with 50-Å-thick SiO_2 films by the method of plasmachemical deposition (Fig. 1a). On the side of the n^+-GaAs substrate, an ohmic contact was formed by depositing a film of GeNi + Au alloy followed by a 5-min annealing at 450°C. The wafers prepared as described above were cut into several samples.

The protective SiO_2 film was removed from half of the area of each sample (Fig. 1b). The unprotected (SiO_2-free) and protected areas of the sample surface will be referred to as U-regions and P-regions, respectively.

The samples were treated with atomic hydrogen using a setup described previously [9] at temperatures in the range T_{tr} = 50–400°C for a time of t_{tr} = 5 min (Fig. 1b). The samples not treated with atomic hydro-

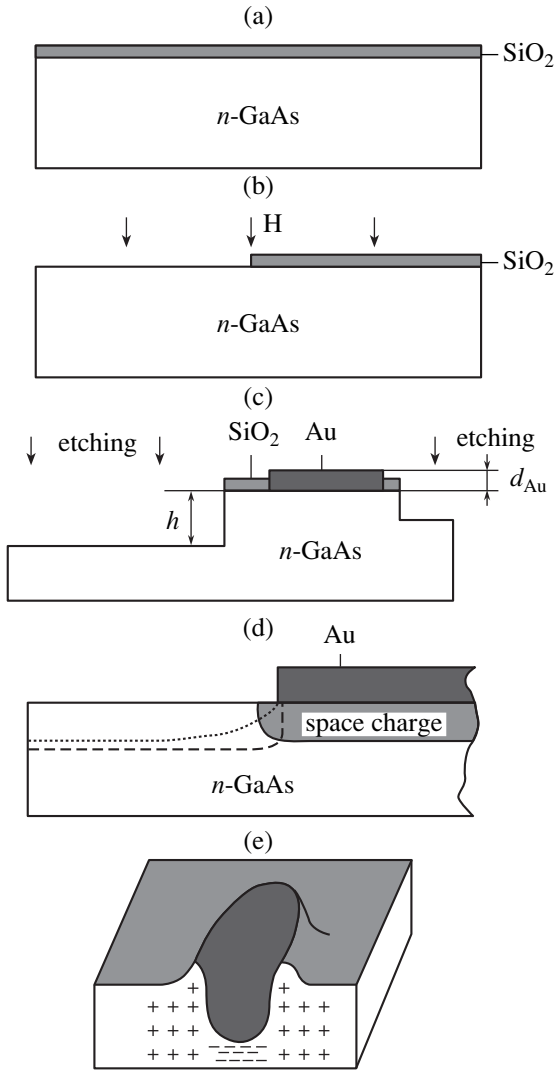

Fig. 1. Schematic diagrams illustrating preparation technology of the diode structures with Schottky barriers (a–d) and the shape of etch pits.

gen will be referred to as initial. The residual pressure in a working chamber evacuated with a turbomolecular pump was 3.7×10^{-6} torr. The hydrogen flow rate in all experiments was maintained on a level of 700 (atm cm^3)/h. The hydrogen plasma was produced using an atomic hydrogen generator described in [9]. The hydrogen pressure in the vacuum chamber during the H treatment was 1.1×10^{-4} torr.

After the H treatment, the samples were characterized by measuring their standard static electrical characteristics. For this purpose, the Schottky barriers were formed on the samples by depositing 0.25-μm-thick gold electrodes with a diameter of 325 μm. The gold film was deposited onto the sample surface within the windows made either in the photoresist (U-region) or in the insulator (P-region) (Fig. 1c). The electrochemical deposition was carried out for t = 1 min at a constant current density through the sample. The samples with Schottky barriers were used to determine the metal layer thickness d_{Au}, to measure the static electrical parameters (including the reverse voltage V_r at a 10 μA current, the ideality factor n, and the Schottky barrier height φ_b), and to study the depth–concentration profiles of the electrically active shallow donor impurity (N_D^+). The ideality factor was determined by the slope of a linear portion of the forward-bias current–voltage (I–V) characteristic plotted in the semilogarithmic scale, the Schottky barrier height was determined using the saturation current density [9], and the concentration profiles were obtained by measuring the capacitance–voltage (C–V) characteristics at a frequency of 1 MHz. Scatter of the C–V parameters over the sample area did not exceed 5% (for V_r, 25%).

In order to study the effect of the H treatment on the rate of surface etching in the DM solution, the SiO_2 film was removed from a part of the P-region of epitaxial n-GaAs films immediately prior to their etching (Fig. 1c). As a result, each sample contained two areas with exposed GaAs surface separated by the remaining P-region, with the remaining SiO_2 film playing the masking role. The rate of etching was determined by measuring the height h of the steps at the U-region/SiO_2 and SiO_2/P-region boundaries with the aid of a MII-4 microinterferometer. The average etching rate was calculated as the ratio of the step height h to the etching time t_{et}. The velocity of gold deposition was estimated as the ratio of the metal layer thickness to the deposition time t.

The surface structure of deposited gold films was studied by STM in an SMM-2000T microscope. The sample surface was scanned under normal conditions in air with a platinum tip in the constant sample current mode at a potential difference of 2 V between the tip and sample.

RESULTS

The results of measurements of the h values showed that the H treatment affects the average rate of etching of the epitaxial n-GaAs films studied (Fig. 2a). As the treatment temperature T_{tr} increases, the average rates of etching both in the P-region (V_P) and in the U-region (V_U) decreased to a minimum value (0.002 μm/min) at T_{tr} = 100°C. On further increasing the T_{tr} value, behavior of the $V_U(T_{tr})$ and $V_P(T_{tr})$ functions becomes sharply different. The former value increases with the treatment temperature and at T_{tr} > 250°C even exceeds the initial level (0.0037 μm/min) to reach a maximum of 0.0045 μm/min. In contrast, the V_P value remains virtually unchanged at T_{tr} > 100°C.

Investigation of the initial sample with an optical microscope after etching in the DM solution showed that the sample surface was covered with elongated etch pits oriented in the (011) direction (Fig. 3a). There was certain correlation between the rate of etching and

the number and size of etch pits in the U-region. In the P-region of samples treated in the entire temperature range studied, the etch pits were either completely absent or were present in insignificant amounts. For the U-region of samples, there was only a very narrow interval of T_{tr} about 100°C where the etch pits were not formed (Fig. 3b).

The insert in Fig 3a shows the image of an etch pit observed with a scanning electron microscope (SEM). As seen, etching is accompanied by the formation of a ridge around the pit. Probably, the ridge is formed by material characterized by a lower etching rate.

According to the results of our experiments, the H treatment also strongly affects the average velocity $V_{U,P}^{Au}$ of the electrochemical deposition of gold in U- and P-regions. Figure 2b shows the plot of the gold contact thickness versus temperature for the U- and P-regions. As the T_{tr} value increases to 200°C, the V_U^{Au} drops from the initial level (0.25 μm/min) to a minimum value (0.04 μm/min). The further growth in T_{tr} is accompanied by increasing deposition velocity, which is restored on the initial level at T_{tr} = 250–300°C. As seen from Fig. 2b, a quite different behavior is observed for the d_{Au} value in the P-region. Here, the deposition velocity V_P^{Au} sharply decreases with increasing temperature and reaches a minimum level (0.035 μm/min) at T_{tr} = 100–150°C. The further increase in T_{tr} leads to only a insignificant increase in V_P^{Au}.

The STM data revealed a difference in the surface structure of gold deposited onto the P-regions (Fig. 4a) and U-regions (Fig. 4b). As seen, the H treatment of the substrate results in that the electrochemically deposited gold film becomes less loose (cf. Figs. 4a and 4b) and appears much like a layer obtained by thermal deposition (Fig. 4c).

Figure 5 shows the plots of static electrical characteristics (V_r, n, and φ_b) versus the H treatment temperature for the diode structures formed in the P- and U-regions of samples. Behavior of the static electrical characteristics of the diodes, as well as the depth–concentration profiles (Fig. 6) of an ionized shallow donor impurity (N_D^+) and the character of influence of a thin protective SiO_2 film, were virtually identical to those reported in [8]. The diode structures formed in the U-region of samples exhibit an optimum temperature interval of the H treatment (150–200°C) featuring a maximum in V_r and a minimum in n. As for the diode structures formed in the P-region, the V_r value increases in the entire range of T_{tr}, while the n and φ_b values virtually remain unchanged.

A minimum passivation effect in both U- and P-regions was observed at T_{tr} = 300°C. Further increase in the H treatment temperature (T_{tr} > 300°C) was accompanied by a decrease in the number of hydrogen

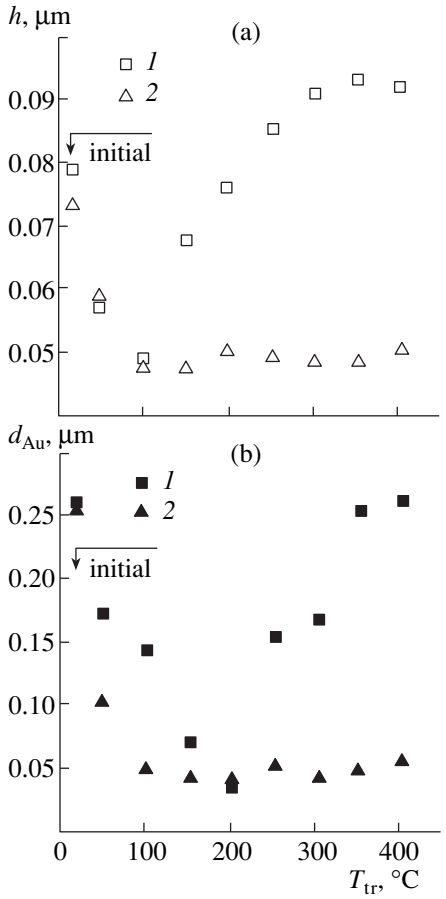

Fig. 2. Plots of the rates of (a) *n*-GaAs etching in the DM solution and (b) electrochemical gold deposition versus temperature of the H treatment for the (*1*) U- and (*2*) P-regions of samples.

complexes $(D–H)^0$ and a growth in the charged impurity concentration (N_D^+). The presence of a dielectric SiO_2 film on the sample surface during the H treatment may slightly increase the passivation effect [7], which is most pronounced at T_{tr} = 350–400°C.

DISCUSSION

The results of our experiments show that the treatment with atomic hydrogen (hydrogenation) not only significantly modifies the electrical characteristics of epitaxial *n*-GaAs layers, but strongly changes their chemical properties as well. This is manifested by the passivation of defects emerging on the surface and by changes in the rate of material etching. According to our results and some other published data [10], it is suggested that changes in the properties of *n*-GaAs occur within a thin near- surface layer with a thickness not exceeding 50 nm. The phenomena observed can be related to a high content of hydrogen in this layer. This may account for a difference in the temperature variation of the etching rate of the material observed in the

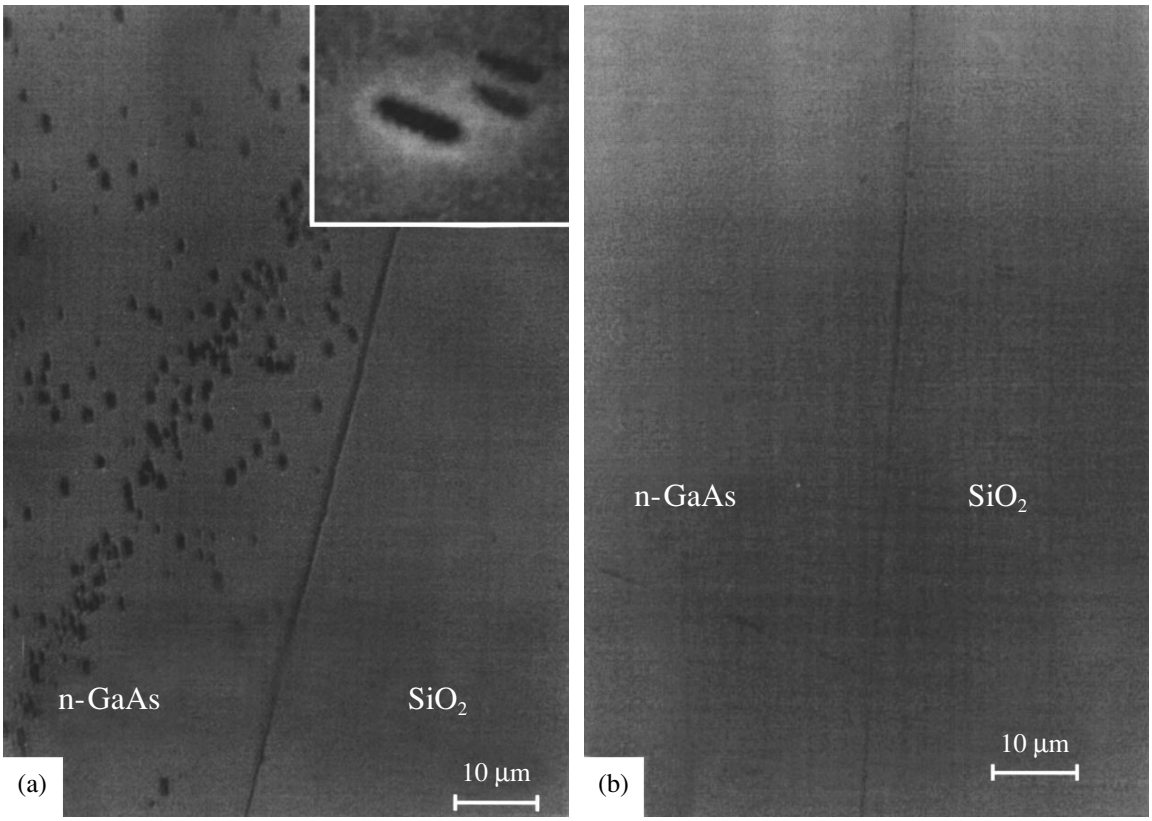

Fig. 3. Microscopic images of the surface of *n*-GaAs samples etched in the DM solution: (a) initial; (b) H-treated. The inset shows a SEM image of etch pits (magnification, ×10000).

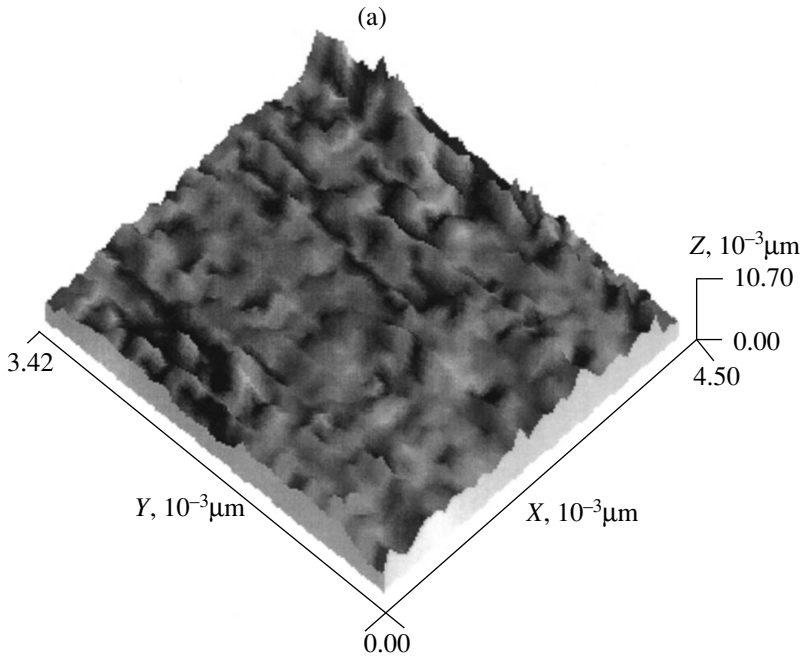

Fig. 4. STM images of the surface of (a, b) gold films, obtained by electrochemical deposition onto the (a) initial and H-treated *n*-GaAs substrates, and (c) a thick (25 μm) Au film prepared by thermal deposition (magnification, $\times 2^{22}$).

U- and P-regions of samples. During the H treatment, the SiO_2 film hinders the outflow of hydrogen from the near-surface layer of the *n*-GaAs film and favors more effective hydrogen saturation of this layer. This is confirmed by the fact that the presence of a SiO_2 film on the sample surface during the H treatment increases the passivation effect [7]. In addition, Johnson *et al.* [11] demonstrated that a SiO_2–Si interphase boundary is an effective sink for deuterium. Probably, the SiO_2–GaAs boundary in our system is also capable of accumulating hydrogen, which would favor more effective hydrogen saturation of the near-surface layer of the *n*-GaAs film and more pronounced modification of the properties of this layer. For this reason, an increase in T_{tr} for the H treatment of the samples with protective SiO_2 films has no significant effect on the atomic hydrogen concentration in the near-surface layer and, hence, does not affect the rate of the material etching.

The H treatment is accompanied by processes limiting the content of hydrogen in the near-surface layer. On the one hand, the increase in T_{tr} leads to an increase in the diffusion coefficient and in the flux of atomic hydrogen from the near-surface layer into deeper bulk layers. On the other hand, the growth in temperature is accompanied by enhanced etching of the intrinsic oxide and the uppermost surface layer, which increases the loss of hydrogen in the form of compounds [7] and the flow of hydrogen through the surface layer to the semiconductor bulk. There may exist an optimum temperature interval featuring a maximum hydrogen content in

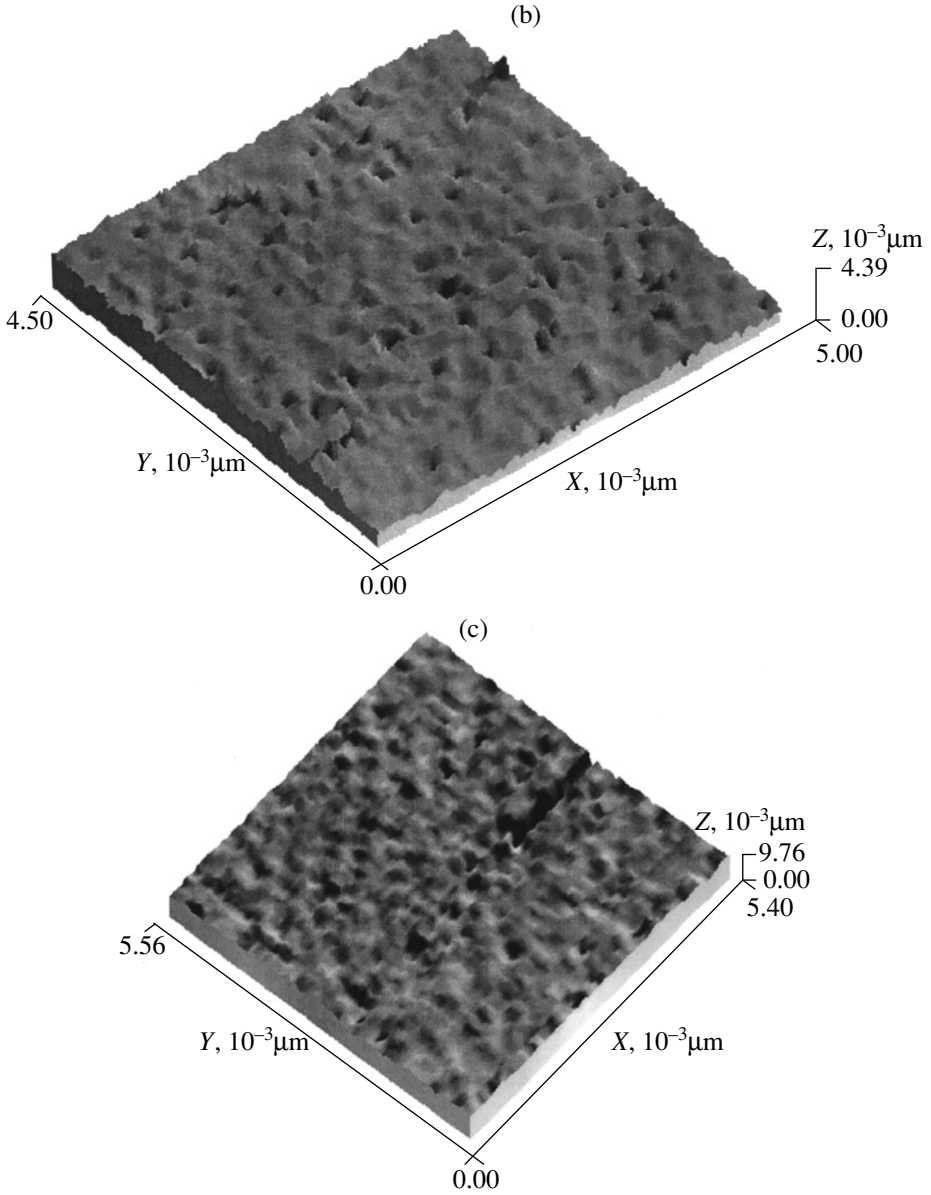

Fig. 4. (Contd.)

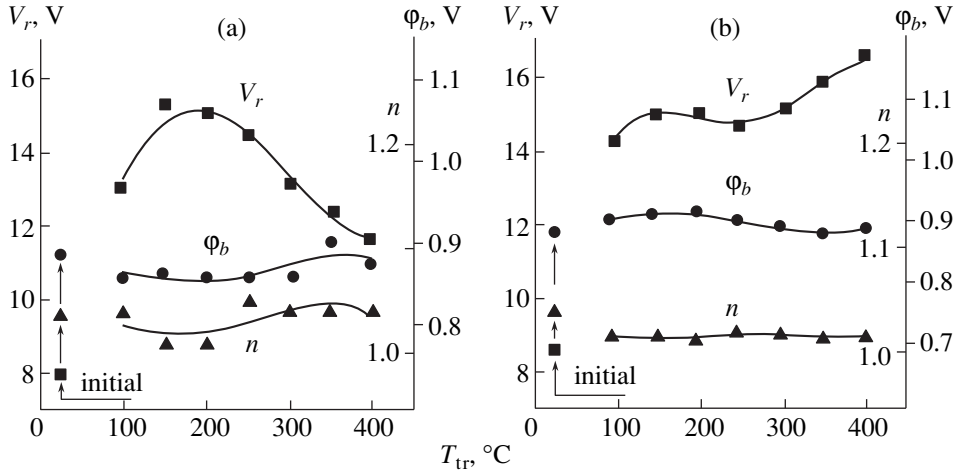

Fig. 5. Plots of static electrical characteristics (V_r, n, and φ_b) versus the H treatment temperature for the diode structures formed in the (a) P- and (b) U-regions of samples.

the near-surface layer. Another mechanism limiting the diffusion of atomic hydrogen into semiconductor is the formation of H_2 molecules [12]. The existence of a near-surface layer retarding the hydrogen diffusion is confirmed by the experimental data presented in Fig. 7. As seen in this figure, etch-off of a thin (50-nm-thick) near-surface layer after the first H treatment and the repeated hydrogenation at the same temperature (but for a shorter time of t_{tr}= 2 min) leads to a greater drop in the charged donor impurity concentration N_D^+ as compared to that observed in both P- and U-regions upon the standard H treatment at T_{tr} = 350°C for t_{tr} = 5 min. In this experiment, the first treatment was performed in the presence of a protective SiO_2 film, which was removed prior to the second exposure to hydrogen. Moreover, the passivation effect here was even stronger than that observed in the optimum regime at T_{tr} = 300°C.

Another possible mechanism decreasing the etching rate can be related to the effect of atomic hydrogen chemisorbed on the *n*- GaAs surface. As a result, the etching process begins after some delay rather than instantaneously.

The absence of the etch pits is most probably related to the suppressed electrical activity (i.e., passivation) of linear defects emerging on the surface. It is suggested that the interaction of hydrogen atoms with defects leads to saturation of the broken bonds and, hence, to a change in the surface potential at the sites of the defect emerging on the surface. According to the experimental data, this results in "healing" of the surface potential inhomogeneities and in more uniform etching over the entire surface of the material (Fig. 3b).

Figure 1e shows a schematic diagram of an etch pit explaining the SEM image (inset in Fig. 3a). A relatively large pit depth indicates that etching of the defect site proceeds at a markedly greater rate, which is related to a change in the chemical potential around the site of the defect emerging on the surface. Additional experiments including etching of a sample with the Schottky barrier in the DM solution revealed a region around the gold contacts characterized by a lower etching rate. This resulted in the formation of a smooth edge (Fig. 1d, dotted line) rather than a steep one (Fig. 1, long-dash line). These changes in the chemical activity are probably related to the formation of an electron-depleted space-charge region along the periphery of the contact. It is suggested that defects, like Schottky barriers, are surrounded by electron-depleted regions. At the same time, the defect proper has an excess negative charge (Fig. 1e). As a result, a potential distribution is set around the defect that favors etching of the *n*-GaAs layer with the ridge formation (Fig. 1e).

Variations in the velocity of electrochemical deposition of gold in the course of metallization can be related, on the one hand, to a decrease in conductivity of the near-surface layer. A preset current in the electrolyte is maintained at the expense of hydrogen ion reduction, which is accompanied by the appearance of hydrogen bubbles on the sample surface. On the other hand, the H treatment may lead to passivation of the electrically active surface defects, which had favored the formation of gold nuclei in the initial deposition stage. In this case, the deposition velocity would depend on the time required for the complete surface coverage with a gold film. The same mechanism, may account for the observed decrease in the Au grain size (smooth microrelief) and an increase in the density of the deposit. The H treatment results in that the gold nuclei are formed uniformly over the entire surface rather than on separate defects. It is not excluded that the H treatment leads to some amorphization of the near-surface layer, which would result in a mutual misorientation of the nuclei and in increasing density of the Au deposit.

The observed behavior of the static diode characteristics (V_r, n, φ_b) as functions of T_{tr} is consistent with the

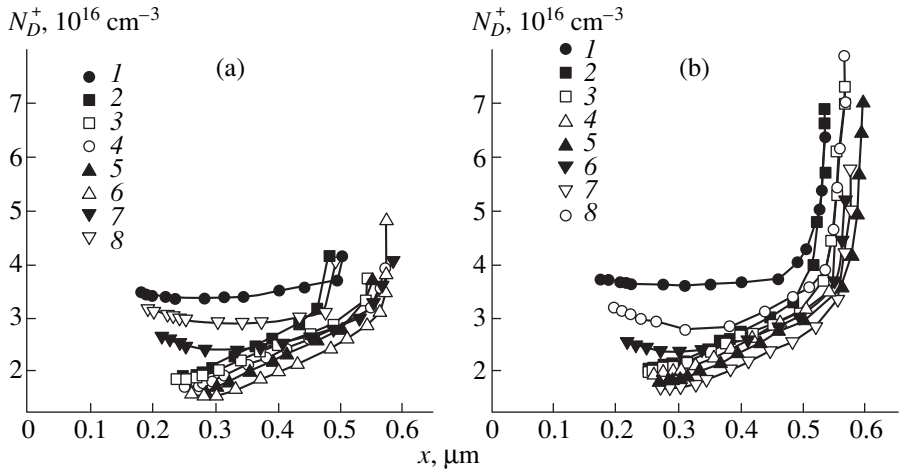

Fig. 6. Variation of the ionized shallow donor impurity concentration N_D^+ with depth x in the (a) U- and (b) P- regions of (*1*) the initial sample and (*2–8*) the samples H- treated at various temperatures T_{tr} = 100 (*2*); 150 (*3*); 200 (*4*); 2540 (*5*); 300 (*6*) 350 (*7*); 400°C (*8*).

temperature variation of h and d_{Au} values. As seen, the H treatment at temperatures in the range from 100 to 200°C, accompanied by an increase in the electrical properties, corresponds to most pronounced changes in chemical properties of the *n*-GaAs surface not protected by the SiO_2 film. On the contrary, the V_r and V_P^{Au} values in the region protected during the H treatment tend to decrease almost in the entire temperature range studied (100–400°C). Apparently, passivation of the surface and a decrease in inhomogeneity of the surface

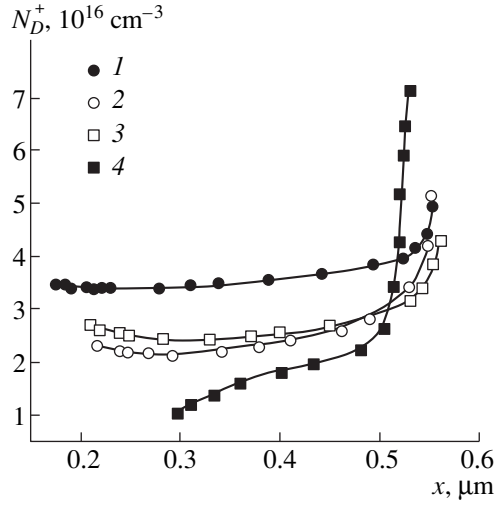

Fig. 7. Variation of the ionized shallow donor impurity concentration N_D^+ with depth x in the (*1*) initial and (*2–4*) H-treated samples: (*2*) P-region, T_{tr} = 350°C/t_{tr} = 5 min; (*3*) U-region, T_{tr} = 350°C/t_{tr} = 5 min; (*4*) P-region, T_{tr} = 350°C/t_{tr} = 1 min + removal of an 0.05-μm-thick near-surface layer + T_{tr} = 350°C/t_{tr} = 2 min.

potential result in a more homogeneous distribution of φ_b over the whole barrier contact area, which would favor the increase in V_r and a decrease in the quality factor n.

CONCLUSION

The results of our experiments showed that the exposure to atomic hydrogen (H treatment) leads to a decrease in the rate of *n*-GaAs etching in the DMF-monoethanol amine (DM) 1:3 solution and in the velocity of electrochemical gold deposition and results in passivation of the linear defects emerging on the surface. There is an optimum temperature regime of the H treatment (about 100°C) of a *n*-GaAs surface not protected with a SiO_2 film, which renders the surface more inert and minimizes the rate of etching in the DM solution. Samples treated in this regime exhibit almost no etch pits on the *n*-GaAs surface. The H treatment of samples with the surface protected with a 50-Å-thick SiO_2 layer led to changes in their properties (a decrease in the *n*-GaAs etching rate, vanishing of the etch pits, decrease in the thickness and structure of Au deposit) virtually in the entire temperature interval studied (100–400°C).

It is shown that changes in the static diode characteristics (increase in V_r and decrease in n) are closely related to the chemical properties of the surface and near-surface region modified by the H treatment. The treatment of *n*-GaAs in a flow of atomic hydrogen results in the formation of a thin (less than 50-nm-thick) near-surface region limiting the diffusion of atomic hydrogen into the bulk of the semiconductor. It was found that Au contacts deposited onto the sample surface markedly affect the process of *n*-GaAs etching in the DM solution.

ACKNOWLEDGMENTS

The authors are grateful to Prof. V.G. Bozhkov for his help in the work, and to V.A. Kagadei for preparation of the samples treated in the flow of atomic hydrogen.

REFERENCES

1. V. L. Gurtovoĭ, V. V. Dremov, V. A. Makarenko, and S.Yu. Shapoval, Fiz. Tekh. Poluprovod. (St. Petersburg) **29**, 1888 (1995).
2. J.A. Schafer, V. Persch, S. Stock, *et al.*, Europhys. Lett. **12**, 563 (1990).
3. A. Kashimoto, I. Suemuni, K. Hamaoka, *et al.*, Jpn. J. Appl. Phys. **29**, 2273 (1990).
4. É. M. Omel'yanovskiĭ, A. V. Pakhomov, A. Ya. Polyakov, *et al.*, Fiz. Tekh. Poluprovodn. (Leningrad) **22**, 1203 (1988) [Sov. Phys. Semicond. **22**, 763 (1988)].
5. U. K. Chakrabarti, S. J. Pearton, W. S. Hobson, *et al.*, Appl. Phys. Lett. **57**, 887 (1990).
6. É. M. Omel'yanovskiĭ and A. Ya. Polyakov, Vysokochist. Veshchestva, No. 5, 5 (1988).
7. V. G. Bozhkov, V. A. Kagadeĭ, and N. A. Torkhov, Fiz. Tekh. Poluprovodn. (St. Petersburg) **32** (11), 1343 (1998) [Semicond. **32**, 1196 (1998)].
8. V. G. Bozhkov, V. A. Kagadeĭ, and N. A. Torkhov, *Proc. Int. Symp. on Urban Radiowave Propagation (URPS-97) and The 2nd Int. Symp. "Conversion in Science to International Collaboration"* (Sibconvers-97) [in Russian] (Tomsk, 1997), p.178.
9. V. G. Bozhkov, V. A. Kagadeĭ, and N. A. Torkhov, Izv. Vyssh. Uchebn. Zaved., Fiz., No. 8, 115 (1997).
10. N. A. Torkhov and V. G. Bozhkov, Dep. VINITI No. 313-B99 (29.01.99) (VINITI, Moscow).
11. N. M. Johnson, D. K. Biegelsen, M. D. Moyer, V. R. Deline, and C.A. Evans, Appl. Phys. Lett. **38** (12), 995 (1981).
12. N. S. Rytova, Fiz. Tekh. Poluprovodn. (Leningrad) **25** (6), 990 (1991) [Sov. Phys. Semicond. **25**, 598 (1991)].

Translated by P. Pozdeev

Semiconductors, Vol. 34, No. 2, 2000, pp. 189–194. Translated from Fizika i Tekhnika Poluprovodnikov, Vol. 34, No. 2, 2000, pp. 194–199.

SEMICONDUCTORS STRUCTURES, INTERFACES, AND SURFACES

Magnetotransport in a Semimetal Channel in p-$Ga_{1-x}In_xAs_ySb_{1-y}$/p-InAs Heterostructures with Various Compositions of the Solid Solution

T. I. Voronina, T. S. Lagunova, M. P. Mikhaĭlova, K. D. Moiseev, A. E. Rozov, and Yu. P. Yakovlev

Ioffe Physicotechnical Institute, Russian Academy of Sciences, Politekhnicheskaya 26, St. Petersburg, 194021 Russia

Submitted May 14, 1999; accepted for publication July 14, 1999

Abstract—Magnetotransport properties of an electron channel at the heteroboundary in type II separated p-$Ga_{1-x}In_xAs_ySb_{1-y}$/p-InAs heterostructures grown by LPE (x = 0.09–0.22) were studied in the temperature range of 77–300 K. It is shown that an electron channel, which is formed at the heteroboundary and has high mobility $\mu = (3–5) \times 10^4$ cm^2 V^{-1} s^{-1}, exists throughout the whole composition range. The band diagram of the heterostructures under study is discussed, and some parameters of the electron channel are evaluated. It is found that the electron channel with high mobility persists up to room temperature. Type II GaInAsSb/p-InAs heterostructures can find application in new Hall sensor devices with an electron channel at the heteroboundary.

1. INTRODUCTION

The heterostructures based on gallium antimonide and indium arsenide attract considerable interest as promising materials for the production of new optoelectronic devices in the medium information band of emission [1]. The type II GaInAsSb/InAs heterojunctions and GaInSb/InAs/GaAlSb superlattices are used to design new-type diode lasers with a semimetal injector [2, 3]. This is dictated by the unique properties of the type II heterojunctions, in which the electrons and holes at a single interface are spatially separated and localized in self-consistent quantum wells at both sides of the heteroboundary [4, 5].

The properties of the semimetal channel can be changed under the action of light, electric and magnetic fields. These properties also depend on the parameters of semiconductor materials of heterostructure (solid solution composition and doping level). In such heterostructures, the strong overlapping of electron and hole wave functions and a high density of semimetal electron–hole system at the type II separated heteroboundary result in a high probability of indirect (tunnel) radiative recombination [6].

Earlier we reported [7–9] the observation of electron channel in separate p-$Ga_{0.83}In_{0.17}As_{0.22}Sb_{0.78}$/$p$-InAs heterostructures. It was established that the electrons in the channel have a high mobility $\mu = (5–7)\times10^4$ cm^2 V^{-1} s^{-1} in heterostructures with undoped layers of solid solution and retain these properties in the temperature range from helium temperatures to T = 200 K. In the case of heavy doping of solid solution with acceptors, an abrupt drop in mobility was observed due to the narrowing and depletion of electron channel and the appearance of an additional mechanism of carrier scattering by the roughness of interface [10].

The aim of this work is to study the modification of transport properties of electron channel at the heteroboundary of the type II separated p-$Ga_{1-x}In_xAs_ySb_{1-y}$/p-InAs heterojunctions with various compositions of solid solution (x = 0.09, 0.16, and 0.22) and the estimation of the possibilities of obtaining the system with high electron mobility at the heteroboundary up to room temperature. Such structures are promising in the development of Hall sensors of new generation [11].

2. EXPERIMENTAL RESULTS AND DISCUSSION

2.1. Characteristics of the Samples

Epitaxial layers of p-$Ga_{1-x}In_xAs_ySb_{1-y}$ solid solutions with various compositions (x = 0.09, 0.16, and 0.22) were deposited on the p-InAs(100) substrate by the liquid-phase epitaxy. The epitaxial layers were grown by using the solution–melt prepared from In and Sb (of 99.9999% and 99.999% purity, respectively) and charges of undoped GaSb and InAs with carrier concentrations $p_{77} = 5 \times 10^{16}$ cm^{-3} and $n_{77} = 2 \times 10^{16}$ cm^{-3}, respectively. The thickness of epilayers was equal to 1.5 μm.

1063-7826/00/3402-0189$20.00 © 2000 MAIK "Nauka/Interperiodica"

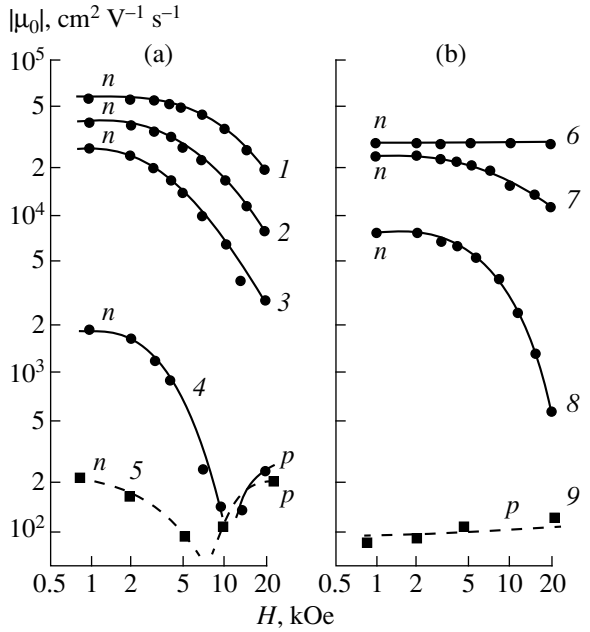

Fig. 1. Hall mobility μ_0 as a function of magnetic-field intensity H for the samples (see the numbers of the samples in the table) and the corresponding substrates: (a) sample 2 and InAs ($p = 10^{16}$ cm^{-3}), (b) sample 4 and InAs ($p = 10^{17}$ cm^{-3}). Dependences $\mu_0(H)$ for InAs substrates are shown by the dashed lines. The curves *1*, *2*, and *3* correspond to 77, 150, and 200 K; the curves *4*, *5*, *8*, and *9*, to 300 K; curve *6*, to 77–200 K; and *7*, to 250 K. The type of conductivity is indicated by *n* and *p*.

The high-resistance wafers of indium arsenide doped with zinc with the hole concentration $p_{300} = 10^{16}$ cm^{-3} and $p_{300} = 10^{17}$ cm^{-3} were used as a material for the substrate. The substrate with $p_{300} = 10^{16}$ cm^{-3} was used in our previous studies [7–10]; however, an early transition to the ambipolar conductivity due to a strong compensation of gallium arsenide restricts the study of transport properties of these heterostructures to the temperature range of $T = 77$–200 K. In the substrate with lower compensation ($p_{300} = 10^{17}$ cm^{-3}), the transition to ambipolar conductivity is shifted towards higher temperatures, which allows one to study the electron channel up to room temperature.

The rectangular-shaped samples were used for the measurements of galvanomagnetic effects. Six indium contacts were deposited on the surface containing epitaxial GaInAsSb layers in order to measure the conductivity σ_0, Hall coefficient R_H, Hall mobility $\mu_0 = R_H\sigma$, and transverse magnetoresistance $(\Delta\rho/\rho)_\perp$ under magnetic fields $H = 0.5$–20 kOe in the temperature range $T = 77$–300 K.

The basic characteristics of the samples studied are given in the table; there, σ is electrical conductivity per unit area. The sign indicates the type of conductivity. It can be seen that at $T = 77$ K the sign of the Hall emf indicates the *n*-type conductivity. A high value of Hall mobility, typical of the mobility of electrons in the channel at the heteroboundary, is observed for all compositions of solid solution. It should be mentioned that the mobility decreases with an increase in indium content in solid solution.

2.2. Mobility of Charge Carriers

The typical dependences of mobility μ_0 on magnetic field intensity at various temperatures for two heterostructures, based on the same composition of solid solution ($x = 0.16$) but grown on different substrates (sample nos. 2 and 4), are shown in Fig. 1.

In structures grown on substrates with concentration $p = 10^{16}$ cm^{-3} (Fig. 1a), a strong dependence of mobility on temperature and magnetic-field intensity is observed, with the mobility decreasing steeply with increasing temperature at $T > 200$ K and with an increase in the magnetic field. The Hall mobility at $T = 300$ K changes its sign from electron-type conductivity to a hole-type in magnetic fields $H > 10$ kOe. Such a strong dependence of mobility on the magnetic-field intensity is related to the shunting of conductivity of heterostructure by the substrate material, because the intrinsic conductivity of substrate can reveal itself even at $T > 200$ K (see the dashed line in Fig. 1a).

A completely different dependence of mobility on temperature and field is observed when the hole concentration in substrate $p = 10^{17}$ cm^{-3} (Fig. 1b). For such samples, the Hall mobility remains constant under all relevant magnetic fields within the temperature range of 77–200 K. Only at higher temperatures ($T > 200$ K),

Basic parameters of p-$Ga_{1-x}In_xAs_ySb_{1-y}$/p-InAs heterostructures at 77 K

Sample	p, cm^{-3}	x	σ_0, Ω^{-1}	μ_0,10^4 cm^2 V^{-1} s^{-1}	d_1, Å	N_s, 10^{11} cm^{-2}	B_r	α
1	10^{16}	0.09	0.013	–4.7	390	1	0.07	0.15
2	10^{16}	0.16	0.017	–4.4	370	1.15	0.03	0.11
3	10^{16}	0.22	0.026	–3.2	320	1.5	0.26	0.02
4	10^{17}	0.09	0.049	–4.4	370	1.15	0.02	0.12
5	10^{17}	0.16	0.045	–3.0	310	1.6	0.03	0.05
6	10^{17}	0.22	0.050	–3.0	310	1.6	0.18	0.03

Note: p is the hole concentration in the substrate.

the mobility begins to decrease with the electron-type of conductivity retained. This occurs owing to the shunting effect of the substrate with concentration $p = 10^{17}$ cm^{-3} on the conductivity of heterostructure becoming less pronounced, because the intrinsic conductivity of this substrate shifts to higher temperatures, and the Hall mobility at $T = 300$ K is determined largely by the holes (see the dashed line in Fig. 1b).

Figure 2 shows the temperature dependence of Hall mobility for various values of H for the p-GaInAsSb/p-InAs heterostructure on the substrate with the hole concentration $p = 10^{17}$ cm^{-3} (sample 6). The dashed line in Fig. 2 represents the temperature dependence of mobility for the p-InAs substrate that was used for deposition of the epilayer of solid solution. Comparing the Hall mobility of the whole heterostructure with that for the substrate of this sample, we may state that at temperatures $T = 200$ K the mobility is determined by the electrons in the channel at the heteroboundary, at $T > 300$ K the mobility is governed by the electrons in the substrate, and within the temperature range of $200 < T < 300$ K the mobility is determined by simultaneous participation of electrons in the channel and holes in the substrate. The parameters of electron channel can be estimated on the basis of the three-dimensional model [12].

The measured values of conductivity σ_0, the Hall concentration of electrons n_0, and mobility μ_0 at $T =$ 200–300 K are determined from the expressions

$$\begin{aligned} \sigma_0 d_0 &= \sigma_1 d_1 + \sigma_2 d_2 + \sigma_3 d_3, \\ \mu_0^2 n_0 d_0 &= \mu_1^2 n_1 d_1 - \mu_2^2 p_2 d_2 - \mu_3^2 p_3 d_3, \end{aligned} \quad (1)$$

where d_i is the thickness, and subscripts 0, 1, 2, and 3 refer to the entire structure, electron channel, substrate, and to the epilayer of solid solution, respectively. The contribution of the epilayer can be neglected since the mobility and hole concentration for the solid solution and substrate are almost the same ($p_2 \approx p_3 \approx 10^{17}$ cm^{-3} and $\mu_2 \approx \mu_3 \approx 100$ cm^2 V^{-1} s^{-1}), and the thickness of the layer is 200 times smaller than that of the substrate. For a weak-field region ($H = 0.5$–3 kOe) where the mobility μ_0 is constant and the assumption $d_0 \approx d_2$, $\mu_2 \ll \mu_0$ is valid, we may estimate the mobility in electron channel on the basis of the formulas for two-layer model as

$$\mu_1 = \mu_0/(1 - \sigma_2/\sigma_0). \quad (2)$$

The estimations of the properties in the electron channel at room temperature show that the mobility in this channel changes insignificantly with the composition of solid solution and is equal to $(2 - 2.5) \times 10^4$ cm^2 V^{-1} s^{-1}.

Contrary to the case of room temperature, the magnetotransport of p-GaInAsSb/p-InAs heterostructures at liquid nitrogen temperature is determined solely by the electron channel (see table). The values of mobility at this temperature allow us to determine the parameters of the electron channel. In [10] we determined the dependence of the mobility in the electron channel on its width d_1 at the Fermi level ($\mu_1 \sim d_1^2$). For the values of mobility in electron channel $\mu_1 = 5 \times 10^4$ cm^2 V^{-1} s^{-1}, the width of the channel was found to be equal to $d_1 =$ 400 Å. From these data we estimated the width of the channel d_1 for our samples at $T = 77$ K (see table). As can be seen, the width of the electron channel slightly diminishes with an increase in indium concentration in solid solution and is estimated to be 300–400 Å.

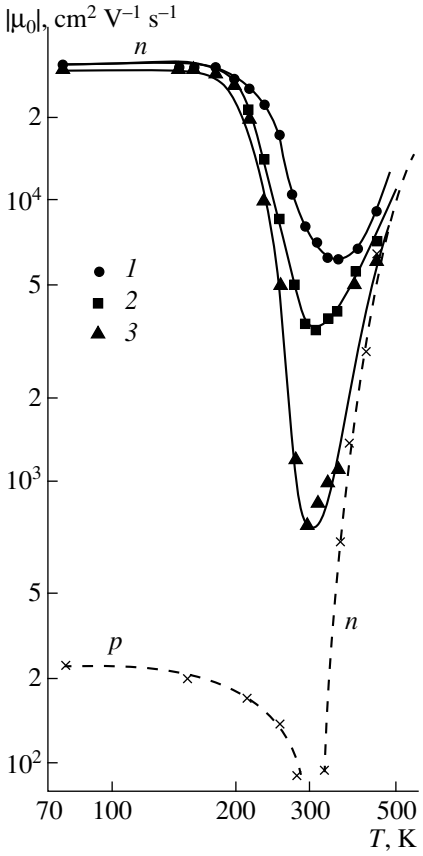

Fig. 2. Hall mobility μ_0 as a function of temperature for sample 6 in the magnetic field of $H =$ (*1*) 1, (*2*) 10, and (*3*) 20 kOe. The type of conductivity is indicated by *n* and *p*. The temperature dependence of μ_0 for the InAs substrate ($p = 10^{17}$ cm^{-3}) is shown by the dashed line.

Using the concepts of two-dimensional model [13], according to which the width of channel at Fermi level $d_1 = \pi/k_F$, where $k_F = (2\pi N_S)^{1/2}$ is the wave vector, it is possible to approximate the two-dimensional concentration of carriers in the electron channel at 77 K (see table). For the samples with indium content $x = 0.09$ and $x = 0.16$, the estimations yield $N_S = 10^{11}$ cm^{-2}, and for $x = 0.22$, the value of concentration is $N_S = 1.6 \times 10^{11}$ cm^{-2}.

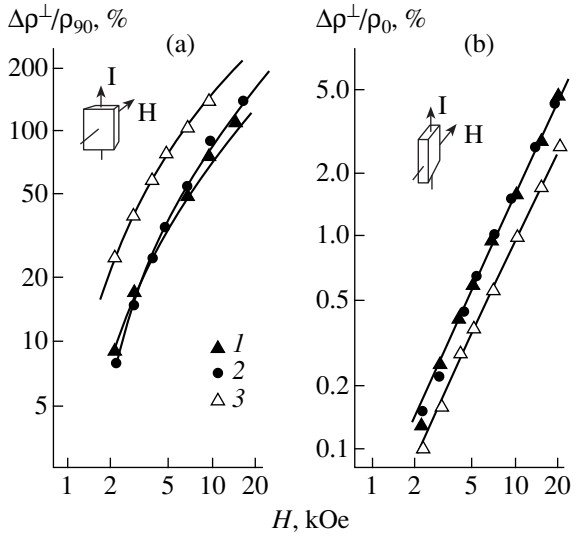

Fig. 3. Transverse magnetoresistance curves for different orientations of the sample with respect to magnetic field at T = 77 K. The numbers correspond to the samples in the table.

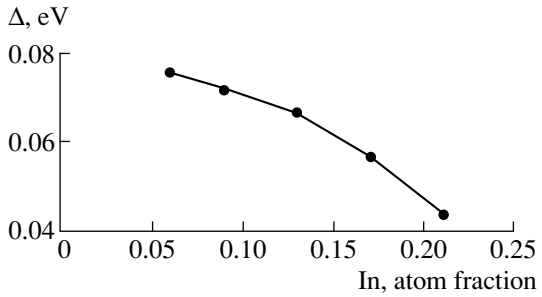

Fig. 4. Energy gap Δ at the heteroboundary in p-$Ga_{1-x}In_xAs_ySb_{1-y}$/p-InAs structures in relation to atomic fraction of In.

2.3. Magnetoresistance

Additional information about galvanomagnetic properties of heterostructures can be gained from the measurements of transverse magnetoresistance $(\Delta\rho/\rho)^{\perp}$ (the current vector is normal to the magnetic-field vector), because the transverse magnetoresistance is very sensitive to the occurrence of two types of current carriers and to dimensional effects.

Figure 3 shows the dependences of the transverse magnetoresistance $(\Delta\rho/\rho)^{\perp}$ on the magnetic field intensity H at T = 77 K for p-GaInAsSb/p-InAs heterostructures that had dissimilar indium content in solid solution and were grown on the substrates with the concentration $p = 10^{16}$ cm^{-3} (samples 1–3). The measurements were carried out for two orientations of the sample with respect to the magnetic field: the vector **H** was either collinear with the normal to the sample surface $(\Delta\rho/\rho)^{\perp}_{90}$ (the standard Hall orientation, Fig. 3a) or perpendicular to the normal $(\Delta\rho/\rho)^{\perp}_{0}$ (Fig. 3b). The dependences of transverse magnetoresistance on the magnetic field at T = 77 K for the samples 4–6 were similar.

As can be seen in Fig. 3a, the magnetoresistance $(\Delta\rho/\rho)^{\perp}_{90}$ in all samples increased proportionally to H^2 in weak magnetic fields $H < 3$ kOe. The quadratic dependence is valid until the condition $\mu H/c = 1$ is reached, which is in accordance with the high values of mobility in electron channel $\mu_1 = (3\text{–}5) \times 10^4$ cm^2 V^{-1} s^{-1}.

When the magnetic field is directed perpendicular to the normal to the sample surface, the value of magnetoresistance $(\Delta\rho/\rho)^{\perp}_{0}$ becomes ten times less than $(\Delta\rho/\rho)^{\perp}_{90}$, and no saturation effect is observed in magnetoresistance curves. Similar anisotropy is typical of dimensional effects [14].

The observed anisotropy of magnetoresistance is determined by the properties of the two-dimensional channel and supports the idea that the major contribution to the conductivity is due to the two-dimensional electron gas in the semimetal channel at the heteroboundary. The magnetoresistance anisotropy $\alpha = (\Delta\rho/\rho)^{\perp}_{0}/(\Delta\rho/\rho)^{\perp}_{90}$ increases with an increase in indium content in solid solution (see table), which indicates that the electron channel somewhat narrows with the increase of indium content.

The values of magnetoresistance coefficient $B_r = (\Delta\rho/\rho)^{\perp}_{90}/\mu_1^2 H^2$ calculated from the quadratic dependence of magnetoresistance (Fig. 3a), and from the estimate of the value of mobility μ_1 in the two-dimensional channel, were found to be less than 0.26 for all samples at T = 77 K (see table). The low values of B_r suggest that the conductivity is determined by a single kind of charge carrier (by electrons in the semimetal channel). A small increase in B_r in the samples with x = 0.22, as well as an increase in anisotropy of magnetoresistance, is related, in our opinion, to a slight decrease in the width d_1 of the electron channel with an increase in indium content in solid solution (see table).

Thus, the results obtained from the measurements of mobility and magnetoresistance show that p-GaInAsSb/p-InAs structures retain the semimetal properties in the electron channel at the interface for all compositions of solid solution.

3. COMPARISON OF EXPERIMENTAL RESULTS WITH THE BAND DIAGRAM OF p-$Ga_{1-x}In_xAs_ySb_{1-y}$/p-InAs HETEROJUNCTION

As is known, the energy gap between the conduction band of InAs and the valence band of GaSb at T = 300 K in GaSb/InAs heterostructure is equal to 150 meV [15]. This value for p-GaInAsSb/p-InAs

should vary with the composition of solid solution, doping level, and conditions at the heteroboundary.

In order to estimate the relative position of the bands and the energy gap Δ between the valence band of solid solution and the conduction band of InAs, we use the electron affinity rule

$$\Delta = \chi_2 - \chi_1 - E_{g1}, \quad (3)$$

where $\chi_2 = 4.9$ eV is the electron affinity in InAs, and χ_1 and E_{g1} are the electron affinity and the width of the forbidden band in the solid solution, respectively.

We calculated the width of the forbidden band and the electron affinity of the solid solution using the model of linear combination of contributions of binary compounds incorporated into GaInAsSb solid solution and taking into account the deviation parameter in $E_{g1}(x)$ function for ternary compounds. The following values for the forbidden gap of $Ga_{1-x}In_xAs_ySb_{1-y}$ solid solution were calculated for $T = 77$ K: $E_{g1} = 0.7$, 0.63, and 0.6 eV; $\chi_1 = 4.128$, 4.213, and 4.26 eV for $x = 0.09$, 0.16, and 0.22, respectively.

Based on these data for 77 K, the energy gap Δ was estimated. As can be seen in Fig. 4, the energy gap Δ persists with an increase in indium content in solid solution; therefore, we can expect that the electron channel exists for all compositions of solid solution. The largest value of energy gap is observed for the lowest indium concentrations in solid phase. Consequently, the depth of electron channel at the heteroboundary as measured from the Fermi level E_F must be larger for indium content in solid solution $x = 0.09$ and smaller for $x = 0.22$. The width of forbidden band E_{g1} at $T = 300$ K decreases (the temperature coefficient of the forbidden gap for the GaInSbAs solid solution is equal to 3.2×10^{-4} eV K^{-1} [16]), and hence the energy gap Δ, according to (3), should increase.

Comparing the experimental results with the above-presented band diagram, we may conclude that, at $T = 77$ K, the high electron mobility in the channel is observed for all compositions of solid solutions ($x \leq 0.22$). A small decrease in mobility in heterostructures with indium content $x = 0.22$ may be attributed both to a narrowing of the energy gap Δ at the heteroboundary and to a lowering of the Fermi level E_F in solid solution due to the increase of hole concentration [17].

At $T = 300$ K the electron channel persists for all compositions of solid solution. However, the mobility of electrons in the channel decreases for all compositions: the higher the electron mobility at $T = 77$ K, the greater the decrease in mobility. The experimentally observed decrease in mobility with increasing temperature may be attributed to the narrowing of the electron channel, as well as to possible broadening of electron quantum levels in the potential well on the InAs side due to the thermal energy kT, which results in an increase in scattering by the lattice [18]. All these factors limit electron mobility at $T = 300$ K by the value of about 2×10^4 cm^2 V^{-1} s^{-1}.

4. CONCLUSION

In this work, the transport properties of heterostructures in the p-$Ga_{1-x}In_xAs_ySb_{1-y}$/p-InAs system were studied. It is shown that, for the solid solution with compositions $x = 0.09$–0.22, type II separated heterojunction is formed at the heteroboundary. This heterojunction is characterized by the electron channel with high electron mobility.

The highest electron mobility in the channel at $T = 77$ K corresponds to the composition with $x = 0.09$ and 0.16 ($\mu_1 = 5 \times 10^4$ cm^2 V^{-1} s^{-1}). The width of the electron channel and the density of electrons at 77 K are estimated to be $d_1 = (300–400)$ Å and $N_S = (1 - 1.5) \times 10^{11}$ cm^{-2}, respectively.

The results of magnetoresistance study suggest two-dimensional nature of electrons in the channel.

At room temperature the carrier mobility in the electron channel decreases. This may be attributed to the scattering of electrons by the lattice vibrations, which restricts the mobility by values no higher than 2×10^4 cm^2 V^{-1} s^{-1}.

It is shown that the transport properties of p-$Ga_{1-x}In_xAs_ySb_{1-y}$/p-InAs heterostructures at high temperatures depend on the doping level of the p-InAs substrate. The utilization of these unique properties of the heterostructures at 300 K requires the elimination of the influence of the substrate.

ACKNOWLEDGMENTS

We thank T.A. Polyanskaya for her fruitful participation in discussion of the results and helpful comments.

This work was supported in part by the Russian Foundation for Basic Research, project no. 99-02-18330.

REFERENCES

1. C. Hidalgo, Plasma Phys. Controlled Fusion **37**, A 53 (1955).
2. T. C. Hasenberg, R. H. Miles, A. R. Kost, *et al.*, IEEE Quantum Electron. **33**, 1403 (1997).
3. A. N. Baranov, N. Bertru, Y. Cumminal, *et al.*, Appl. Phys. Lett. **71**, 735 (1997).
4. J. R. Meyer, C. A. Hoffman, and F. J. Bartoli, Appl. Phys. Lett. **67**, 757 (1955).
5. M. P. Mikhaĭlova, K. D. Moiseev, O. G. Ershov, *et al.*, Fiz. Tekh. Poluprovodn. (St. Petersburg) **30**, 399 (1996) [Semicond. **30**, 223 (1996)].
6. M. P. Mikhaĭlova and A. N. Titkov, Semicond. Sci. Technol. **9**, 1279 (1994).

7. N. L. Bazhenov, G. G. Zegrya, M. P. Mikhaĭlova, *et al.*, Fiz. Tekh. Poluprovodn. (St. Petersburg) **31**, 658 (1997) [Semicond. **31**, 560 (1997)].
8. T. I. Voronina, T. S. Lagunova, M. P. Mikhaĭlova, *et al.*, Fiz. Tekh. Poluprovodn. (St. Petersburg) **30**, 985 (1996) [Semicond. **30**, 523 (1996)].
9. T. I. Voronina, T. S. Lagunova, M. P. Mikhaĭlova, *et al.*, Fiz. Tekh. Poluprovodn. (St. Petersburg) **31**, 897 (1997) [Semicond. **31**, 763 (1997)].
10. I. A. Andreev, T. I. Voronina, T. S. Lagunova, *et al.*, Fiz. Tekh. Poluprovodn. (St. Petersburg) **29**, 678 (1995) [Semicond. **29**, 353 (1995)].
11. T. I. Voronina, T. S. Lagunova, M. P. Mikhaĭlova, *et al.*, Fiz. Tekh. Poluprovodn. (St. Petersburg) **32**, 215 (1998) [Semicond. **32**, 195 (1998)].
12. N. Kuze and I. Shibasaki, *III–V Review* (1997), Vol. 10, p. 28.
13. V. K. Subashiev and S. A. Plotnikov, Fiz. Tekh. Poluprovodn. (Leningrad) **2**, 1169 (1960).
14. T. Ando, A. Fowler, and F. Stern, Rev. Mod. Phys. **54**, No. 2, 1982 [*Electronic Properties of Two-Dimensional Systems* (Mir, Moscow, 1985)].
15. A. I. Klimovskaya, O. V. Snitko, and S. I. Kirilliva, Pis'ma Zh. Éksp. Teor. Fiz. **11**, 1191 (1970).
16. G. H. Dohler, Surf. Sci. **98**, 108 (1980).
17. T. I. Voronina, T. S. Lagunova, M. P. Mikhaĭlova, *et al.*, Fiz. Tekh. Poluprovodn. (Leningrad) **25**, 276 (1991) [Sov. Phys. Semicond. **25**, 167 (1991)].
18. A. N. Baranov, A. N. Dakhno, B. E. Dzhurtanov, *et al.*, Fiz. Tekh. Poluprovodn. (Leningrad) **24**, 98 (1990) [Sov. Phys. Semicond. **24**, 59 (1990)].
19. A. I. Ansel'm, *Introduction to the Theory of Semiconductors* (Nauka, Moscow, 1970).

Translated by A. Zalesskiĭ

Semiconductors, Vol. 34, No. 2, 2000, pp. 195–204. Translated from Fizika i Tekhnika Poluprovodnikov, Vol. 34, No. 2, 2000, pp. 200–210.

LOW-DIMENSIONAL SYSTEMS

Thermal Annealing of Defects in InGaAs/GaAs Heterostructures with Three-Dimensional Islands

M. M. Sobolev, I. V. Kochnev, V. M. Lantratov, N. A. Bert, N. A. Cherkashin, N. N. Ledentsov, and D. A. Bedarev

Ioffe Physicotechnical Institute, Russian Academy of Sciences, Politekhnicheskaya ul. 26, St. Petersburg, 194021 Russia

Submitted July 14, 1999; accepted for publication July 15, 1999

Abstract—A report is presented on the investigation of the influence of *in situ* annealing of the InGaAs layer in *p–n* InGaAs/GaAs structures grown by the metalloorganic chemical vapor deposition upon the formation of coherently strained three-dimensional islands. The structures were studied by the methods of capacitance–voltage measurements, deep-level transient spectroscopy, transmission electron microscopy, and photoluminescence. It is established that three-dimensional islands with misfit dislocations are formed in the unannealed structure *A*, while quantum dots are formed in the annealed structure *B*. The deep-level defects were investigated. In structure *A*, defects of various types (*EL*2, *EL*3 (*I*3), *I*2, *HL*3, *HS*2, and *H*5) are present in the electron-accumulation layer. Concentrations of these traps are comparable to the shallow donor concentration, and the number of hole traps is higher than that of the electron traps. On the *in situ* annealing, the *EL*2 and *EL*3 defects, which are related to the formation of dislocations, disappear, and concentrations of the other defects decrease by an order of magnitude or more. For structure *A*, it is established that the population of the quantum states in the islands is controlled by the deep-level defects. In structure *B*, the effect of the Coulomb interaction of the charge carriers localized in the quantum dot with the ionized defects is observed. © *2000 MAIK "Nauka/Interperiodica".*

1. INTRODUCTION

Intensive studies of the optical, structural, and electrical properties of zero-dimensional semiconductor structures have been carried out in recent years in many laboratories [1]. Interest in these structures is related to their possible applications in lasers, single-electron transistors, and memory devices. The most considerable advances in the fabrication of quantum dots (QDs) were made with the technique of the self-organized nanostructure growth, first described by Stranski and Krastanow [2]. It is known [1, 2] that the Stranski–Krastanow growth mode can be realized if there is a lattice mismatch between the substrate and the heteroepitaxial layer being deposited. In this case, the epilayer acquires large elastic energy, which tends to be reduced. This may occur in two ways: by the formation of isolated strained islands (quantum dots), or by the formation of islands with misfit dislocations; both types of islands can also coexist in the structure. The electronic spectrum of such an isolated island is similar to the spectrum of a single atom [1]. In most cases, QDs can be formed without employment of any additional technological processes; e.g., this is true in the case of direct three-dimensional (3D) growth of the InAs/GaAs heterostructures by molecular-beam epitaxy. When 3D InGaAs/GaAs heterostructures are grown by the metal-organic chemical vapor deposition (MOCVD) under the standard conditions, the 3D In-rich dislocation clusters, coexisting with the QDs, can be produced. It was noted in [4] that the formation of dislocations can be avoided by switching off the arsine flux during the growth interruption. It is also possible to fabricate the dislocation-free QDs using the postgrowth annealing of the near-surface region, which results in the formation of the quasi-regular 3D islands [5]. Such an annealing has been tested for the growth of InSb/InP heterostructures [6]; the QDs were of better crystalline quality, and the 3D defects were absent in the annealed sample, in contrast to the unannealed one. The effect of the postgrowth annealing on the quality and properties of the structures with the QDs is usually examined through structural and optical studies [6, 7]. There are virtually no reports on studies of the deep-level defects and impurities (present in both annealed and unannealed structures) and their influence on the population of the quantum-confined states in the dots. At the same time, deep-level transient spectroscopy (DLTS) is the most effective technique for studies of the spectra of the deep-level defects and impurities [8]. In recent years, this method has been applied with good results to the spectroscopic studies of the quantum states in the InAs/GaAs dots [9–12]. Another technique that is successfully used to determine the effective profile of the carrier distribution in the structures with QDs is capacitance–voltage (*C–V*) spectroscopy. Serious problems are known to arise in the identification of the peaks in the DLTS spectra of the structures containing both defect deep levels and QD levels. It has been noted in

1063-7826/00/3402-0195$20.00 © 2000 MAIK "Nauka/Interperiodica"

our previous publications [11, 12] that the dependence of the DLTS signal amplitude on the position of the Fermi level is different for the spatially localized states and those distributed over the thickness of the epitaxial layer. It was proposed that the Fermi level position and the population of the QD states for certain ratios of the concentrations of shallow and deep centers in the GaAs matrix can be controlled by isochronal thermal annealing with or without application of the reverse bias and under illumination with white light.

In this paper, we report the results of our studies on the influence of annealing performed after the overgrowth of the InGaAs layer with GaAs on the formation of the 3D coherently strained dislocation-free islands and point defects at or near the heteroboundaries with QDs. We observed and investigated the effect of control of the QD-state population by the deep-level defects in the unannealed samples and the effect of the Coulomb interaction of the carriers localized in the QDs with the ionized deep-level defects. The structures under study were grown by MOCVD. The structural studies were carried out by the transmission electron microscopy (TEM) technique. The optical and electrical properties of the heterostructures with the InGaAs islands embedded into the GaAs matrix were investigated with the photoluminescence (PL), *C–V,* and DLTS techniques.

2. EXPERIMENTAL

The InGaAs/GaAs heterostructures studied in this work were fabricated by the MOCVD technique in a horizontal low-pressure (76 torr) reactor. Trimethylgallium, trimethylaluminum, ethyldimethylindium, and arsine were used as sources for the main constituents, and Cp_2Mg was used for *p*-type doping of GaAs. Two structures, designated hereinafter as *A* and *B*, were grown with different growth conditions and subsequent treatment. The growth temperature was 480°C. In both cases, a 0.5-μm-thick undoped GaAs layer (with carrier concentration $n = 3 \times 10^{15}$ cm^{-3}) was grown on the n^+-GaAs substrate. Next, an InGaAs layer was deposited. In structure *A*, the entire process was carried on without interruptions in growth. In structure *B*, growth was interrupted after the deposition of the InGaAs QD layer; next, a thin 50-Å-thick layer of GaAs was deposited over the QD layer and the temperature was raised to 600°C and *in situ* annealing was performed for 10 min. Subsequently, an *n*-GaAs layer 1.0 μm thick in structure *A* and 0.5 μm thick in structure *B* was deposited at 480°C. To form the *p–n* junction, a layer of doped p^+-type GaAs was next grown over the *n*-GaAs; its thickness was 0.3 and 0.1 μm in structures *A* and *B*, respectively. Spatially localized states in the islands, defect- and impurity-related deep levels, and the profile of the carrier distribution in the heterostructures were studied by DLTS and *C–V* methods with a DL4600 BIO-RAD spectrometer operating in the dual-gate averaging mode. A Boonton-72B bridge working at 1 MHz frequency was used for the capacitance measurements. The sensitivity of this bridge is $\Delta C/C_0 \approx 10^{-4}$. Nonrectifying contacts were thermally deposited onto the n^+-GaAs substrate and the p^+-GaAs layer to permit the DLTS and *C–V* measurements. Prior to measuring each of the DLTS or *C–V* spectra, the sample was subjected to isochronal annealing for 1 min at a fixed temperature T_a (from 80 to 450 K) under one of the three bias conditions: reverse-bias voltage applied ($U_{ra} < 0$), zero voltage ($U_{ra} = 0$), and forward-bias voltage applied ($U_{fa} > 0$). When annealing was performed at $U_{ra} < 0$, the sample was first heated to 450 K, then kept for 1 min at $U_{ra} = 0$ and next cooled to the annealing temperature. Before annealing was performed at $U_{ra} = 0$ or $U_{fa} > 0$, the sample was kept at $U_{ra} < 0$. Then, the sample was cooled to 80 K under one of three conditions: $U_{ra} < 0$, $U_{ra} = 0$, or $U_{fa} > 0$. Next, the DLTS or *C–V* measurements began, either in the dark or under white-light illumination. The thermal activation energies E_a and carrier capture cross sections $\sigma_{n,p}$, which characterize the trapping centers, were determined from the corresponding Arrhenius plots.

In the PL studies, the 514.5-nm green line from an Ar-ion laser was used to excite the samples, which were placed in a liquid-nitrogen (LN_2) cryostat. The luminescence spectra were measured using a 0.5-nm monochromator equipped with an LN_2-cooled germanium diode.

The structural studies of the 3D InGaAs/GaAs islands were carried out with an EM420 Philips transmission electron microscope operating at an accelerating voltage of 100 kV; both planar and cross-sectional geometries were employed. Samples for the cross-sectional studies were prepared by the standard procedure using final sputtering with 4-kV Ar ions at the grazing angle of incidence in a Gatan Duo-Mill 600 system. To prepare the samples for studies in planar geometry, they were etched in the $H_2SO_4 : H_2O_2 : H_2O$ (5 : 1 : 1) after the upper layer of the material was removed.

3. RESULTS

Images of the InGaAs islands embedded in the GaAs matrix and observed in the planar and cross-sectional geometry are presented in Fig. 1 both for unannealed sample *A* (a, b) and *in situ* annealed sample *B* (c, d). The planar-geometry images were obtained in the bright-field mode under double-beam conditions; the direction of the incident electron beam was [001], and that of the reflected beam was [220]. The cross-sectional images were obtained under the double-beam conditions in the dark-field mode with the use of the [200] reflection spot, with the incident beam being oriented along the [011] direction. With such a choice of imaging modes, maximum information about the strain distribution in the InGaAs layer can be obtained, and

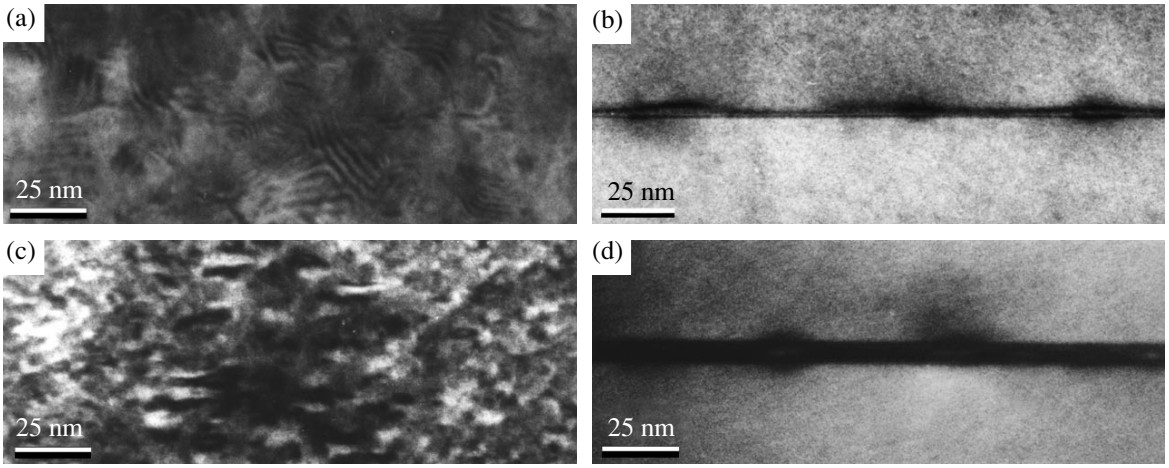

Fig. 1. Electron-microscope images of the InGaAs islands in the GaAs matrix for [(a) and (b)] unannealed sample *A* and [(c) and (d)] *in situ* annealed sample *B*. The images are taken [(a) and (c)] in the planar geometry under the bright-field (220) mode and [(b) and (d)] in the cross-sectional geometry under the dark-field (200) mode.

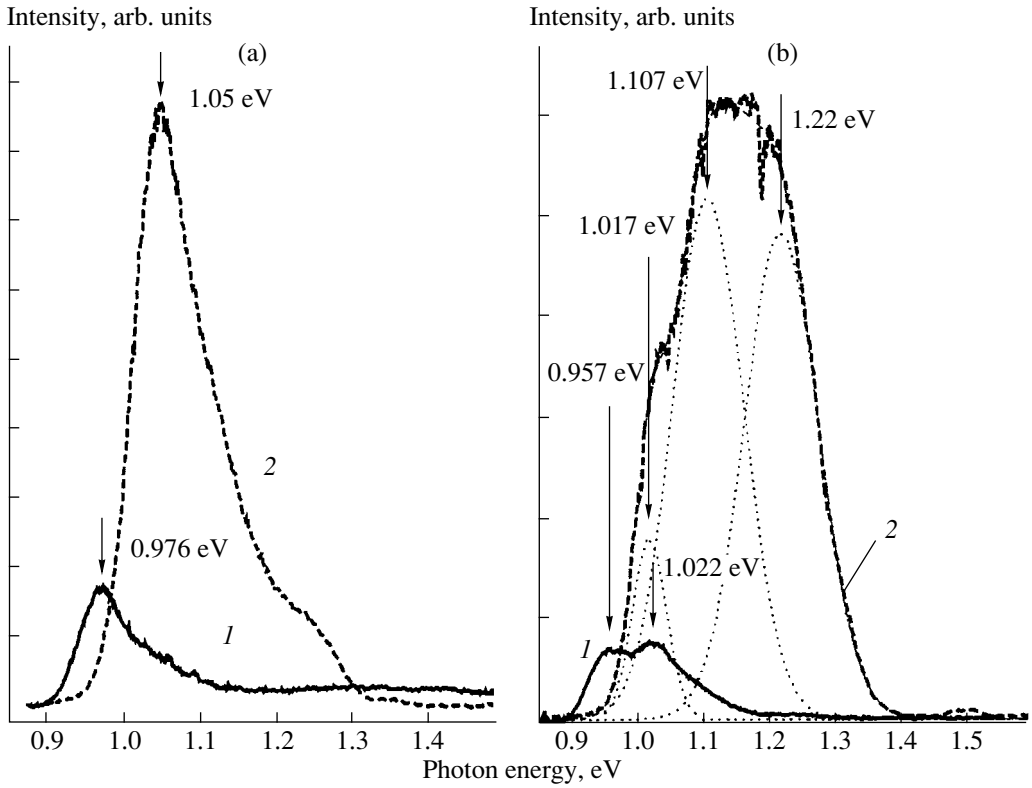

Fig. 2. Photoluminescence spectra of the InGaAs/GaAs structures with the three-dimensional islands for (a) unannealed sample *A* and (b) *in situ* annealed sample *B*. The measurement temperatures are (*1*) 300 K and (*2*) 77 K.

both the lateral size of the observed strained islands and their height can be estimated. In sample *A*, the InGaAs layer has an island structure with the lattice relaxed via generation of misfit dislocations, which is evidenced by the moire pattern seen in the island images in Fig. 1a. Examining the moire pattern, one can find that the average lattice constant in the islands is ~5.98 Å. With the influence of strain taken into account, this corresponds to the InAs lattice constant. Existence of dislocations at the interface between the wetting layer and the islands in sample *A* is confirmed by the image in Fig. 1b: the contrast in the region of the 3D islands is asymmetric and nonuniform. The estimated areal density of the islands is about 8×10^{10} cm^{-2}, and their mean lateral

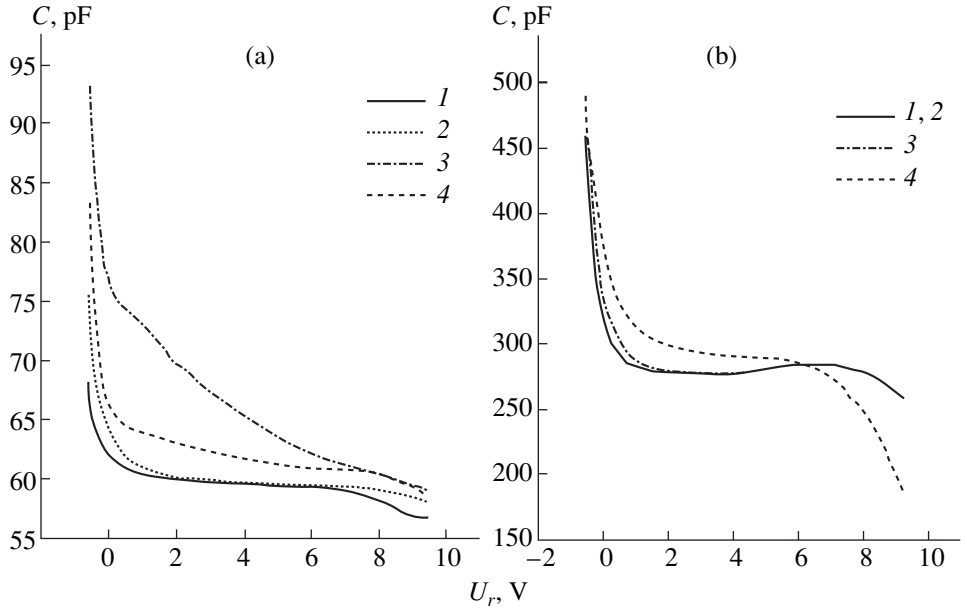

Fig. 3. *C–V* characteristics of the *p–n* heterostructure containing the three-dimensional islands: (a) unannealed sample *A* and (b) *in situ* annealed sample *B*. The measurements were carried out after isochronal annealing at T_a = 450 K with subsequent cooling to 80 K under the following conditions: (*1*) $U_{ra} < 0$, without illumination; (*2*) $U_{ra} = 0$, without illumination; (*3*) $U_{ra} < 0$, white-light illumination; and (*4*) $U_{ra} < 0$, increased final temperature (240 K).

size equals 20–30 nm. The island height estimated from the image in Fig. 1b is ~5–6 nm. In the *in situ* annealed sample *B*, the surface relief pattern of the InGaAs layer is quite complicated, as can be seen in Figs. 1c and 1d; the contrast observed is typical of the QDs. The estimated density of these dots is about 5×10^{10} cm^{-2}; their mean lateral size and height are about 14 and 7 nm, respectively.

PL spectra of samples *A* and *B* at high excitation energy are shown in Figs. 2a and 2b, respectively. The PL line observed at the photon energy $h\nu$ = 1.05 eV in the spectrum of the first structure at LN_2 temperature is related to the electron and hole ground states in the dots [1]. Another feature in this spectrum is a high-energy shoulder, whose energy position estimated from the fitting of the line shape with the Gaussian functions is about 1.23 eV. In the PL spectra of the second sample (Fig. 2b), a number of peaks at 1.017, 1.107, and 1.22 eV are observed. The relative heights of these peaks are independent of the excitation level, unlike the second peak in the spectra of sample *A*, which disappears at low excitation levels.

The *C–V* characteristics of samples *A* and *B*, taken at different temperatures, are shown in Figs. 3a and 3b for different conditions of isochronal annealing. An extended plateau in the *C–V* curves can be seen at low measurement temperatures, which is typical of the structures with QDs. The width of the plateau in the *C–V* curve depends on the population of QD levels with charge carriers. Upon raising the temperature to 240–300 K, an increase in capacitance occurs; instead of a wide, clearly pronounced plateau, a decrease in capacitance with the reverse bias voltage U_r is observed. The rate of this decrease is significantly higher in sample *A* (Fig. 3a) than in sample *B* (Fig. 3b). At low temperatures, rather sharp peaks coinciding with those calculated for the InGaAs layer appear in the distribution profiles $n^*(x)$ of the free electron concentration (calculated from the *C–V* curves) in both samples. In sample *A*, the electron accumulation region expands towards the *p–n* junction as the temperature increases. The free electron concentration $n^*(x)$ in this region increases from 2×10^{15} cm^{-3} at 77 K to 3.4×10^{16} cm^{-3} at 300 K. In sample *B*, no such changes were observed. The electron accumulation peak merely decreases and broadens at 300 K, which is typical of the QDs, and the free electron concentration in the *n*-GaAs layer changes slightly from 5×10^{15} to 8.5×10^{15} cm^{-3}. For sample *A*, significant reversible changes in the *C–V* characteristics were observed with changing the conditions of isochronal annealing ($U_{ra} = 0$ or $U_{ra} < 0$) and with switching on the white-light illumination. After isochronal annealing at $U_{ra} < 0$, the capacitance shows an increase in the *C–V* plateau region, as compared to annealing at $U_{ra} = 0$. The white-light illumination results in an even larger increase in capacitance. For sample *B*, isochronally annealed at $U_{ra} = 0$ and $U_{ra} < 0$, the *C–V* characteristics do not differ from each other. Upon white-light illumination, the capacitance shows a slight increase in the voltage range from 0.5 V of forward bias to U_r = 2.0 V.

From the *C–V* measurements, we get information about the spatial localization of the islands and find the

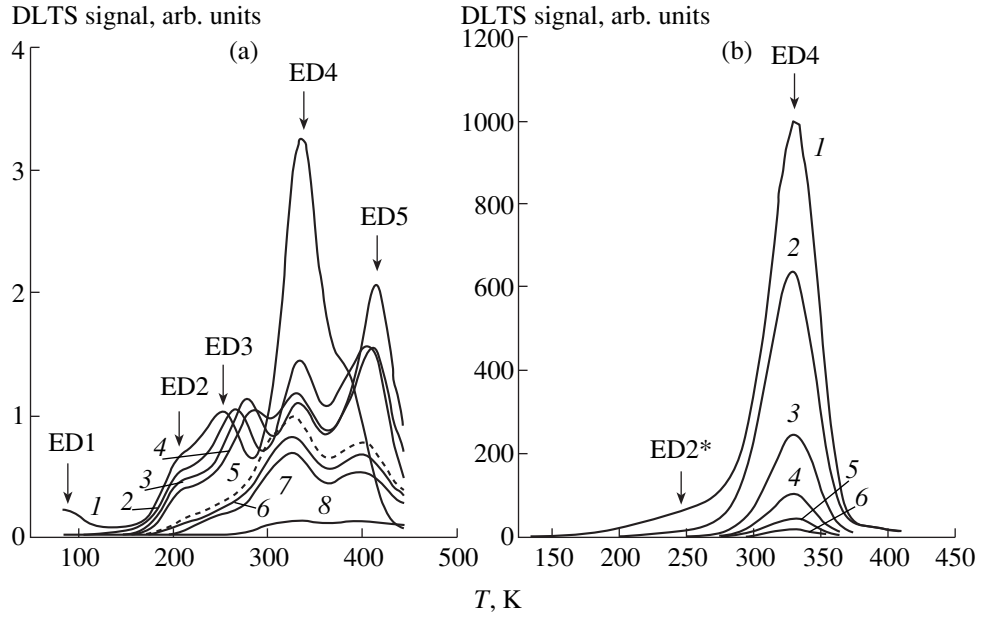

Fig. 4. DLTS spectra of the *p–n* InGaAs/GaAs heterostructures containing the three-dimensional islands at different voltages of the reverse-bias pulse U_r and the filling pulse U_p, with fixed $\Delta U = U_r - U_p = 0.5$ V: (a) unannealed sample *A* under reverse bias voltage equal to (*1*) 0.5, (*2*) 1.0, (*3*) 1.5, (*4*) 2.0, (*5*) 3.5, (*6*) 4.0, (*7*) 4.5, and (*8*) 8.0 V; (b) *in situ* annealed sample *B* under reverse bias voltage equal to (*1*) 0.5, (*2*) 1.0, (*3*) 1.5, (*4*) 2.0, (*5*) 2.5, and (*6*) 3.0 V. All spectra were taken with the emission rate window set at 200 s^{-1} and the filling pulse duration of 5 ms.

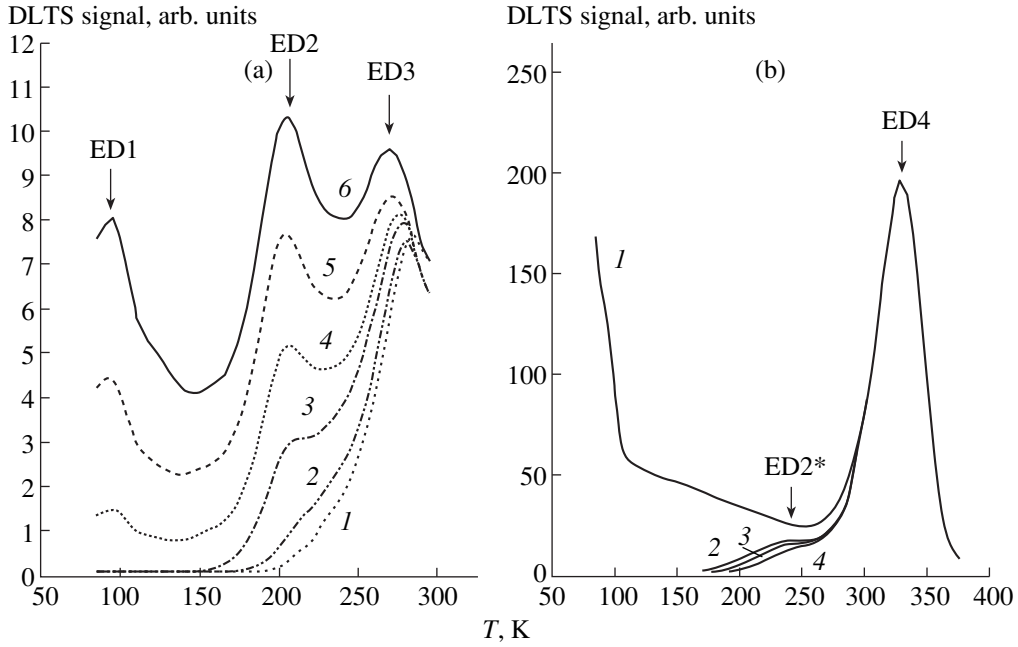

Fig. 5. DLTS spectra of the *p–n* InGaAs/GaAs heterostructures with the three-dimensional islands: (a) unannealed sample *A*, with U_r = (*1*) 2.5 and (*2*, *4*) 2.0 V and U_p (forward bias) equals (*1*, *3*) 1.84, (*2*) 1.4, and (*4*) 4.65 V; (b) *in situ* annealed sample *B*, U_r = 0.2 V and U_p (forward bias) equals (*1*) 4.7 and (*2*) 0 V. All spectra were taken with the emission rate window set at 200 s^{-1} and the filling pulse duration of 5 ms.

conditions for observation of the DLTS peaks corresponding to the carrier emission from the quantum states within the islands and the defects located nearby.

To determine the spatial localization of the DLTS signal in both samples, we performed a series of measurements with varying amplitudes of the filling pulse U_p

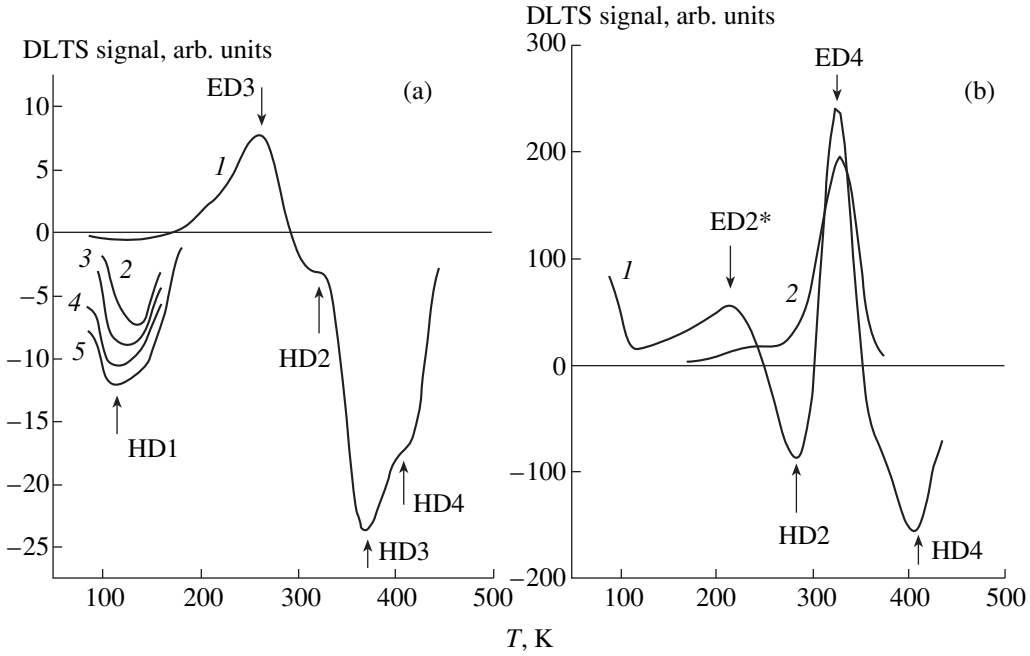

Fig. 6. DLTS spectra of the *p–n* InGaAs/GaAs heterostructures with the three-dimensional islands. (a) Unannealed sample *A* isochronally annealed at T_a = 450 K and cooled under the following conditions: (*1*) $U_{ra} = 0$; (*2*) $U_{ra} < 0$; (*3*) $U_{fa} = 1.9$ V; and (*4*)–(*6*) $U_{ra} < 0$; in cases (*4*)–(*6*), the spectra were measured under illumination by the white light with intensity $I_4 < I_5 < I_6$; $U_p = 1$ V (reverse bias); and $U_r = 1.5$ V. (b) *In situ* annealed sample *B* isochronally annealed at T_a = 405 K and cooled under the following conditions: [(*1*) and (*2*)] $U_{ra} < 0$, (*3*) $U_{ra} = 0$, and (*4*) $U_{fa} = 1.9$ V; spectrum (*1*) was taken under illumination by the white light; $U_p = 0$ V, U_r = 0.25 V.

and reverse-bias pulse U_r, keeping the difference $\Delta U = U_r - U_p = 0.5$ V constant and equal to 0.5 V; the corresponding spectra are shown in Fig. 4. In the DLTS spectra of sample *A* (Fig. 4a), which was not subjected to annealing during growth, five peaks, related to the electron emission from the traps, are clearly seen. The amplitudes of these peaks vary, reaching a maximum and then decreasing with U_r and U_p. For the peaks *ED*1, *ED*2, and *ED*4, the maximum appears at $U_r = 0.5$ V. The peak *ED*3 shifts to higher temperatures when U_r is varied from 0.5 to 2.0 V, while its amplitude changes under these conditions only slightly. The energy of thermal activation E_a of this level and the capture cross section σ_n vary from 347 to 530 meV and from 1.9×10^{-16} to 3.4×10^{-14} cm^{2}2, respectively. Upon further increase in U_r, the amplitude of this peak decreases rapidly. For this sample, dependence of the DLTS spectra on the temperature and conditions of the premeasurement isochronal annealing ($U_{fa} > 0$, $U_{ra} < 0$, or $U_{ra} = 0$) and on the optical illumination was studied (Fig. 5a). Nothing unusual was observed in the behavior of the peaks *ED*4 and *ED*5, which obviously correspond to the well-known GaAs defects (see table), whereas the *ED*1, *ED*2, and *ED*3 peaks were found to be quite sensitive to the isochronal annealing conditions and optical illumination. The peaks *ED*1 and *ED*2 virtually disappear upon annealing at $U_{ra} = 0$. The peak *ED*2 appears on annealing with $U_{ra} < 0$. Upon annealing under the forward bias $U_{fa} > 0$, the amplitude of the *ED*2 peak grows, and the *ED*1 peak appears. Both of these peaks grow even more when the DLTS measurements are carried out under white-light illumination, their amplitudes increasing with the light intensity. The *ED*2 peak also shifts slightly to lower temperatures. The thermal activation energy of the level corresponding to *ED*2 varies from 287 to 252 meV, and the capture cross section varies from 1.1×10^{-16} to 2.4×10^{-17} cm^2. The *ED*3 peak under these measurement conditions also shifts to lower temperatures, and its amplitude increases somewhat. The maximum concentrations of the *ED*4, *ED*5, and *ED*3 centers, derived from the amplitudes of the corresponding DLTS peaks, are given in the table. The DLTS spectra were also taken for different amplitudes U_p of the filling voltage pulses applied in the forward direction, in which case the holes are injected and the hole traps are filled. Four hole traps were revealed; three of them (*HD*2, *HD*3, and *HD*4) can be attributed to the well-known defect levels (see table). The concentration of acceptor levels is nearly three times higher than that of the donor levels (see table). The *HD*1 DLTS peak is bell-shaped with the maximum shifted with respect to the centroid; its position depends on the reverse bias voltage and the filling pulse amplitude. This level cannot be identified with any of the known levels. The thermal activation energy E_a of the *HD*1

Summary of the defect parameters

Levels	E_a, meV	Capture cross section $\sigma_{n,p}$, cm^2	Defect concentration N_t, cm^{-3}		Level identification
			sample *A*	sample *B*	
*ED*1	165	6.5×10^{-14}			
*ED*2	252	2.4×10^{-17}			
*ED*2*	293	1.9×10^{-17}			
*ED*3	530	3.4×10^{-14}	1.2×10^{15}	–	*EL*3 [15], *I*3 [13]
*ED*4	667	7.4×10^{-14}	3.6×10^{15}	2.0×10^{14}	*E*4 [14], *I*2 [13]
*ED*5	825	1.1×10^{-13}	2.2×10^{15}	–	*EL*2 [15]
*HD*1	199	4.7×10^{-16}			
*HD*2	525	2.5×10^{-16}	1.3×10^{16}	7.0×10^{13}	*HL*3 [16, 17]
*HD*3	553	3.0×10^{-17}	2.5×10^{16}	–	*HS*2 [16]
*HD*4	821	1.0×10^{-16}	2.4×10^{16}	1.1×10^{14}	*H*5 [18]

level varies from 126 to 199 meV, and the hole capture cross section σ_p varies from 1.6×10^{-17} to 4.7×10^{-16} cm^2.

In the DLTS spectra of sample *B*, which has been subjected to thermal annealing during growth, significant changes can be observed in comparison with the spectra of sample *A* (see Figs. 4b, 5b, 6b). The defects related to peaks *ED*3, *ED*5, and *HD*3 vanish (Figs. 4b, 6b) and concentration of the defects related to the other peaks decreases by more than an order of magnitude (see table). In the DLTS spectra taken after the premeasurement isochronal annealing and optical illumination, major changes occurred in the behavior of the peak *ED*2, so we denote it as *ED*2* in sample *B* (Fig. 5b). The *ED*2* peak does not vanish upon annealing at $U_{ra} = 0$; it merely shifts to lower temperatures. A still larger shift in the same direction takes place upon annealing at $U_{fa} > 0$. Optical illumination results in a slight increase of the peak amplitude; in addition, a large low-temperature (~80 K) DLTS signal appears.

4. DISCUSSION

From the TEM data (Figs. 1a, 1b), one can see that in the MOCVD-grown *p–n* InGaAs/GaAs heterostructures under study, 3D islands with misfit dislocations are formed in unannealed sample *A*, while coherently strained 3D islands, i.e., the quantum dots, are formed in *in situ* annealed sample *B*. The behavior of the *C–V* characteristics taken at different temperatures and isochronal annealing conditions (Figs. 3a, 3b) indicate that spatially localized states accumulating electrons exist in these heterostructures. In sample *A* at low temperatures, the electrons are accumulated both in the quantum states within the InGaAs islands and in the deep donor and acceptor levels present in GaAs. In this sample, concentration of deep donors N_{td} is comparable to the concentration of the shallow donors N_d, and the concentration of the compensating deep acceptors N_{ta} is higher than N_{td}. With a decrease in temperature, the rate of electron emission from the deep near-midgap levels becomes extremely low, and the plateau observed in the *C–V* characteristics is caused by the quantum-confined states in the islands. The plateau width is determined by the population of the levels at a given temperature. The surface density n_d of the electrons occupying the quantum states in the islands can be estimated from the bias voltages at the starting (U_{r1}) and ending (U_{r2}) points of the plateau, the magnitude C^* of the capacitance at the plateau, and the diode area S: $n_d = C^*(U_{r1} - U_{r2})/S$. This estimate yields the value of 4.9×10^{11} cm^{-2} for unannealed structure *A* and 5.7×10^{11} cm^{-2} for *in situ* annealed structure *B*. With an increase in temperature, the rate of electron emission from the deep levels increases and becomes comparable with the rate of emission from the quantum-confined states in the islands. Since the deep-donor concentration is of the same order as the concentration of the shallow donors and the density of the quantum states, this leads to a significant enhancement of the capacitance and to an increase in the slope of the *C–V* curve in the plateau region (Fig. 3a). In sample *B*, the concentration of the deep donor and acceptor levels is lower than that of the shallow donor impurities, and their recharging, which takes place under isochronal annealing, does not affect the *C–V* curve. A minor rise of the *C–V* curve in the plateau region is observed in this sample, starting from $U_r > 4$ V. This is related to the enhancement of the field-induced electron tunneling through the barrier from the states in the QDs into the GaAs layer. Under the optical illumination at low U_r, an increase in the capacitance apparently occurs due to trapping of the electrons, which are excited in the neutral *n*-GaAs layer, by the dots. This result indicates that, contrary to the conclusions made in [19], the rate of electron trapping by the dots is higher than that of trapping the holes, which are also generated by the illumination. The surface density of the electrons occupying the quantum states in the dots in the *in situ* annealed structure *B* was estimated

from the above-given formula and was found to be 5.7×10^{11} cm^{-2}. The DLTS studies also demonstrated that a large number of deep-level donor and acceptor defects are present in unannealed sample *A*, with the concentration of the deep acceptors higher than that of the deep donors (see table). Using the parameters of the deep levels determined from the Arrhenius plots and the observed variations of the DLTS spectra in different conditions (see Figs. 4a, 5a, and 6a), we were able to identify some of the donor (*ED*3, *ED*4, and *ED*5) and acceptor (*HD*2, *HD*3, and *HD*4) levels with those well known from previous publications. The parameters of the *ED*4 level proved to be close to those of the defect *I*2 [13] (*E*4 [14]), which is produced in GaAs by ionizing radiation and is related to the cluster composed of the arsenic vacancy V_{As} and the antisite defect As_{Ga}. These clusters were detected in both of the samples investigated. The distribution profile of this defect has two maxima: the higher one corresponds to $U_r = 0.5$ V, and the lower one to $U_r = 2.0$ V (Fig. 4a). Parameters of the next donor level, *ED*5, coincide with those of the *EL*2 defect [15]; this was found only in the unannealed structure *A* containing the 3D InGaAs islands with misfit dislocations. The *EL*2 defect is usually observed in the layers that contain dislocations and forms the Cottrell environment around them [20]. The trap related to the misfit dislocation core forms a level with the energy of 0.58 eV [20]. It is conceivable that the trap manifests itself in our DLTS spectra as a low-temperature shoulder of the *ED*5 peak. The maximum in the *EL*2 defect distribution corresponds to $U_r = 1.5$ V; it coincides with the dip in the distribution profile of the V_{As}–As_{Ga} clusters. The properties of the *HD*2 level are close to those of the *HL*3 level, first observed in the GaAs grown by the liquid-phase epitaxy [16]. This state is related to the complex of native defects, which includes the arsenic vacancy V_{As} [17] and is produced when excess Ga is present in the melt–solution. In our case, appearance of the V_{As}-containing defects may result, in particular, from the local stoichiometry variations due to the In diffusion during the growth of the epitaxial GaAs layer and the formation of the QDs [21]. The maximum concentration of the *HD*2 centers in sample *A* is $N_t = 1.3 \times 10^{16}$ cm^{-3} at $U_r = 0.5$ V, and in sample *B*, it is reduced by two orders of magnitude ($N_t = 1.4 \times 10^{14}$ cm^{-3}). Another DLTS peak, *HD*3, is also present in the spectra of sample *A* and absent in sample *B*. It can be identified with the *HS*2 defect in GaAs [16] and, like *HL*3, is produced when there is an excess of Ga in the melt–solution. The parameters of the *HD*4 level are close to the parameters of the Cr^{3+} [16] as well as to those of the *H*5 defect, which is generated by ionizing radiation [18]. Now, to establish the nature of the peaks *ED*1, *ED*2, and *ED*3 (Fig. 5a) in sample *A*, and peak *ED*2* (Fig. 5b) in sample *B*, let us consider in more detail their behavior under different conditions of preliminary isochronal annealing and optical illumination. In sample *A*, annealing and illumination lead to changes in the amplitudes of the *ED*1 and *ED*2 peaks and to the slight shift of the *ED*1 peak to lower temperatures (Fig. 5a). Simultaneously, corresponding changes in the *C–V* characteristics occur (Fig. 3a). We demonstrated in our previous work [11, 12] that the amplitude ΔC of the DLTS signal from the spatially localized states depends on the variations in the Fermi level position and in the population of the quantum-confined or surface states and is determined from the relation

$$\Delta C/C = n_d L/2N_d W^2, \quad (1)$$

where C is the capacitance of the space-charge layer for the reverse-bias voltage, which is set to perform the DLTS measurement; n_d is the surface density of the electrons trapped by the localized state; L is the depth of the QD layer; W is the width of the space-charge region; and N_d is the donor concentration in the GaAs layer. This relation is typical of the spatially localized states and enables us to distinguish them from the deep defect levels distributed over the depth of the semiconductor. On the change of the isochronal annealing conditions from $U_{ra} = 0$ to $U_{ra} < 0$, the capacitance of sample *A* increases (Fig. 3a), which can be explained in the following way. Upon annealing at 450 K at $U_{ra} = 0$ and subsequent cooling to 80 K, the deep donor levels *ED*4 and *ED*5 trap electrons and become neutral. The concentration of the uncompensated donors is reduced, the Fermi level shifts downwards, the population of the spatially localized states decreases, and the amplitudes of the *ED*1 and *ED*2 DLTS peaks decrease (Fig. 5a). Upon annealing and cooling at $U_{ra} < 0$, the donor levels remain unfilled at low temperatures; hence, the population of the localized states and the amplitudes of the low-temperature peaks *ED*1 and *ED*2 do not change. Correspondingly, upon annealing and subsequent cooling at $U_{fa} > 0$, the holes are injected through the *p–n* junction, with some fraction of them being then captured at the deep acceptor levels in the neutral region of the GaAs. Since $N_{ta} > N_{td}$, the concentration of the uncompensated donors increases, the capacitance grows, the Fermi level shifts closer to the conduction band, and the population of the quantum-confined states is increased. This results in an increase in the *ED*1 and *ED*2 DLTS peaks in comparison to the case of annealing performed at $U_{ra} < 0$. It was mentioned above that optical illumination of sample *A* during measurements of *C–V* characteristics at low temperatures resulted in much larger values of the capacitance (Fig. 3a) and in the amplitudes of the *ED*1 and *ED*2 DLTS peaks (Fig. 5a). The growth of the amplitudes of these peaks depends on the light intensity and occurs due to the trapping of the photogenerated electrons and holes by the deep donor and acceptor traps. Similarly to the case of annealing at $U_{fa} > 0$, the concentration of the uncompensated donors increases with the light intensity (because $N_{ta} > N_{td}$) and all other quantities change accordingly. It follows unambiguously from these studies that the *ED*1 and *ED*2 peaks correspond to the spa-

tially localized states. Their location coincides with the electron accumulation region $n^*(U_r)$ and with the position of the 3D islands determined from the TEM studies. Furthermore, the maximum of the *ED*2 DLTS peak shifts to lower temperatures with the growth of the population of the corresponding level (Fig. 4a), which is typical of the QDs. The origin of this shift is explained in [9, 10]: it is related to the effect of the Coulomb repulsion between the electrons populating the quantum states in the dots. Owing to this repulsion, the larger the number of these electrons in the ground and excited states, the greater is the reduction of the emission energy. The amplitudes of the DLTS peaks *ED*1 and *ED*2 decrease for large U_r (Fig. 4a), which is also characteristic of the QDs and is accounted for by the field effect [22]. The PL spectra of sample *A* include a band corresponding to the ground-state exciton in the QD at $h\nu$ = 1.05 eV with a width of 116 meV and a shoulder at $h\nu$ = 1.25 eV (Fig. 2a). There are strong indications, such as the observed shift of the maximum of the DLTS signal with the reverse bias voltage U_r and the filling pulse amplitude U_p (Fig. 6a), that the levels *HD*1 and *ED*3 also correspond to the spatially localized states. Previously, we had observed such dependences for the quantum-confined and surface states [11, 12]. As for the *ED*3 level, it is most probably related to the surface states at the InGaAs/GaAs heteroboundary, and its characteristics are close to those of the defects *EL*3 [15] and *I*3 [13]; the latter is produced in GaAs by ionizing radiation and is related to the V_{As} and interstitial As. The variation of the energy of thermal activation of electrons from the surface states may be explained by the effect of the electrostatic-dipole appearance caused by the Coulomb interaction of the electrons in the wetting layer located closer to the n^+ substrate with the ionized states at the heteroboundary. The built-in field of this dipole should be oriented in the opposite direction to the *p–n* junction field, thereby reducing the effective electric field. With an increase in the reverse bias voltage, the number of electrons localized in the wetting layer is reduced due to the field-stimulated tunneling emission. Consequently, the effective field is also reduced. The activation energy of the electron emission then increases, corresponding to the shift of the *ED*3 DLTS peak to higher temperatures (Fig. 4a). With an increase in the filling pulse amplitude U_p, the effective field and the electron population in the quantum well of the wetting layer increase, and the electron activation energy is reduced due to the field effect. In the case of the hole level *HD*1, which is apparently related to the ground hole state in a QD, electrostatic dipoles are formed by holes localized at the *HD*1 state and the deep acceptor levels that trapped an electron. The electric field of the dipole is now oriented in the same direction as the *p–n* junction field, and the variations in the activation energy for the hole emission from the *HD*1 state should be opposite to those observed for the *ED*3 level. Summing the energies of the electron and hole levels, *ED*2 and *HD*1, with the energy of the ground state of the QD exciton, we obtain a value close to the bandgap. The same value is obtained from the summation of the energies of the levels *ED*1 and *HD*1 with $h\nu$ = 1.25 eV. This corroborates our assumption that the levels *ED*2 and *HD*1 correspond to the ground electron and hole states, and that the level *ED*1 corresponds to the excited state in the QD. The DLTS measurements performed on the annealed sample K1383 (Figs. 4b, 5b, 6b) demonstrated that a number of donor- and acceptor-type defects disappear. These are *EL*2, related to the misfit dislocations; *EL*3 (*I*3); and *HS*2, related to V_{As}. The concentration of the acceptor defects *HL*3 and *H*5 drops by nearly two orders of magnitude. Because of this, the Fermi level position, and, correspondingly, the population of the quantum-confined states in the dots, is no longer determined by the recharging of the deep-level donor and acceptor defects. The behavior of the *ED*2* DLTS peak under different isochronal annealing conditions is now determined by the influence of the electrostatic dipole formed owing to the Coulomb interaction of the electrons localized in the dots and the ionized deep donor states. On the isochronal annealing with subsequent cooling to 80 K (both at $U_{ra} < 0$), the deep donor levels remain ionized. At low-temperature DLTS measurement, the electrons are captured by the QDs after application of the filling pulse. The deep donor traps, on the other hand, are still ionized, because the electron energy is insufficient to overcome a potential barrier and be captured by a trap. Thus, the dipole is formed, with the field oriented in the same direction as the *p–n* junction field, and the energy of electron thermal activation from the quantum states is reduced due to the field effect. Upon annealing and cooling at $U_{ra} = 0$, the donor states are partially filled and the dipole electrostatic field is reduced. Hence, the *ED*2* DLTS peak shifts to higher temperatures. Annealing and cooling at $U_{fa} > 0$ results in a still higher shift of the *ED*2* peak in the same direction as for $U_{ra} = 0$. This takes place, because, in the structure *B* under consideration, the double injection of electrons and holes occurs under the forward bias. The increase in the occupation of the hole traps in this case is higher than that upon annealing at $U_{ra} = 0$. This is confirmed by the observed growth of the *ED*2* peak when the DLTS spectra are measured with the filling pulses $U_{fa} > 0$ (Fig. 5b).

5. CONCLUSION

Using the methods of *C–V* measurements and DLTS, as well as TEM and PL, we carried out a detailed investigation of the MOCVD-grown InGaAs/GaAs *p–n* structures to examine the influence of the postgrowth annealing of the InGaAs layer on the formation of the coherently strained dislocation-free 3D islands. In addition, deep-level defects and their influence on the population of the quantum-confined states in the 3D islands (quantum dots) were investigated both in the

unannealed and *in situ* annealed structures. The Coulomb interaction of the carriers localized in the QDs with the ionized deep donors and acceptors was also studied. We established that 3D islands with misfit dislocations are formed in the unannealed structure, and dislocation-free QDs are formed in the annealed structure. The *C–V* measurements indicate that a region of electron accumulation exists in the unannealed structure; this region is related both to the quantum-confined states in the dots and to the deep-level defects. The DLTS measurements demonstrate that different types of already known defects, such as *EL*2, *EL*3 (*I*2), *I*3, *HL*3, *HS*2, and *H*5, are present in the neighborhood of the QDs. The concentration of the traps is comparable to that of the shallow donors, and the number of hole traps exceeds the number of electron ones. Upon *in situ* annealing, the defects *EL*2 and *EL*3 related to dislocations disappear, and the concentration of the other defects decreases by an order of magnitude or more. It was found that, in the unannealed structures, the population of the electron quantum-confined states *ED*1 and *ED*2 and the defect states *EL*3 located at the InGaAs/GaAs heteroboundary is controlled by the recharging of the donor and acceptor defects under isochronal annealing (at $U_{ra} = 0$, $U_{ra} < 0$, and $U_{fa} > 0$) or white-light illumination. The effect of isochronal annealing on the acceptor quantum state in the unannealed structure, as well as on the electron quantum state *ED*2* in the *in situ* annealed structure, is determined by the formation of the electrostatic dipole and the Coulomb interaction between the carriers localized in the QD and the ionized deep-level defects located near the dots.

ACKNOWLEDGMENTS

The work was supported by the Ministry of Science of Russia under the Program “Physics of the Solid-State Nanostructures” (project no. 99-1115).

REFERENCES

1. D. Bimberg, M. Grundmann, and N. N. Ledentsov, *Quantum Dot Heterostructures* (Wiley, Chichester, 1998).
2. I. N. Stranski and L. Krastanow, Sitzungsber. Akad. Wiss. Wien, Abt. Lib. **146**, 797 (1937).
3. F. Heinrichsdorff, A. Krost, D. Bimberg, *et al.*, Appl. Phys. Lett. **68**, 3284 (1996).
4. F. Heinrichsdorff, M.-H. Mao, N. Kirstaedter, *et al.*, Appl. Phys. Lett. **71**, 22 (1997).
5. D. Bimberg, V. A. Shchukin, N. N. Ledentsov, *et al.*, Appl. Surf. Sci. **130–132**, 713 (1998).
6. J. C. Ferrer, F. Peiro, A. Cornet, *et al.*, in *Proceedings of 19th International Conference on Defects in Semiconductors, Aveiro, Portugal, 1997* [Mater. Sci. Forum **258–263**, 1689 (1997)].
7. A. O. Kosogov, P. Werner, U. Gosele, *et al.*, Appl. Phys. Lett. **69**, 3072 (1996).
8. D. V. Lang, J. Appl. Phys. **45**, 3023 (1974).
9. M. M. Sobolev, A. R. Kovsh, V. M. Ustinov, *et al.*, in *Proceedings of 19th International Conference on Defects in Semiconductors, Aveiro, Portugal, 1997* [Mater. Sci. Forum **258–263**, Part 3, 1619 (1997)].
10. M. M. Sobolev, A. R. Kovsh, V. M. Ustinov, *et al.*, Fiz. Tekh. Poluprovodn. (St. Petersburg) **31**, 1249 (1997) [Semicond. **31**, 1074 (1997)].
11. M. M. Sobolev, A. R. Kovsh, V. M. Ustinov, *et al.*, Fiz. Tekh. Poluprovodn. (St. Petersburg) **33**, 184 (1999) [Semicond. **33**, 157 (1999)].
12. M. M. Sobolev, A. R. Kovsh, V. M. Ustinov, *et al.*, J. Electron. Mater. **28** (5), 491 (1999).
13. D. Stievenard and J. C. Bourgoin, J. Appl. Phys. **59**, 743 (1986).
14. D. Pons, P. M. Mooney, and J. C. Bourgoin, J. Appl. Phys. **51**, 2038 (1980).
15. G. M. Martin, A. Mitonneau, and A. Mircea, Electron. Lett. **13**, 191 (1977).
16. A. Mitonneau, G. M. Martin, and A. Mircea, Electron. Lett. **13**, 191 (1977).
17. P. N. Brunkov, S. Gaĭbullaev, S. G. Konnikov, *et al.*, Fiz. Tekh. Poluprovodn. (Leningrad) **25**, 338 (1991) [Sov. Phys. Semicond. **25**, 205 (1991)].
18. D. Stievenard, X. Boddaert, J. C. Bourgoin, *et al.*, Phys. Rev. B: Condens. Matter **41**, 5271 (1990).
19. G. Yusa and H. Sakaki, Appl. Phys. Lett. **70**, 345 (1997).
20. G. P. Watson, D. G. Ast, T. J. Anderson, *et al.*, J. Appl. Phys. **71**, 3399 (1992).
21. P. D. Siverns, S. Malik, G. McPherson, *et al.*, Phys. Rev. B: Condens. Matter **58**, R10127 (1998).
22. S. Anand, N. Carlsson, M.-E. Pistol, *et al.*, Appl. Phys. Lett. **67**, 3016 (1995).

Translated by M. Skorikov

Semiconductors, Vol. 34, No. 2, 2000, pp. 205–212. Translated from Fizika i Tekhnika Poluprovodnikov, Vol. 34, No. 2, 2000, pp. 211–218.

LOW-DIMENSIONAL SYSTEMS

On the Constriction of the Hall Current in the Corbino Disk under Quantum Hall Effect Conditions

V. B. Shikin* and Yu. V. Shikina**

** Institute of Solid-State Physics, Russian Academy of Sciences, Chernogolovka, Moscow oblast, 142432, Russia*

*** Institute of Microelectronics Technology and Ultrahigh Purity Materials, Russian Academy of Sciences, Chernogolovka, Moscow oblast, 142432, Russia*

Submitted June 8, 1999; accepted for publication August 26, 1999

Abstract—Modification of the theory describing the current–voltage characteristics of the shielded Corbino disk with spinless two-dimensional (2D) electron system under a magnetic field for nearly integer filling factors in the case of a weak pulling electric field (i.e., its energy being much lower than the cyclotron energy) is suggested. Features of the *I–V* characteristics in the limits of "pure" and "dirty" 2D electron system are considered. The results are compared with experimental data. Local parameters characterizing the disk with flowing current that can be measured via a linear electrooptical effect (distribution of the 2D electron density, and electric and electrochemical potentials) are determined. © *2000 MAIK "Nauka/Interperiodica".*

Interesting data on the specific nonlinear effects in the current–voltage characteristics of a shielded Corbino disk with spinless two-dimensional (2D) electron system under quantizing magnetic field at nearly integer filling factors were reported in [1]. Details of the dependence of the potential distribution at the edges of the Corbino disk under a current on the magnetic filling factor, which is varied by the gate voltage, are of interest.

An attractive feature of the theoretical interpretation of the results, given in [1] along with the experimental data, is its relative simplicity. It should be noted that, despite numerous publications on the quantum Hall effect (QHE) breakdown that have appeared since the original report [2], quantitative agreement between experimental observations of the different nonlinear effects in the *I–V* characteristics and their theoretical explanation is usually rather poor (see, e.g., [2–9]). Thus, it is desirable to get rigorous justification of the theory in those rare cases (as in [1]), when good agreement can be achieved.

In this respect, the calculation presented in [1] is carried out using a number of assumptions, whose correctness is actually not obvious. In this paper, we consider the self-consistent set of equations that determine the *I–V* characteristic of the shielded Corbino disk under QHE conditions. The proposed theory enables generalization of the results from [1] to the case of the pure 2D systems, gives corrections to some of the statements from [1] regarding the limiting case of the dirty system, and accounts for a number of observed features in the *I–V* characteristics of the Corbino disk in a quantizing magnetic field.

DEFINITIONS

1. To interpret their results, the authors of [1] used the local Ohm's law in the form

$$J/2\pi r = -\sigma_{rr}(\varphi)d\varphi/dr, \tag{1}$$

where J is the full Corbino current in the radial direction, φ is the local potential difference between the screening gate and the 2D electron layer in the silicon MIS structure, and $\sigma_{rr}(\varphi)$ is the diagonal part of the 2D system conductivity tensor, which, in general, depends on the potential φ. In the case of the nearly integer filling factor, the conductivity temperature dependence is of activation nature, typical of the QHE (see [1, 10]):

$$\sigma_{rr} = \sigma_0 e^{\Delta/T}\cosh(\epsilon_F/T), \tag{2}$$

where ϵ_F is the Fermi energy measured from the middle of the distance between the Landau levels, Δ is the activation energy for $\epsilon_F = 0$, and T is the temperature.

Because of the basic importance of equation (2) for the understanding of the nonlinear processes in the Corbino disk considered here, let us mention also the results from the paper [11]. Assuming that existence of the smooth random potential is the main factor responsible for the finiteness of the diagonal conductivity, the following formula was obtained [11]:

$$\sigma_{xx} = \frac{e^2}{\hbar}\exp[(\mu - V_c/T)]\int w(E)\exp(-E/T)dE/T. \tag{2a}$$

Here, V_c is the percolation level; $w(E)$ is the probability of passing the typical saddle point, which is expressed in terms of the random potential characteristics; and μ is electrochemical potential.

1063-7826/00/3402-0205$20.00 © 2000 MAIK "Nauka/Interperiodica"

Obviously, definitions (2) and (2a) become identical, if we assume that

$$\exp(-\Delta/T) \longrightarrow \exp(-V_c/T), \quad \epsilon_F \longrightarrow \mu,$$

$$\sigma_0 \longrightarrow \frac{e^2}{\hbar}\int w(E)\exp(-E/T)dE/T,$$

and take into account that symmetrization with respect to electron and hole excitations is implied in expression (2).

The system of definitions becomes closed with the addition of the relationship between ϵ_F and voltage V_g at the gate of MIS structure, which, following [1], can be taken as

$$\varphi - V_g = p\epsilon_F, \quad p = eD/C_0. \tag{3}$$

Here, D is the density of states in the gap between Landau levels, and C_0 is the capacitance of the MIS structure per unit area. The simplicity of equation (3) is rather relative and is achieved only in the case where the distance d from the gate to the 2D system is much smaller than its size (the so-called capacitor approximation), which is well fulfilled in the experimental conditions of [1].

The simultaneous solution of equations (1)–(3) results in a certain nonlinear relation between J and V, where the voltage V is introduced as

$$V = \varphi(r_1) - \varphi(r_0). \tag{4}$$

With this relation, experimental data from [1], especially those obtained in the range of large currents, can be explained quite well (the notion of "large current" is specified below).

2. At this moment, it should be noted that, generally speaking, it is electrochemical (rather than electric) potential that should appear in the right-hand side of the Ohm's law:

$$eJ/2\pi r = -\sigma_{rr}(\delta\mu)d\mu/dr. \tag{5}$$

The difference between (1) and (5) is quite significant, because, unlike electric potential, the electrochemical potential is a nonlinear (in some cases even singular) function of the electron density at nearly integer filling factors $\nu = 1, 2, 3, \ldots$. For instance, in the case of an ideal spinless 2D system under a normal magnetic field, we have

$$\mu(r) = \hbar\omega_c/2 + e\varphi(r) - T\ln S(\nu), \quad \nu < 2, \quad T > \Gamma, \tag{6}$$

$$\begin{aligned} S(H,\nu) &= (1/2)(1/\nu - 1) \\ &+ \sqrt{(1/4)(1/\nu - 1)^2 + \epsilon(2/\nu - 1)}, \\ \nu(r) &= \pi l_H^2 n(r), \quad n(r) = n_s + \delta n(r), \\ \epsilon &= \exp(-\hbar\omega_c/T) \ll 1. \end{aligned} \tag{6a}$$

Here, $n(r)$ is the local electron density, n_s is the average electron density when there is no current, l_H is the magnetic length, and ω_c is the cyclotron frequency. The inequality $T > \Gamma$ (where Γ is the variance of the density of states) is included to make the assumption of the ideality of the system consistent with the assumption of the nonzero value of its diagonal conductivity in the magnetic field.

In the "dirty" limit $T \ll \Gamma$, it is ν that can be relatively simply expressed as a function of μ [in (6), the relation is inverse]:

$$\begin{aligned} \nu &= \phi(\delta\mu_1/\Gamma\sqrt{2}) + \phi(\delta\mu_2/\Gamma\sqrt{2}) + 1, \\ \delta\mu_1 &= \mu - \hbar\omega_c/2 - e\varphi, \quad \delta\mu_2 = \mu - 3\hbar\omega_c/2 - e\varphi, \end{aligned} \tag{7}$$

where $\phi(x)$ is the error function, $\phi(-x) = -\phi(x)$. Apparently, neither (6) nor (7) give any reasons to express Ohm's law in the form (1) instead of (5).

The second assumption from [1] that needs additional consideration is the use of equation (2) to express σ_{rr} for near integer filling factors. First of all, the significance of ϵ_F is unclear. On the one hand, in the nonuniform case the Fermi energy, which determines the exponent of the hyperbolic cosine in (2), is equivalent to electrochemical potential $\delta\mu(r)$. This is substantiated by equation (2a) for the conductivity, as obtained in [11]. Let us refer to such a procedure for determining conductivity as the μ-representation. On the other hand, we believe that the μ-representation yields physically meaningless results for the current–voltage characteristic; this motivates one to seek for the other interpretations considered below.

Another, seemingly just technical, issue that requires special consideration is related to the explicit relationship between ϵ_F and $\varphi(r)$. As will be seen from further consideration, the calculation using universal expansion (3) over the entire Corbino disk can lead to a distorted shape of the I–V curve.

3. Before proceeding to an analysis of the corrections to definitions (1)–(3), we first consider the capabilities of the μ-representation; i.e., we assume that Ohm's law is given by (5) and formula (2) for the conductivity is understood as

$$\sigma_{rr} = \sigma_0 e^{-\Delta/T}\cosh(\delta\mu/T). \tag{8}$$

In addition, the substitution $\varphi \longrightarrow \mu$ should be performed in the boundary conditions (4).

It can easily be seen that, combining expressions (5) and (8), we can reduce the problem of the current–voltage characteristic to a single equation for $\delta\mu$. In addition, there is no need to use the controversial expansion (3); this adds to the merits of the μ-representation. Influence of the gate voltage V_g, which appears in expansion (3), on the I–V characteristic can be taken into account by assuming, following [1], that, for zero current J, the value of $\delta\mu$ is constant over the entire Corbino disk and is equal to

$$\delta\mu\ (J = 0) = \delta\mu_0, \quad \delta\mu_0 \propto V_g. \tag{9}$$

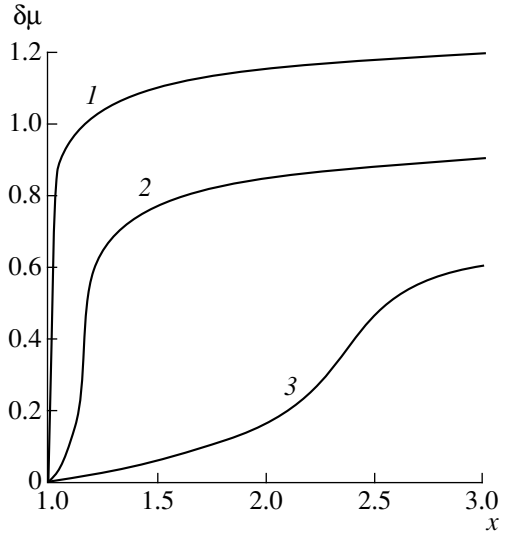

Fig. 1. Distribution of δμ normalized by $\hbar\omega_c$ along the current direction $x = r/r_0$ for $\nu_0 = 0.8$; $t = 0.1$; $q = 3$; and $\nu =$ (*1*) 0.6, (*2*) 0.8, and (*3*) 1.2 (ν_0 is the filling factor for zero current).

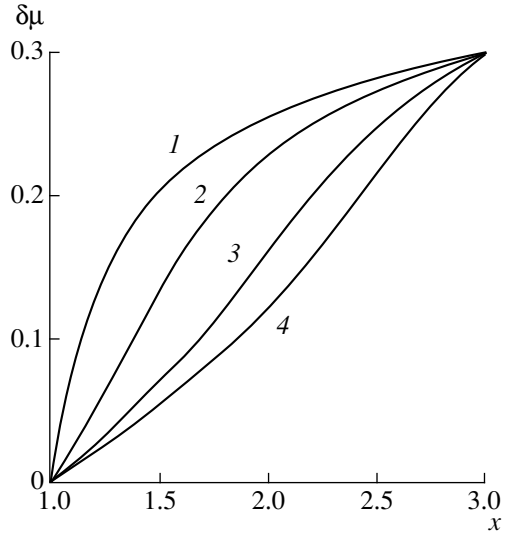

Fig. 2. The same as in Fig. 1, but for fixed $\nu = 0.5$; $t = 0.1$; $q = 3$; and $\nu_0 =$ (*1*) 1.00, (*2*) 0.98, (*3*) 0.96, and (*4*) 0.94.

Thus, to solve equations (5) and (8) for δμ, we can take the boundary conditions in the form

$$\delta\mu(r_0)/\hbar\omega_c = \delta\mu_0, \quad \delta\mu(r_1)/\hbar\omega_c = \delta\mu_0 + \upsilon, \quad \upsilon = eV/\hbar\omega_c, \tag{10}$$

where substitution $\varphi \longrightarrow \mu$ is properly accounted for. Henceforth, all energy parameters are expressed in the units of cyclotron energy. The solution with boundary conditions (10) is given by

$$\delta\mu(x) = t\,\mathrm{arcsinh}\left[\sinh\left(\frac{\delta\mu_0}{t}\right)\left(1-\frac{\ln x}{\ln q}\right) + \sinh\left(\frac{\delta\mu_0+\upsilon}{t}\right)\frac{\ln x}{\ln q}\right], \quad q = r_1/r_0, \quad x = r/r_0. \tag{11}$$

The relationship between the current J and the voltage V is then written as

$$j/t = \left[\sinh\frac{\delta\mu_0+\upsilon}{t} - \sinh\frac{\delta\mu_0}{t}\right], \quad j = \frac{eJ\ln q}{2\pi\sigma_0\hbar\omega_c}\exp\frac{\Delta}{T}. \tag{12}$$

It follows from (11) that the spatial distribution of δμ along the current direction becomes essentially nonlinear with an increase in υ. The extent of nonlinearity is determined by the ratio eV/T rather than by $eV/\hbar\omega_c$, as one could expect intuitively. As an example, we present in Figs. 1–3 the calculated dependences $\delta\mu(x)$ for different initial values $\delta\mu_0$, different υ for fixed t, and different t for fixed $\delta\mu_0$ and υ.

The properties of the solution (11) and (12) and the data given in Figs. 1–3 indicate that nonuniform distribution $\delta\mu(x)$ sets in with an increase in υ. This means that the range of the integer filling factors becomes localized; i.e., the Hall current becomes constricted in the Corbino disk. Such behavior of $\delta\mu(x)$ is not surprising in view of the exponential dependence $\sigma_{xx}(\delta\mu)$.

Along with the qualitatively clear features of formulas (11) and (12), there exists a certain paradox, which cannot be resolved in the context of μ-representation: it appears that these formulas are independent of the features of the electron spectrum within the cyclotron gap. This universality is more likely to be a drawback than a merit of the theory, because experimental studies of the QHE breakdown [1–9] indicate that the latter is sensitive to the distribution of the electron density of states between the Landau levels.

As we believe, this paradox is due to the fact that, although definition (8) and resulting formulas (11) and (12) adequately represent the exponential dependence of the conductivity on the level of electrochemical potential, they do not account for possible influence of electric potential φ on σ_{rr}. This can change the position of electrochemical potential relative to the Landau levels and, consequently, influence the structure of equations (2) and (2a). Taking this into consideration, it is reasonable to use, along with the μ-representation (8), an alternative phenomenological definition of conductivity, which we call "ζ-representation" for the sake of definiteness; thus, we have

$$\sigma_{rr} = \sigma_0 e^{-\Delta/T}\cosh[(\zeta - \hbar\omega_c)/T], \quad \zeta = \mu - e\varphi. \tag{13}$$

This expression adequately accounts for the spatial nonuniformity of $\mu(x)$, as well as possible coordinate dependence of $\varphi(x)$. Definition (13) is written for the specific case of the filling factor approximately equal to

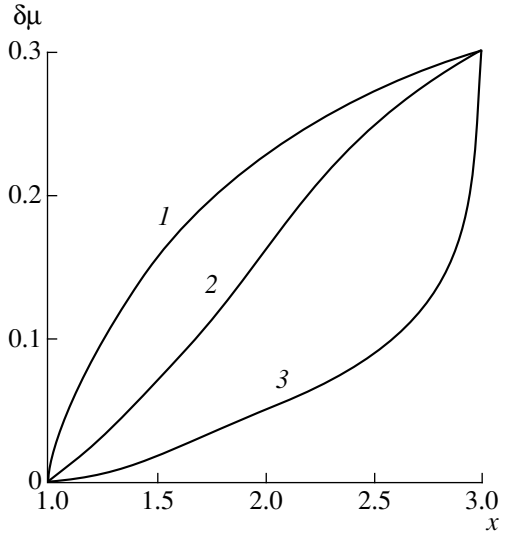

Fig. 3. The same as in Fig. 1, but for fixed $\nu = 0.3$; $\nu_0 = 0.96$; $q = 3$; and $t =$ (*1*) 0.2, (*2*) 0.1, and (*3*) 0.05.

1. As will be shown further, the alternative expression (13) enables us to circumvent the aforementioned paradoxical behavior of $\delta\mu$.

In ζ-representation the problem becomes more complicated, because the potential combination

$$\zeta = \mu - e\varphi$$

now appears in (13), and universal solution of the kind (11) and (12) cannot be derived. On the other hand, using, e.g., relation (6), one can transform (13) into physically a transparent form

$$\sigma_{rr} = \sigma_0 e^{-\Delta/T}\cosh\left[\frac{-\hbar\omega_c/2 - T\ln S(\nu)}{T}\right]. \qquad (14)$$

For $\nu = 1$, i.e., in the region with an integer filling factor, the argument of the hyperbolic sine in the right-hand side of expression (11) vanishes, and, hence, the conductivity attains a minimum. Furthermore, it is known [12–14] that in the magnetically quantized 2D system in the nonuniform conditions the size of the integer-filling channel remains constant in a certain range of external parameters, with the channel size being defined more sharply at lower temperatures. This feature is lacking in the μ-representation (8) and is distinct in the ζ-representation of conductivity (13).

4. To complete the system (5), (6), and (13) [or (5), (7), and (13)], an additional independent relationship between the electric potential φ and local density of the 2D system is needed. To obtain this relationship, which is of electrostatic origin, one needs to determine simultaneously the distribution of charge density over the 2D system and the gate. Here, there is room also for quantitative improvement of the existing definitions. However, restricting our goals to derivation of merely qualitatively meaningful results, we adhere, like the authors of [1], to the commonly used capacitor approximation, valid in the case of the distance $2d$ between the 2D system and the gate being much smaller than $r_1 - r_0$:

$$2d \ll r_1 - r_0. \qquad (15)$$

In this case,

$$\varphi(r) \simeq 2ed[\nu(r) - \nu_0]/\kappa l_H^2, \qquad (16)$$

where $\nu(r)$ is the local value of the filling factor; ν_0 is its value for zero current; and κ is the dielectric constant.

Thus, the complete system of equations in ζ-representation, from which the variables μ, φ, ζ, and ν are to be determined, consists of formulas (5), (6), (13), and (16) [or (5), (7), (13), and (16)]. The goal of the theory is to derive the relationship between J and V, as well as the distribution of the local electric potential over the Corbino disk; this distribution can be measured experimentally using the linear electrooptical effect [13].

5. Combining (5), (6), (14), and (16), we obtain an equation in $\nu(r)$ for the ideal 2D system:

$$\frac{j}{\ln q}\int_1^x \frac{dx}{x\cosh\{-1/2t - \ln S[\nu(x)]\}} = 2d_*(\nu - \nu_0) - t\ln[S(\nu)/S(\nu_0)], \qquad (17)$$

$$1 > t > \gamma, \quad \gamma = \Gamma/\hbar\omega_c \ll 1,$$

where $S(\nu)$ is given by (6a). The condition $1 > t > \gamma$ is included to ensure that the 2D system is not far from its ground state and the diagonal conductivity is finite. Within the validity range of this theory the dimensionless parameter j (defined by (12)) varies from zero to the values slightly exceeding unity:

$$0 \le j \le 2. \qquad (17a)$$

The relation between the current and the voltage is given by

$$\frac{j}{\ln q}\int_1^q \frac{dx}{x\cosh\{-1/2t - \ln S[\nu(x)]\}} = \upsilon, \qquad (18)$$

$$q = r_1/r_0 > 1.$$

The corresponding equations for the case of the "dirty" system cannot be expressed in a form similar to (17). The structure of the *I–V* characteristic definition appropriate for the experimental situation realized in [1] is discussed below.

DIFFERENT APPROXIMATIONS TO THE CURRENT–VOLTAGE CHARACTERISTIC

1. First, we consider the *I–V* characteristics of the samples with an ideal 2D electron gas. According to (17), at low temperatures ($\gamma < t < 1$) the distribution of electron density over the Corbino disk with the radial

current j is, to a large extent, determined by the interplay of the two parameters, υ and ν_0.

1a. The most interesting case is $\nu_0 = 0$ where the entropy term is dominant in expression (6) for the electrochemical potential. As a consequence, electron current is of predominantly diffusion origin, electric potential is virtually constant over the Corbino disk (this can be verified by experimental techniques described in [13]), and the shape of the *I–V* characteristic is determined by equation (12) with $\delta\mu_0 = 0$.

1b. If $\nu_0 \neq 0$, the shape of the *I–V* curve depends, in particular, on the sign of $(1 - \nu_0)$. If this quantity is positive, the sample resistivity increases nonlinearly with V, because the flowing current perturbs the electron density of the 2D system, and, in the case of $(1 - \nu_0) > 0$, the state of the system shifts towards that with $\nu(x) = 0$ at some parallel of the Corbino disk; naturally, this leads to an increase in effective resistivity. In the case of $(1 - \nu_0) < 0$, the disk resistivity decreases nonlinearly for similar reasons. If, for instance,

$$\upsilon \le 2d_*(1 - \nu_0) \le 1 \tag{19}$$

(where $d^* = d/r_0$), $\nu(x)$ increases gradually from its initial value ν_0 to the maximum $\nu(q) < 1$ at the outer boundary of the Corbino disk. To calculate the *I–V* curve, we use (17) and (18) with the two additional simplifications. First, we assume that

$$\begin{gathered} -1/2 - t\ln S(\nu) \simeq \delta\zeta_1^* + (D_1^*)^{-1}\nu_1' x, \\ \nu_1' \equiv d\nu(1)/dx, \quad \zeta^* = \zeta/\hbar\omega_c, \\ \delta\zeta_1^* = -1/2 - t\ln S(\nu_1) < 0, \\ (D_1^*)^{-1} = \left.\frac{d\zeta^*}{d\nu}\right|_{\nu=\nu_0} = -\frac{t}{S(\nu_0)}\frac{dS(\nu_0)}{d\nu} > 0. \end{gathered} \tag{20}$$

Expressions for the $\delta\zeta_1^*$ and $(D_1^*)^{-1}$ are written for an ideal 2D system. The unknown derivative $d\nu(1)/dx$, which appears in expansion (20), is calculated using (17) as

$$j/\cosh\left[\frac{(D_1^*)^{-1}\nu_1' + \delta\zeta_1^*}{t}\right] = \left[2d_* + (D_1^*)^{-1}\right]\nu_1'. \tag{21}$$

Second, it is reasonable to assume that expansion (20) is valid over the whole range $1 \le x \le q$. Then, in view of (20), equation (18) takes the form

$$\begin{gathered} \frac{2j}{b\ln q}\{\arctan[\exp(a + bq)] \\ - \arctan[\exp(a + b)]\} = \upsilon, \end{gathered} \tag{22}$$

where

$$a = \delta\zeta_1^*, \quad b = (D_1^*)^{-1}\nu_1'$$

and $\nu_1' \propto j$ in view of (21).

As expected, effective renormalization of resistivity, represented by the term in the square brackets in (22), becomes more important with an increase in j.

1c. When υ is increased so that

$$2d_*(1 - \nu_0) \le \upsilon \le 1, \tag{23}$$

where $d_* = d/r_0$, a kink occurs in the $\nu(x)$ dependence. The inflection point $x_\wedge$ separates the region with finite gradient of electron density from the integer-filling density plateau. Next, if

$$2d_*(1 - \nu_0) < 1 \le \upsilon, \tag{24}$$

two kinks appear in the electron density profile at the points $x_\wedge$ and $x_\vee$, with an integer-filling region between them forming a channel of width $2a = x_\wedge - x_\vee$; etc. It can be shown that

$$2a = tD_{\min}^*/\nu_{\min}' = 2/\pi j, \tag{24a}$$

where $D_{\min}^*$ is the minimum density of states in the interval between the Landau levels. However, in general, reliable determination of the current–voltage characteristic and other features of the 2D system behavior in the cases (23) and (24) requires numerical calculations and is not discussed in this work.

2. Let us now consider the case of the nonideal (dirty) 2D systems, corresponding to the experimentally studied situation [1]. As we have already mentioned above, in this limiting case, it is impossible to write an equation for $\nu(r)$ in closed form, similar to (17). However, advances in describing the properties of the "dirty" Corbino disk can be achieved by using the expansions similar to (20). Correspondence between the cases of pure and dirty systems is preserved if, instead of (20), we use the following definitions for D_1^* and ζ_1^*:

$$(D_1^*)^{-1} = \frac{d\zeta^*}{d\nu} > 0, \quad \delta\zeta_1^* = \zeta^* = [\nu(0)]. \tag{25}$$

The derivative $d\zeta/d\nu$ is calculated with the use of equation (7) as

$$\frac{d\nu}{d\zeta} = \sqrt{\frac{2}{\pi}}\left\{\exp\left[\frac{-\left(\zeta - \frac{1}{2}\hbar\omega_c\right)^2}{2\Gamma^2}\right] + \exp\left[\frac{-\left(\zeta - \frac{3}{2}\hbar\omega_c\right)^2}{2\Gamma^2}\right]\right\}\Big/\Gamma.$$

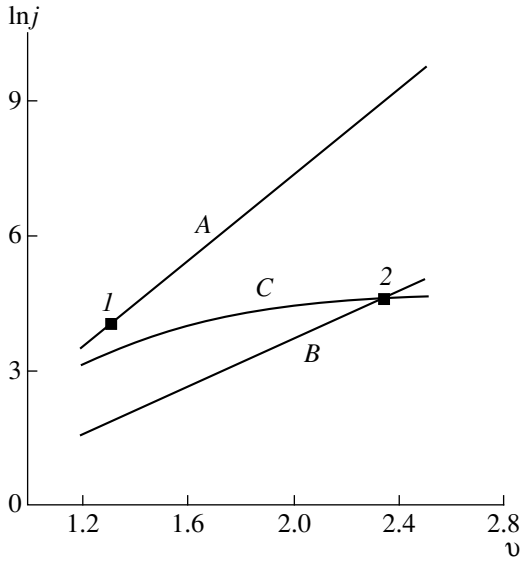

Fig. 4. Examples of the current–voltage characteristics of the "dirty" 2D system in Corbino disk configuration, illustrating definitions (29) and (31). *1* and *2* are the experimental points; the curves are calculated with (*A*) equation (29) with $\lambda = \lambda_1 = 0.12$, (*B*) equation (29) with $\lambda = \lambda_2 = 0.067$, and (*C*) equation (31) with $\lambda = \lambda^* = 0.16$ and $\eta = 0.05$.

It has a minimum at

$$\zeta_{\min} = \hbar\omega_c, \quad \left(\frac{d\nu}{d\zeta}\right)\Big|_{\min} = \frac{2}{\Gamma}\sqrt{\frac{2}{\pi}}\exp\left[-\frac{\left(\frac{1}{2}\hbar\omega_c\right)^2}{2\Gamma^2}\right].$$

Here, the value of ν determined from (7) is equal exactly to unity, because $\delta\mu_1 = -\hbar\omega_c/2$, $\delta\mu_2 = +\hbar\omega_c/2$, and $\phi(-x) = -\phi(x)$.

Thus, the behavior of the "dirty" 2D system is qualitatively similar to that of the pure system, if the temperature is substituted by the parameter Γ in the formulas obtained for the ideal case.

Using expansions similar to (20), we can also gain insight into approximations used in [1]. It is clear from the previous calculations that outside the integer-filling channel the following equality holds with good accuracy:

$$\mu(x) \simeq e\varphi(x). \tag{26}$$

Then, the right-hand sides of expressions (1) and (5) coincide. Next, we assume that, similar to (20),

$$\delta\zeta^*(x) \simeq \delta\zeta_1^* + (D_1^*)^{-1}\delta\nu. \tag{27}$$

Also, from (16) we have

$$\delta\nu = \kappa l_H^2\varphi(x)/2ed.$$

Taking (27) and (16) into account, one can see that expression (13) for the conductivity in ζ-representation becomes similar to that given by (2) and (3), if

$$\delta\zeta \equiv \zeta(1) = -V_g/p, \quad (D_1^*)^{-1}\kappa l_H^2/2ed = 1/p. \tag{28}$$

Comparing the definitions of p from (3) and D_1^* from (20), one can readily see that there is only one difference between formulas (3) and (28): the minimum density of states $D_{\min}^*$ is used in the former, while the density of states D_1^* at the inner edge of the Corbino disk appears in the latter.

Keeping all this in mind, we present two expressions for the current–voltage characteristic of the "dirty" 2D system in the Corbino geometry.

The first of them reproduces calculations from [1]:

$$j = \frac{t}{\lambda}\left[\sinh\frac{\lambda(\delta\mu_0 + \upsilon)}{t} - \sinh\frac{\lambda\delta\mu_0}{t}\right],$$
$$j = \frac{eJ\ln q}{2\pi\sigma_0\hbar\omega_c}\exp\frac{\Delta}{T}, \quad \lambda = \frac{\kappa l_H^2}{2e^2 dD_1^*} \ll 1. \tag{29}$$

This result is obtained with the use of expansion (27) [or (3)] over the entire range $r_0 < r < r_1$. It is interesting to derive the conditions for nonrectifying *I–V* characteristic. Linear regime occurs if

$$\lambda\upsilon/t \ll 1. \tag{30}$$

In the case $\lambda \ll 1$ the conditions for nonrectifying behavior are significantly milder than those just given by inequality $\upsilon \ll t$, which appears in the μ-representation.

The second expression for the *I–V* curve is derived under the assumption that the validity of the linear expansion (27) is limited, and contribution from the higher terms of this series becomes noticeable with an increase in the parameter $\lambda\upsilon/t$. Restricting ourselves to the first two terms of the series and assuming that $\delta\mu_0 = 0$, we obtain

$$j = \int_0^{\nu}\cosh\left(\frac{\lambda}{t}\varphi - \frac{\eta}{t}\varphi^2\right)d\varphi. \tag{31}$$

This definition contains two fitting constants λ and η that actually characterize the minimum density of states and the first corrections to this quantity with an increase in distance from the neighborhood of the saddle point.

Our final goal is to compare the calculated current–voltage characteristics (29) and (31) with experimental results from [1]. Among the data available we can only use here two points in the vicinity of $\nu \le 2$; most of the measurements in [1] were made for $\nu > 2$ where our calculations are not valid. Figure 4 illustrates the agreement between theoretical and experimental results. In Fig. 4, the dimensionless variable υ is the ratio of eV to cyclotron energy determined for $H = 10.6$ T and effec-

tive mass $m^* = 0.19m_e$ ($\hbar\omega_c = 5.25$ meV). The quantities that appear in the expression for the dimensionless variable j are $k = 7$, $\Delta = 30$ K, $\sigma_0 = 1.7 \times 10^{-6}\ \Omega^{-1}$, and $q = 3$. Dimensionless coordinates in the (υ, j) plane of the two experimental points *1* and *2* given in Fig. 4 and the maximum values attained in [1] are

$$\upsilon_1 = 1.32, \quad j_1 = 50; \quad \upsilon_2 = 2.33, \quad j_2 = 99; \qquad \upsilon_{max} = 8.7 \quad j_{max} = 4090. \tag{32}$$

The curve *A* corresponds to expression (29) for $\delta\mu_0 = 0$. The constant $\lambda = \lambda_1$ was chosen from the condition that the curve should include the point (υ_1, j_1). As a result, we have

$$\lambda = \lambda_1 = 0.12. \tag{33}$$

Curve *B* is similar to line *A* but should pass through the point (υ_2, j_2). As a result, we arrive at

$$\lambda = \lambda_2 = 0.067. \tag{33a}$$

The same fitting procedure for the point $(\upsilon_{max}, j_{max})$ leads to

$$\lambda = \lambda_{min} = 0.026. \tag{33b}$$

Curve *C* corresponds to equation (31) with the parameters fitted to draw the curve as close to the experimental points *1* and *2* as possible. This results in

$$\lambda = \lambda^* = 0.16, \quad \eta = 0.05. \tag{34}$$

An analysis of the agreement between the experimental and theoretical results presented in Fig. 4 is indicative of the low "quality" of the 2D electron gas system in the sample used in [1]. Thus, it is reasonable to describe its behavior in terms of the "dirty" system. Estimating the minimum density of states, the authors of [1] used the numerical values (33b), which yielded

$$D/D_0 = 6.6 \times 10^{-2}.$$

With the use of (33) or (33a) for points *1* and *2* we obtain an even higher value for the minimum density of states.

It is also obvious that the linear expansion (20) used to derive the expression (29) for the *I–V* characteristic is apparently not very effective in the region $\lambda\upsilon/t > 1$. This is evidenced by the large spread in the values obtained with (33)–(33b) for the parameter λ, as well as by the relatively good results obtained with formula (31).

DISCUSSION

Let us summarize. We have studied the weak nonlinear effects in the current–voltage characteristic of the 2D electron system in the Corbino disk configuration for a normal magnetic field under the QHE conditions. The basic cause of these nonlinearities is the lack of spatial uniformity in the 2D system, even in the one ideally uniform at equilibrium, when the current flows through it. Anomalous development of the current nonuniformities in the QHE regime against the background of the linear or logarithmic increase in electron density, which occurs in any 2D system, proceeds via two mechanisms. One of them is characteristic of the 2D systems with near integer filling factor and functions in equilibrium conditions as well, resulting in the formation of the integer-filling stripes in nonuniform systems. The flowing of the current modifies the parameters of such stripes or creates the conditions for their formation. Another mechanism, the current constriction, has qualitatively similar nature in any conducting system characterized by the nonlinear dependence of electrical conductivity on the problem variables (see [15]). Its effect in the case of Corbino disk with the current under the QHE conditions, first noticed in [1], is illustrated by Figs. 1–3, which are obtained from the theory of the current–voltage characteristic in the μ-representation.

However, both nonuniformity mechanisms are in fact interrelated. It is shown above that in the middle of the Hall pinch there exists an integer-filling plateau, which forms the core of the minimum-conductivity region.

The size of the plateau depends on the current strength and can be calculated analytically in some limiting cases [see (24a)]. Such plateaus can be observed experimentally with the use of the linear electrooptical effect [16].

The integer-filling channels are well-defined in the pure systems and in the ohmic (quasi-ohmic) modes. Constriction of the Hall current takes place up to very high values of $\upsilon \gg 1$, although the theory of such constriction should be modified to take into account other possible mechanisms of the nonlinearities in the *I–V* characteristics (such as overheating of the electron system etc.).

ACKNOWLEDGMENTS

We thank V.T. Dolgopolov for his participation in discussions of the results.

This work was supported in part by the Russian Foundation for Basic Research (project no. 98-02-16640) and the Russian Ministry of Science under the Program "Physics of the Solid-State Nanostructures" (project no. 99-1126).

REFERENCES

1. A. A. Shashkin, V. T. Dolgopolov, and S. I. Dorozhkin, Zh. Éksp. Teor. Fiz. **91**, 1897 (1986) [Sov. Phys. JETP **64**, 1124 (1986)].
2. G. Eber, K. von Klitzing, K. Ploog, *et al.*, J. Phys. C **16**, 5441 (1983).
3. M. E. Cage, R. F. Dziuba, B. F. Field, *et al.*, Phys. Rev. Lett. **51**, 1374 (1983).
4. O. Heinonen, P. Taylor, and S. Girvin, Phys. Rev. B: Condens. Matter **30**, 3016 (1984).
5. P. Streda and K. von Klitzing, J. Phys. C **17**, 483 (1984).

6. S. Komiyama, T. Takkumasu, S. Hiamizu, *et al.*, Solid-State Commun. **54**, 479 (1985).
7. Ch. Simon, B. B. Goldberg, F. Fang, *et al.*, Phys. Rev. B: Condens. Matter **33**, 1190 (1986).
8. S. Kawaji, K. Hirakawa, and M. Nagata, Physica B (Amsterdam) **184**, 17 (1993).
9. N. Q. Balaban, U. Meirav, H. Shtrikman, *et al.*, Phys. Rev. B: Condens. Matter **26**, 3648 (1983).
10. M. G. Gavrilov and I. V. Kukushkin, Pis'ma Zh. Éksp. Teor. Fiz. **43**, 79 (1986) [JETP Letters **43**, 103 (1986)].
11. S. V. Iordanskiĭ and B. A. Muzykantskiĭ, Zh. Éksp. Teor. Fiz. **103**, 2116 (1993) [JETP **76**, 105 (1993)].
12. D. B. Chklovskiĭ, B. I. Shklovskiĭ, and L. I. Glazman, Phys. Rev. B: Condens. Matter **46**, 4026 (1992).
13. D. B. Chklovskiĭ, K. F. Matveev, and B. I. Shklovskiĭ, Phys. Rev. B: Condens. Matter **47**, 12605 (1993).
14. D. Chklovskiĭ and P. Lee, Phys. Rev. B: Condens. Matter **48**, 18060 (1993).
15. V. L. Bonch-Bruevich and S. G. Kalashnikov, *Physics of Semiconductors* (Nauka, Moscow, 1977).
16. W. Dietsche, K. von Klitzing, and K. Ploog, Surf. Sci. **361**, 289 (1996).

Translated by M. Skorikov

Semiconductors, Vol. 34, No. 2, 2000, pp. 213–216. Translated from Fizika i Tekhnika Poluprovodnikov, Vol. 34, No. 2, 2000, pp. 219–222.

AMORPHOUS, VITREOUS, AND POROUS SEMICONDUCTORS

The Effect of Ultrafast Low-Temperature Doping of Vitreous As–Se Films with Copper, Silver, Gold, and Chromium (The Khan Effect)

M. A. Korzhuev

Baikov Institute of Metallurgy, Russian Academy of Sciences, Leninskiĭ pr. 49, Moscow, 117334 Russia
e-mail: Korzhuev@lesr.imet.ac.ru

Submitted January 11, 1999; accepted for publication August 18, 1999

Abstract—The effect of ultrafast doping of chalcogenide vitreous As–Se, Ge–Se, and other films with Cu, Ag, Au, Cr, and other metals previously discovered in metal/chalcogenide vitreous film heterostructures at 250–350 K is analyzed. © *2000 MAIK "Nauka/Interperiodica".*

The effect of ultrafast low-temperature doping of chalcogenide (CGF) vitreous As–Se, Ge–Se, and other films with Cu, Ag, Au, Cr, and other metals (M) (the Khan effect) has been reported in [1, 2]. The effect has been observed in Pyroceram/metal/CGF heterostructures obtained by layer deposition from the vapor phase at liquid nitrogen temperature. Spontaneous variation of the electrical and optical properties of the films due to ultrafast penetration into CGF (in a time t^* equal to several minutes) of a significant amount of metal (x^* = 20 at. % and more when the system attains the critical temperature T^* = 250–350 K corresponding to the transformation of M/CGF ⟶ CGF : M [the transition (a) ⟶ (b) in Fig. 1]) has previously been pointed out.

The effect of ultrafast doping was observed earlier at room temperature in crystal semiconductors (superionic conductors (SIC)) such as $Cu_{2-x}Se$, Bi_2Se_3, and others, with M = Cu or Ag. They have the highest ion mobility among solids due to ion acceleration by electrons in mixed electron–ion conductors (diffusion coefficients of Cu and Ag $\tilde{D}_{Cu, Ag} \sim 10^{-4}$–$10^{-6}$ cm^2/s at T = 300 K [3]). The study of a similar doping effect in amorphous medium where the ion and electron mobilities are usually low due to disorder of the system [4] and where doping impurities are almost electrically inactive because of the Fermi level stabilization [5] is of certain interest.

In this paper, we intend to explain the doping effect [1, 2], including ultrafast diffusion, high solubility, and electrical activity of metals in CGF.

ANALYSIS OF DIFFUSION PROCESSES IN THE SYSTEM

The rate of metal penetration into the film is determined by the processes at the M/CGF phase boundary, chemical potential gradients $\nabla\mu_M$, and the metal diffusion coefficients in CGF [6]. Assuming that, at $T > T^*$, the M/CGF phase boundary is transparent for metal (the potential barrier $\Delta W \sim k_0 T^*$, where k_0 is the Boltzmann constant), we obtain the metal effective diffusion coefficient in CGF $D \sim 10^{-11}$ cm^2/s at T = 300 K from the relation $\tau = d^2/\pi D \sim 0.1t^*$ [6–8] (here τ is the diffusion time and d is the film thickness equal to 3000 Å) for t^* = 5 min [1].

The coefficient of ion acceleration by electrons is given by

$$\tilde{D}/D_i = (t_e + t_i D_e/D_i) \simeq (N/n + 1), \qquad (1)$$

where t_i and t_e ($t_i + t_e = 1$), N and n, and D_i and D_e are the transport numbers, concentrations and diffusion coefficients of mobile ions and electrons, respectively. $\tilde{D}$ is the adjoint-diffusion coefficient of mobile ions and electrons (holes) [6, 8]. Relation (1) follows from the condition for local electroneutrality of the sample ($\Delta n + \Delta N = 0$); in this case, the resulting adjoint-diffusion coefficient $\tilde{D}$ in (1) is determined by the minority-carrier diffusion coefficient ($\tilde{D} = D_e$ for $t_e \longrightarrow 0$ and $\tilde{D} = D_i$ for $t_i \longrightarrow 0$). It follows from (1) that if the mobile ions and electrons are formed in pairs due to impurity ionization according to the scheme $M^0 \longrightarrow M^{1+} + e^{1-}$ ($N = n$), then the maximum value of the ion acceleration coefficient by electrons does not exceed $\tilde{D}/D_i = 2$ [6]. At the same time, in SIC, where the processes of charge-carrier generation (electrons and ions) are more complicated and include, in particular, the exchange of electrons with the core, we have $N \gg n$ and $\tilde{D} \gg D_i$ [6].

The results of calculation of $\tilde{D}/D_i$ as a function of metal concentration x for different n in CGF are shown in Fig. 2a. One can see from Fig. 2a that, at a low level of doping (x, $N \longrightarrow 0$), the acceleration effect in CGF

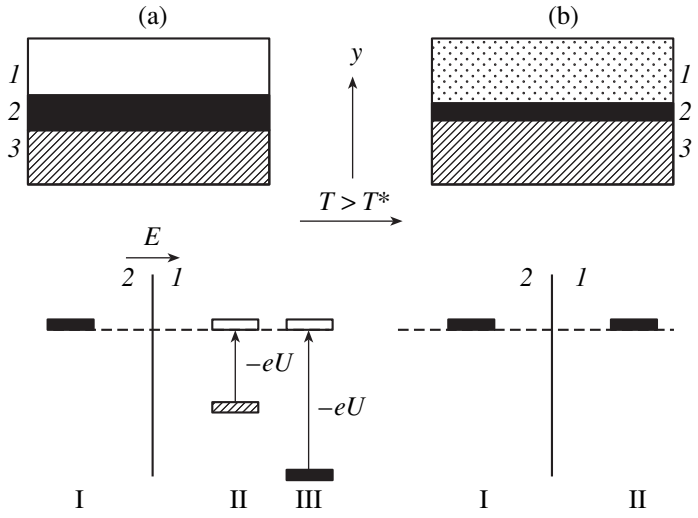

Fig. 1. M/CGF heterostructures (above) and chemical (μ_M) and electrochemical ($\mu_M - eU$) metal-potential levels (below); (a) before and (b) after doping. (a) CGF (*1*), metal (*2*), substrate (*3*); (b) CGF : M (*1*), metal (*2*), substrate (*3*).

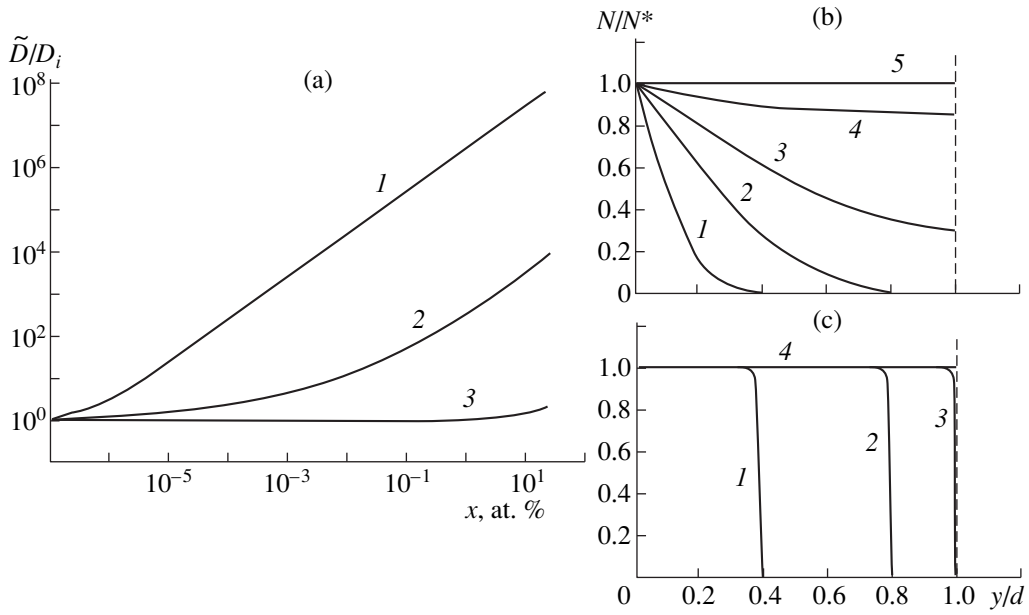

Fig. 2. (a) The coefficient of ion acceleration by electrons $\tilde{D}/D_i$ as a function of the metal concentration (x) in the sample. Concentration of electrons (holes) is n = (*1*) 10^{14}, (*2*) 10^{18}, and (*3*) 10^{22} cm^{-3}. The propagation of the diffusion front in the film for (b) D = const and $\tilde{t} = Dt/d^2$: (*1*) 0.001, (*2*) 0.09, (*3*) 1, (*4*) 4, and (*5*) ∞; and for (c) $D = f(N)$ and $\tilde{t} = Dt/d^2$: (*1*) 0.001, (*2*) 0.09, (*3*) 0.16, and (*4*) ∞. Here, N^* is the maximum metal solubility in the film, y is the coordinate, and d is the film thickness.

is minimal ($\tilde{D}/D_i \longrightarrow 1$). In CGF $As_{1.2}Cu_{0.3}Se$ for $x^* \simeq$ 20 at. %, we have $N_{Cu} \simeq 4 \times 10^{21}$ cm^{-3}. Estimation shows that $\tilde{D}/D_i \sim 10^7$ for $n \simeq 10^{14}$ cm^{-3} [1, 5] (Fig. 2a, curve *1*). For comparison, in crystalline SIC, $\tilde{D}/D_i$ = 10^3–10^4, curve *2* [3, 6]. This is related to the high metal solubility N and the low electron concentration n in CGF.

HIGH METAL SOLUBILITY IN CGF

The effect of an increase in metal solubility at the transition from crystal to glass is well known and is related to the reduced (by 10–20%) density of glass [5]. Thus, for example, the solubility of copper at T = 300 K is about 5% in the crystalline As_2Se [9], and is 19–25% in the amorphous $As_{1.5}Se$ [10].

This phenomenon may be regarded as an inverse pressure diffusion effect occurring under the influence of negative hydrostatic pressure ($\Delta P < 0$, $\Delta V > 0$, where V is the sample volume). The corresponding direct effect ($\Delta P > 0$, $\Delta V < 0$), which was studied previously for a number of SIC chalcogenides, has a negative sign (solubility of metal decreases with increasing pressure). For copper, $\Delta N_{Cu}/\Delta P \simeq -2 \times 10^{-20}$ cm^{-3} GPa^{-1} [11–13]. Extrapolating this dependence to the range of $\Delta V = 0.1$–$0.2 > 0$ and using the relation $\Delta N_{Cu} = (-\Delta N_{Cu}/\Delta P)\kappa^{-1}\Delta V$, where $\kappa(\Delta V/\Delta P)_T \sim 10^{-1}$ GPa^{-1} is the material isothermal compressibility [14], we obtain an estimate of the copper additional solubility in chalcogen at crystal to glass transition $\Delta N_{Cu} \sim (2$–$4) \times 10^{21}$ cm^{-3} (about 10–20 at. % Cu) in accordance with [1, 10].

THERMODYNAMIC DRIVING FORCE OF THE DOPING PROCESS

The chemical potential levels (μ) in crystalline chalcogenide and CGF correspond to the copper solubility: $\mu_{Cu}^{Cu} > \mu_{cr}^{Cu} > \mu_{gl}^{Cu}$ (Fig. 1a, I $\longrightarrow$ II $\longrightarrow$ III), where

$$\mu = \mu^0 + k_0 T \ln a_M; \qquad (2)$$

μ_{Cu}^{Cu}, μ_{cr}^{Cu}, μ_{gl}^{Cu} are the copper atom chemical potential in metallic copper, crystalline chalcogenide, and CGF of the same composition (before doping), respectively; a_M is the metal activity; $\mu^0 = \mu$ ($a_M = 1$); and T is the temperature [15]. After completion of the doping process ($x \longrightarrow x^*$), the copper chemical potential levels in the metal layer and CGF are equalized: $\mu_{gl}^{Cu} = \mu_{cr}^{Cu'} = \mu_{Cu}^{Cu'}$ (Fig. 1b, I $\longrightarrow$ II). Hence, in the approximation of the ideal system ($a_M \longleftrightarrow N$) for $N_{gl} \sim 4N_{cr}$ [1, 2], we use (2) to estimate $\mu_{cr}^{Cu} - \mu_{gl}^{Cu} \sim 0.04$ eV for $\mu_{Cu}^{Cu} - \mu_{cr}^{Cu} \sim 0.1$ eV [3, 15].

Thus, in passing from crystal to glass, the copper chemical potential level in chalcogenide is lowered approximately 1.4 times (Fig. 1a). This stimulates the process of metal introduction into CGF (free energy $\Delta G = \Delta\mu x^* N_0 \simeq 2$ kJ/mol, entropy variation $\Delta S = \Delta G/T \simeq 7$ J/mol K, and N_0 is the Avogadro number). The obtained value of ΔS is comparable to the chalcogenide entropy of melting ($\Delta S_m \simeq 10$–40 J/mol K) [14, 16]. This is indicative of the significant thermodynamic instability of the M/CGF heterostructure after its growth (Fig. 1a). The system is stabilized by way of diffusion. Due to the fact that the electrochemical potential of metal atoms is equalized in the layers $\mu_{Cu}^{Cu} = \mu_{gl}^{Cu}(\mu_{cr}^{Cu}) - eU$, the internal electric field $E = U/d \sim 1$ kV/cm, with maximum at the M/CGF phase boundary, arises, where the main voltage $U \sim 0.1$ V is applied (Fig. 1a) [3, 4]. Under the influence of the internal field E, metal ions are introduced into the film ($Cu^0 \longrightarrow Cu^{1+} + e^{1-}$) and then diffuse through the sample, changing the carrier concentration in CGF [1, 2].

ELECTRICAL ACTIVITY OF DOPING IMPURITY

Electron conductivity conversion ($p \longrightarrow n$) in CGF $As_{0.4}Se_{0.6}$ is observed when copper concentration is increased from 0 to $N_{Cu}^* \simeq 4 \times 10^{21}$ cm^{-3} ($x^* \simeq 20$ at. %). In this case, electron concentration variation is $\Delta n \sim 2 \times 10^{14}$ cm^{-3} [1, 2]. Assuming that each copper atom in CGF is singly ionized [6], we arrive at (like in most amorphous materials) rather low copper electrical activity in CGF: $\eta = \Delta n / N_{Cu}^* \sim 10^{-7}$ (in crystals, $\eta = 1$) [3, 13].

Thus, the doping effect observed in [1, 2] is minimal and may be related to the anomalously high metal solubility (N) exceeding the self-compensation limit in CGF, or to the onset of glass-crystal transition stimulated by transformation Cu + CGF $\longrightarrow$ CGF : Cu. The Fermi energy variation in the course of doping is also small: $\Delta E_F \sim \hbar^2(3\pi^2 n)^{2/3}/m_0 \sim 10^{-2}$–$10^{-3}$ eV (where $\hbar$ is Planck's constant, $m = 0.01$–$0.1 m_0$ is the effective mass of electrons (holes) near E_F in CGF, and m_0 is the free electron mass); i.e., the Fermi level positions in glass are restricted to the narrow energy range near the middle of the CGF energy gap (quasi-gap) [5]. Due to this, the electron (hole) concentrations $n(p)$ in CGF are also low at any doping stage, which explains the rapid metal diffusion in CGF (Fig. 2a, curve *1*).

DIFFUSION FRONT PROPAGATION THROUGH THE SAMPLE

Diffusion front propagation through the sample in the process of CGF doping is described by $D = f(N)$ dependence (Fig. 2a, curve *1*). The results of calculation of the dependence of the metal-diffusion front position on the effective time $\tilde{t} = Dt/d^2$ in the case of diffusion from a constant source into the plate through the side surface for $D = \text{const}$ (Fig. 2b) [17] and for $D = f(N)$ (Fig. 2c) are shown in Fig. 2. The dependence of $D = f(N)$ is approximately considered in calculations in terms of the dependence of $\tilde{t} = f(D)$ (Fig. 2a, curve *1*). One can see from Figs. 2b and 2c that the shape of the propagating diffusion front in CGF varies from diffuse to rectangular, and the doping is completed by $\tilde{t} = 0.16$. The effective diffusion coefficient $D \sim 2 \times 10^{-11}$ cm^2/s (Fig. 2c, curves *1–3*). At the same time, in the case of the maximum doping level, the copper diffusion coefficients in the film may be as large as $\tilde{D} \sim (\tilde{D}/D_i)D \sim 10^{-4}$ cm^2/s, which is typical of crystalline SIC.

Thus, the doping rate of CGF is limited by small metal-diffusion coefficients in the undoped region. The

rate of the diffusion process in the system may increase significantly (t^* up to several seconds) in the case of a small amount of metal presented in CGF before doping (CGF contamination by copper, silver, and so forth). We also note that $D = f(N)$ dependence (Fig. 2a, curve *1*) reduces the M/CGF phase-boundary's relative contribution to the diffusion process kinetics in the system [18]. In fact, to maintain the diffusion front velocity in the film during doping (Fig. 2c) at $\tilde{D}/D_i \sim 10^7$, it is sufficient to maintain the diffusion contact on the $\sim 10^{-5}$ fraction of the M/CGF phase-boundary area.

CONCLUSION

Thus, the effect of ultrafast low-temperature CGF doping with metals (Cu, Ag, Au, Cr, and others) has a superionic character [1, 2]. It is possible to conceive of the M/CGF heterostructure as a highly nonequilibrium, self-organized system, where CGF plays the part of the SIC core (matrix), coming into contact with metal (the superionic agent). Metal diffusion into the shell is promoted in the system at $T > T^*$, and M/CGF $\longrightarrow$ CGF⟨M⟩ transformation occurs. The high speed of this transformation is determined by the thermodynamic driving force related to CGF' state of nonequilibrium as well as by the ion acceleration by electrons, which is rather pronounced in CGF⟨M⟩ glass due to the large values of the N/n ratio (N and n are concentrations of dissolved metal ions and electrons, respectively) typical of CGF.

REFERENCES

1. V. P. Khan and V. Ya. Kogai, in *Proceedings of 18th International Congress on Glass*, San Francisco, USA, (1998), p. 5.
2. V. P. Khan and Ye. V. Alexandrovich, in *Proceedings of 18th International Congress on Glass*, San Francisco, USA, (1998), p. 7.
3. M. A. Korzhuev, T. E. Svechnikova, and S. N. Chizhevskaya, Fiz. Khim. Obrab. Mater., No. 4, 122 (1995).
4. Yu. Ya. Gurevich and Yu. I. Kharkats, *Superionic Conductors* [in Russian] (GR FML, Moscow, 1992).
5. N. F. Mott and E. A. Davis, *Electronic Processes in Non-Crystalline Materials* (Clarendon, Oxford, 1979; Mir, Moscow, 1982).
6. V. N. Chebotin, *Chemical Diffusion in Solids* [in Russian] (Nauka, Moscow, 1989).
7. M. A. Korzhuev, Fiz. Tverd. Tela (St. Petersburg) **34** (4), 1209 (1992) [Sov. Phys. Solid State **34**, 639 (1992)].
8. M. A. Korzhuev, Neorg. Mater. **34**, 504 (1998).
9. *Solid Solutions in Semiconductor Systems: A Reference Book* [in Russian], Ed. by V. S. Zemskov (Nauka, Moscow, 1978).
10. G. Z. Vinogradova, *Glass Formation and Phase Equilibrium in Chalcogenide Systems* [in Russian] (Nauka, Moscow, 1984).
11. M. A. Korzhuev and A. V. Laptev, Fiz. Tverd. Tela (Leningrad) **29**, 2646 (1987) [Sov. Phys. Solid State **29**, 1524 (1987)].
12. M. A. Korzhuev, N. Kh. Abrikosov, and I. V. Kuznetsova, Pis'ma Zh. Tekh. Fiz. **13**, 9 (1987).
13. M. A. Korzhuev and T. E. Svechnikov, Fiz. Tekh. Poluprovodn. (Leningrad) **25**, 2141 (1991) [Sov. Phys. Semicond. **25**, 1288 (1991)].
14. *Physical Quantities: A Reference Book* [in Russian], Ed. by I. S. Grigor'ev and E. Z. Meĭlikov (Énergoizdat, Moscow, 1991).
15. B. B. Damaskin and O. A. Petriĭ, *Electrochemistry* [in Russian] (Vysshaya Shkola, Moscow, 1987).
16. M. A. Korzhuev, V. V. Baranchikov, N. Kh. Abrikosov, *et al.*, Fiz. Tverd. Tela (Leningrad) **26**, 2209 (1984) [Sov. Phys. Solid State **26**, 1341 (1984)].
17. B. I. Boltaks, *Diffusion in Semiconductors* (Fizmatgiz, Moscow, 1961; Academic, New York, 1963).
18. T. D. Dzhafarov, *Radiation-Enhanced Diffusion in Semiconductors* [in Russian] (Énergoizdat, Moscow, 1991).

Translated by I. Kucherenko

Semiconductors, Vol. 34, No. 2, 2000, pp. 217–220. Translated from Fizika i Tekhnika Poluprovodnikov, Vol. 34, No. 2, 2000, pp. 223–226.

AMORPHOUS, VITREOUS, AND POROUS SEMICONDUCTORS

Scanning Tunneling Microscopy of Films of Amorphous Carbon Doped with Copper

A. O. Golubok*, O. M. Gorbenko*, T. K. Zvonareva, S. A. Masalov*, V. V. Rozanov*, S. G. Yastrebov**, and V. I. Ivanov-Omskiĭ****

** Institute for Analytical Instrumentation, Russian Academy of Sciences, Rizhskiĭ pr. 26, St. Petersburg, 198103 Russia*
e-mail: golub@ianin.spb.su

*** Ioffe Physicotechnical Institute, Russian Academy of Sciences, Politekhnicheskaya ul. 26, St. Petersburg, 194021 Russia*
Submitted August 16, 1999; accepted for publication August 18, 1999

Abstract—The results of experimental studies of the copper-doped hydrogenated amorphous carbon films by scanning tunneling microscopy and spectroscopy are reported. These results are indicative of the effect of spatial ordering of nanostructures in thin films based on carbon and copper. Geometric parameters of nanostructures were measured. In the context of the Simmons model, the work function was estimated to be equal to $\varphi \sim 0.05$ eV. Oscillations in differential conductance with a period in a voltage of $\Delta V = 200$–400 mV were detected in tunneling contacts of Ir with the films. The origin of the observed oscillations is discussed. © *2000 MAIK "Nauka/Interperiodica".*

Films of amorphous carbon have a smooth, chemically inert surface with high hardness, a small friction coefficient, and a low threshold for electron emission. The latter fact makes these films promising for the development of cold cathodes in field-emission displays. Interest in the studies of doped films of amorphous carbon is related to the possibility of controlling their properties within a wide range. In addition, studies of the formation of mesoscopic structures based on amorphous carbon have aroused certain interest in relation to the prospects for their use in nanoelectronics. In this paper, we report the results of studies of films of amorphous hydrogenated carbon doped with copper [(*a*-C:H):Cu]. The films were obtained as a result of magnetron cosputtering of copper and graphite targets in an argon–hydrogen atmosphere with subsequent deposition on the Si(111) substrate coated with a chromium layer 200 nm thick [1]. We studied 50- and 100-nm thick (*a*-C:H):Cu(9 at. %) films deposited on the substrate. The measurements were performed in a scanning tunneling microscope (STM) operating under normal atmospheric conditions and using mechanically formed iridium tips. The STM images were obtained in the mode of constant tunneling current (I). We measured the slope of the $I(z)$ dependence (z is the tunneling gap) with the negative-feedback loop closed and the current–voltage $I(V)$ characteristics with an open (for a time $t \le 0.2$ s) negative-feedback loop and linearly scanned bias voltage.

Figures 1 and 2 show the characteristic STM images of the surface and the surface profiles for the (*a*-C:H):Cu films 50 and 100 nm in thickness. The STM images were obtained using the bias voltage $V = -1$ V applied to the sample and the tunneling current of $I = 0.05$ nA.

It is evident from the STM images that the surface profiles of (*a*-C:H):Cu films depend on the film thickness and indicate a granular structure of the surface. For a film 100 nm thick, the difference in heights in the profile is about 10 nm, with the characteristic size of granules being 10–100 nm. A film 50 nm thick features a ~3-nm difference in the surface-profile heights and a characteristic granule size of 2–10 nm. It is noteworthy that the medium- and large-sized granules include self-similar structures of smaller size, which indicate a possible fractal mechanism of forming the film surface.

In order to gain information about a potential barrier in a system consisting of metal, an air gap, and the film, we performed local measurements of the dependence of tunneling current on the interelectrode distance. The measurements were carried out with the tunneling gap modulated with the amplitude $\Delta z \approx 0.1$ nm at a frequency of $\omega = 3.7$ kHz. The value of dI/dz was measured by synchronously detecting the ac component of the tunneling current ΔI at the frequency ω, with the tunneling gap corresponding to a current of $I = 0.1$ nA and a bias voltage of $V = -1$ V. The modulation frequency is chosen such that the condition $\omega > \omega_c$, where ω_c is the cutoff frequency of tracking system, is satisfied. In the context of the Simmons model [2] and in the case of tunneling through a trapezoidal barrier of width z, the tunneling current is given by

$$I = 3.38 \times 10^3 \frac{S}{\varphi}\left(\frac{V}{z}\right)^2 \exp\left(\frac{-6.89 \times 10^{-2} z \varphi^{3/2}}{V}\right),$$

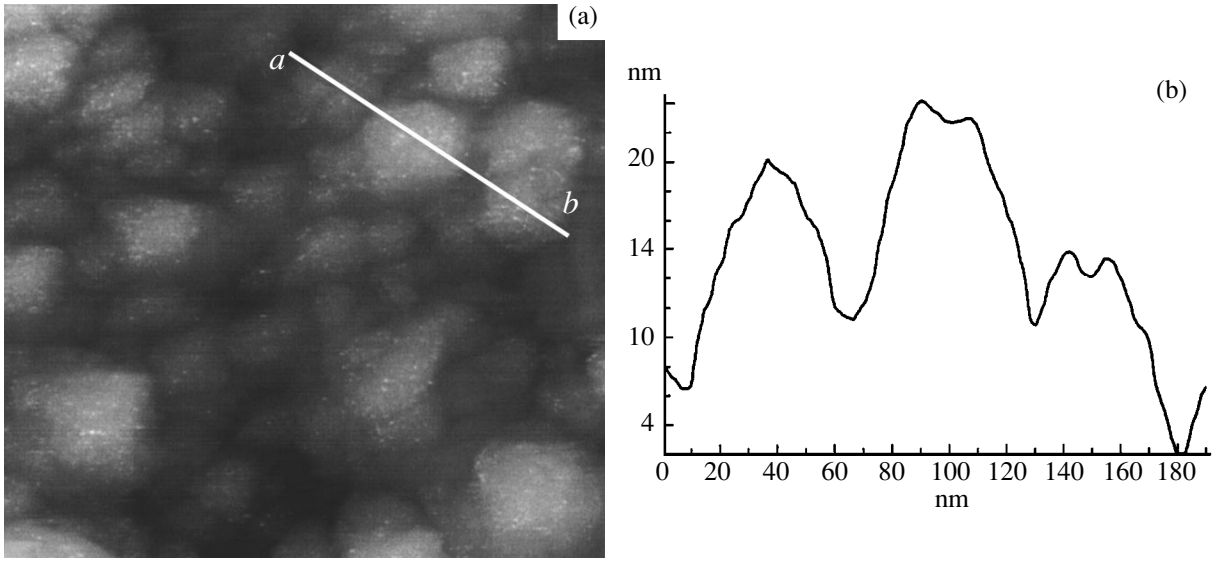

Fig. 1. (a) STM image (top view) and (b) cross section in the *a*–*b* direction of the surface of an (*a*-C:H):Cu(9 at. %) film 100 nm thick. The scanned area is $S = 200 \times 200$ nm^2.

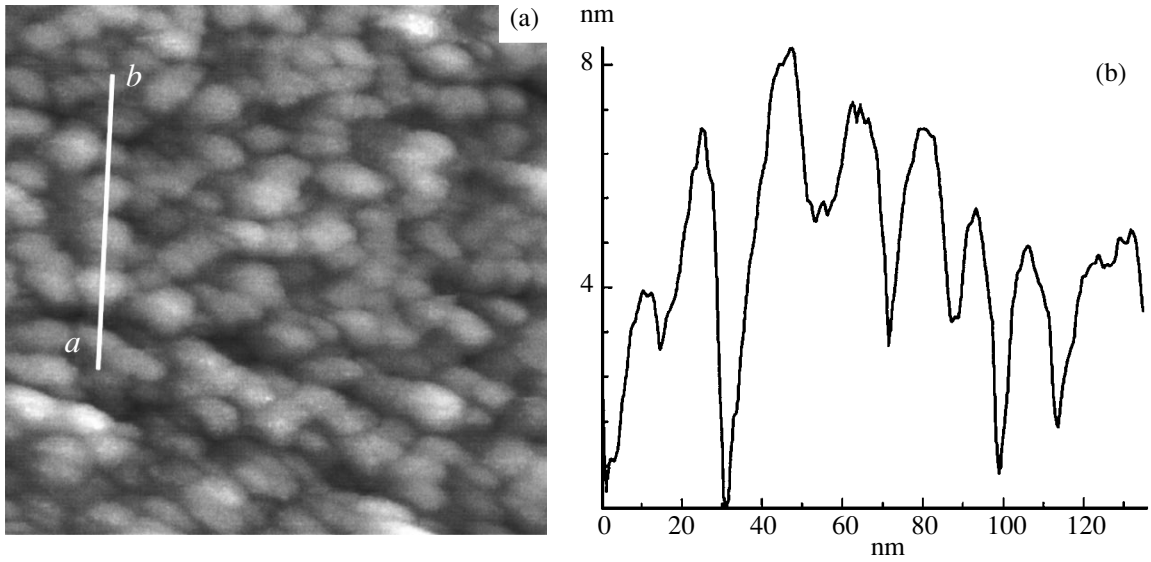

Fig. 2. (a) STM image (top view) and (b) cross section in the *a*–*b* direction of the surface of an (*a*-C:H):Cu (9 at. %) film 50 nm thick. The scanned area $S = 200 \times 200$ nm^2.

where I is the tunneling current (in nA), z is the tunneling gap (in nm), S is the area of tunneling contact (expressed in nm^2), V is the bias voltage (in V), and φ is the average height of the potential barrier (expressed in eV). We now use the condition $\Delta z/z \ll \Delta I/I$ to obtain the following approximate expression for φ:

$$\varphi \simeq \left(\frac{dI}{dz}\frac{V}{6.89 \times 10^{-2} I}\right)^{2/3}.$$

This expression may be regarded as an estimate for the work function of the film for electron emission. Since in the case under consideration $\Delta I/I \sim 9 \times 10^{-3}$, the condition $\Delta z/z \ll \Delta I/I$ is fulfilled for $z \geq 100$ nm. The tunneling gap was estimated from the results of direct measurements of the dependence $I(z)$; the estimates validated the use of the aforementioned approximation. The measurements yielded $\varphi = (0.06 \pm 0.01)$ eV and $\varphi = (0.05 \pm 0.01)$ eV for the films 100 and 50 nm thick, respectively.

The data we obtained are consistent with the results of studies of nitrogen-doped *a*-C:H films reported in [3], where the work function was estimated from integral measurements of the dependence $I(V)$ in the con-

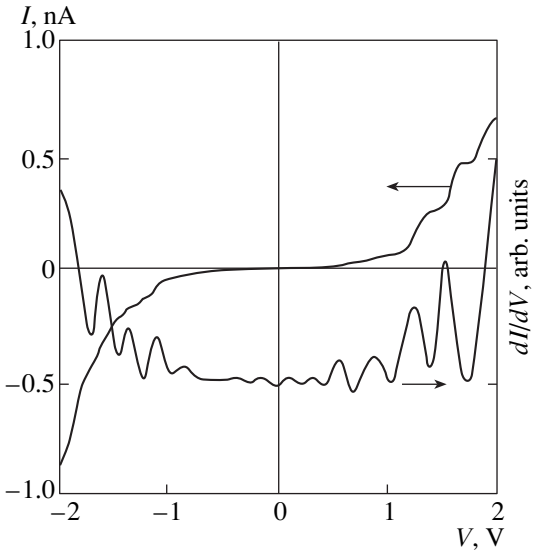

Fig. 3. Current–voltage characteristic $I(V)$ and the first derivative dI/dV for a 100-nm thick *a*-C:H film containing 9 at. % of Cu.

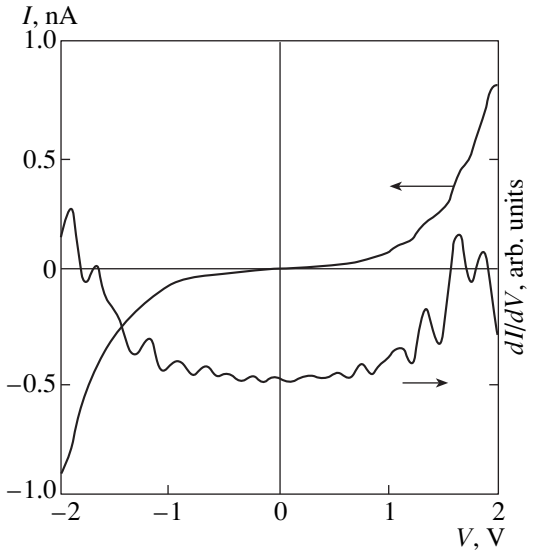

Fig. 4. Current–voltage characteristic $I(V)$ and the first derivative dI/dV for a 50-nm thick *a*-C:H film containing 9 at. % of Cu.

text of the Fowler–Nordheim theory. For the samples with a different doping level, the work function was found to be equal to $\varphi = 0.03$–0.05 eV. It is worth noting that the measurements of the average work function according to the conventional Fowler–Nordheim method should involve experimental determination of the area of the emitting surface, which decreases the accuracy of determined values of the work function. The opportunity to modulate the tunneling gap in STM makes it possible to estimate experimentally the work function by knowing just three precisely measured parameters: the tunneling current I, the tunneling bias voltage V, and the slope of the dependence $I(z)$. A certain discrepancy between the values of the work function obtained for the films differing in sizes of granules and in thickness is consistent with a model according to which the film of amorphous carbon acts as a peculiar concentrator of electric field [4]. In this model, the electron-emission current attains its maximum for an optimal thickness of the film deposited on the substrate capable of emitting the electrons.

In order to study local electronic properties of (*a*-C:H):Cu films at various sites on the surface of the sample, we measured the current–voltage (I–V) characteristics of the tunneling contact. The I–V characteristics were nonlinear, and, in about 30% of all cases, steplike features were observed in the current. If the feedback loop was open, measurements of the dependence $I(V)$ were accompanied by noise interferences. The noise could be caused by small random variations in the distance between the tip and the sample due to mechanical vibrations and acoustic interferences and by changes in the physical conditions for the tunneling current due to the presence of a high nonuniform electric field, layers with adsorbed moisture and gases, and so on. In order to reduce the noise, we used an active filtering of the tunneling current. Since the energy resolution in determining the positions of singularities in the dependence $I(V)$ is limited by the thermally induced broadening of the tunneling contact in the vicinity of the Fermi level and amounts to $\Delta \simeq 50$ meV at room temperature, it is acceptable that the filtering of the dependence $I(V)$ broadens the vertical steps by an amount no larger than ~100 mV. We used a filter that convolved the tunneling current with the spread function $F(V)$ given by

$$F(V) = 2 \times 10^{-1}\sin(2\pi V/\Delta V)/(2\pi V/\Delta V),$$

where $\Delta V \simeq 100$ mV.

Figures 3 and 4 show the dependences $I(V)$ and $dI/dV = f(V)$ measured with the tip above arbitrarily chosen spots at the surface of (*a*-C:H):Cu films; quasiperiodic singularities (steps in current) with characteristic period $\Delta V = 200$–400 mV are observed.

Similar singularities in the dependence $I(V)$ for the films of tetrahedral amorphous carbon doped with nitrogen were observed in [5]. In that publication, the emergence of stable singularities in differential conductance $dI/dV = f(V)$ for bias voltages of 1.7, 2.8, and 3.6 V was related to localized π states arising in the near-surface layer enriched in sp^2 bonds. However, it may be assumed that oscillations in differential conductance in local tunneling contacts can be also related to one-electron effects [6] occurring in tunneling through a small-sized high-conductivity cluster located in the tunneling-barrier near-surface layer of the sample. The process of tunneling through an isolated cluster as the bias voltage increases is accompanied by a steady increase in the electric charge of the cluster by an amount multiple to the elementary charge; this pro-

cess is not stochastic if the condition $e^2/2C \gg kT$ is fulfilled (here, e is the elementary charge, C is capacitance of a cluster, k is the Boltzmann constant, T is absolute temperature, and $e^2/2C$ is the Coulomb energy required to transfer an elementary charge to the cluster). As a result of a Coulomb blockade, differential conductance of tunneling contact oscillates with a period of e/C.

Assuming that the conducting cluster with the radius r is located in the dielectric layer with a thickness of $d \sim r$, we may estimate the effective capacitance of a cluster as [7]

$$C \sim 8\pi\varepsilon\varepsilon_0 r,$$

where ε is the permittivity of the medium and ε_0 is the permittivity of vacuum. Assuming then that $\varepsilon > 1$, we estimate the size of the conducting cluster as $r < e/8\pi\varepsilon\varepsilon_0\Delta V = 2$–$4$ nm. Slow-moving clusters of such size can reside at the film surface. In addition, a fraction of sp^2 bonds is increased in the near-surface layer of the doped diamond-like film, which brings about an increase in the number of localized π states. In our opinion, the localized π states can also cause the one-electron oscillations; in this case, the aforementioned estimate for the size of metallic cluster may be regarded as an estimate of the size of the charge-localization region and is consistent with the observed conductance oscillations having a period of 400 mV. Furthermore, the effect of resonance tunneling through localized states can also be responsible for the oscillations observed. Further studies are needed to elucidate the origin of singularities observed in the local-tunneling spectra of diamond-like films doped with copper.

ACKNOWLEDGMENTS

This work was performed using the equipment of the St. Petersburg Joint Research Center; the work was supported by the State Scientific–Technological Program on the Physics of Solid-State Nanostructures (project no. 98-3010) and, in part, by the Russian Foundation for Basic Research (project no. 97-02-18110).

REFERENCES

1. V. I. Ivanov-Omskiĭ, A. O. Golubok, S. G. Yastrebov, *et al.*, Pis'ma Zh. Tekh. Fiz. **24**, 28 (1998).
2. J. G. Simmons, J. Appl. Phys. **34**, 2581 (1963).
3. G. A. J. Amaratunga and S. R. P. Silva, Appl. Phys. Lett. **68**, 2529 (1996).
4. R. D. Forrest, A. P. Burden, S. R. P. Silva, *et al.*, Appl. Phys. Lett. **73**, 3784 (1998).
5. C. Arena, B. Kleinsorge, J. Robertson, *et al.*, J. Appl. Phys. **85**, 1609 (1999).
6. D. V. Likharev and K. K. Averin, Zh. Éksp. Teor. Fiz. **90**, 733 (1986).
7. V. I. Ivanov-Omskiĭ, A. B. Lodygin, A. A. Sitnikova, A. A. Suvorova, S. G. Yastrebov, and A. V. Tolmachev, in *Diamond and Diamond-like Film Applications*, Ed. by P. Gielisse, V. I. Ivanov-Omskiĭ, G. Popovichi, and V. Prelas (Technomic, Lancaster-Basel, 1998), p. 486.

Translated by A. Spitsyn

Semiconductors, Vol. 34, No. 2, 2000, pp. 221–227. Translated from Fizika i Tekhnika Poluprovodnikov, Vol. 34, No. 2, 2000, pp. 227–233.

AMORPHOUS, VITREOUS, AND POROUS SEMICONDUCTORS

Mechanisms of Transport and Injection of Carriers into a Porous Silicon: Electroluminescence in Electrolytes

D. N. Goryachev, G. Polisskiĭ*, and O. M. Sreseli

Ioffe Physicotechnical Institute, Russian Academy of Sciences, Politekhnicheskaya ul. 26, St.-Petersburg, 194021 Russia
e-mail: olga.sreseli@pop.ioffe.rssi.ru
** München Technical University, E-16, D-85747 Garching, Germany*
Submitted September 20, 1999; accepted for publication September 23, 1999

Abstract—A model describing the transport and injection of carriers into a heterophase system (silicon substrate)/(silicon nanocrystals)/(electrolyte) under excitation of electroluminescence is proposed. The main fraction of current passes from the electrolyte directly into a substrate by-passing the nanocrystals. Electromechanical processes at the electrolyte–substrate interface produce the electroactive particles, which inject one or both types of carriers in macro- and nanocrystals, respectively. For the bipolar injection, the nanocrystals play the role of catalyst in the exothermal reaction of charge exchange between the electroactive particles, which possess the opposite charges. In this case, the particles transfer the energy to nanocrystals, which they accumulated in the process of their formation. A fraction of this energy is released by the radiative recombination. The resulting efficient visible electroluminescence is weakly dependent on the doping level and conduction type of the initial silicon. *© 2000 MAIK "Nauka/Interperiodica".*

INTRODUCTION

The porous silicon (*por*-Si) has already been known for more than four decades [1], but the intense study of its unique properties was started rather recently after the discovery of *por*-Si intense photoluminescence in the visible part of the spectrum and after this phenomenon was explained as a quantum-size effect in silicon nanocrystals [2, 3]. A short time later, a red-orange electroluminescence (EL) of *por*-Si in aqueous solutions of electrolyte was observed and was found almost as intense as the luminescence mentioned above [4, 5]. At the same time, despite the numerous attempts of development of solid state electroluminescent structures based on *por*-Si, their efficiency turned out to be by several orders lower [6, 7]. This problem is actually not solved at present. Up to the last years, there were no publications considering the origin of the remarkably high (up to 1%) EL efficiency of *por*-Si in contact with electrolyte solutions.

Two kinds of EL of *por*-Si in solutions are known: cathodic and anodic EL. They differ in the current direction across the system, which consists of the operating electrode (silicon substrate and *por*-Si layer), electrolyte and counter electrode, usually made of platinum. A negative or positive bias is applied to the operating electrode from the external power supply, respectively.

Observation and studies of cathodic EL of *por*-Si was a logical continuation of the studies started in the 1960s of cathodic EL of a number of bulk wide-gap semiconductors in contact with solutions of strong oxidants [8]. Morrison has shown in [9] the possibility of hole injection from such an electrolyte into bulk silicon, and since 1992, the publications on the visible intense cathodic EL of *por*-Si in contact with the electrolyte appeared [5, 10, 11]. The anodic EL of *por*-Si in the visible part of the spectrum was observed as likely for the first time also in 1960 [12], but intense study began after the appearance of [4].

One can consider the following concept as generally accepted: the nanocrystals with prevalent sizes no larger than 5 nm with an effective forbidden gap enhanced due to a quantum-size effect up to 2–3 eV [13] are responsible for visible emission in *por*-Si or at least for its red-orange part. Such an explanation is common both for the photoluminescence and for the anodic and cathodic EL [14–18]. In this case, the question of the mechanism of carrier drift to the nanocrystals in the electrolytic system still remains open. This problem is of obvious importance as it is directly related to the efficiency of EL of *por*-Si. Analogously to the well-studied EL of bulk wide-gap semiconductors in contact with electrolytes, it is assumed in many works that one type of carriers is transported to the nanocrystals by their drift from the silicon substrate, whereas the other type of carriers is injected into them out of the electrolyte, i.e., from the side of the counter electrode [16–18]. However, as was shown in [19, 20], such an approach cannot be justified owing to the specific properties of *por*-Si.

The mechanisms of bipolar injection of carriers from the electrolyte into nanocrystals for cathodic and anodic processes of EL of *por*-Si were first suggested in [19] and [20], respectively, and were analyzed in

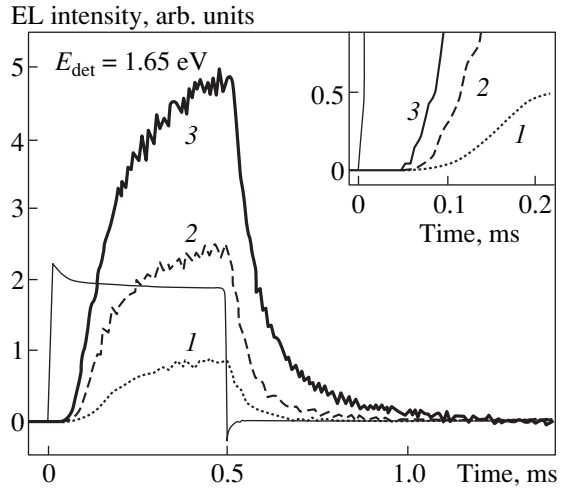

Fig. 1. Kinetics of changes in cathodic EL pulse with photon energy E_{det} = 1.65 eV for current densities equal to (*1*) 20, (*2*) 40, and (*3*) 60 mA/cm^2. Current pulse is drawn by a thin line. In the insert, the dependence of "dead" time on the current density is shown in more detail.

detail. It was also shown that the injection schemes suggested account for many known properties of EL.

In this paper, we suggest a generalized scheme of carrier injection into the nanocrystals both for cathodic and for anodic processes of electrolytic EL. The energy exchange in such processes is considered. From the standpoint of bipolar carrier injection the experimental data (both known and new) on EL of Si/Si-nanocrystals/electrolyte structure are considered.

FEATURES OF TRANSPORT MECHANISM IN A SYSTEM Si/Si-NANOCRYSTALS/ELECTROLYTE

Small sizes of nanocrystals induce the forbidden-gap broadening and cause a high electrical resistance of the *por*-Si layer irrespective of the conduction type and carrier concentration in the initial silicon substrate. Insulating properties of *por*-Si films are well known [21]. According to data in [22, 23], the resistivity of nanocrystals can exceed that of the initial silicon by 6–8 orders of magnitude. Direct measurements on free-standing *por*-Si films yield the values of resistivity of about 10^7 Ω cm, with the drift electron and hole mobilities being about 10^{-1} and 10^{-3} cm^2/V s, respectively, which is characteristic of materials with disordered structure [24]. In addition, the charge transfer between a substrate and nanocrystals, to a considerable extent, is blocked by an electrostatic barrier existing at the corresponding interface [25]. Finally, one cannot but infer that there exist a certain number of nanocrystals which lost an electrical connection with a substrate and are separated from it by oxide films. It is known that *por*-Si can contain up to 40% silicon oxide [26].

A complicated character of current flow through the *por*-Si layers is confirmed by numerous measurements of *I–V* characteristics of solid state *por*-Si-based structures (see, e.g., [27]). The non-ideality coefficients of these characteristics for Schottky-diodes are, as a rule, represented by a two-digit number [28]. In combination with the features of *por*-Si structure mentioned above, it testifies that the current flow mechanisms in these structures resemble more the currents in dielectrics rather than those in semiconductors. For an explanation of the through current across the *por*-Si layer, one usually invokes either carrier tunneling through the oxide shell of nanocrystals [29], or the transport over the localized levels (the carrier traps [30]).

As distinct from the solid-state systems, the resistance of *por*-Si layers impregnated by various electrolytes (their resistivity usually does not exceed 10 Ω cm), is lower by several orders of magnitude than that of a dry layer, despite the definite hydrophoby of *por*-Si structures [31, 32]. The use of hydrophilic additives to the electrolyte (e.g., acetone) lowers the resistivity of *por*-Si even more, up to values of about 1 Ω/cm^2, which are characteristic of smooth silicon surfaces. These results testify that the electrolyte impregnates the *por*-Si layer practically throughout its depth and efficiently shunts the high-resistivity nanocrystals. It is reasonable to assume that the main fraction of current flows through the electrolyte into a silicon substrate bypassing the nanocrystals and, consequently, is not involved in the carrier injection into the nanocrystals (the so-called bypass current).

When measuring the pulsed cathodic EL, a significant delay between the current pulse onset and EL appearance was found out (Fig. 1) [33]. The value of this "dead" time depends on the current density and amounts to fractions of a millisecond (see insert in Fig. 1). This effect is positive proof of the fact that, at least, a part of the current bypasses the nanocrystals.

An idea was put forward for the first time in [32] that it was a bypass current which provides generation of electrically active substances; these substances then simultaneously inject both electrons and holes into nanocrystals. This concept of bipolar carrier injection from the electrolyte was subsequently developed for various particular cases of *por*-Si EL in [19, 20]. Generalizing the results of these works, we can formulate the general laws of charge transport in a Si/Si-nanocrystals/electrolyte system.

Under the action of the bypass current, a number of electrochemical and other accompanying secondary chemical processes take place at the interface of the electrolyte with silicon substrate surface and with electrically connected with it macrocrystallites (non-quantum-sized). These processes generate the electrically active particles possessing clearly pronounced donor and acceptor properties. The charge carriers which are necessary for supporting these reactions come directly from the bulk of silicon substrate.

These particles are unstable, short-living entities. Nonetheless, a definite quasi-equilibrium concentration of electrically active particles is established in the process of electrolysis in the immediate neighborhood of nanocrystals. These particles carry the opposite electrical charges, but the probability of their interaction with each other, directly in solution, is low [34]. The probability of the charge interchange where solid-state surface [35] (in particular, the surface of nanocrystals in *por*-Si) is involved, is significantly higher. Diffusing in the electrolyte, electrically active particles reach the nanocrystal surface, efficiently exchanging their charges and injecting the carriers of both types into nanocrystals. In this case, the electrical neutrality of nanocrystals is retained even if they do not have an electrical coupling with the substrate.

It is shown in [19] and [20] in detail what the reactions, occurring at the electrolyte–silicon-substrate interface, are for cathodic and anodic connection of *por*-Si. The electrically active particles that provide the bipolar carrier injection into the nanocrystals are identified. One should be reminded that in the case of cathodic EL (with a persulfate electrolyte), these are free hydrogen atoms (donors) and ion-radicals $(SO_4)^{\bullet -}$ (acceptors), and in anodic processes, these are the free hydrogen and oxygen atoms, respectively.

The processes responsible for the EL emergence are shown schematically by the example of cathodic EL in Fig. 2. The bypass current produces ion-radicals $(SO_4)^{*-}$ (acceptors) and free hydrogen atoms H^0 (donors), as is shown in the oval (a). As a result of carrier injection into crystals, EL appears (oval (b) in Fig. 2). The scheme of processes occurring in the case of anode EL is similar.

The main energy levels in silicon and in the electrolyte (in the absence of contact between them) are shown in Fig. 3. The position of conduction and valence bands for bulk silicon and *por*-Si is shown on the right-hand scale. These data are given in accordance with silicon affinity to electron and with gap discontinuities between silicon and *por*-Si [36]. The standard potentials of electrochemical reactions (φ_0) are given on the left-hand scale. These values are defined as $\varphi_v = 4.5\text{V} + \varphi_0$ with respect to electron level in a vacuum [37].

Reactions of charge exchange between electrically active particles are exothermal. The energy released in this reaction is determined by the difference of corresponding electrochemical potentials involved in the particle exchange. This energy depends also on the particle concentration in solution and can reach 3–4 eV and more (see Fig. 3). Thus, the energy transferred to nanocrystals by injected carriers significantly exceeds the width of the nanocrystals' forbidden gap. A portion of this energy is spent on carrier radiative recombination and serves as a source of visible EL. Consequently, an energy source of EL is the energy acquired by electroactive particles in the course of their formation under the action of bypass current.

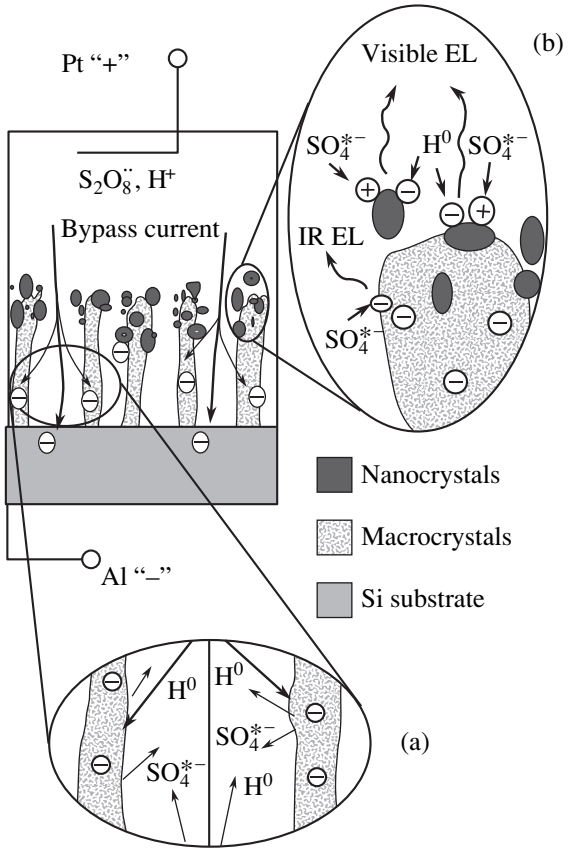

Fig. 2. Schematic representation of processes occurring in the course of current flow in a Si/Si-nanocrystals/electrolyte system. Comments are in text.

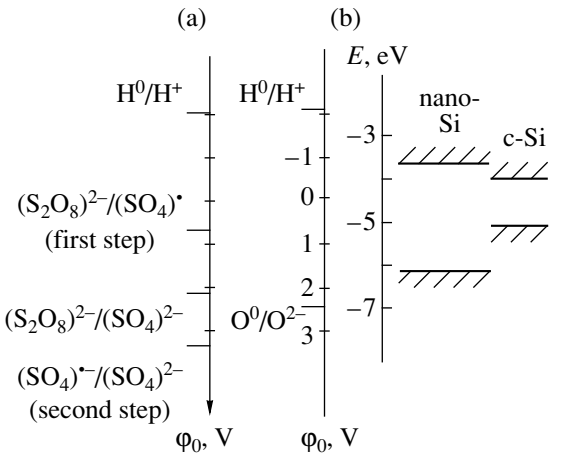

Fig. 3. Main energy levels in silicon and in *por*-Si (on the right) and standard potentials of electrochemical reactions for cathodic (a) and anodic (b) processes in electrolyte (on the left) in the absence of interphase contact.

The experimental data given below confirm the injection mechanism of charge transfer in the Si/Si-

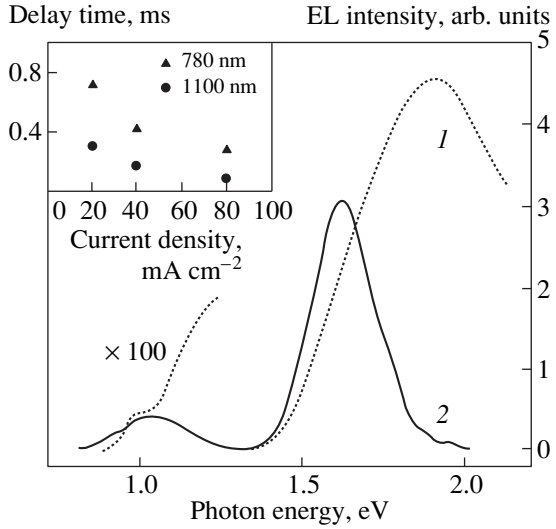

Fig. 4. Two spectral bands (visible and IR) of cathodic EL in Si/Si-nanocrystals/electrolyte system: (*1*) the spectrum of a sample prepared by conventional method (by anodizing with illumination by white light) and (*2*) the spectrum of a sample is prepared according to [39] (spectrum with a well pronounced IR band). In the insert, the delay times for the EL onset of both bands for various current densities are shown. The pulse repetition rate f = 11 Hz, and the pulse duration τ_p = 2 ms.

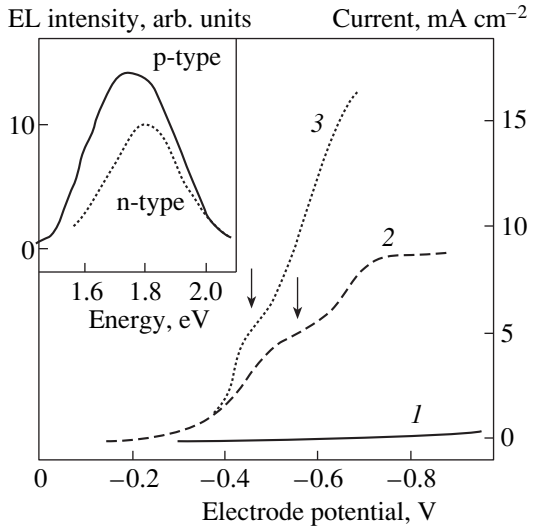

Fig. 5. Cathodic polarization curves for a *p*-Si/Si-nanocrystals/electrolyte system (with the 50% additive of acetone): (*1*) in dark; (*2*) with a weak IR illumination, and (*3*) with a more intense IR illumination. Electrode potentials are measured with respect to a standard calomel electrode (SCE). The onset of visible EL is indicated by arrows. In the insert, the EL spectra for *por*-Si grown on the substrates of *n*- and *p*-type conduction are shown.

nanocrystals/electrolyte system and the results of a number of experiments are explained from the standpoint of the concept suggested.

EXPERIMENTAL RESULTS. DISCUSSION

It follows from the process scheme suggested that carrier transport in Si/Si-nanocrystals/electrolyte system is ionic rather than electronic. This fact explains the large times of EL delay with respect to current pulse (Fig. 1), because the EL appearance is caused by the accumulation of sufficient concentration of electrically active particles, as well as by their time of diffusion towards the nanocrystals [19].

The mechanism of accumulation of electrically active particles also explains the EL pulse delay-time dependence on the current density (see the insert in Fig. 1). The larger the current, the faster the required concentration of particles accumulates and the earlier the EL appears.

It was shown in [38, 39] that, along with the visible emission in the spectrum of cathode EL, the infrared (IR) radiation is present (Fig. 4), with the delay time of IR EL being less, than in the case of visible EL (see the insert in Fig. 4). IR band of EL is the result of radiative recombination of injected holes with electrons coming from the substrate and microcrystallites electrically connected with it. The generation and accumulation of atomic hydrogen (which injects the electrons from the electrolyte) is not required for the excitation of IR EL; EL emerges after the required concentration of $(SO_4)^{*-}$ ions injecting the holes is accumulated (see oval (b) in Fig. 2). Therefore, the delays between the current pulse onset and IR EL appearance are shorter than in the case of visible EL. The decrease of EL delay with the current density increase is seen in the insert in Fig. 4 for the visible and IR EL. The nonlinearity of these dependences is caused by the diffusion limitations of the ion-radical formation rate in the solution.

An efficient EL of *por*-Si is observed also if the carriers in a silicon substrate providing the flow of bypass current are the minority carriers. This takes place, e.g., in the case of cathodic EL of *por*-Si grown on the substrate of *p*-type conduction. It is necessary only to increase the concentration of minority carriers in Si-substrate, e.g., by illumination [19, 40, 41]. In this case, both the polarization curves and the EL spectrum turned out to be similar to the dependences for the substrates of *n*-type conduction (Fig. 5).

The model suggested for the carrier transport well explains the similarity of EL spectra of *por*-Si layers on the substrates of various types of conduction (see the insert in Fig. 5). Due to the universal character of transport mechanisms, the spectrum shape and intensity are determined primarily by the distributions of crystallite sizes and to a significantly lesser extent by the electrolyte composition, current density, and other factors.

A distinct correlation between the appearance of visible emission and the onset of gaseous-hydrogen release in the Si/Si-nanocrystals/electrolyte system

under the cathode bias was established in [32]. This can also be seen in Fig. 5: the bend of polarization curves induced by the onset of hydrogen formation coincides with the onset of the visible EL indicated by arrows. These observations confirm the mechanism of bipolar injection, which is directly connected with formation of free hydrogen atoms.

A significant reversible "blue" shift of the spectral maximum under changes of voltage applied to the electrolytic cell [16] is a characteristic feature of the cathodic EL spectra. The results of our experiments show that similar effects are also observed under changes of the amplitude of pulse current which excites EL (Fig. 6a). Moreover, the time delay of pulse EL for a given current density depends on the energy of EL detection (Fig. 6b). For lower energies of detection, the EL pulse increases faster, but decays slower. The reconstruction of spectra is observed also in the time-resolved spectra (boxcar technique) measured by the method when the signal detection is carried out within the temporal window, which can move with respect to the current-pulse onset. The shift of the narrow (τ_g = 0.2 ms) detection window from the onset of the current pulse (τ_p = 2 ms) towards its end causes a significant shift of the EL spectrum towards the higher energies (Fig. 6c).

All variants of the EL spectrum control (by the voltage, current density, time-delay changes) find a reasonable explanation in the context of the charge-transfer mechanism suggested.

Actual electrochemical potentials of electrically active particles (φ), which provide the charge transport to nanocrystals, are defined by their standard electrochemical potentials (φ_0) and activity concentrations of their oxidized and reduced forms (A_{ox} and A_{red}) according to the equation

$$\varphi = \varphi_0 + \text{const} \times \ln(A_{ox}/A_{red}). \quad (1)$$

With an increase in the voltage or current density in the electrolytic cell, the generation rate of these particles increases, and, correspondingly, their quasi-equilibrium concentration in the solution increases too. In accordance with (1), the magnitudes of electrochemical potentials of oxidizing and reducing particles increase. The distance between the energy levels of donors and acceptors increase, which makes possible the carrier injection into the conduction and valence bands of smaller and smaller nanocrystals. Thus, the voltage and current increase induces the shift of EL spectral peak to shorter wavelengths (Fig. 6a).

Changes of the EL pulse spectra in Figs. 6b and 6c can also be explained within the context of the model suggested. Even for a constant value of external voltage (current), accumulation of electrically active particles with time results in an increase of their concentration in the electrolyte and in a continuous enhancement of the energy distance between electrochemical potentials in consistency with equation (1). Due to these facts the

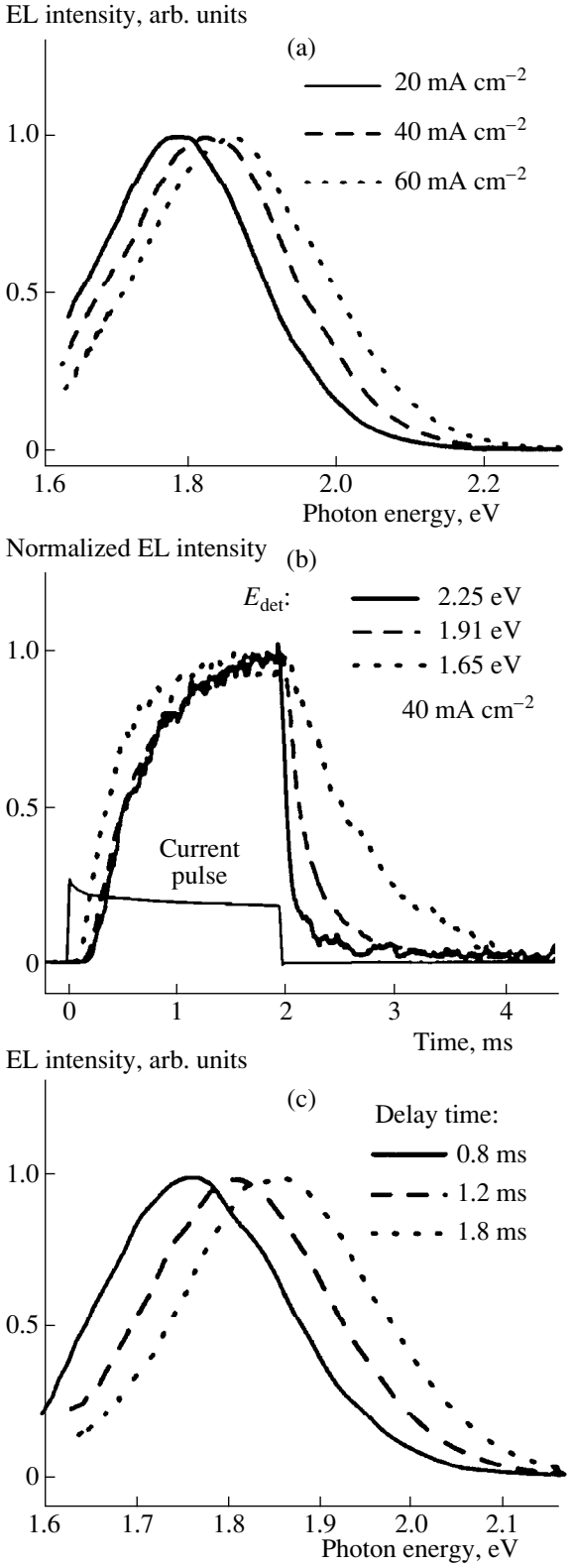

Fig. 6. Spectral and temporal changes in cathodic EL for *n*-Si/Si-nanocrystals/electrolyte system in relation to the pulse current density (a), detection energy E_{det} (b) and position of the detecting temporal window with respect to the onset of a current pulse (c). The pulse repetition rate f = 11 Hz, pulse duration τ_p = 2 ms.

efficiency of carrier injection and EL intensity becomes dependent on time and detection energy. The smallest (with the widest forbidden gap) nanocrystals are excited later than the other, and their luminescence quenches first. The time-resolved spectra confirm this fact: a significant shift of EL peak to higher energies is seen for large delay times of signal detection (Fig. 6c).

Our view on the similarity of cathodic and anodic processes of EL is confirmed in [17]; it is shown there that the dependence of the spectral shift on the electrode potential has the same coefficient of proportionality both in cathodic and in anodic processes.

It is known that the anodic EL is quenched in several minutes after its appearance [14, 15]. This phenomenon is usually attributed to oxidation of silicon nanocrystals, which occurs under the action of current passing through them. We now consider these processes from the standpoint of the suggested mechanism of carrier transport towards the nanocrystals. In accordance with [20], the main anodic process occurring on the silicon substrate is the silicon oxidation with formation of silicon monoxide first, and then, of silicon dioxide:

$$\mathrm{Si} + 2h^+ + \mathrm{H_2O} \longrightarrow \mathrm{SiO} + 2\mathrm{H}^+, \quad (2)$$

$$\mathrm{SiO} + 2h^+ + \mathrm{H_2O} \longrightarrow \mathrm{SiO_2} + 2\mathrm{H}^+. \quad (3)$$

Free hydrogen atoms serve as the carriers of electrons towards the nanocrystals. They are formed as a result of chemical reaction between silicon monoxide (SiO) and water in consistency with the reaction

$$\mathrm{SiO} + \mathrm{H_2O} \longrightarrow \mathrm{SiO_2} + 2\mathrm{H}^0. \quad (4)$$

However, as it follows from the above stated, SiO is formed only at the interface between a silicon substrate and a growing SiO_2 layer. With an increase in the thickness of this layer, the atomic hydrogen diffusion becomes more and more difficult and afterwards ceases completely. The electron injection into nanocrystals and anode EL is also terminated.

CONCLUSION

It is shown in this work that in the process of electroluminescence, a significant portion of a current in Si/Si-nanocrystals/electrolyte system passes immediately from the silicon substrate into electrolyte, bypassing the silicon nanocrystals. This current generates the electrically active species at the interface of substrate and electrolyte, which act as donors and acceptors for electrons and can diffuse inside the electrolyte and be adsorbed by the semiconductor surface. Due to a large energy stored in these species in the course of their formation, they easily inject carriers into the valence and conduction bands not only of bulk silicon, but also of wide-gap nanocrystals. In the process of such bipolar injection of carriers, the nanocrystals retain electrical neutrality and serve as catalysts in the course of carrier transport between the electrically active particles. The fraction of carriers recombine then radiatively providing an intense electroluminescence in the visible part of the spectrum. The model suggested well explains all the main features of porous silicon electroluminescence on the substrates of *n*- and *p*-type conduction under both cathodic and anodic biases.

ACKNOWLEDGMENTS

This work was supported by the Program of Ministry of Science “Physics of Solid State Nanostructures”, project nos. 99-1107 and 97-1035.

REFERENCES

1. A. Uhler, Bell Syst. Tech. J. **35**, 333 (1956).
2. L. T. Canham, Appl. Phys. Lett. **57**, 1046 (1990).
3. V. Lehmann and U. Gösele, Appl. Phys. Lett. **58**, 856 (1991).
4. A. Halimaoui, C. Oules, G. Bomchil, *et al.*, Appl. Phys. Lett. **59**, 304 (1991).
5. P. M. M. C. Bressers, J. W. J. Knapen, E. A. Meulenkamp, *et al.*, Appl. Phys. Lett. **61**, 108 (1992).
6. Z. Chen, G. Bosman, and R. Ochoa, Appl. Phys. Lett. **62**, 708 (1993).
7. N. Koshida, H. Koyama, Y. Yamamoto, *et al.*, Appl. Phys. Lett. **63**, 2655 (1993).
8. R. Memming and G. Schwandt, Electrochim. Acta **13**, 1299 (1968); R. Memming, J. Electrochem. Soc. **116**, 785 (1969).
9. S. R. Morrison, J. Appl. Phys. **53**, 1233 (1982).
10. L. T. Canham, W. Y. Leong, M. I. J. Beale, *et al.*, Appl. Phys. Lett. **61**, 2563 (1992).
11. L. V. Belyakov, D. N. Goryachev, O. M. Sreseli, *et al.*, Fiz. Tekh. Poluprovodn. (St. Petersburg) **27**, 1815 (1993) [Semicond. **27**, 999 (1993)].
12. A. Gee, J. Electrochem. Soc. **107**, 787 (1960).
13. A. G. Gullis, L. T. Canham, and D. J. Calcott, J. Appl. Phys. **82**, 909 (1997).
14. P. C. Searson, S. M. Prokes, and O. J. Glembocki, J. Electrochem. Soc. **140**, 3327 (1993).
15. M. Ligeon, F. Muller, R. Herino, *et al.*, J. Appl. Phys. **74**, 1265 (1993).
16. A. Bsiesy, F. Muller, M. Ligeon, *et al.*, J. Appl. Phys. **74**, 1265 (1993).
17. A. Bsiesy, M. A. Hory, F. Gaspard, *et al.*, in *Microcrystalline and Nanocrystalline Semiconductors* (Pittsburg, PA, 1995) [Mater. Res. Symp. Proc. **358**, 619 (1995)].
18. A. Bsiesy, B. Gellos, M. A. Hory, *et al.*, *Advanced Luminescent Materials*, Ed. by D. J. Lockwood, P. M. Fauchet, N. Koshida, and S. R. J. Brueck, **PV95–25** (Pennington, NJ, 1996), p. 1.
19. D. N. Goryachev, L. V. Belyakov, G. Polisskiĭ, *et al.*, Fiz. Tekh. Poluprovodn. (St. Petersburg) **31**, 844 (1997) [Semicond. **31**, 716 (1997)].
20. D. N. Goryachev, L. V. Belyakov, G. Polisskiĭ, *et al.*, Fiz. Tekh. Poluprovodn. (St. Petersburg) **32**, 591 (1998) [Semicond. **32**, 529 (1998)].
21. Y. Arita, K. Kato, and T. Sudo, IEEE Trans. Electron Devices **24**, 756 (1977).

22. A. J. Simons, T. I. Cox, M. J. Uren, *et al.*, Thin Solid Films **255**, 12 (1995).
23. S. P. Zimin, Pis'ma Zh. Tekh. Fiz. **20** (7), 55 (1994).
24. E. A. Lebedev, G. Polisskiĭ, and V. Petrova-Koch, Semicond. **30**, 772 (1996); E. A. Lebedev, G. Polisskiĭ, and E. A. Smorgonskaya, Phys. Rev. B: Condens. Matter **57**, 14607 (1998).
25. Th. Dittrich, J. Rappich, and V. Yu. Timoshenko, Appl. Phys. Lett. **70**, 2705 (1997).
26. L. V. Belyakov, T. L. Makarova, V. I. Sakharov, *et al.*, Fiz. Tekh. Poluprovodn. **32**, 1122 (1998) [Semicond. **32**, 1003 (1998)].
27. M. Ben-Chorin, F. Moeller, and F. Koch, Phys. Rev. B: Condens. Matter **49**, 2981 (1994); L. Pavesi, M. Ceschini, G. Marioto, *et al.*, J. Appl. Phys. **75**, 1118 (1994).
28. N. Koshida and H. Koyama, Appl. Phys. Lett. **60**, 347 (1992).
29. L. Tsybeskov, S. P. Duttagupta, K. D. Hirschman, *et al.*, *Advanced Luminescent Materials*, Ed. by D. J. Lockwood, P. M. Fauchet, N. Koshida, and S. R. J. Brueck, **PV95–25** (Pennington, NJ, 1996), p. 34.
30. N. F. Mott and E. A. Davis, *Electronic Processes in Non-Crystalline Materials* (Clarendon, Oxford, 1971; Mir, Moscow, 1974).
31. L. T. Canham and A. Groszek, J. Appl. Phys. **72**, 1558 (1992).
32. D. N. Goryachev, O. M. Sreseli, and L. V. Belyakov, Pis'ma Zh. Tekh. Fiz. **23**, 59 (1997) [Techn. Phys. Lett. **23**, 35 (1997)].
33. O. M. Sreseli, G. Polisskiĭ, D. Kovalev, *et al.*, *Advances Luminescent Materials*, Ed. by D. J. Lockwood, P. M. Fauchet, N. Koshida, and S. R. J. Brueck, **PV95–25** (Pennington, NJ, 1996), p. 24.
34. S. R. Morrison, *The Chemical Physics of Surfaces* (Plenum, New York, 1977; Mir, Moscow,1980).
35. F. F. Volkenstein, *The Electronic Theory of Catalysis on Semiconductors* (Fizmatgiz, Moscow, 1959; Pergamon, New York, 1963).
36. T. van Buuren, T. Tiedje, J. R. Dahn, *et al.*, Appl. Phys. Lett. **63**, 2911 (1993).
37. F. Lohmann, Z. Naturforsch., A: Phys. Sci. **22**, 813 (1967).
38. O. M. Sreseli, V. Petrova-Koch, D. Kovalev, *et al.*, *The Physics of Semiconductors* (World Scientific, Canada, Vancouver, 1994), Vol. 2, p. 2117.
39. G. Polisskiĭ, O. M. Sreseli, A. V. Andrianov, *et al.*, Fiz. Tekh. Poluprovodn. (St. Petersburg) **31** (3), 112 (1997) [Semicond. **31**, 304 (1997)].
40. O. M. Sreseli, D. N. Goryachev, G. Polisskiĭ, *et al.*, *Pits and Pores: Formation, Properties, and Significance for Advanced Luminescent Materials*, Ed. by P. Schmucki, D. J. Lockwood, H. Isaace, *et al.*, **PV 97-7** (Pennington, NJ, USA, 1997), p. 104.
41. L. M. Peter and R. I. Wielgosz, Appl. Phys. Lett. **69**, 806 (1996).

Translated by T. Galkina

Semiconductors, Vol. 34, No. 2, 2000, pp. 228–232. Translated from Fizika i Tekhnika Poluprovodnikov, Vol. 34, No. 2, 2000, pp. 234–238.

PHYSICS OF SEMICONDUCTOR DEVICES

Quantum-Mechanical Features of the Field Effect in Heterotransistors with Modulation- and δ-Doped Regions

V. A. Gergel', V. G. Mokerov, and M. V. Timofeev

Institute of Radio Engineering and Electronics, Russian Academy of Sciences, ul. Mokhovaya 18, Moscow, 103907 Russia

Submitted June 25, 1999; accepted for publication July 13, 1999

Abstract—A closed theoretical model of the field effect in heterotransistor structures with modulation- and δ-doped regions is developed. In this model, the quantization of the energy spectrum of electrons in the channel and the Fermi-statistics-governed occupancy of the relevant energy subbands are consistently accounted for. An unconventional approximate method for summation of partial electron densities in lower spatial-quantization subbands is used to obtain the resultant dependences of the surface density of electrons on chemical potential and on the voltage applied to the transistor gate; these dependences hold in the entire range of possible concentrations of charge carriers in the channel, from low (subthreshold) to ultrahigh (ultraquantum) concentrations. *© 2000 MAIK "Nauka/Interperiodica".*

1. INTRODUCTION

The field effect (i.e., the concentration-related variation in electrical conductivity of the near-surface layer of semiconductor structure under the effect of control voltage applied to an external electrode) forms the basis for the functioning of any field-effect transistors (FETs); the latter include the state-of-the-art designs, such as the heterotransistors of the high-electron-mobility transistor (HEMT) type involving the modulation- and δ-doped semiconductors. The corresponding heterostructures are fabricated by molecular-beam epitaxy on the basis of III–V compounds with high mobility of charge carriers; these heterostructures include a comparatively thick (≈1 μm) layer made of narrow-gap undoped material and grown on a high-resistivity substrate; on this layer, a comparatively thin (20–40 nm) doped wide-gap semiconductor layer is grown; finally, the latter layer is coated with metal forming the Schottky barrier with the wide-gap semiconductor (Fig. 1) [1, 2]. In a number of modern device structures, an additional thin layer of semiconductor with a still narrower gap is introduced between the wide- and narrow-gap semiconductor layers (a pseudomorphous heterotransistor [3]). Basically, such a heterostructure could operate as a conventional MIS transistor [4], in which the wide-gap semiconductor layer would function as the gate oxide insulating the channel from the gate. However, as a result of an insufficiently high potential barrier at the heteroboundary, appreciable leakage currents occur between the gate and the channel of transistor for comparatively low voltages $V > V_C \approx 0.5$ V. This invalidates the concept of the field (high-resistance) control over the channel conductance and makes these structures inoperative. In order to shift the range of operating voltages to the region of acceptable values ($V < V_C$), the wide-gap semiconductor layer of heterotransistor structure is doped with donor impurity, either uniformly over the thickness [in this case, a modulation-doping FET (MODFET) is obtained], or by forming a doped monolayer within the thickness of the wide-gap semiconductor layer (a δ-doped FET). It is noteworthy that, for such heterotransistors with heavily doped wide-gap semiconductor layer, a closer analogue is a metal-Schottky FET (a MESFET), rather than the aforementioned insulated-gate transistor (MISFET).

Comparatively small thickness of functional layers and high electric fields, which are characteristic of the transistor structures under consideration, give grounds to expect that two essentially quantum-mechanical

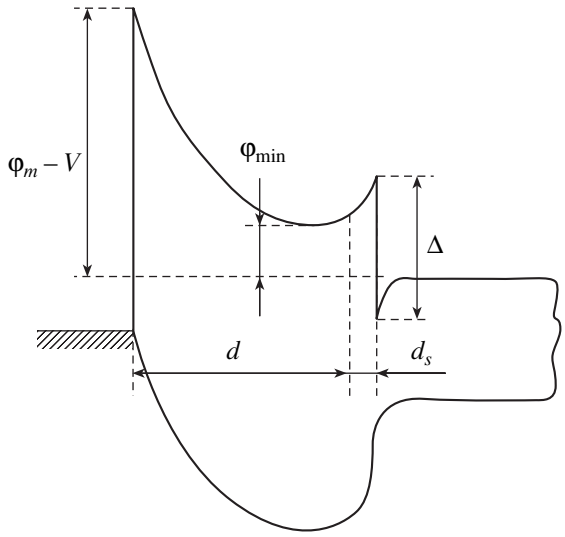

Fig. 1. Energy-band diagram of heterotransistor with modulation-doped semiconductor.

effects can manifest themselves in electrical characteristics of these structures: (i) discretization of electron energy spectrum in a strong electric field, which was repeatedly mentioned in the relevant publications [2, 5] and (ii) the Fermi-statistics-governed occupancy of corresponding two-dimensional energy subbands of spatial quantization. However, contrary to these expectations, the current–voltage characteristics of HEMTs do not demonstrate any significant quantum-mechanical features and are similar (both in shape and in the values of the corresponding transconductance) to the characteristics of conventional MESFETs. In this paper, we attempt to remove this apparent contradiction by devising a closed theoretical model of the field effect, i.e., the dependence of conductance (the concentration of free electrons) of the channel on the gate potential; this model consistently and, no less important, self-consistently, accounts for the aforementioned quantum-mechanical effects.

2. EFFECTIVE (SELF-CONSISTENT) DENSITY OF ELECTRON STATES IN THE HETEROTRANSISTOR CHANNEL

In order to write the correct expression for surface density of electrons in the heterotransistor channel, we should first of all take into account the splitting of the electron energy spectrum into a system of energy subbands of spatial quantization of lateral motion of electrons in an electric field that keeps the electrons of the narrow-gap semiconductor layer close to the heteroboundary; i.e., we have

$$\varepsilon_n(p) = E_C + \frac{p^2}{2m} + \varepsilon_n(E_{\text{ef}}). \qquad (1)$$

Here, p is the two-dimensional lateral momentum and $\varepsilon_n(E_{\text{ef}})$ is the energy of the sublevels of lateral motion. It should be specially emphasized that the latter energy is defined by the effective electric field

$$E_{\text{ef}} = \frac{1}{2}E_e + E_i,$$

where E_e is the component of the electric field at the heteroboundary and is induced by the surface electron charge itself, whereas the component E_i is induced by extraneous (with respect to electrons) impurity centers located in the thickness of the narrow-gap semiconductor layer and at its interface with semiinsulating substrate. Further consideration is appreciably simplified in view of the possibility of ignoring the external field E_i as compared to the electron-induced field E_e; i.e., we may assume that $E_i = 0$ because the impurity concentration in the narrow-gap semiconductor layer is low and the distance between the heteroboundary and the boundary of semiinsulating substrate is large. Therefore, in further consideration, we assume that the field at the heteroboundary is completely electronic (i.e., $E = E_e$). It is noteworthy that the physical significance of the introduced effective electric field consists in elimination of the so-called self-action of electrons that are kept close to the heteroboundary only by the field's component induced by the charges of donors in the wide-gap semiconductor layer, rather than by the intrinsic field. To put it differently, we should calculate the energies of spatial-quantization levels for an effective triangular potential well with the slope of $E/2$, as it is illustrated by the corresponding band diagram shown in Fig. 2.

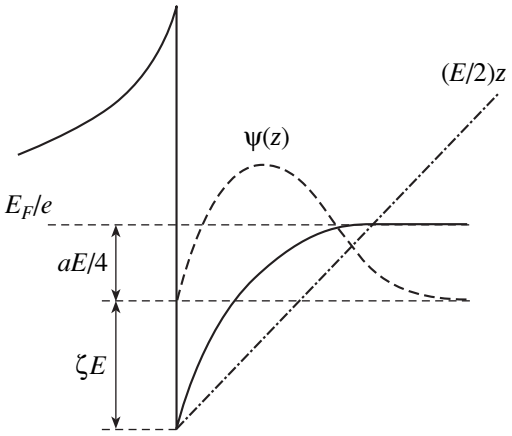

Fig. 2. Effective field and the features of zone bending in the vicinity of the heteroboundary.

We determine the spatial-quantization energy $\varepsilon_0(E_{\text{ef}})$ by using the estimate corresponding, according to the known uncertainty principle [6], to minimization of the characteristic energy $\hbar^2/2m\zeta^2 + eE\zeta$ over the characteristic extent ζ of the wave function; thus, we have

$$\varepsilon_0 = \frac{3}{4}\left(\frac{2\hbar^2}{meE}\right)^{1/3} eE \approx eE\left(\frac{\hbar^2}{meE}\right)^{1/3} \equiv eE\zeta, \qquad (2)$$

where the parameter $\zeta = (\hbar^2/meE)^{1/3} \approx 4$ nm is a slow varying function of the field. In order to simplify the subsequent calculations, we henceforth assume that a system of levels under consideration is equidistant; i.e.,

$$\varepsilon_n = n\varepsilon_0 \quad (n = 1, 2, \ldots).$$

It is worth noting that the use in certain publications of more precise (as it appears at first sight) definition of the spectra of $\varepsilon_n(E)$ on the basis of distribution of zeros of the Airy function is, in our opinion, equivalent to exceeding the actual accuracy, because this introduces further questions concerning the consideration of nonparabolicity of the conduction band of the narrow-gap material, the insufficient height of the left-hand energy barrier, the adequacy of boundary conditions for the wave function at the heteroboundary, and so on.

We now follow the known rules of quantum statistics to write the following expression for the surface density of electrons:

$$n_s = \frac{1}{\pi\hbar^2}\sum_{n=1}^{\infty}\int_0^{\infty} p\,dp \times\left[\exp\left(\frac{E_C - E_F + neE\zeta + p^2/2m}{T}\right)+1\right]^{-1}. \quad (3)$$

This expression can be integrated, which, after multiplication by $4\pi e/\varepsilon$, yields

$$E = \frac{4\pi e}{\varepsilon}n_s = 4\frac{T}{a}\sum_{n=1}^{\infty}\ln\left[\exp\left(\frac{E_F - E_C - neE\zeta}{T}\right)+1\right], \quad (4)$$

where the fundamental constants, the permittivity ε, and the effective mass m are nicely combined in the Bohr radius $a = \hbar^2\varepsilon/me^2$. It is clear that the self-consistency of the obtained expression relies on the fact that it accounts for an increase in separation of spatial-quantization levels with an increase in electric-field strength as the difference in the energies $E_F - E_C$ increases. This effect certainly decreases the rate of an increase in the field strength as the edge of the conduction band E_C approaches the Fermi level E_F.

We first consider the Boltzmann asymptotic approximation to expression (4) by expanding the logarithms appearing in (4) under the assumption that $E_C + \zeta eE - E_F > 2T$. In this case, we use the formula of geometric progression to easily perform the summation over the all levels of spatial quantization; thus, we arrive at

$$eE\left(e^{\frac{eE\zeta}{T}}-1\right) = \frac{4T}{a}\exp\left(\frac{E_F - E_C}{T}\right). \quad (5)$$

For small $eE \ll T/\zeta$, formula (5) can be transformed into the expression

$$eE = \frac{2T}{\sqrt{\zeta a}}\exp\left(\frac{E_F - E_C}{2T}\right), \quad (6)$$

which almost exactly coincides with the known quasi-classical formula obtained from the conventional Poisson equation with the Boltzmann asymptotic behavior of three-dimensional electron density [4]. This situation is not at all surprising because the condition $eE \ll T/\zeta$ corresponds to uniform occupancy of a comparatively large number of spatial-quantization sublevels, which renders the electron density three-dimensional and quasi-classical.

In the opposite limiting case of high fields (and high electron densities), occupation of the lowest ($n = 1$) level of spatial quantization becomes the most important according to formula (5); at the same time, the sum of the electron densities over the all remaining levels with higher energy becomes exponentially small as compared to the electron density at the lowest level. However, it is evident that, in the range of high fields, the assumption of the Boltzmann statistics governing the occupation of the first level, which we used in deriving (5), may become invalid. Therefore, in the range of high fields, it would be more correct to use the expression

$$(e^{eEa/4T}-1)e^{eE\zeta/T} = \exp\left(\frac{E_F - E_C}{T}\right), \quad (7)$$

which adequately accounts for both the Fermi-statistics-based occupancy and the field-induced shift of the first level of spatial quantization. Formula (7) follows from general relationship (4) if the contribution of higher states with $n \geq 2$ is ignored in (4). It is convenient to interpolate formulas (5) and (7); as a result, we obtain the unified expression

$$(e^{eEa/4T}-1)(e^{eE\zeta/T}-1) = \exp\left(\frac{E_F - E_C}{T}\right), \quad (8)$$

which is valid in the entire range of possible fields for any sign of the difference $E_F - E_C$. In the case of high fields, the asymptotic behavior of (8) is described by the following formula corresponding to the Fermi statistics:

$$eE = \frac{E_F - E_C}{\zeta + \frac{a}{4}}. \quad (9)$$

In the case of very low fields, formula (8) transforms into quasi-classical expression (6).

To within a numerical factor, the effective density of states is given by the derivative of the electric field with respect to the position of the Fermi level. Differentiating (8), we arrive at

$$\frac{\partial eE}{\partial E_F} = \left[\frac{a}{4}\left(1-e^{-eEa/4T}\right)^{-1} + \zeta\left(1-e^{-eE\zeta/T}\right)^{-1}\right]^{-1} = \begin{cases}\left(\frac{a}{4}+\zeta\right)^{-1}, & eE > \max\left\{\frac{4T}{a}, \frac{T}{\zeta}\right\},\\ \frac{eE}{2T}, & eE < \min\left\{\frac{4T}{a}, \frac{T}{\zeta}\right\},\end{cases} \quad (10)$$

As is known, an electric analogue to the density of states is the capacitance of the corresponding effective capacitor. Using this convenient analogy, we may state that the above relationship (10) corresponds to the series connection of capacitance of ideal two-dimensional Fermi gas $4/a$ to an effective capacitance of spa-

tial quantization ζ^{-1} that accounts for the field-induced shift of electron energy.

3. CALCULATION OF ELECTRON DENSITIES IN THE CHANNEL OF HETEROTRANSISTOR

Under the operating conditions of a correctly designed heterotransistor, the density of electrons in the subgate region of wide-gap semiconductor layer is negligibly small. Therefore, the distribution of potential in this region is defined by the Poisson equation involving only the charge of ionized impurities (the depleted-layer approximation). We consider a MODFET with the wide-gap semiconductor layer containing the charged donor centers with concentration N, which are distributed uniformly over the thickness of the layer except for a thin spacer with thickness d_s in the vicinity of heteroboundary (see Fig. 1) The corresponding solution for such a MODFET is given by[1]

$$\varphi(z) = \varphi_{\min} + \frac{eN}{2\varepsilon\varepsilon_0}(z - z_0)^2. \qquad (11)$$

The values of integration constants (the potential of energy minimum $\varphi_{\min}$ and its position z_0) appearing in (11) define the corresponding boundary conditions, one of which is equivalent to the Schottky condition at the boundary between the wide-gap semiconductor layer and metal and is written as $\varphi(0) = \varphi_m - V$, where V is the voltage applied to the gate and $\varphi_m = 1.5$ V is the contact potential difference; in the strict sense, the latter is equal to the difference between the electron affinity of wide-gap semiconductor and the work function of metal. It is noteworthy that the use of the Schottky boundary condition means, among other things, that the position of the Fermi level E_F is chosen as the potential origin, and the value of potential specifies the position of the conduction-band edge in the wide-gap semiconductor layer in reference to E_F. On simple transformations, the Schottky condition makes it possible to express the potential at the opposite boundary of the wide-gap semiconductor layer

$$\varphi|_{d+d_s} = \varphi_s = \varphi_m - V - \frac{eN_s}{2\varepsilon\varepsilon_0}d^2 + E(d + d_s) \qquad (12)$$

in terms of electric field at the same boundary $E = (eN/\varepsilon\varepsilon_0)(d - z_0)$. The same procedure for a heterotransistor with δ-doped semiconductor yields a similar expression; i.e., we have

$$\varphi_s = \varphi_m - V - \frac{eN_s}{\varepsilon\varepsilon_0}d + E(d + d_s), \qquad (12a)$$

where N_s is the surface density of charged donors in the monolayer.

[1] In this Section, we use the SI system of units with ε_0 being the permittivity of vacuum, as distinct from the formulas in Section 2 where the cgs system was used.

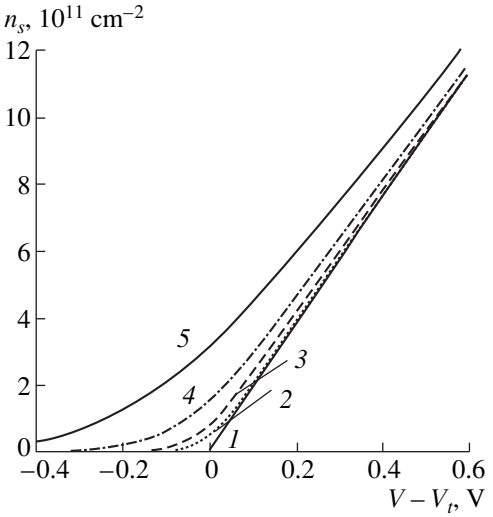

Fig. 3. Dependences of the near-surface electron density (n_s) on the control gate voltage V of the transistor at the temperatures T amounting to (*1*) 0, (*2*) 0.007, (*3*) 0.013, (*4*) 0.026, and (*5*) 0.052 eV.

On the other hand, according to the energy band diagram (Figs. 1, 2), the surface potential φ_s defines the difference between the Fermi level and the conduction-band edge of narrow-gap semiconductor as this difference appears in expression (8) for the field E and in expression (3) for the surface density n_s; thus, we have

$$E_F - E_C = \Delta E_C - e\varphi_s \equiv (\Delta - \varphi_s)e. \qquad (13)$$

On substituting (13) into formula (8), the latter becomes equivalent to the second boundary condition for the Poisson equation in wide-gap semiconductor layer and makes it possible to obtain the sought-for nonlinear relationship defining the dependence of the transverse field E (i.e., the surface density of electrons) on the control voltage at the transistor gate $V - V_t$ as

$$E(d + d_s) + \frac{T}{e}\ln[(e^{eEa/4T} - 1)(e^{eE\zeta/T} - 1)] = V - V_t, \qquad (14)$$

where $V_t = \varphi_m - \Delta - (eN/2\varepsilon\varepsilon_0)d^2$ is the corresponding threshold voltage. Plots of dependences (14) calculated for several typical temperatures T = 0.007, 0.013, 0.026, and 0.052 eV are shown in Fig. 3; electron density in the channel clearly features the threshold behavior that is characteristic of FETs. The asymptotic behavior that corresponds to the Fermi statistics in (14) for $T = 0$ and is described by

$$E = (V - V_t)\left(d + d_s + \frac{a}{4} + \zeta\right)^{-1} \equiv \frac{e}{\varepsilon\varepsilon_0}n_s \qquad (15)$$

is also illustrated in Fig. 3. Formula (15) rather adequately describes the on portion of the characteristic at

almost any of the temperatures indicated. The following typical values of the parameters were used in calculating the dependences shown in Fig. 3: $d = 30$ nm, $a = 10$ nm, and $d_s = \zeta = 3$ nm. Approximate formula (15) clearly demonstrates the way in which the purely electrical capacitance of the wide-gap semiconductor layer $\sim(d + d_s)^{-1}$ is connected in series to the effective quantum-mechanical capacitance $\sim(a/4 + \zeta)^{-1}$ and thus suppresses the influence of quantum-mechanical effects on the resultant surface density of charge carriers in the channel.

4. CONCLUSION

It should be mentioned in conclusion that the simple relationship (15) derived for the electron charge in the channel under the assumption of constant mobility could be used to obtain the conventional expression for the current–voltage (drain–source) characteristic of a transistor with quadratic dependence of saturation current on the gate voltage. However, even preliminary estimates show that, for the devices with submicrometer length of the gate, the assumption about the constant mobility is completely inadequate because the drift electric field in the transistor channel in such transistors heats electrons to the temperatures of several hundred degrees, in which case the effect of a decrease in mobility becomes determining. Such a study of the heat-up of charge carriers in the channel of submicrometer heterotransistor and quasi-hydrodynamic model of calculating the corresponding current–voltage characteristics will be reported in the paper to follow.

REFERENCES

1. A. A. Kal'fa and A. S. Tager, in *Multilayer Semiconductor Structures and Superlattices* [in Russian] (Gor'kiĭ, 1985), p. 104.
2. M. S. Shur, *GaAs Devices and Circuits* (Plenum, New York, 1987; Mir, Moscow, 1991).
3. V. G. Mokerov, D. V. Amelin, A. V. Hook, V. E. Kaminsky, Yu. V. Fedorov, and A. S. Shubin, in *Compound Semiconductors* (Inst. Phys. Conf. Ser., Philadelphia, 1996).
4. S. M. Sze, *Physics of Semiconductor Devices* (Wiley, New York, 1981; Mir, Moscow, 1984).
5. T. Ando, A. B. Fowler, and F. Stern, Rev. Mod. Phys. **54**, 437 (1982) [Mir, Moscow (1985)].
6. L. D. Landau and E. M. Lifshits, *Quantum Mechanics* [in Russian] (Fizmatgiz, Moscow, 1963).

Translated by A. Spitsyn

Semiconductors, Vol. 34, No. 2, 2000, pp. 233–236. Translated from Fizika i Tekhnika Poluprovodnikov, Vol. 34, No. 2, 2000, pp. 239–242.

PHYSICS OF SEMICONDUCTOR DEVICES

Ultraquasi-Hydrodynamic Electron Transport in Submicrometer Field Effect MIS Transistors and Heterotransistors

V. A. Gergel', V. G. Mokerov, M. V. Timofeev, and Yu. V. Fedorov

Institute of Radio Engineering and Electronics, Russian Academy of Sciences, Mokhovaya ul. 18, Moscow, 103907 Russia

Submitted June 25, 1999; accepted for publication July 13, 1999

Abstract—It is shown that electrons in the channel of submicrometer field effect transistors have no time to be heated to quasi-steady-state temperatures corresponding to a balance between the Joule heating and thermal relaxation. This "underheating" contributes to an increase in the effective mobility of charge carriers as compared to the value of $\mu(E)$ corresponding to the drift–diffusion approximation. Using a reduction of the thermal-balance equation by eliminating the relaxation-related term, a simple analytical expression is obtained for current–voltage characteristics. In particular, the saturation current in the developed ultraquasi-hydrodynamic model is found to be proportional to $(V_G - V_t)^{3/2}$. The results of measurements of characteristics of the test GaAlAs/InGaAs/GaAs P-HEMTs with the channel length of about 0.3 μm are reported; these results verify the adequacy of the developed model, the accuracy of which can only increase with a further decrease in the channel length. © *2000 MAIK "Nauka/Interperiodica"*.

In spite of the practical importance of calculation and analysis of current–voltage (*I–V*) characteristics and profound scientific interest in electrical conduction in quasi-two-dimensional systems, the issue concerning the specific features of electron transport in submicrometer field-effect transistors (FETs) still remains open. The authors of the numerous relevant publications agree only on the fact that the conventional drift–diffusion model is inadequate in the case of submicrometer lengths of the channels. In some of the publications, a model of the so-called ballistic transport is used [1, 2] as an alternative approach, in which case it is assumed that electrons travel through the submicrometer channel without any collisions at all. The so-called hydrodynamic approach [3, 4] is also hardly justified; here, the expression for the current is obtained directly from the Boltzmann equation with the use of a shifted velocity (momentum) distribution function for charge carriers. We believe that the only correct approach to the description of electron transport in FETs with submicrometer channel consists in the use of a quasi-hydrodynamic (or temperature-related) model, in which it is assumed, as is known, that it is possible to partition the distribution function into a large symmetric component and a small directional component.

In fact, the entire body of experimental data available now indicate that, even in ultrasubmicrometer (~0.1 μm) transistors, the transport velocity of electrons does not exceed about 10^7 cm/s. Elementary estimations show that these velocities are much lower than both the directional velocity acquired by electron in ballistic transit over the potential difference amounting even to several tenths of a volt (this discredits the applicability of the ballistic-transistor model) and the values of the thermal or the Fermi velocities of electrons in the channel. Naturally, the latter consideration discredits the applicability of hydrodynamic model of electron transport and, at the same time, justifies the use of a quasi-hydrodynamic (thermal) model in the situations under study.

Without dwelling in detail on the known special features of conventional procedures for partitioning the Boltzmann equation into the equations for symmetric and asymmetric components of the distribution function, we formulate here only the main, basic assumptions of the quasi-hydrodynamic model. First, the kinetic energy of chaotic motion of electrons $W = \frac{3}{2}T$ (T is the effective electron temperature) is much higher than the energy of directional motion $mv^2/2$. Second, the flux densities of particles and energy that are proportional to the corresponding gradients are expressed in terms of the temperature-dependent mobility $\mu(T)$. Third, the dependence of effective mobility on thermal energy (temperature) is the major factor relating the continuity equations for the fluxes of particles and thermal energy.

If, for the sake of simplicity, we restrict ourselves to the drift component of electron flux j alone, the input equations in quasi-hydrodynamic model of electron transport in the channel should be written as

$$j = n\mu(T)\frac{d\varphi}{dx} = \text{const}, \quad (1)$$

1063-7826/00/3402-0233$20.00

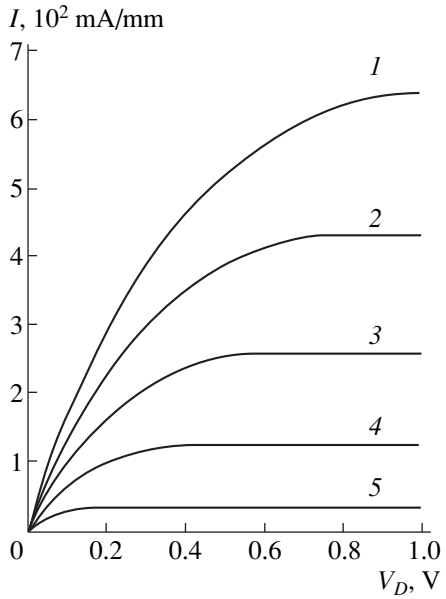

Fig. 1. A series of submicrometer-transistor current–voltage characteristics calculated with formula (7) for $V = V_G - V_t =$ (*1*) 1, (*2*) 0.8, (*3*) 0.6, (*4*) 0.4, and (*5*) 0.2 V.

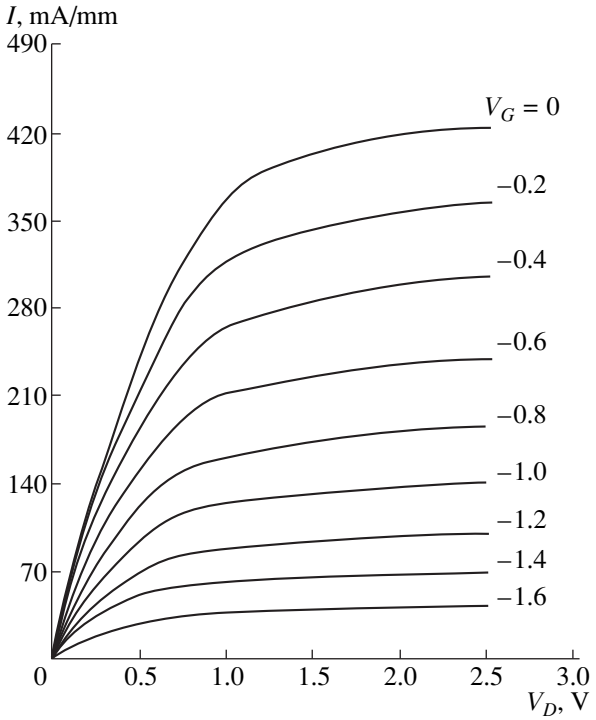

Fig. 2. Experimental current–voltage characteristics of a GaAlAs/InGaAs/GaAs P-HEMT (L = 0.3 μm) for the indicated values of the gate voltage V_G.

$$-\frac{5}{2}j\frac{dT}{dx} + j\frac{ed\varphi}{dx} = n\frac{T - T_0}{\tau}, \qquad (2)$$

where n and μ are the concentration and mobility of electrons in the channel, $\varphi(x)$ is the potential in the transistor channel, and τ is the relaxation time for the momentum of electrons. The second equation is referred to as the thermal balance equation. The first term in (2) represents the divergence of convective heat flux, the second term corresponds to the Joule heating, and the third term accounts for the transfer of thermal electron energy to the phonon subsystem whose temperature is regarded as corresponding to the equilibrium state.

Qualitative analysis of the first-order equation (2) reveals the basic features of the electron-temperature distribution over the length of the transistor channel. In the immediate vicinity of the source injecting the electrons into the channel with equilibrium temperature of $T = T_0$, an intermediate region with characteristic extent of $l_T = \mu E\tau = 0.1 - 1.0$ μm (E is the electric field) is bound to be found; in this region, the electron temperature increases steadily from T_0 to the quasi-steady-state value

$$T = T_0 + e\mu(T)\tau(T)E^2, \qquad (3)$$

corresponding to the local balance between the Joule heating and the energy transferred to the constant-temperature crystal lattice. The region with quasi-steady-state temperature (3) occupies the remaining part of the channel as far as the boundary with the drain. In this part of the channel, the thermal flux remains virtually unchanged, and its divergence [the first term in (2)] is negligibly small as compared to the Joule heating and thermal relaxation. It is the reduction of equation (2) to algebraic equation (3) that constitutes, as is known [5, 6], the essence of the so-called drift–diffusion approximation; the latter is correct only for transistors with sufficiently long channels, in which case the extent of the region of quasi-steady-state heating is dominant.

It is noteworthy that, by now, inadequacy of the drift–diffusion model for description of device structures with submicrometer channels has been quite clearly recognized by the experts in the field. However, a full-scale consideration of nonlocality of electron heating [equation (2) with divergent term] appreciably increases mathematical difficulties in calculating the *I–V* characteristics of short-channel transistor; the results of numerical methods that become necessary are structurally specific and are difficult to interpret physically and to generalize. We may state that cumbersome numerical results obtained in the context of nonreduced quasi-hydrodynamics do not form the basis for a submicrometer-transistor model suitable for subsequent use in circuit design.

The main idea of this work consists in the development of the transistor model based on "ultrashort-channel" reduction of equation (2). Namely, we will disregard the term corresponding to thermal relaxation (transfer of heat to the lattice) in this equation. This reduction of equation (2) is the reason why we used the term "ultra" in the title of this paper. In this case, we

immediately obtain the following elementary expression for electron temperature in the channel:

$$T = T_0 + \frac{2}{5}e\varphi(x). \quad (4)$$

Here, $\varphi(x)$ is the local potential in the transistor channel. This potential vanishes at the boundary between the channel and the source. At the opposite channel boundary with the drain (for $x = L$), $\varphi L = \min\{V, V_D\}$, where $V \equiv V_G - V_t$ is the excess of the gate voltage over the threshold and V_D is the drain voltage. Physical significance of approximation (4) consists in the fact that, if thermal relaxation is ignored, the flux of thermal energy of electrons accumulates the total electrostatic energy acquired by electrons traveling along the channel. Transfer of this energy to the lattice occurs in the drain region of the transistor.

We regard the scattering by longitudinal acoustic phonons [6] as the dominant scattering mechanism defining the temperature dependence of mobility; as a result, we have

$$\mu(T) = \mu(T_0)\left(\frac{T_C + T_0}{T_C + T}\right)^{1/2}, \quad (5)$$

where T_0 is the equilibrium temperature; the characteristic quantity $T_C \approx T_0$ was introduced into (5) in order to approximately account for alternative mechanisms of scattering (for example, by charged impurities) that are important at low temperatures.

We are now all set for direct calculation of the I–V characteristic; to this end, we substitute (4), (5), and $en = C(V - \varphi)$, where C is specific capacitance of the transistor gate, into formula (1). As a result, the current density can be expressed as

$$I = \frac{C\mu}{L}\int_0^{V_D} d\varphi\left(\frac{V + \varphi_0}{\sqrt{\varphi_0 + \varphi}} - \sqrt{\varphi_0 + \varphi}\right), \quad (6)$$

where we introduced the notation $\frac{5}{2}(T_C + T_0) = e\varphi_0$. On performing an elementary integration, we finally arrive at

$$I = \frac{C\mu}{L}2\sqrt{\varphi_0}\left[\left(V + \frac{2}{3}\varphi_0\right)\left(\sqrt{V_D + \varphi_0} - \sqrt{\varphi_0}\right) - \frac{V_D}{3}\sqrt{V_D + \varphi_0}\right]. \quad (7)$$

For small $V_D < \varphi_0$, expression (7) is transformed (as would be expected) into

$$I = \frac{C\mu}{L}VV_D.$$

In the case under consideration, the problem of the channel cutoff and, correspondingly, the saturation mode of the transistor is solved exactly as it is done in the known classical model. In connection with this, we remind the reader that the drain junction cannot electroneutrally transfer the potential larger than V to the channel because otherwise the near-drain region of the channel becomes completely depleted. Consequently, the validity of (7) is limited by the condition $V_D < V$, and, for higher drain voltages $V_D > V$, the transistor current may be treated as constant defined by the same formula (7) for $V_D = V$. Such a replacement yields a formula for the transistor saturation current and for its dependence on the gate voltage. The plots of the $I(V)$ dependences described by formula (7) and calculated for $\mu = 1500$ cm^2(V s), $C = \varepsilon\varepsilon_0/d = 3.8 \times 10^{-7}$ F/cm^2, and $\varphi_0 = 0.1$ V are shown in Fig. 1.

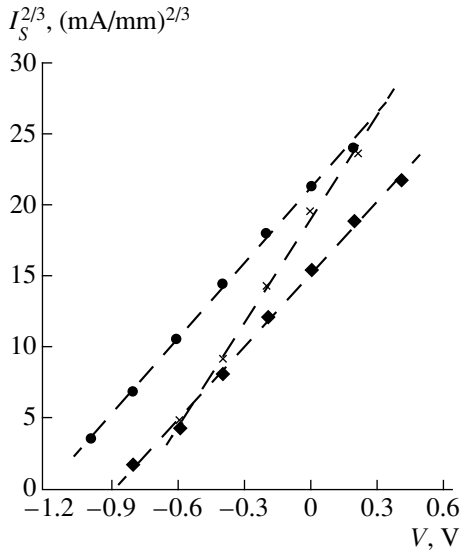

Fig. 3. Saturation current as a function of the control gate voltage for a number of test P-HEMTs.

For not-too-low voltages $V > \varphi_0 \approx 0.1$ V, the voltage dependence of saturation current is described by the following fairly compact approximate expression:

$$I_S \approx \frac{C\mu}{2L}V^{3/2}\sqrt{7\varphi_0}. \quad (8)$$

This current is evidently smaller than the saturation current $I_S \approx C\mu V^2/2L$ in the classical model where the heating and the corresponding decrease in mobility are not accounted for. On the other hand, the current given by (8) is larger than the saturation current $I_S \approx CVv_S$, where v_S is the saturation velocity, in the model with local heating (i.e., when the field dependence of mobility is taken into account).

Physical significance of the developed ultraquasi-hydrodynamic model can be formulated in the following way: electric fields V_D/L in the channel of a submicrometer transistor are so high that the potential difference V_D is inadequate to heat the electrons to the temperatures corresponding to the quasi-steady-state

conditions; i.e., $V_D < \mu\tau V_D^2/L^2$. It is this "underheating" that brings about an increased velocity of electron flux in the submicrometer channel $v = \mu\sqrt{7\varphi_0 V}/L > v_S$. We note in conclusion that the model suggested does not have a lower bound on the channel length; i.e., the shorter the channel, the more adequate the results yielded by formulas (7) and (8).

In order to perform a comparison with experimental data and to verify the suggested model of "ultraquasi-hydrodynamic" electron drift, we used the results of measurements of electrical characteristics of short-channel GaAlAs/InGaAs/GaAs P-HEMTs. The family of corresponding curves is shown in Fig. 2.

The dependences of saturation current on gate voltage shown in Fig. 3 for several transistors with differing parameters lend even more support to the adequacy of the model developed here; as expected, an $I_S^{2/3}$–V plot yields straight lines.

REFERENCES

1. V. A. Fedirko, Élektron. Tekh., Ser. 3: Mikroélektronika, No. 3, 23 (1984).
2. V. I. Ryzhiĭ, N. A. Bannov, and V. A. Fedirko, Fiz. Tekh. Poluprovodn. (Leningrad) **18** (5), 769 (1984) [Sov. Phys. Semicond. **18**, 481 (1984)].
3. I. C. Kizilyalli, K. Hess, J. L. Larson, *et al.*, IEEE Trans. Electron Devices **33** (10), 1427 (1986).
4. V. É. Kaminskiĭ, Mikroélektronika **17** (5), 421 (1988).
5. K. Lee, M. S. Shur, T. J. Drummond, *et al.*, IEEE Trans. Electron Devices **31** (1), 29 (1984).
6. A. A. Kal'fa, Élektron. Tekh., Ser. 1, No. 1, 383 (1985).

Translated by A. Spitsyn

Semiconductors, Vol. 34, No. 2, 2000, pp. 237–242. Translated from Fizika i Tekhnika Poluprovodnikov, Vol. 34, No. 2, 2000, pp. 243–248.

PHYSICS OF SEMICONDUCTOR DEVICES

Single-Mode InAsSb/InAsSbP Laser ($\lambda \approx 3.2$ μm) Tunable over 100 Å

A. P. Danilova*, A. N. Imenkov*, N. M. Kolchanova*, S. Civis, V. V. Sherstnev*, and Yu. P. Yakovlev***

** Ioffe Physicotechnical Institute, Russian Academy of Sciences, St. Petersburg, 194021 Russia;*

e-mail: yak@iropt.ioffe.rssi.ru

*** Heyrovsky Institute of Physical Chemistry, Czech Academy of Sciences, 18223 Prague 8, Czech Republic*

Submitted July 14, 1999; accepted for publication July 15, 1999

Abstract—A report is presented on the development of a single-mode laser based on the InAsSb/InAsSbP double heterostructure and operating at wavelengths of 3.2–3.3 μm in a temperature range of 12–90 K. The single-mode regime is assumed to be realized due to a smooth optical waveguide formed across the laser cavity in which the radiation flux oscillates and maintains its oscillations and intensity. An analysis is made of the effect of the current-induced shifts of the lasing frequency and the peak of the gain spectrum on the probability of single-mode lasing. Experiments were made on the scanning of OCS, NH_3, CH_3Cl, and H_2O gas media with radiation of the given laser in the frequency range with a record width of 10 cm^{-1} (104 Å). © *2000 MAIK "Nauka/Interperiodica".*

INTRODUCTION

Recently, tunable lasers on the basis of InAsSb/InAsSbP heterostructures, with frequency controlled over a wide range (~5 cm^{-1}) by injection current, have been developed [1–5]. Their design is based on the concepts of a controllable distribution of injection density across the cavity and of a decrease in the spread of nonequilibrium charge carriers. A decrease in laser radiation intensity and an increase in injection density towards the cavity edges create conditions for an increase in the charge carrier concentration in this direction and the formation of a smooth optical waveguide across the cavity. The radiation flux may vary across a cavity and provide lasing on a single axial spatial mode. As a result, only those spectral modes that correspond to the single spatial mode are excited. The optical gain at the cavity edges is higher than the gain at its center. In this case, the averaged gain spectrum becomes wider with increasing current, and its peak shifts to the short-wavelength region, which favors single-mode lasing. One can increase the probability of single-mode lasing by forming the conditions under which the current-induced shift of the gain peak is the same as the mode shift. To decrease the probability of lasing on subsidiary modes, it is desirable to lower the energy "burning out" of the charge carrier.

Our aim was to construct and study a single-mode laser based on the InAsSb/InAsSbP double heterostructure, with a wide range of laser frequency tuning, and to scan different gas media with the aid of its emission.

LASER DIODES

The InAsSb/InAsSbP double heterostructure was grown by liquid-phase epitaxy on a *p*-InAs (100) substrate with a hole concentration of $(6–8) \times 10^{18}$ cm^{-3} by the technology developed in [5, 6].

The charge carrier concentrations in the substrate and layers and the geometrical parameters of the structure were chosen in such a way to provide an increased injection density at the strip edges in comparison to the center and a low differential resistance at the boundary of the confining layers and the active region.

The narrow-band InAsSb active layer ~1 μm thick with a band gap of 0.39 eV at 77 K formed heterojunctions of type 1; the InAsSbP confining layers ~2 μm thick with a band gap of 0.59 eV at 77 K were adjacent to it. The structure was coated on the outside with the contact *n*-InAs layer, which was heavily doped with Sn up to an electron concentration of ~10^{19} cm^{-3}. The active region was undoped and had an electron concentration of ~4×10^{16} cm^{-3}. The confining layer adjacent to the substrate was doped with Zn up to a hole concentration of ~10^{18} cm^{-3}. The other confining layer was doped with Sn up to an electron concentration of ~6×10^{18} cm^{-3}. Upon the epitaxial growth of layers, the substrate was ground down to a thickness of 100 μm. By using the photolithographic technique, chips with a step of 500 μm and a mesa stripe 16 μm wide were fabricated. The cavities were produced by cleavage and

1063-7826/00/3402-0237$20.00

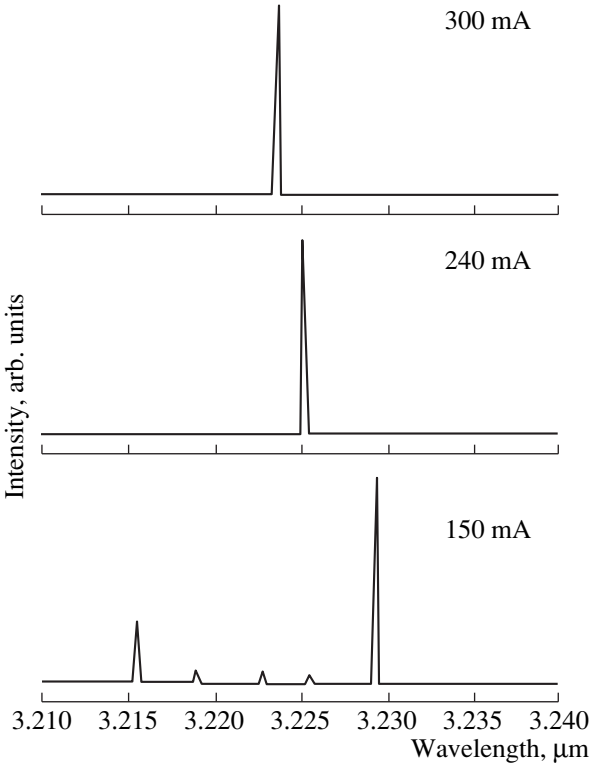

Fig. 1. Emission spectra of the V12191-3 laser for different currents at a temperature of 77 K.

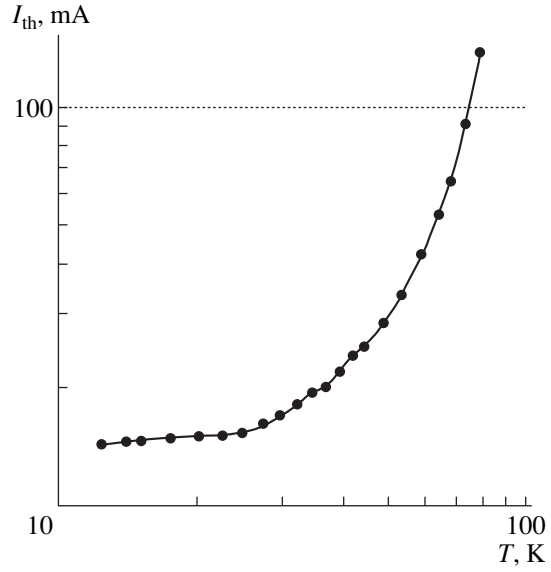

Fig. 2. Temperature dependence of the threshold current of the V12191-3 laser.

were 375 μm long. The chips, with their substrate facing downward, were mounted on a special copper heat sink [7], which made it possible to place a laser in a thermostat with a closed helium cycle.

EXPERIMENTAL

The emission spectra of a laser placed in a pumped-off nitrogen thermostat and pumped with rectangular current pulses 14 μs long with a duty factor of 2 were studied at a temperature of 77 K. The laser spectrometry of gas media was carried out on a spectrometer containing an L5731 Laser Photonics thermostat in which a laser was placed, a power supply, a 5820 Laser Photonics temperature controller, a monochromator, and an InSb photodiode cooled with liquid nitrogen. The signal proportional to the intensity of the laser radiation transmitted through a gas medium was observed on an oscilloscope screen. The laser was excited by current pulses with a repetition frequency of 1 kHz. The second derivative of the signal with respect to current, which was continuously varied, was recorded with the aid of a computer and an SP530 lock-in amplifier. In this case, the injection current was continuously increased in a prescribed range for ~30 s. The current was modulated by 1–5% at a frequency of ~1 kHz. The objects chosen for the study by laser spectroscopy were gases, namely carbon oxysulfide (OCS), ammonium (NH_3), methyl chloride (CH_3Cl), and water vapors. The OCS and CH_3Cl gases were enclosed in cells 21 cm long at a pressure of 2 torr; NH_3 was enclosed in a cell 40 cm long at a pressure of 3 torr; and the H_2O vapors were at the atmospheric pressure, with absorption length equal to 200 cm.

EXPERIMENTAL RESULTS

At only the lasing threshold, we observed in the laser emission spectrum two strong modes, which were separated by four intermode intervals, and a number of weak modes (Fig. 1). For the injection current exceeding the threshold value by 10%, only one long-wavelength mode remained in the spectrum. The radiation wavelength decreased from 3.229 to 3.223 μm with current increasing from 150 to 300 mA at 77 K. The wavelength change exceeded the intermode interval by a factor of about 2.

The threshold current I_{th} decreased from 138 to 14 mA with decreasing temperature T from 80 to 12 K (Fig. 2). In this case, the characteristic temperature T_0 continuously increased from 33 to 380 K. Our tests showed that the laser could be used to scan the gas media in the entire range of operating temperatures mentioned above. The widest range of the spectroscopy of gas media, from 3091.6 to 3101.6 cm^{-1} (10 cm^{-1}, 104 Å), was obtained at the laser temperature T = 62 K.

Because of an abundance of absorption lines in this range, it was divided into 5–6 regions, and we carried out scanning in each of them. The first region is presented in Fig. 3. The greatest number of characteristic absorption lines [8, 9] is given by the OCS gas (Fig, 3). Moreover, a large number of known absorption lines is

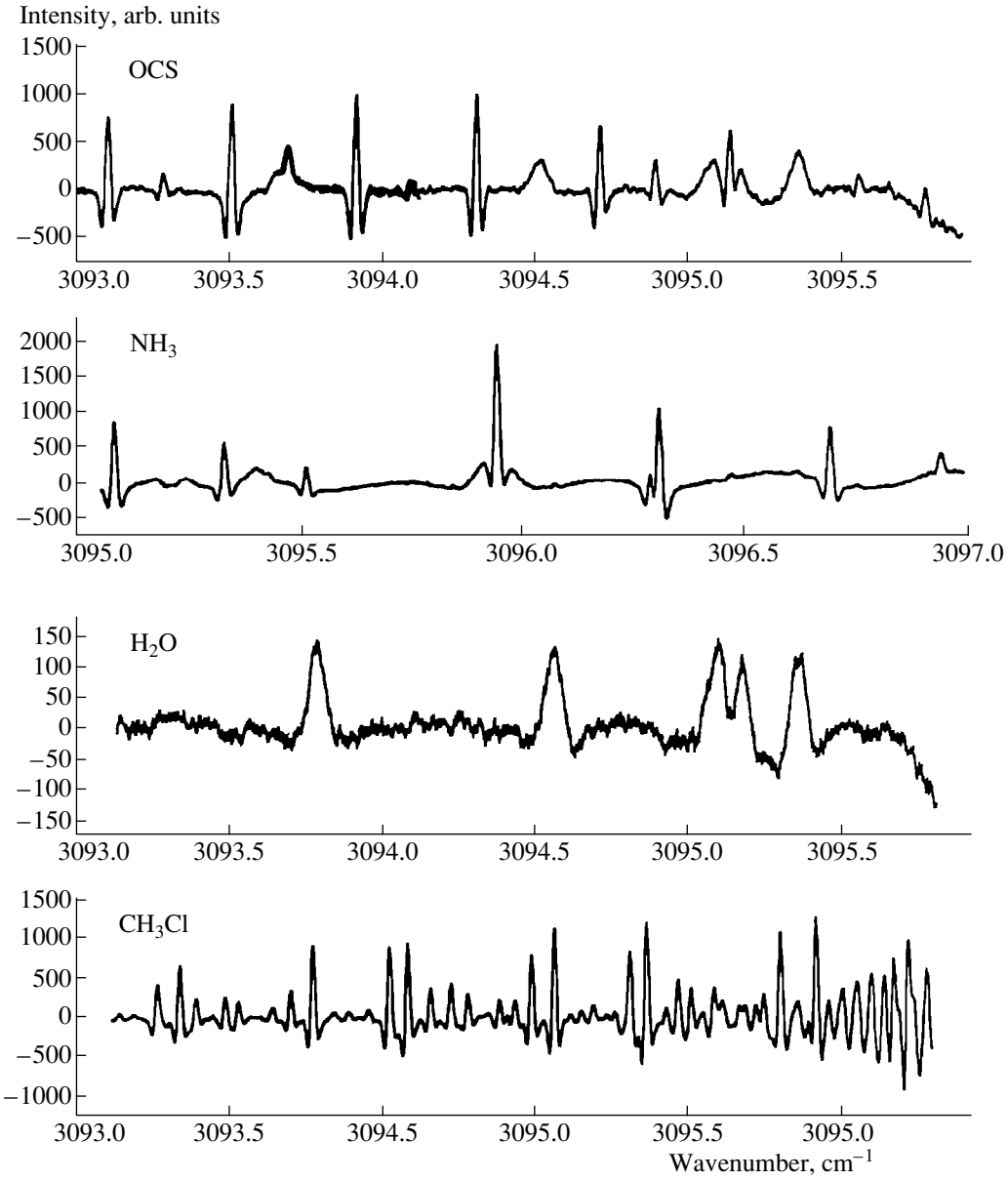

Fig. 3. Transmission spectra measured for OCS, NH_3, H_2O, and CH_3Cl gases by scanning with a laser beam.

produced by NH_3 [9] (Fig. 3). The spectrum of H_2O vapor contains wide lines known in the literature [10] (Fig. 3). In this figure, the lines with frequencies of 3093.690 and 3094.548 cm^{-1} represent characteristic lines of the water vapors, and the lines with frequencies near 3095 cm^{-1} were not identified. CH_3Cl produced the largest number of interesting lines (Fig. 3). In the figure, one can see six doublets, a triplet, and characteristic corrugations. Unfortunately, CH_3Cl is poorly studied in this spectral region. By using the lines identified for OCS, NH_3, and H_2O, we obtained coinciding dependences of the lasing frequency on the current at a temperature of 62 K. Figure 4 presents the dependence of the lasing frequency on the current. It was obtained with the aid of strong absorption lines of carbon oxysulfide.

The gas media can be scanned with the aid of a laser operating in a temperature range of 12–90 K. At the edges of this interval, the tuning range is narrower than the widest one by a factor of about two.

DISCUSSION OF THE EXPERIMENTAL RESULTS

A continuous decrease in the threshold current (Fig. 3) observed with decreasing temperature down to

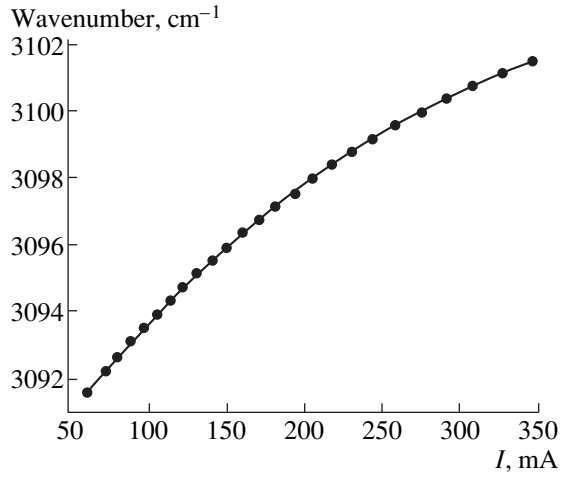

Fig. 4. Dependence of the lasing frequency of the V12191-3 laser on the current at a temperature of 62 K.

the lowest values (12 K) gives evidence of a rather high doping level for the confining layers and the absence of carrier freeze-out and creates the possibility of using the laser in a wide temperature range for scanning the gas media.

The temperature dependence of the threshold current cannot be described in the entire temperature range by a single law. In the range from 35 to 65 K, we have $I_{th} \sim T^{3/2}$, which corresponds to the case where the radiative recombination is the dominant recombination mechanism and the active region is undoped [11]. An increase in the slope of the dependence $I_{th} = f(T)$ for $T >$ 65 K is due to a substantial contribution by Auger recombination [11]. The weakening of the dependence $I_{th} = f(T)$ for temperatures below 35 K may be caused by the fact that the concentration of nonequilibrium charge carriers becomes lower than the concentration of equilibrium electrons.

The presence of several modes in the emission spectrum for a large excess over the threshold provides evidence for the conventional performance of the laser under these conditions. However, the change of the laser to the single-mode regime for currents exceeding the threshold value by more than 10% and up to 200–300% suggests that the conditions required to separate out a single mode and maintain it, which were mentioned in the introduction, are fulfilled in the laser. The transverse spatial modes and the frequency modes corresponding to them are suppressed in the smooth waveguide formed due to an increase of injection density across the cavity from the center to its edges, a low radiation intensity at the edges, and an insignificant spread of charge carriers over the width of the active region. The simplified solution [4] yields a single value of the radiation propagation constant (speed of light in a crystal), which increases with increasing current. In the process of spatial oscillations, the light flux passes from one edge to the other through the central region with a decreased gain and changes the gain spectrum, which maintains the oscillations formed in the system; i.e., the oscillations of the radiation flux are self-sustained. In this way, conditions for single-mode lasing in a wide range of currents are fulfilled. Determining the domain of existence of these conditions may be the object of further studies.

The basic condition of single-mode lasing is that the shift of the spectral position of modes caused by changes of current is equal to the shift of the gain spectrum. Let us compare the mode shift and the shift of the peak of the gain spectrum on changing the concentration of nonequilibrium charge carriers N. The energy of photons in the lasing mode $h\nu_L$ changes with the concentration of nonequilibrium charge carriers largely because of a change of refractive index n:

$$\frac{dh\nu_L}{dN} = -\frac{E_g}{n}\frac{dn}{dN}, \qquad (1)$$

where E_g is the band gap in the active region.

Let us write the gain spectrum in the simplified form

$$g \simeq \alpha\left[1 - \exp\left(\frac{E}{kT} - \frac{F}{kT}\right)\right]\left[2 + \exp\frac{F_i}{kT}\right]^{-1}, \qquad (2)$$

where α is the interband absorption coefficient for the active region, $h\nu$ is the photon energy, $E = h\nu - E_g$, $F = eV - E_g$, eV is the difference of quasi-Fermi level energies for electrons and holes, F_i is the depth of the quasi-Fermi level in the conduction band at the threshold of inversion, k is Boltzmann constant, and T is the absolute temperature.

Let us assume that the interband absorption coefficient α has the form typical of direct-gap semiconductors

$$\alpha = A\sqrt{T}\sqrt{\frac{E}{kT}}, \qquad (3)$$

where A is the coefficient whose value for III–V semiconductors is about 200 cm^{-1} K$^{-1/2}$.

According to (2) and (3), the gain peaks at $E = F/3$ in the case of low radiation losses for $F \le kT$. Because of this, the photon energy at the gain spectral peak is given by

$$h\nu_m \simeq E_g + F/3. \qquad (4)$$

According to (4), the photon energy at the peak of the gain spectrum changes when the position of quasi-Fermi levels and the band gap change.

Taking into account the strong degeneracy of electrons and the fact that holes are nondegenerate, we obtain

$$\frac{dF}{dN} = \frac{2}{3}\frac{F_{\text{th}}}{N_{\text{th}}} + \frac{kT}{N_{\text{th}}}, \quad (5)$$

where F_{th} and N_{th} are the depth of the quasi-Fermi level in the conduction band and the electron concentration at the lasing threshold, respectively.

The band-gap narrowing under the conditions of injection is related to the concentration of nonequilibrium charge carriers by the formula $\Delta F_g \sim N^{1/6}$. Thus, we obtain

$$\frac{dE_g}{dN} = \frac{1}{6}\frac{\Delta E_g}{N_{\text{th}}}. \quad (6)$$

From (4)–(6) it follows that

$$\frac{dh\nu_m}{dN} = \frac{1}{N_{\text{th}}}\left(\frac{2}{9}F_{\text{th}} + \frac{1}{9}kT + \frac{1}{6}\Delta E_g\right). \quad (7)$$

In the temperature range under study, the band-gap narrowing ΔE_g exceeded in magnitude the free-exciton binding energy and was calculated by the formula

$$\Delta E_g = -\frac{\pi^{11/6}3^{1/6}e^3 m_n^{1/2} N^{1/6}}{12n^{3/4}\hbar}, \quad (8)$$

where m_n and e are the effective mass of an electron and its charge.

According to (7), the sign and magnitude of $dh\nu_m/dN$ are determined by the relation between F_{th} and ΔE_g (T = const), with $\Delta E_g < 0$. In the semiconductor studied by us, $|F_{\text{th}}| > |\Delta E_g|$ because the effective electron mass is small in comparison to the effective hole mass, and, therefore, $dh\nu_m/dN > 0$. In a mechanically stressed active region, one may obtain the opposite sign as well. Because of this, it is possible to control the magnitude and sign of $dh\nu_m/dN$ by producing internal mechanical stresses. In the unstressed laser structures under study, $|\Delta E_g| < F_{\text{th}}$, $\Delta E_g < 0$, and $dn/dN < 0$. The derivatives $dh\nu_m/dN$ and $dh\nu_L/dN$ have opposite signs.

Our estimates show that the ratio $dh\nu_m/dh\nu_L$ changes from 1 to 2.9 when temperature increases from 10 to 100 K. According to these estimates, the conditions taking place at a temperature of 10 K are most favorable for single-mode lasing. However, the middle and the edges of a laser stripe make different contributions to the shift of the gain spectrum and the mode positions. Because of this, the optimum temperature may be somewhat different from the aforementioned value and should be determined in the experiment. Moreover, it is desirable to study the possibility of controlling this temperature.

In the laser under study, the widest tuning range is obtained at a temperature of ~60 K. The fact that the threshold current gradually decreases with decreasing temperature suggests that the charge carrier freeze-out is absent, which makes it possible to use the laser at temperatures down to 12 K. The increase of threshold current with increasing temperature from 60 to 90 K is not so great that the laser is overheated in the course of measurements. All this makes it possible to use the laser in a temperature range of 12–90 K. At the boundaries of this interval, the tuning range narrows by a factor of about 2 in comparison with the maximum width.

The experiments made with laser spectroscopy of gas media showed that the laser was convenient for applications and demonstrated the feasibility of observation of a large number of absorption lines of different gases. The calibration of the laser frequency scale is simplified owing to the record-breaking width of the tuning range (10 cm^{-1}) in the single-mode regime.

CONCLUSION

The study of the laser emission spectra showed that single-mode lasing was realized in a wide range of currents and temperatures. This is associated with the formation of a smooth waveguide across the cavity in which the radiation flux oscillates from one cavity edge to the other and back again, changes the gain spectrum, and maintains in this way its own intensity and oscillations. The equality of the current-induced shift of the peak of the gain spectrum to the shift of the lasing mode is shown to be one of the conditions for single-mode lasing.

We did experiments with laser spectroscopy of gases (OCS, NH_3, CH_3Cl, and H_2O) in the frequency range of the record-breaking width from 3091.6 to 3101.6 cm^{-1} and determined the dependence of the laser radiation frequency on the current.

ACKNOWLEDGMENTS

This work was supported in part by INCO-Copernicus under contract no. 1C15-CT97-0802 (DG12-CDPF), the Ministry of Science of the Russian Federation ("Optics and Laser Physics" Program), the Czech Academy of Sciences (grant no. 4040708), and the Russian Foundation for Basic Research (project no. 99-02-18109).

REFERENCES

1. T. N. Danilova, A. P. Danilova, O. G. Ershov, *et al.*, Fiz. Tekh. Poluprovodn. (St. Petersburg) **31**, 1392 (1997).
2. T. N. Danilova, O. I. Evseenko, A. N. Imenkov, *et al.*, Pis'ma Zh. Tekh. Fiz. **24**, 77 (1998).
3. T. N. Danilova, A. P. Danilova, A. N. Imenkov, *et al.*, in *Proceedings of the Conference "Physics at the Threshold of the XXI Century"* (St. Petersburg, Russia, 1998).

4. T. N. Danilova, A. P. Danilova, A. N. Imenkov, *et al.*, Fiz. Tekh. Poluprovodn. (St. Petersburg) **33**, 1088 (1999) [Semiconductors **33**, 991 (1999)].
5. A. N. Baranov, T. N. Danilova, O. G. Ershov, *et al.*, Pis'ma Zh. Tekh. Fiz. **18**, 6 (1992).
6. Yu. P. Yakovlev, A. N. Baranov, A. N. Imenkov, *et al.*, Kvantovaya Élektron. (Moscow) **20**, 839 (1993).
7. A. Popov, V. Sherstnev, Yu. Yakovlev, *et al.*, Spectrochim. Acta A **54**, 821 (1998).
8. A. G. Maki and J. S. Wells, *Wavenumber Calibration Tables from Heterodyne Frequency Measurements*, NIST Special Publication 821 (Washington, DC 20548, December 1991).
9. G. Guelachvili and K. Narahari Rao, *Handbook of Infrared Standards II with Spectral Coverage of 1.4–4 μm and 6.2–7.7 μm* (Academic, New York, 1993).
10. J.-M. Flaud, C. Camy-Peyret, and R. A. Toth, *Water Vapor Line Parameters from Microwave to Medium Infrared* (Pergamon, Oxford, 1981).
11. A. A. Andaspaeva, A. N. Baranov, B. L. Gel'mont, *et al.*, Fiz. Tekh. Poluprovodn. (Leningrad) **25**, 394 (1991) [Sov. Phys. Semicond. **25**, 240 (1991)].

Translated by A. Kirkin

Semiconductors, Vol. 34, No. 2, 2000, pp. 243–249. Translated from Fizika i Tekhnika Poluprovodnikov, Vol. 34, No. 2, 2000, pp. 249–255.

PHYSICS OF SEMICONDUCTOR DEVICES

6H-SiC Epilayers as Nuclear Particle Detectors

A. A. Lebedev, N. S. Savkina, A. M. Ivanov, N. B. Strokan, and D. V. Davydov

Ioffe Physicotechnical Institute, Russian Academy of Sciences, Politekhnicheskaya ul. 26, St. Petersburg, 194021 Russia

Submitted August 25, 1999; accepted for publication August 25, 1999

Abstract—Schottky diodes based on the n–n^+ 6H-SiC epilayers grown by sublimation epitaxy and also the layers produced by CREE company (USA) were used as detectors of α-particles of spontaneous decay. Since the thickness of n-layers was smaller than the range of the particles, geometrical parameters of the experiment differed from conventional ones; in the latter case, a particle is brought to rest in the region of electric field in the detector. The calculated and experimental data were compared to study the special features of transport of nonequilibrium charge under the conditions of complete and partial depletion of the structure. It is shown that characteristics of the material that govern the transport of charge carriers can be deduced from the analysis of the behavior of the signal amplitude and the shape of the pulse-height spectrum in relation to bias voltage applied to the Schottky diode. It follows from the results that the present-day sublimation-grown SiC layers are suitable for use as the basis for fabrication of nuclear particle detectors. © *2000 MAIK "Nauka/Interperiodica".*

Interest in SiC as starting material for nuclear radiation detectors is related to the fact that SiC is radiation-resistant and the SiC-based devices can operate at elevated temperatures [1, 2]. We remind the reader that the detectors are fabricated on the basis of p^+–n structures or Schottky diodes and, in fact, constitute a solid-state ionization chamber.

Until recently, a major obstacle to the development of detectors has been the poor quality of SiC films. The recent progress in technology has resulted in fabrication of the films whose thickness was comparable to the slowing-down length of short-range ions. Thus, for example, the method of sublimation–condensation was used to grow epitaxial 6H-SiC layers with concentration of noncompensated impurities $N_D^+ - N_A^- \approx 10^{15}$ cm^{-3} and the diffusion length of holes of 2–3 μm [3]. A high electric-field strength corresponding to the breakdown in SiC makes it possible to obtain the space charge layer with the thickness of several micrometers for the above value of $N_D^+ - N_A^-$. A low concentration of nonradiative-recombination centers in these layers ensures that the lifetimes of charge carriers are sufficiently long for effective transport.

In this work, we used the Schottky diodes formed by magnetron sputtering of Ni onto the surface of 6H-SiC layers grown by the sublimation epitaxy. The diameters of barriers were 600–1200 μm. A number of methodological measurements were performed with epitaxial n – n^+ structures produced by CREE Company (USA).

The structures were placed in a forevacuum chamber and were irradiated with ^{244}Cm α-particles having the average energy E_α = 5.77 MeV. Since the thickness of the films was smaller than the range of α-particles (~20 μm), only a fraction of the energy was released in the film. Thus, the detector operated in the mode close to the mode corresponding to determination of specific energy losses dE_α/dx. In this case, the profile of charge-carrier generation may be assumed to be linearly increasing with the distance from the surface of the film because the peak of ionization in the Bragg curve is located close to the end of the path length of a particle.

The nonequilibrium charge induced at the structure's electrodes was detected in the mode of counting the individual particles with the use of conventional spectrometric instrumentation. The latter included a charge-sensitive preamplifier, an amplifier with passband formed by *RC* integrating–differentiating networks, and a generator of stable-amplitude signals. The resulting spectrum of charges was fed to a pulse-height analyzer. The energy calibration of each of the analyzer's channels was performed with the use of a precision silicon detector on the basis of the lines corresponding to the ^{228}Th α-decay. The shape of the spectrum, the average amplitude, and the spectrum's width at the half-height were determined. Simultaneously, the current–voltage and capacitance–voltage characteristics were measured.

As shown below, the combination of the aforementioned measurements makes it basically possible to determine important parameters of the detector. These

1063-7826/00/3402-0243$20.00

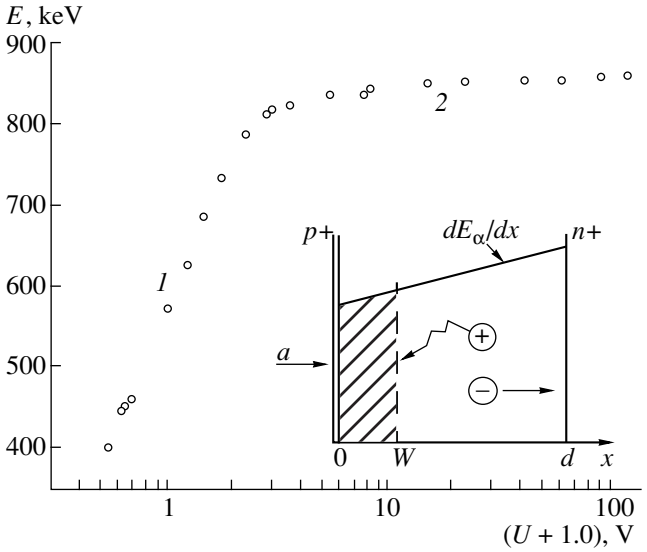

Fig. 1. Average signal amplitude as a function of bias applied to the detector. The portions corresponding to the modes before (*1*) depletion and (*2*) complete depletion are indicated. The configuration used in the analysis of diffusion is illustrated in the insert; the shaded area corresponds to the field region with the width *W*.

include the average formation energy ε of electron–hole pair, the diffusion length of holes $L_0 = (D\tau_0)^{1/2}$, the degree of nonuniformity of the lifetime of holes $\Delta\tau/\tau_0$ over the structure's base, and the lifetimes of charge carriers prior to their trapping during the drift in the depletion region. Here, D is the diffusion coefficient and τ_0 is the average value of lifetime.

1. AVERAGE ENERGY OF FORMATION OF AN ELECTRON–HOLE PAIR

A typical dependence of the average signal amplitude on the bias applied to the detector is shown in Fig. 1. The relevant curve has two portions differing in the rate of an increase in amplitude, which correspond to the bias voltages prior to and after the complete depletion of the structure. In fact, as long as the electric field region occupies a fraction of the *n*-base, diffusion of holes in the base should be considered along with the drift of charge carriers in the region of the field. The fact that the diffusion has a lower rate as compared to the drift brings about substantial losses of charge due to charge-carrier recombination. To the first approximation, the signal increases proportionally to the width of the field region.

When the depletion is attained and the field region occupies the entire thickness of the film, only the drift of charge carriers is of importance. Since the electrons and holes are effectively separated by the field, the losses of charge in this case are defined by localization of charge carriers at the trapping centers, rather than by recombination. In this case, the centers trapping the charge carriers for a time larger than the time needed to form the pulse by the measuring instrumentation (on the order of 1 μs) are most important. The signal amplitude increases with an increase in the bias voltage owing to an increase in the drift velocity. The charge transport may be regarded as lossless in the saturation region.

In order to determine ε, we have to find the energy deposited in the film. To this end, we use the results of mathematical simulation of the slowing-down of α-particles with the use of the TRIM code (see [4]). According to [4], the specific energy losses of α-particles in SiC in the case of small thicknesses under consideration increase linearly with the coordinate x as $dE_\alpha/dx = (14.3 + 0.36x)$ eV/Å. As a result, the energy $E = 10^4(14.3 + 0.36d/2)d$ eV, where d is the film thickness in micrometers, equal approximately to 1.6 MeV for $d = 10$ μm is released in the film. The film thickness is determined from the capacitance measurements and specifies the value of E.

As was mentioned above, the detected signal is proportional to the charge introduced by the particle $Q_0 = eN$, where N is the number of generated electron–hole pairs and e is the elementary charge. Therefore, the proportion $E/\varepsilon = E_{sat}/\varepsilon_{Si}$ is used; here, E_{sat} is the energy determined with silicon detector in the saturation region and $\varepsilon_{Si} = 3.62$ eV. In this way, the value of ε = 6.8 eV was obtained. As will be shown below, the value of ε can be refined by analyzing the portion of the diffusion–drift transport.

2. THE DIFFUSION LENGTH OF HOLES

The case of steady-state and spatially uniform charge-carrier generation induced by light or electrons [5, 6] was considered previously. It is noteworthy that a steady-state excitation changes the population of deep levels. In the case of generation of charge carriers by individual α-particles, diffusion of charge carriers occurs under the conditions of equilibrium population, which can affect the values of the diffusion length L.

In order to take into account the dependence of generation on the coordinate (in the case under consideration, $dE_\alpha/dx = G(x) = 1 + bx$), we should calculate the losses of the charge $\lambda = 1 - Q/Q_0$ (see [6, 7]) using the following formula valid for $(d - W)/L_0 > 2$:

$$\lambda = \frac{\int_W^d G(x - W)[1 - \exp(W - x)/L_0]d(x - W)}{d(1 + bd/2)}. \quad (1)$$

Here, Q is the detected charge and $Q_0 \propto d(1 + bd/2)$. For $G(x) = 1$, formula (1) yields the known result

$$Q/Q_0 = (W + L_0)/d. \quad (2)$$

The expression for the dependence $\lambda(W, L_0)$ turns out to be cumbersome; therefore, it is not written out here. However, it is possible to use this expression for fitting with the use of two parameters (L_0 and d, see Fig. 2). In this case, the values of λ are calculated from the data of Fig. 1 as $\lambda = (E_{sat} - E)/E_{sat}$, and the quantity W is determined from the capacitance measurements. As a result, the value of $L_0 = 2.42$ μm is determined, and the value of d is refined. In the case under consideration, it follows from the capacitance measurements that $d = 10$ μm. The fitting procedure yielded $d = 9.76$ μm, which defined the value of the average formation energy of electron–hole more correctly as $\varepsilon = 6.7$ eV.

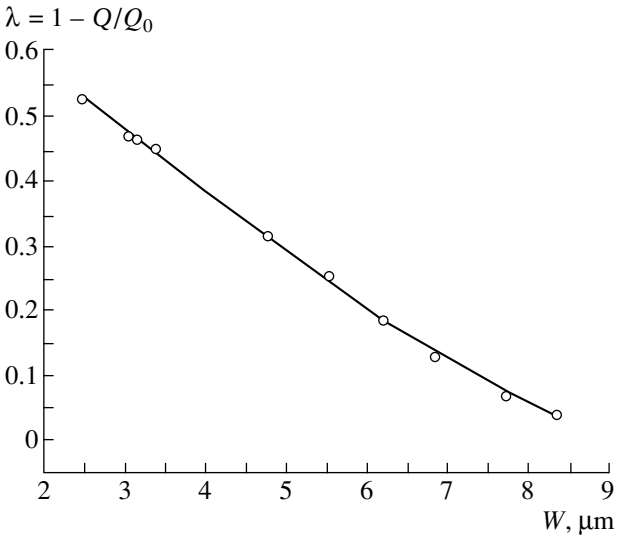

Fig. 2. The experimental recombination-related losses of the hole-transported charge diffusing in the base as a function of the extent of the field region. Comparison with formula (1) yields the values of 2.42 and 9.76 μm for the diffusion length L of holes and the film thickness d, respectively; the value of L is close to the corresponding value measured in the same films by the method of electron-beam induced current (EBIC) [3].

3. THE SHAPE OF THE PULSE-HEIGHT SPECTRUM IN THE CASE OF DIFFUSION AND ITS RELATION TO THE HOLE LIFETIME

The use of α-particles makes it possible to determine the nonuniformity of distribution of τ over the film area [8]. In fact, the tracks of α-particles constitute dense bunches of electron–hole pairs with the diameter of about several tens of micrometers. Therefore, the amount of the charge contributed by each particle is representative of the conditions of transport in a microscopic volume. It is due to chaotic incidence of particles on the detector that the statistical distribution of τ (as a parameter most sensitive to structural imperfections) over the sample's area manifests itself. As a result, the shape of pulse-height spectrum happens to be related to the nonuniformity of distribution of τ.

3.1. Calculation of the Shape of the Spectrum

The pulse-height spectrum is plotted in the coordinates $dN/dq = f(q)$, where dN is the number of counts in the amplitude range dq and the values of q are normalized to the introduced charge. In order to represent the spectrum, we use the approach reported in [8]. Namely, the identity $dN/dq \equiv (dN/d\tau)(d\tau/dq)$ is used, and the problem consists of the choice of the form, the distribution of τ, and the function $q = f(\tau)$. Following the reasoning used in [8], we assume that the $dN/d\tau$ distribution is Gaussian with the variance equal to σ; thus, we have

$$dN/d\tau = \exp[-(\tau - \tau_0)^2/2\sigma^2]/(\sqrt{2\pi}\sigma). \quad (3)$$

We also introduce the width of the range of values of τ at the spectrum's half-height as $\Delta\tau = 2.35\sigma$. For the sake of simplification, we regard the generation as uniform over the thickness of the film; in this case, the form of $d\tau/dq$ can be determined from (2). As a result, discarding the numerical factors, we arrive at the following system of equations:

$$dN/dq = (\tau/\tau_0)^{1/2}\exp[-(\tau/\tau_0 - 1)^2/0.362(\Delta\tau/\tau_0)^2], \quad (4)$$
$$q = (W + L_0\sqrt{\tau/\tau_0})/d.$$

It follows from (4) that W/d, L_0/d, and $\Delta\tau/\tau_0$ are the basic parameters of the spectra. Furthermore, their influence on the spectrum's shape is different. Thus, the quantity W/d merely shifts the positions of the peaks, without affecting the spectral width. On the other hand, the nonuniformity of τ defines the width alone. The values of L_0/d affect the spectrum as a whole. Figure 3 shows how the charge-signal spectrum is transformed when $\Delta\tau/\tau_0$ is varied. It is evident that the spectra are symmetric up to the value of relative nonuniformity equal to 50% ($\Delta\tau/\tau_0 = 0.5$). As the value of $\Delta\tau/\tau_0$ increases to unity, an asymmetry arises owing to the emergence of an extended region of small amplitudes at the left wing of the spectrum. However, the full width at half maximum (FWHM) is described by a linear function (see the insert in Fig. 3) in the entire range of values of $\Delta\tau/\tau_0$.

The dependence of the line width on L_0/d indicates that this dependence is also linear, with the slope being proportional to $\Delta\tau/\tau_0$. As a result, we obtain the following expression for the spectral-line width normalized to the introduced charge:

$$(Q_2 - Q_1)/Q_0 = 0.48(\Delta\tau/\tau_0)(L_0/d). \quad (5)$$

It is evident that the linewidth is independent of the value of W/d, i.e., of the bias voltage. The latter is obvious because the fluctuations of the detected charge were related to the diffusion of charge carriers.

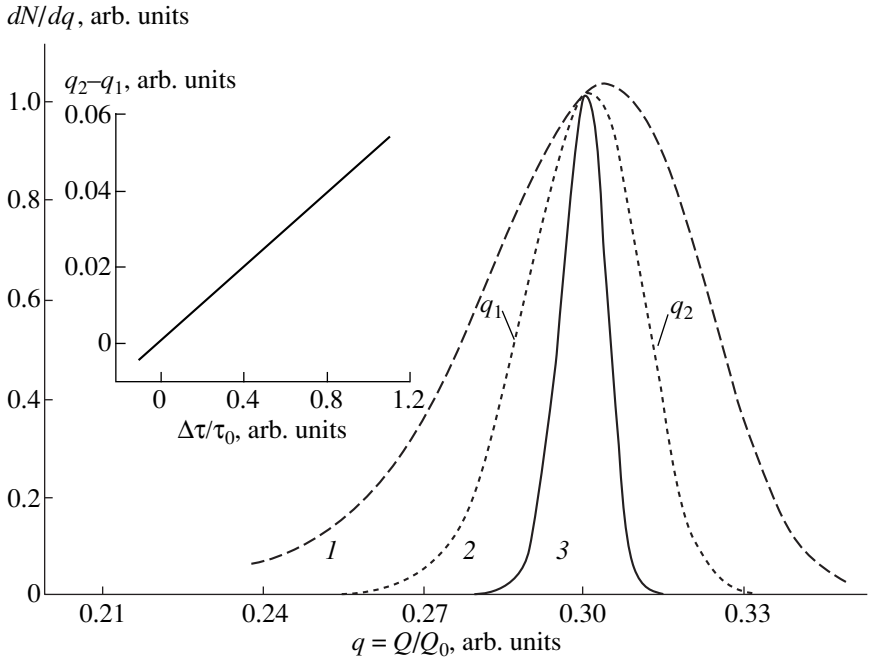

Fig. 3. The results of calculations of the pulse-height spectrum in the case of hole diffusion in the base of the structure with allowance made for fluctuations of lifetime over the film area. The distribution of lifetime is assumed to be described by a Gaussian function. $W/d = 0.2$; $L_0/d = 0.1$; and $\Delta\tau/\tau_0$ = (*1*) 100%, (*2*) 50%, and (*3*) 20%. The spectral-line width as a function of $\Delta\tau/\tau_0$ is shown in the insert.

3.2. Experiment

The pulse-height spectrum was measured in the films with $N_D^+ - N_A^- = 10^{16}$ cm^{-3}. The value of L_0 determined according to (2) was equal to 0.64 μm. In view of large values of $N_D^+ - N_A^-$ and small values of L_0, the signals were also small and the noise interferences contributed additionally to symmetrization of the spectra. Visually, the spectra were Gaussian, from which it was possible to infer that the nonuniformity of τ did not exceed 100%. Unfortunately, depletion was not attained in these samples, and it was impossible to identify the film thickness d in order to determine the nonuniformity of the lifetime distribution $\Delta\tau/\tau_0$ according to formula (5).

This procedure was used for a film of higher purity with $L_0 = 2.4$ μm and $d = 9.76$ μm. Figure 4 shows the trend of the linewidth normalized to the introduced charge in relation to the extent of the field region. An increase in the linewidth with an increase in W is inconsistent with formula (5) and indicates that the charge-carrier drift in the field region yields a certain contribution to the fluctuations of the resulting amplitude. As follows from Fig. 4, the dependence $(q_2 - q_1) = f(W)$ is linear; therefore, the extrapolation of this dependence to $W = 0$ yields the value of $q_2 - q_1$ for the diffusion-related transport.

The value of $q_2 - q_1 = 0.075$ thus obtained makes it possible to use formula (5) to determine $\Delta\tau/\tau_0 = (0.075/0.48)(d/L_0) \approx 0.6$ (or 60%), which corresponds to the average level of nonuniformity of lifetime in silicon.

4. DRIFT TRANSPORT AND THE TRAPPING TIME OF CHARGE CARRIERS

4.1. Calculation

Following the attainment of complete depletion in the base, the field distribution and the profile of generation of charge carriers in the structure have the form shown in the insert in Fig. 5. We here adhere to the configuration reported in [9], where the drift of charge carriers in a linearly varying field for generation at an arbitrary point x was considered. In the case under consideration, we should also take into account the nonuniform distribution of generation and determine the average charge magnitude for the given conditions.

To this end, it is necessary to perform a number of calculations; first of all, we should calculate the concentration of charge carriers as a function of coordinate when the generation is located at an arbitrary point y; we should then find the charge $q(y)$ induced at the electrodes; and finally we should determine the average magnitude of the charge with the allowance made for the generation profile $G(y)$.

For example, for holes, the above procedure is written as

$$p(x) = G(y)\exp\left(-\int_y^x dx/\mu\tau_1 E\right);$$

$$q(y) = 1/d\int_y^d p(x)dx;$$

$$\bar{q} = \left[\int_0^d G(y)q(y)dy\right]/d(1-k/2).$$

Here, the electric-field strength $E(x) = a + \rho x$, where $\rho = (4\pi/\chi)\rho_0$; χ is the permittivity; ρ_0 is the space-charge density; $G(y) = 1 - k(y/d)$; $Q_0 \propto d(1 - k/2)$; μ is the mobility of holes; and τ_1 is the lifetime of holes until they are localized at the trapping centers.

For the sake of simplification, we treat the trapping rate as low and describe it by the linear term in the expansion of exponential function. In this case, we have

$$p(x) = G(y)\left[1 - \int_y^x dx/\mu\tau_1 E\right].$$

In this treatment, the solutions are easily interpretable in the case of uniform field $E(x) = \text{const}$ and the equiprobable generation $G(y) = 1$. In this case, we have

$$q(y) = (1 - y/d)[1 - (d - y)/2\mu\tau_1 E];$$

$$\bar{q} = 0.5(1 - d/3\mu\tau_1 E).$$

Similar expressions are valid for electrons. The linear behavior of the field complicates the above relationships by introducing into them the logarithmic dependence on voltage (see [9]). In order to make the differences clearer, Fig. 5 shows the ratio of the charge losses in localization for the cases of linear (λ_{lin}) and uniform (λ_{const}) spatial distributions of the field. We used the following formula:

$$\lambda_{lin}/\lambda_{const} = 1.5U_*^2\left[1 - 0.5\left(\frac{U_*^2 - 1}{U_*}\right)\ln\frac{U_* + 1}{U_* - 1}\right]. \quad (6)$$

Here, U_* is the ratio of the voltage applied to the structure to the voltage V_{dep} corresponding to complete depletion. It is evident from Fig. 5 that, for $U_* \geq 10$, there is no difference in the amount of losses. It is characteristic that, in the case of uniform generation, the expressions for the charges transported by electrons and holes are identical.

If the generation is nonuniform over the depth, the formulas for electrons and holes become different. The formulas lose their clarity, and the end result is given below without derivation; i.e.,

$$\lambda_h = \frac{0.25d^2}{(1-k/2)V_{dep}(\mu\tau)_h}\left\{U_* + \frac{k}{3} - \frac{k}{4}(U_* + 1)(2 - U_*) - \frac{U_*^2 - 1}{2}\left[1 + \frac{k}{4}(U_* - 1)\right]\ln\frac{U_* + 1}{U_* - 1}\right\}, \quad (7)$$

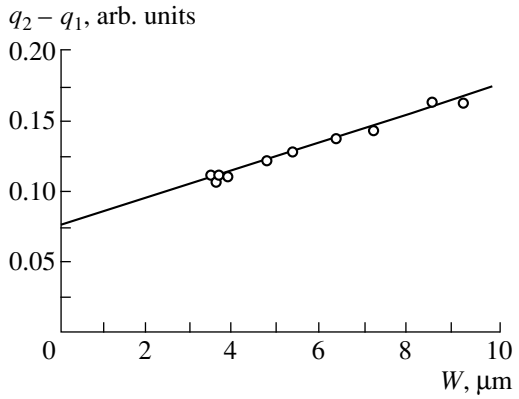

Fig. 4. Experimental dependence of the spectrum width on the extent of the field region. The value of the width for $W = 0$ corresponds to fluctuations in the course of diffusion of holes.

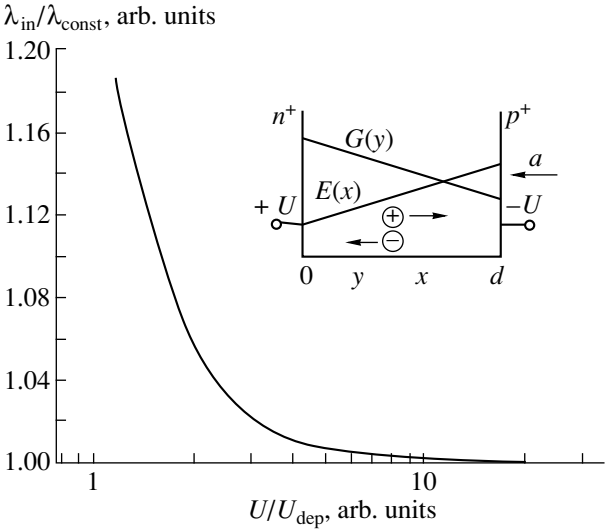

Fig. 5. Losses of charge in the course of drift of holes in two typical cases of spatial dependence of the field strength. We have here the mode of complete depletion of the structure. The quantities λ_{const} and λ_{lin} correspond to the constant field strength and the field strength that depends linearly on the coordinate. The configuration of the detector in the mode of complete depletion is shown in the insert; the field strength and the density of generation of charge carriers depend linearly on the coordinate.

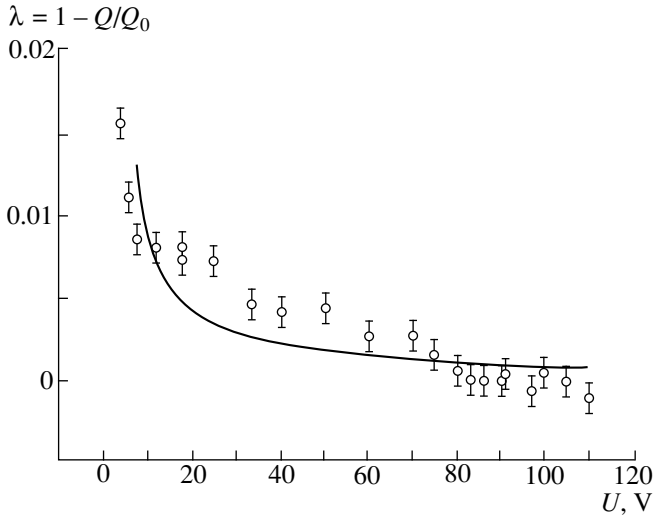

Fig. 6. Loss of the charge transported by holes as a function of voltage applied to the detector in the case of drift transport. The circles correspond to experimental data, and the solid line represents the results of calculations by formula (7) for τ_h = 35 ns and V_{dep} = 6.7 V.

$$\lambda_e = \frac{0.25d^2}{(1-k/2)V_{dep}(\mu\tau)_e}\left\{U_* - \frac{2}{3}k - \frac{k}{4}(U_*-1)(2-U_*) - \frac{U_*^2-1}{2}\left[1-\frac{k}{4}(3-U_*)\right]\ln\frac{U_*+1}{U_*-1}\right\}. \quad (8)$$

4.2. Experiment

In order to illustrate the analysis of the charge losses measured in the drift mode, we use the data shown in Fig. 1. These data make it possible to plot the amount of losses as a function of voltage, so that the experimental data can be compared with the results of calculations by formulas (7) and (8) (Fig. 6). The value of V_{dep} was determined from the capacitance measurements and, thus, was taken equal to 6.7 V. The lifetimes τ_e and τ_h were used as the adjustable parameters. The test for an agreement between the results of calculations and experimental data consisted in the requirement that the rms deviation be as small as possible. This deviation was found to be significantly smaller, if we used formula (7) where hole-related losses were prevalent. The value τ_h = 35 ns obtained in this case is smaller than the hole lifetime determined from the diffusion-mode transport and equal to 62 ns (see Fig. 2 where the diffusion length L = 2.42 μm was determined). In our opinion, this discrepancy is related to a difference in population of trapping centers. In fact, diffusion occurs under the conditions of equilibrium population of the levels, whereas the drift takes place under nonequilibrium conditions, in which case the population of trapping levels is much lower.

DISCUSSION OF RESULTS

It is important from the practical standpoint that, in the state-of-the-art SiC films, the concentration of impurities is sufficiently low, so that these films may be used to fabricate the ion detectors. First, the actual difference between the concentrations of donors and acceptors makes it possible to obtain the required extent of the space-charge region. Second, the small total number of deep-level centers ensures that the lifetime is sufficiently large for effective transport of charge carriers in the operating zone of the detector. The structures based on SiC films (for example, the α-particle counters) detect the particles even if they operate under zero bias, i.e., when the diffusion is prevalent in the transport.

The efficiency of conversion of the particle energy to the nonequilibrium charge is governed by the value of average energy ε spent for generating an electron–hole pair. These pairs are generated in the collision cascades brought about by δ-electrons. Furthermore, the energy of hot charge carriers is spent for an exciting the phonons. There are empirical formulas available that relate the band gap E_g, the losses due to phonons E_{ph}, and the resulting value of ε, and are written as $\varepsilon = 2.16E_g + E_{ph}$ (see [10, 11]). For different materials, the values of E_{ph} are found to be in close agreement; for example, the values of E_{ph} are approximately equal to 1.2 eV for diamond and GaAs. Using this value, we find that, in the case under consideration, the multiplier of E_g is equal to ~1.9. To put it differently, the ionization occurs with somewhat higher efficiency in the SiC films we studied than it does in the aforementioned materials.

CONCLUSION

We demonstrated that the present-day level of sublimation-based technology of SiC makes it possible to produce epitaxial layers whose quality satisfies the conditions for the ion detection. Even for $N_D^+ - N_A^- \approx 10^{16}$ cm^{-3}, the lifetime is sufficiently large for efficient drift transport of charge in the detector.

The dependence of induced charge on the bias applied to the detector has two characteristic portions related to the mechanism of the charge transport: either the drift under the conditions of complete depletion or the drift with the diffusion involved prior to the stage of complete depletion.

We derived the formulas describing the losses of charge in the aforementioned operating modes. Using these formulas, we determined the key transport parameters, such as the lifetimes of charge carriers in the course of drift, the diffusion length of the minority

charge carriers in the base, and the degree of the lifetime nonuniformity over the area of the film.

REFERENCES

1. R. V. Babcock and H. C. Chang, *Neutron Dosimetry* (Springer-Verlag, Vienna, 1963), Vol. 1.
2. P. C. Canepa, P. Malinaric, R. B. Campbell, *et al.*, IEEE Trans. Nucl. Sci. **11** (3), 262 (1964).
3. N. S. Savkina, A. A. Lebedev, D. V. Davydov, *et al.*, in *Abstracts of the International Conference on SiC* (Montpellier, 1998), p. 135.
4. *Ion Implantation. Science and Technology*, Ed. by J. F. Ziegler (Academic, New York, 1984).
5. R. A. Logan and A. G. Chynoweth, J. Appl. Phys. **33**, 1649 (1962).
6. V. V. Makarov, Fiz. Tekh. Poluprovodn. (Leningrad) **9** (6), 1098 (1975) [Sov. Phys. Semicond. **9**, 722 (1975)].
7. I. N. Il'yashenko and N. B. Strokan, Fiz. Tekh. Poluprovodn. (St. Petersburg) **30** (2), 302 (1996).
8. N. B. Strokan, Pis'ma Zh. Tekh. Fiz. **24** (5), 44 (1998).
9. V. K. Eremin, S. G. Danengirsh, N. B. Strokan, *et al.*, Fiz. Tekh. Poluprovodn. (Leningrad) **8** (3), 556 (1974) [Sov. Phys. Semicond. **8**, 355 (1974)].
10. C. Canali, M. Martini, G. Ottaviani, *et al.*, IEEE Trans. Nucl. Sci. **19** (4), 9 (1972).
11. R. D. Ryan, Nucl. Instrum. Methods Phys. Res. **120** (1), 201 (1974).

Translated by A. Spitsyn